Modelling Nonlinear Acoustics in Brass Instruments

by

Freddie Jensen

Thesis
A thesis submitted in partial fulfilment of the requirements
for the degree of
Doctor of Philosophy in Mathematics

University of Warwick, Mathematics Institute

October 2025

THE UNIVERSITY OF
WARWICK

Contents

List of Figures

Acknowledgments

This thesis would not have reached its current state, or any state of completion at all, without the help of those close to me. I cannot thank my parents enough for their unconditional support, and for encouraging me to do a PhD in the first place; thank you to Monica for being an endless source of entertainment and good humour; thank you to Granny for always providing a place to rest whenever I've needed time away from work, and to Farfar, whose eternal ability to find the fun side of technical subjects has played a big part in my enjoyment of my own. Thanks finally to Defne for making the last year so wonderful.

I am grateful to my supervisor, Dr Ed Brambley, for being so generous with his time and his invaluable expertise; I would additionally like to thank him for encouraging me to travel widely for the conferences that I attended during the PhD, as this has resulted in some unforgettable and eye-opening trips. I would like to thank Dr Shreyas Mandre for his help and advice near the beginning of the PhD, and for his very inspiring lecture course on surface tension during my first year; thanks also to Harry Turnbull for making astonishing progress on the duct exit condition during his URSS project, without which chapter 5 here would barely be a fraction of its current length.

Thanks must also go to the friends who have made my time at Warwick special in myriad ways, such as organising departmental pub quizzes, film nights and concert trips, keeping the office well-stocked with snacks, offering sometimes-useful bouldering advice, getting stuck in stationary traffic for 3 hours on my behalf, buying me books in German that I will almost certainly never be fluent enough to read, and providing thoughtful guidance on how best to present plots of the duct geometries featured herein. A necessarily non-exhaustive list of those I would like to thank is as follows: Kat, Khalid, Dan, Alvaro, Phil, Thomas, Arjun, Diana, Seth, Cam, Marc, Darragh, Phoebe, Tara, Jack, Yorick, Nicola, Poppy, Sasha, Toby, Paweł, Luisa. I will miss you all.

Declarations

This thesis is submitted to the University of Warwick in support of my application for the degree of Doctor of Philosophy in Mathematics. It has been composed by myself and has not been submitted in any previous application for any degree. The work presented (including data generated and data analysis) was carried out by the author. In particular, while the author is grateful to Harry Turnbull for the notes from his URSS project concerning sections 5.1.1–4, the derivation of these sections as presented here is entirely due to the author.

Parts of this thesis have been published by the author:

- Chapters 2 and 3 as Jensen and Brambley [2025].
- Chapters 4 and 5 as Jensen, Turnbull, and Brambley [2025].

Abstract

This thesis develops a weakly-nonlinear model of zero-mean-flow duct acoustics in 2D and 3D, and a weakly-nonlinear exit condition for open duct ends. The model allows for duct curvature and width variation, and in 3D extends to torsion. To this author's knowledge, it is the first instance of nonlinearity's combination with either complex duct geometry in 3D or an acoustic open end: these three phenomena become inextricably linked when considering sound in brass instruments, since their distinctive timbre is understood to be due to nonlinearity. Although here simple examples are used to illustrate the model's results, brass instruments are the primary intended future application; others include woodwind instruments, air-conditioning ducts, exhaust pipes, and elephant trunks.

The method begins with the double series-expansion of the weakly-nonlinear gas dynamics PDEs, first in time, and then in space. This results in an infinite set of coupled ODEs, which are advantageous both due to the relative computational ease of their solution, and the intuition they provide as to nonlinearity's interaction with geometry. The interaction is first modelled with a simplified nonreflecting exit condition; while physically idealised, this provides numerical validation, before novel study of, for instance, the effective acoustic length of a bend.

An open exit condition is then formulated. Free space is approximated by considering the open-ended duct to be enclosed within a much larger concentric duct, within which the smaller duct's outlet is modelled as an acoustic discontinuity. The model does not rely upon the superposition principle, allowing for its application in the nonlinear regime; first, however, the model's validity in the linear regime is established by comparison with the classical Wiener–Hopf end correction result. The application is then the computation of a newly-proposed nonlinear end correction, alongside other numerical examples.

Chapter 1

Introduction

This thesis concerns itself with the study of duct acoustics in the absence of mean flow. The primary physical application of this work is that of sound in woodwind or brass instruments, but others include air-conditioning ducts, elephant trunks, or automotive exhaust pipes. Approaching the maths from a physical angle, there are naturally many different effects one could choose to include, such as the biomechanics of the human mouth at the duct inlet, the material properties of the wall (which may be wooden, metallic, or in some contemporary instruments even plastic) and the presence of valves or keys to change the resonating length of the instrument. However, the specific interest here is the phenomenon of nonlinearity, and how it interacts with a) the complicated geometry that woodwind and brass instruments can exhibit and b) wave reflection and propagation at the duct outlet. The other effects mentioned above will not be focused on here, as these two interactions provide the two main research aims.

Formerly, the three phenomena (nonlinearity, duct geometry and the duct exit condition) have been modelled separately (see figure 1.1), since each is a rich source of mathematical interest on its own, and equations easily become intractable if too much physics is considered at once. To lay the groundwork for the combination of these three areas, an overview of the preexisting work within each of them is given first.

Brass instruments are understood to sound brassy due to nonlinear wave-steepening within the instrument [Hirschberg et al., 1996]. This has been observed experimentally for a trombone [Hirschberg et al., 1996; Rendón et al., 2010] and for a trumpet [Pandya et al., 2003; Rendón et al., 2013, see figure 1.2], and is supported by relatively simple physical models [e.g. Gilbert et al., 2008]. It is thought that the difference in sound quality between a brass instrument and a woodwind instrument is due to the presence of nonlinearity in the former but not the latter: for the latter, a linear acoustic model would therefore be valid. In the studies just mentioned, attention is often given to the width, or bore, of an instrument, and its variation along the instrument's length. Varying the bore so that it progressively gets wider lowers the amplitude of the outward-propagating wave, resulting in less nonlinear steepening and

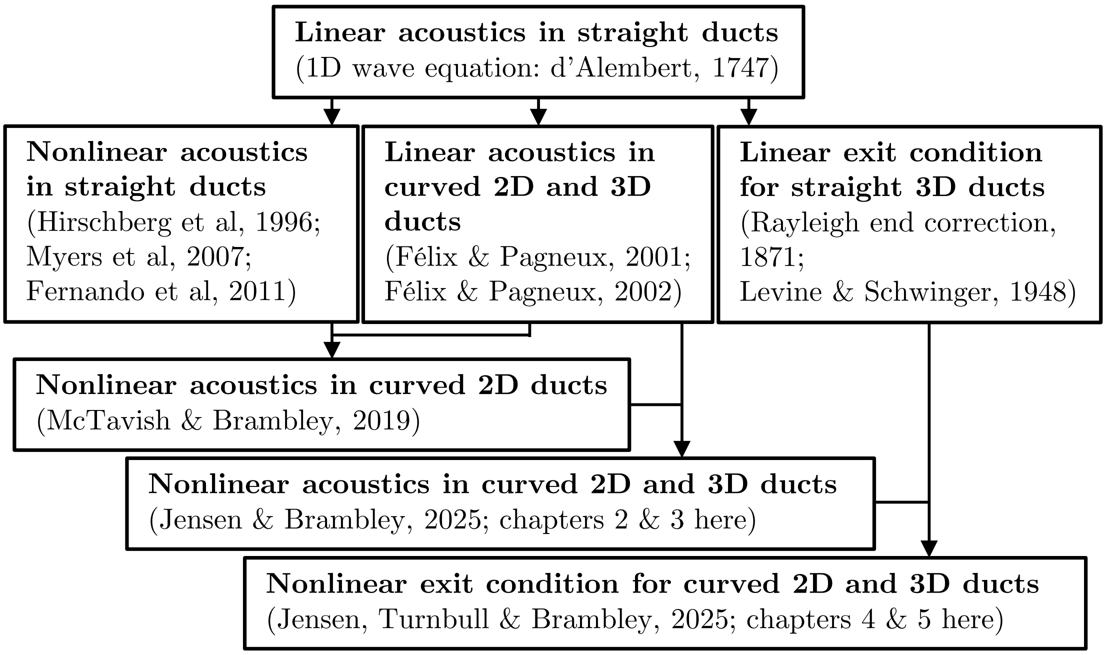

Figure 1.1: Overview of the research areas being combined here, and their source [d'Alembert, 1747].

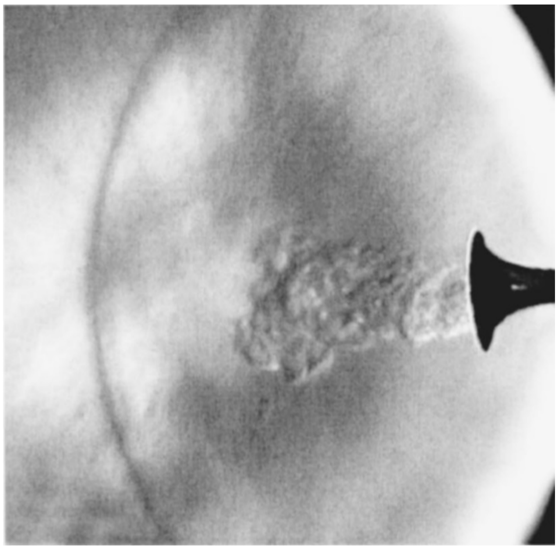

Figure 1.2: Schlieren image of a shock wave emanating from the bell of a trumpet, taken from Pandya et al. [2003].

a less brassy sound. Conversely, a cylindrical bore that does not widen (such as is necessary for a trombone slide to be able to slide) allows nonlinear steepening to occur, exciting higher harmonics and leading to a more brassy sound. Myers et al. [2012] even proposed a dimensionless brassiness parameter B based on the bore variation in order to quantitatively classify musical instruments by their brassiness.

Nonlinearity can be quantified by the *perturbation Mach number* M. The Mach number is typically a ratio of a velocity-scale within a problem, for instance the mean flow through an aircraft engine, to the speed of sound: thus, a Mach number greater than 1 is a *supersonic* flow. The perturbation Mach number more specifically refers to the ratio of a disturbance's velocity (specifically a disturbance to the mean flow) to the sound speed; in a zero-mean-flow setting like brass instrument acoustics, the perturbation Mach number is really therefore the *only* measure of nonlinearity. The Mach number need not be greater than 1 for shocks to be achievable in a model: the model presented in this thesis in fact relies on a small, subsonic perturbation Mach number. The resulting *weak shocks* are then small discontinuities travelling at the sound speed, unlike *strong shocks*, which are larger discontinuities travelling faster than the sound speed. The Mach number M may be related to sound volume (in room-temperature air) by

$$\mathrm{SPL} \sim 194 + 20\log_{10} M\,\mathrm{dB} \tag{1.1}$$

where 'SPL' is the root-mean-squared *sound pressure level.* At the mouthpiece of a brass instrument, the SPL can reach up to 170dB, corresponding to a Mach number of just under 0.1, so throughout this thesis the Mach number is taken to be small but significant enough for shocks to form (this argument was made in McTavish and Brambley [2019], but equally applies here). The fundamental of a tenor trombone in first position is B$\flat_1$, or 58 Hz, corresponding to a wavelength of $\hat{\lambda} = 5.9\,\mathrm{m}$; for Mach number $M = 0.1$ this corresponds to a shock-formation distance of $\hat{s}_{\mathrm{sf}} = \hat{\lambda}/M\pi(\gamma+1) = 7.8\,\mathrm{m}$, with every n-th higher harmonic in first position then corresponding to a division of the shock-formation distance by n. A trombone has a length of about 2.7 m, so frequencies from the 3rd harmonic upwards will cause shocks to form within the instrument.

Most of the modelling in this area assumes plane-wave propagation and straight ducts, although Fernando and Druon [2011] allowed for non-plane-wave propagation by introducing a cross-duct modal expansion while retaining the straight duct approximation. However, very few brassy-sounding musical instruments are straight; for example, a traditional B$\flat$ trumpet has a duct that, if straightened, would be about three times as long as the instrument. Thus, previous modelling is valid only for examination of instruments like those shown in figure 1.3. In order to investigate the acoustics of curved ducts, Félix and Pagneux [2001] generalized the multi-modal method previously developed by Pagneux et al. [1996] for ducts with width variation. Initially developed in 2D, it was subsequently extended to 3D [Félix and Pagneux, 2002]. The multi-modal method involves the projection of the curved-duct acoustics equations for pressure and

Figure 1.3: Illustration (from the *Cantigas of Santa Maria*) of Spanish trumpeters playing the *buisine*, a medieval ancestor of the trumpet with width variation but no curvature or torsion. The buisine is a brass instrument, making a nonlinear model necessary: this together with its relatively simple geometry makes it an ideal application of Fernando and Druon [2011]. Taken from Wikipedia [2025].

Figure 1.4: A bass flute. This is a woodwind instrument, meaning that linear acoustic modelling is valid; it is 3D and exhibits curvature, but no torsion or width variation, making it an ideal application of Félix and Pagneux [2002]. Photograph from Yamaha Corp. [2017].

velocity onto a basis of straight-duct modes, converting the governing PDEs into an infinite coupled set of ODEs for the amplitude of each mode. The ratio of the velocity and pressure, known as the admittance, is then taken, and a Riccati-style equation for the admittance is solved. As well as being computationally tractable, this formulation has the potential to provide better physical intuition than, for example, direct numerical simulation, as the admittance encodes the downstream effects of the duct geometry independently of the form of the acoustic wave introduced upstream. This will be seen below, as a similar procedure here will be followed here. However, this multi-modal method depends on the linearity of the acoustic equations, and so is not able to model the weak nonlinearity necessary for investigating brassiness. Thus, it would be suitable for modelling the acoustics in woodwind instruments such as the bass flute (see figure 1.4), but not the acoustics in any brass instrument.

The tuning of a wind instrument is given by the effective length of the duct, and acoustic modes travelling around the outside of a duct bend would see a different effective length compared with acoustic modes travelling around the inside of a duct bend, resulting in a different resonant pitch. Brass instruments shift their pitch slightly when played louder. Could perhaps nonlinear steepening affect the effective length of a duct bend? Could instruments be designed for pitch stability as the sound amplitude

Figure 1.5: A trumpet. This is a brass instrument, meaning that nonlinear acoustic modelling is necessary; it is 3D and exhibits curvature, torsion and width variation, making its *internal* acoustics an ideal application of Jensen and Brambley [2025] (the work of chapters 2 and 3 here). Photograph by Yamaha Corp. [2022].

is varied? Or, if curved ducts behave similarly to straight ducts, is it possible to say why and to quantify the extent to which they do so? Such an analysis would require a framework capable of analysing nonlinear acoustics in curved ducts, i.e. the first aim of the work presented here.

Recently, McTavish and Brambley [2019] combined the curved-duct linear multimodal method of Félix and Pagneux [2001] with the straight-duct nonlinear multimodal method of Fernando and Druon [2011] to describe the weakly-nonlinear acoustics of curved ducts in 2D. Even restricted to 2D, the algebraic complexity of the resulting system was prohibitive, and so a linear matrix and nonlinear tensor convolution notation was developed. However, because the matrices and tensors involved in the governing equations varied as the duct geometry varied, the technique was computationally inefficient; nonetheless, it was possible to analyse a range of curved geometries in both the linear and nonlinear regimes, meaning that this was the first model capable of modelling the acoustics of brass instruments specifically (a suitable application would be the trumpet in figure 1.5, for example).

One notable example that caused numerical difficulties was the ‘elephant’s trunk’, a bend of constant curvature with width that decreases cubically along the duct. Ducts of decreasing width pose problems because they can give rise to nodes in certain pressure modes: within the multi-modal framework, nodes correspond to singularities in the admittance. McTavish and Brambley [2019] dealt with this problem by adding a stabilising imaginary component to the wavenumber; another option is the use of a ‘Magnus–Möbius scheme’. This unites the ‘Möbius method’ [Schiff and Shnider, 1999], a means of integrating across singularities in scalar Riccati equations, with the Magnus expansion as applied to linear matrix ODEs [Iserles and Nørsett, 1999]. In this thesis, there is a predominant reliance on the complex wavenumber, but the Magnus-Möbius method is developed in chapter 2 and tested in chapter 3.

The key drawback of the model used in McTavish and Brambley [2019] (and previous models mentioned), was its use of the *characteristic admittance* as an outlet condition: this is essentially a mathematical contrivance corresponding physically to the duct outlet continuing in an infinite straight line with internal forward propagation only. In other words, minimal attention was given to the *duct exit condition*.

Study of the duct exit condition is an important component of a model of duct acoustics. An accurate picture of wave reflection and transmission at a duct outlet will inform modelling of both the duct's interior acoustics and its exterior radiative properties. For example, the fundamental resonance of a cylindrical duct closed at one end and open at the other is a quarter wavelength, with, at the closed end, a velocity node giving a pressure anti-node, and a pressure node located a short distance beyond the open end; this distance, known as the *end-correction*, was postulated by [Rayleigh, 1871] to be about $0.6R$, where R is the duct radius. Subsequently, Levine and Schwinger [1948] made great progress in using the complex-analytic Wiener–Hopf technique to calculate the acoustic radiation from an unflanged cylindrical pipe, enabling them to calculate an end correction of $0.6133R$. Subsequent work has attempted to extend their low-frequency calculation to higher spatial modes and frequencies [e.g. Weinstein, 1948; Snakowska et al., 2011]; however, all analytical work to date in this area has been *linear*.

This leads to the second aim of this thesis: to create an analytical model of the duct exit that is compatible with the weak nonlinearity of Jensen and Brambley [2025]. To do so, inspiration is taken from the linear duct exit studies of Kemp et al. [2017], Félix et al. [2018], and Mangin [2023] in their use of another, larger duct, concentric with the original duct, as the 'room' into which radiation is emitted; this is intended to approximate free space as the outer duct's walls are widened. The inspiration from Kemp et al. [2017] stops there, however: this work will not follow them in taking an average of their 'baffle' and 'dipole' exit conditions, since this relies on the superposition principle and therefore cannot be generalised to the nonlinear regime. Instead, Félix et al. [2018] and Mangin [2023] are followed in the use of a mode-matching condition, although there is inclusion here of weakly nonlinear effects that were neglected in their linear modelling.

Chapter 2 was originally intended to extend the 2D analysis of McTavish and Brambley [2019] to 3D. In so doing, a modified mathematical framework was developed that combines the 2D and 3D cases, is computationally more efficient, and is easier to understand in terms of the interplay between nonlinearity and duct geometry (consisting of width variation, curvature, and, in 3D, torsion). Section 2.1 derives this mathematical framework from the governing fluid mechanical equations, resulting in the multimodal set of governing ODEs valid in both 2D and 3D (given in section 2.1.6). A method for solving these equations using the multi-modal method is presented in section 2.2, first by introducing the admittance (§2.2.1) and then by truncating and numerically solving (§2.3). A simplified boundary condition for the admittance is derived in section 2.2.2.

Chapter 3 presents a number of numerical results that make use of this boundary condition. These include validation for a straight duct (§3.2), a constant curvature bend in 2D and 3D (§3.3 and §3.4.1), and an exponential horn (§3.5), along with more interesting cases involving combinations of curvature, width variation, torsion, and nonlinearity. In particular, the leakage of acoustics from a duct owing to either curvature or nonlinearity is demonstrated in section 3.7, a direct comparison of 2D results against 3D results made possible by the combined mathematical framework is given in section 3.9, and an investigation of the effective acoustic length of a bend is given in section 3.10.

Chapter 4 provides an interlude from numerical testing, instead looking at a semi-analytical technique for modelling the duct outlet in the linear case. This is done both in 2D and 3D, and lays the groundwork for a linear-regime validation of the model developed in chapter 5. This derivation relies heavily on Noble [1958], but is more specific about the form the solution takes for higher frequencies, and provides more direct guidance concerning numerical computation of the solution in 3D. This chapter also includes a formulation of the end correction problem to which the semi-analytical linear acoustic model may be applied (section 4.1).

Chapter 5 presents a weakly-nonlinear model of the outlet condition. The derivation of the outlet condition is carried out in section 5.1. In particular, section 5.1.4 derives the relations needed for transforming the acoustic field at the outlet into a boundary condition for the computation of the external acoustic field. Section 5.2 generalises chapter 4's formulation of the end correction problem to include nonlinearity; linear results are then validated against the Wiener–Hopf technique in section 5.3.1, providing a baseline for nonlinear testing in section 5.3.2. Another application of the model is the calculation of the impedance at the duct inlet across a range of frequencies; this is informative as to the resonant frequencies (and, therefore, the harmonic series) of a particular duct geometry. Theory and results for the model's application to this phenomenon are included in section 5.3.3. Sections 5.3.4–8 are then numerical examples of various geometries in 2D and 3D, focussing predominantly on the linear case but also including a nonlinear result.

The model's findings are summarised in chapter 6 alongside a general discussion, including possibilities for future work to be done with or on the model.

Chapter 2

Multi-modal duct acoustics

This chapter introduces the equations of gas dynamics before transforming them into weakly-nonlinear PDEs for zero-mean-flow acoustics in nonuniform curved waveguides. These PDEs are projected onto modal bases arising from straight-duct acoustics, and in the process become countably-infinite sets of coupled ODEs. We then apply the concept of the *admittance* to these ODEs as a means of solving them, before briefly discussing some features of the numerical method used to do so. This work is under consideration for publication [Jensen and Brambley, 2025].

2.1 Formulation of the governing equations

In this section, we derive the governing equations in the weakly-nonlinear limit that will be solved in subsequent sections. The derivation follows that of McTavish and Brambley [2019], although here we do not limit ourselves to the 2D case only.

2.1.1 Derivation of the weakly nonlinear equations

We start with the equations of mass and momentum conservation for an inviscid fluid,

$$\frac{\partial \hat{\rho}}{\partial \hat{t}} + \hat{\nabla}\cdot(\hat{\rho}\hat{\mathbf{u}}) = 0, \qquad \hat{\rho}\left(\frac{\partial \hat{\mathbf{u}}}{\partial \hat{t}} + \hat{\mathbf{u}}\cdot\hat{\nabla}\hat{\mathbf{u}}\right) = -\hat{\nabla}\hat{p}. \tag{2.1}$$

Dimensional quantities are written with hats. Here we work in either 2D or 3D; note that in n dimensions, these give us $n+1$ equations in $n+2$ variables (one density, n velocities, and one pressure). We therefore close the system of equations using the equation of state in combination with the thermal energy equation for an adiabatic gas (consistent with an inviscid non-heat-conducting fluid),

$$\hat{p} = \hat{p}(\hat{S}, \hat{\rho}), \qquad \frac{\mathrm{D}\hat{S}}{\mathrm{D}\hat{t}} = 0. \tag{2.2}$$

Since we are interested in acoustics, we expand these equations for a small perturbation about an ambient state of rest. To do so, we first need some notion of size, so we introduce reference quantities and non-dimensionalise. Let the ambient density, pressure and entropy be denoted by $\hat{\rho}_0$, $\hat{p}_0$ and $\hat{S}_0$ respectively. The ambient speed of sound $\hat{c}_0$ is then given by

$$\hat{c}_0^2 = \left.\frac{\partial \hat{p}}{\partial \hat{\rho}}\right|_{\hat{S}} (\hat{\rho}_0, \hat{S}_0), \tag{2.3}$$

where the subscript zero here (and elsewhere in this section) denotes evaluation at the ambient state. Using $\hat{\rho}_0$ and $\hat{c}_0$, non-dimensional variables are defined by setting

$$\hat{\rho} = \hat{\rho}_0 \rho, \qquad \hat{\mathbf{u}} = \hat{c}_0 \mathbf{u}, \qquad \hat{p} = \hat{\rho}_0 \hat{c}_0^2 p. \tag{2.4}$$

We also need spatial and temporal reference scales. The spatial reference lengthscale is denoted $\hat{\ell}_0$, typically given by the inlet radius of the duct. The timescale is then $\hat{c}_0/\hat{\ell}_0$, so the nondimensional operators are

$$\hat{\nabla} = \frac{1}{\hat{\ell}_0}\nabla \qquad \text{and} \qquad \frac{\partial}{\partial \hat{t}} = \frac{\hat{c}_0}{\hat{\ell}_0}\frac{\partial}{\partial t}. \tag{2.5}$$

We now perturb about an ambient state of rest,

$$\rho = 1 + \rho', \qquad \mathbf{u} = \mathbf{0} + \mathbf{u}', \qquad p = p_0 + p', \tag{2.6}$$

taking $\rho' \sim p' \sim |\mathbf{u}'| \sim M$, where $M \ll 1$ is the perturbation Mach number. Note that we have also introduced the non-dimensional ambient pressure p_0, given by $\hat{p}_0/\hat{\rho}_0\hat{c}_0^2$: this can be calculated later on with the help of further assumptions. Since we are interested in *weak* nonlinearity, we will neglect terms of order $O(M^3)$ or smaller but retain both the linear acoustic $O(M)$ and weakly nonlinear $O(M^2)$ terms. Using the nondimensionalisations (2.4, 2.5) in the governing equations (2.1) and substituting the perturbed quantities (2.6), this results in

$$\frac{\partial \rho'}{\partial t} + \nabla \cdot \mathbf{u}' = -\rho' \nabla \cdot \mathbf{u}' - \mathbf{u}' \cdot \nabla \rho' = \rho' \frac{\partial \rho'}{\partial t} - \mathbf{u}' \cdot \nabla \rho' + O(M^3), \tag{2.7a}$$

$$\frac{\partial \mathbf{u}'}{\partial t} + \nabla p' = -\mathbf{u}' \cdot \nabla \mathbf{u}' - \rho' \frac{\partial \mathbf{u}'}{\partial t} + O(M^3). \tag{2.7b}$$

Here, and in what follows, we write the linear acoustic $O(M)$ quantities on the left hand side of equations and the nonlinear $O(M^2)$ terms on the right hand side. Note that in (2.7a) the linear expression $\nabla \cdot \mathbf{u}' = -\partial \rho'/\partial t + O(M^2)$ was substituted in the right hand side, resulting in an expression that is still correct to order $O(M^3)$. This is a technique we will make further use of below.

This work is primarily concerned with acoustic perturbations, so we will neglect entropy perturbations, meaning that $S' \equiv 0$ and so $\hat{S} \equiv \hat{S}_0$ everywhere. This means all perturbations are adiabatic, and so we may eliminate either the pressure or density perturbation using the expanded equation of state:

$$p' = \rho' + \frac{1}{2}\frac{\partial^2 p}{\partial \rho^2}\bigg|_S \rho'^2 + O(M^3) \qquad \Leftrightarrow \qquad \rho' = p' - \frac{1}{2}\frac{\partial^2 p}{\partial \rho^2}\bigg|_S p'^2 + O(M^3), \tag{2.8}$$

where the second-order partial derivative is evaluated at the ambient state (ρ_0, S_0), and the identity $p' = \rho' + O(M^2)$ has been used to rearrange between the left and right expressions. If we consider a perfect gas, a consequence of adiabacity is that $(\hat{p}/\hat{p}_0) = (\hat{\rho}/\hat{\rho}_0)^\gamma$, where the adiabatic index γ is the ratio of specific heats. Consequently, for a perfect gas

$$\hat{c}_0^2 = \frac{\partial \hat{p}}{\partial \hat{\rho}}\bigg|_{\hat{S}} = \frac{\gamma \hat{p}_0}{\hat{\rho}_0}, \qquad \text{and} \qquad \frac{\partial^2 \hat{p}}{\partial \hat{\rho}^2}\bigg|_{\hat{S}} = \gamma(\gamma-1)\frac{\hat{p}_0}{\hat{\rho}_0^2} = (\gamma-1)\frac{\hat{c}_0^2}{\hat{\rho}_0}, \tag{2.9}$$

so that $p_0 = 1/\gamma$ and $\partial^2 p/\partial \rho^2|_S = (\gamma - 1)$ when $\rho_0 = 1$ and $c_0 = 1$. In what follows, for simplicity we will use this perfect gas notation, although the derivation is general provided it is taken that $\gamma = 1 + \partial^2 p/\partial \rho^2|_S$ and p_0 is not assumed to be $1/\gamma$.

We now eliminate the density perturbation ρ' using (2.8), and, correct to $O(M^2)$ and dropping the $O(M^3)$ from each equation for brevity, this finally results in

$$\frac{\partial p'}{\partial t} + \nabla\cdot\mathbf{u}' = \gamma p'\frac{\partial p'}{\partial t} - \mathbf{u}'\cdot\nabla p' = \frac{1}{2}\frac{\partial}{\partial t}\left(\gamma p'^2 + |\mathbf{u}'|^2\right), \tag{2.10a}$$

$$\frac{\partial \mathbf{u}'}{\partial t} + \nabla p' = -\mathbf{u}'\cdot\nabla\mathbf{u}' - p'\frac{\partial \mathbf{u}'}{\partial t} = \frac{1}{2}\nabla\left(p'^2\right) - \mathbf{u}'\cdot\nabla\mathbf{u}', \tag{2.10b}$$

where again the $O(M)$ identity $\partial\mathbf{u}'/\partial t = -\nabla p' + O(M^2)$ from the left hand side of (2.10b) has been used to rearrange the right-hand sides of both equations.

2.1.2 Further assumptions

Equations (2.10) may be simplified further. Taking ∇ of both sides of (2.10b), we apply symmetry of mixed partial derivatives on $\nabla\nabla p'$ and find that the spin tensor of the velocity is linearly constant in time, i.e.

$$\frac{\partial}{\partial t}\left(\nabla\mathbf{u}' - (\nabla\mathbf{u}')^{\mathrm{T}}\right) = 0 + O(M^2). \tag{2.11}$$

If we assume all acoustic variables to be periodic (because we are interested in tonal acoustics), we can define a time-average $\langle\bullet\rangle$, and then deduce that

$$\nabla\mathbf{u}' - (\nabla\mathbf{u}')^{\mathrm{T}} = \left\langle \nabla\mathbf{u}' - (\nabla\mathbf{u}')^{\mathrm{T}} \right\rangle + O(M^2). \tag{2.12}$$

Having worked to a relatively high degree of generality so far, we now outline a hierarchy of physically-justified assumptions, ordered by strength, that will simplify the coming calculations.

- **Assumption 1 (weakest):** Taking the time average of (2.10a) shows that $\nabla\cdot\langle\mathbf{u}'\rangle = O(M^3)$, meaning $\langle\mathbf{u}'\rangle$ corresponds to a steady, viscosity-free incompressible mean flow to the order considered here. Under these circumstances, we would expect this mean flow to be vorticity-free, implying $\nabla\langle\mathbf{u}'\rangle - (\nabla\langle\mathbf{u}'\rangle)^T = O(M^2)$, and consequently in light of (2.12) that (2.10b) may be equivalently written as

  $$\frac{\partial \mathbf{u}'}{\partial t} + \nabla p' = \frac{1}{2}\nabla\left(p'^2 - |\mathbf{u}'|^2\right). \tag{2.13}$$

  This assumption may also be justified physically by noting that we would expect the flow in a musical instrument to be vorticity-free.

- **Assumption 2a (stronger):** On top of assumption 1, by taking a time average of (2.13) we see that the quantity $\langle p'\rangle - \frac{1}{2}\left\langle p'^2 - |\mathbf{u}'|^2\right\rangle$ is spatially constant to the order considered, where the constant corresponds to an $O(M)$ change in the far-field ambient pressure p_0. By suitably choosing an $O(M)$ correction to p_0 (which we recall has an $O(1)$ value of $1/\gamma$) we may therefore set this change in ambient pressure to be zero, and consequently $\langle p'\rangle = O(M^2)$.

- **Assumption 2b (also stronger):** On top of assumption 1, we may assume the mean flow $\langle\mathbf{u}'\rangle$ to be identically zero. This is justified by imposing an inlet condition with no mean flow, and noting that no mean flow is induced by the nonzero frequency modes. Thus, $\langle\mathbf{u}'\rangle = \mathbf{0}$. This agrees with our physical intuition that, when musical instruments are played, no flow of significant Mach number is expected. This assumption would therefore be valid for musical instruments, but perhaps not for, for example, thermoacoustic engines, where the acoustics driving a mean flow is an important component of the engine.

Henceforth we will take all of these assumptions to be true. Defining the coefficient of nonlinearity $\beta_0 := (\gamma+1)/2$, and introducing the $O(M^2)$ quantity $Q' := (p'^2 - |\mathbf{u}'|^2)/2$ (which could arguably be thought of as a Lagrangian of the perturbation), we have

$$\frac{\partial p'}{\partial t} + \nabla\cdot\mathbf{u}' = \frac{\partial}{\partial t}\left(\beta_0 p'^2 - Q'\right), \qquad \frac{\partial \mathbf{u}'}{\partial t} + \nabla p' = \nabla Q'. \tag{2.14}$$

Note that β_0 has been written with a zero subscript in order to avoid confusion with the spatial mode enumerator β used later on.[1]

---

[1] The second equation here may optionally be simplified by a change of variable. Q' may be absorbed into the pressure, resulting in a modified pressure given by $\tilde{p}' = p' - Q'$. Under this transformation, the right-hand side of the momentum equation vanishes, simplifying some of the coming algebra. However, this muddies the waters physically, and the resulting loss of intuition outweighs the benefits in page space. Furthermore, the reverse transformation (to recover the acoustic pressure) is a messy addition to an already complicated computational process. Therefore, we will continue to use the actual physical quantities p' and $\mathbf{u}'$.

2.1.3 Fourier modal decomposition

At this point, because we are interested in tonal acoustics, we assume a base frequency ω and decompose pressure and velocity into Fourier modes by writing

$$p'(\mathbf{x},t) = \sum_{a=-\infty}^{\infty} P^a(\mathbf{x})\mathrm{e}^{-\mathrm{i}a\omega t}, \qquad \mathbf{u}'(\mathbf{x},t) = \sum_{a=-\infty}^{\infty} \mathbf{U}^a(\mathbf{x})\mathrm{e}^{-\mathrm{i}a\omega t}. \tag{2.15}$$

Here ω is a dimensionless frequency, representing the Helmholtz number. To ensure that p' and $\mathbf{u}'$ are real (and can therefore be substituted into quadratic terms without a phase shift), we must have $P^{-a} = P^{a*}$ and $\mathbf{U}^{-a} = \mathbf{U}^{a*}$, where an asterisk denotes the complex conjugate. Our equations for p' and $\mathbf{u}'$ (with $a = 0$ modes discounted due to assumptions 2a and 2b above) become

$$\sum_{\substack{a=-\infty,\\ a\neq 0}}^{\infty} (-\mathrm{i}a\omega P^a + \nabla\cdot\mathbf{U}^a)\mathrm{e}^{-\mathrm{i}a\omega t} = \sum_{\substack{b,c=-\infty,\\ b,c\neq 0}}^{\infty} -\mathrm{i}(b+c)\omega\left(\beta_0 P^b P^c - \frac{P^b P^c - \mathbf{U}^b\cdot\mathbf{U}^c}{2}\right)\mathrm{e}^{-\mathrm{i}(b+c)\omega t}, \tag{2.16a}$$

$$\sum_{\substack{a=-\infty,\\ a\neq 0}}^{\infty} (-\mathrm{i}a\omega \mathbf{U}^a + \nabla P^a)\mathrm{e}^{-\mathrm{i}a\omega t} = \sum_{\substack{b,c=\infty,\\ b,c\neq 0}}^{\infty} \nabla\left(\frac{P^b P^c - \mathbf{U}^b\cdot\mathbf{U}^c}{2}\right)\mathrm{e}^{-\mathrm{i}(b+c)\omega t}. \tag{2.16b}$$

Here we have purposely not written these equations in terms of Q', so as to determine more clearly how products of acoustic variables behave under Fourier series expansion. After exploiting orthogonality by setting $a = b + c$, we find that

$$-\mathrm{i}a\omega P^a + \nabla\cdot\mathbf{U}^a = -\mathrm{i}a\omega\left(-Q^a + \sum_{\substack{b=-\infty,\\ b\neq 0,a}}^{\infty} \beta_0 P^{a-b}P^b\right), \tag{2.17a}$$

$$-\mathrm{i}a\omega\mathbf{U}^a + \nabla P^a = \nabla Q^a, \tag{2.17b}$$

where we have reintroduced Q' as a Fourier series coefficient, knowing now that it is given by

$$Q^a = \frac{1}{2}\sum_{\substack{b=-\infty,\\ b\neq 0,a}}^{\infty} P^{a-b}P^b - \mathbf{U}^{\mathbf{a-b}}\cdot\mathbf{U}^{\mathbf{b}}. \tag{2.18}$$

In order to conserve page space, we will henceforth write only b beneath sums; all future Fourier sums are understood to have the limits and exemptions of those above.

2.1.4 Duct coordinate system

Since we have already non-dimensionalised, all of the following geometric quantities are dimensionless from their introduction. Physical quantities may be recovered from their dimensionless counterparts by an appropriate multiplication with the three dimensional

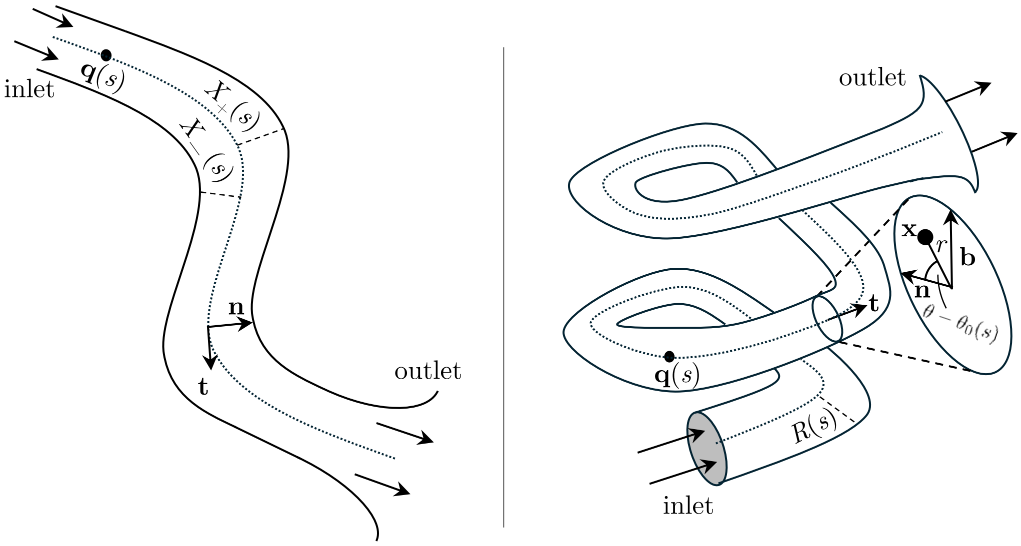

Figure 2.1: The duct geometry in 2D (left) and 3D (right). A Frenet-Serret frame is employed in each case, with centreline $\mathbf{q}(s)$, tangent $\mathbf{t}(s)$ and normal $\mathbf{n}(s)$; additionally in 3D we have a binormal $\mathbf{b}(s)$. The 2D duct has independently varying wall widths $X_+(s)$ and $X_-(s)$, whereas the 3D duct has a single axisymmetrically-varying wall width $R(s)$.

constants $\hat{\rho}_0$, $\hat{c}_0$ and $\hat{\ell}_0$.

The coordinate system in 2D

As shown in figure 2.1 (left), the 2D duct is defined by a centreline $\mathbf{q}(s)$ (where s is the arc-length, parameterising distance along the duct), a total width at each point $X(s)$, and independently varying wall widths $X_-(s) < 0$ and $X_+(s) > 0$, defined such that $X(s) = X_+(s) - X_-(s)$.[2] The direction along the duct is the *longitudinal* direction, and the direction perpendicular to this is the *transverse* direction. The longitudinal direction has coordinate s, and for the transverse direction we introduce a coordinate $x \in [X_-(s), X_+(s)]$. This coordinate basis arises from the Frenet–Serret frame defined by the centreline $\mathbf{q}(s)$, i.e. the tangent and normal unit vectors $\mathbf{t}$ and $\mathbf{n}$ satisfying

$$\frac{\mathrm{d}\mathbf{q}}{\mathrm{d}s} = \mathbf{t}, \qquad \frac{\mathrm{d}\mathbf{t}}{\mathrm{d}s} = \kappa\mathbf{n}, \qquad \frac{\mathrm{d}\mathbf{n}}{\mathrm{d}s} = -\kappa\mathbf{t}, \tag{2.19}$$

---

[2] The choice to include independently varying wall widths was made early in the formulation of the model, in order to increase the degrees of freedom and to maintain consistency with McTavish and Brambley [2019]; in this thesis, however, we take the centreline to remain in the centre throughout. Asymmetric wall-width variation would be an interesting area of future study, for example for ducts with cavities on only one side.

with the scalar $\kappa(s)$ representing the curvature of the duct. Any point in the duct then has coordinates (s, x) and position vector

$$\mathbf{x} = \mathbf{q}(s) + x\mathbf{n}(s). \tag{2.20}$$

We have a differential $\mathrm{d}\mathbf{x}$ and a metric $\mathrm{d}\mathbf{x}\cdot\mathrm{d}\mathbf{x}$ given by

$$\mathrm{d}\mathbf{x} = \mathbf{t}(1-\kappa x)\mathrm{d}s + \mathbf{n}\mathrm{d}x, \qquad \mathrm{d}\mathbf{x}\cdot\mathrm{d}\mathbf{x} = (1-\kappa x)^2\mathrm{d}s^2 + \mathrm{d}x^2, \tag{2.21}$$

from which we may read off the Lamé coefficients and (s, x) basis vectors

$$h_s = 1-\kappa x, \qquad h_x = 1, \qquad \mathbf{e}_s = \mathbf{t}, \qquad \mathbf{e}_x = \mathbf{n}. \tag{2.22}$$

This is all of the machinery necessary to project the governing equations (2.17). Setting $\mathbf{U}^a = U^a\mathbf{e}_s + V^a\mathbf{e}_x$, we use $\nabla = \sum_i (1/h_i)\mathbf{e}_i\partial_i$ along with the relations

$$\begin{pmatrix} \frac{1}{h_s}\partial_s \\ \frac{1}{h_x}\partial_x \end{pmatrix} \begin{pmatrix} \mathbf{e}_s \\ \mathbf{e}_x \end{pmatrix}^{\mathrm{T}} = \begin{pmatrix} \frac{\kappa}{h_s}\mathbf{e}_x & -\frac{\kappa}{h_s}\mathbf{e}_s \\ 0 & 0 \end{pmatrix}, \tag{2.23}$$

to get

$$-\mathrm{i}a\omega P^a + \frac{1}{h_s}\frac{\partial U^a}{\partial s} + \frac{1}{h_s}\frac{\partial (h_s V^a)}{\partial x} = -\mathrm{i}a\omega\left(\sum_b \beta_0 P^{a-b}P^b - Q^a\right), \tag{2.24a}$$

$$-\mathrm{i}a\omega U^a + \frac{1}{h_s}\frac{\partial P^a}{\partial s} = \frac{1}{h_s}\frac{\partial Q^a}{\partial s}, \qquad -\mathrm{i}a\omega V^a + \frac{\partial P^a}{\partial x} = \frac{\partial Q^a}{\partial x}. \tag{2.24b}$$

We now proceed to eliminate the transverse velocities. Since we are neglecting $O(M^3)$ or smaller terms, we can form an expression for V^a in terms of the other acoustic variables:

$$V^a = \frac{1}{\mathrm{i}a\omega}\frac{\partial}{\partial x}\left(P^a - Q^a\right), \quad \text{with} \quad Q^a = \frac{1}{2}\sum_b\left(P^{a-b}P^b - U^{a-b}U^b + \frac{\partial_x P^{a-b}\partial_x P^b}{(a-b)b\omega^2}\right), \tag{2.25}$$

where ∂_x denotes $\partial/\partial x$ and the error in this expression for Q^a is $O(M^3)$. Since our eventual goal is to obtain ODEs in s for spatial-mode coefficients of P^a and U^a, these will be simplest to implement if we have as few s-derivatives present as possible. Therefore, we also wish to eliminate s-derivatives from the right-hand sides of our equations, using

$$\frac{\partial P^a}{\partial s} = \mathrm{i}a\omega h_s U^a + O(M^2), \tag{2.26a}$$

$$\frac{\partial U^a}{\partial s} = \mathrm{i}a\omega\left[h_s\left(1 + \frac{1}{a^2\omega^2}\frac{\partial^2}{\partial x^2}\right) - \frac{\kappa}{a^2\omega^2}\frac{\partial}{\partial x}\right]P^a + O(M^2), \tag{2.26b}$$

$$\frac{\partial V^a}{\partial s} = \frac{1}{\mathrm{i}a\omega}\frac{\partial^2 P^a}{\partial s \partial x} + O(M^2) = \frac{\partial}{\partial x}\left(h_s U^a\right) + O(M^2). \tag{2.26c}$$

Once we have eliminated V^a and all s-derivatives at second order, we are left with

$$\frac{\partial U^a}{\partial s} - \mathrm{i}a\omega\left[h_s\left(1 + \frac{1}{a^2\omega^2}\frac{\partial^2}{\partial x^2}\right) - \frac{\kappa}{a^2\omega^2}\frac{\partial}{\partial x}\right]P^a \tag{2.27a}$$
$$= \mathrm{i}a\omega\left\{-\beta_0 h_s \sum_b P^{a-b}P^b + \left[h_s\left(1 - \frac{1}{a^2\omega^2}\frac{\partial^2}{\partial x^2}\right) + \frac{\kappa}{a^2\omega^2}\frac{\partial}{\partial x}\right]Q^a\right\},$$

$$\frac{\partial P^a}{\partial s} - \mathrm{i}a\omega h_s U^a = \mathrm{i}\omega h_s \sum_b \left\{U^{a-b}\left[(a-b) - b\left(1 + \frac{1}{b^2\omega^2}\frac{\partial^2}{\partial x^2}\right)\right]P^b + \frac{\partial_x U^{a-b}\partial_x P^b}{b\omega^2}\right\}. \tag{2.27b}$$

The other piece of information that needs expression in the coordinate system is the hard-walled boundary condition $\mathbf{u}\cdot\boldsymbol{\nu}_\pm = 0$ at $x = X_\pm$, where $\boldsymbol{\nu}_\pm$ is the normal to each duct wall (distinct from the Frenet-Serret normal $\mathbf{n}$). The duct walls are defined by the equations $x - X_\pm = 0$, so the normals can be found by taking the gradients of $x - X_\pm$, i.e.

$$\boldsymbol{\nu}_\pm = \nabla(x - X_\pm)\Big|_{x=X_\pm} = \left(\mathbf{e}_x - (X_\pm'/h_s)\mathbf{e}_s\right)\Big|_{x=X_\pm}. \tag{2.28}$$

The boundary condition is then given by the equation

$$X_\pm' U^a\Big|_{x=X\pm} = \left(h_s V^a\right)\Big|_{x=X\pm} = \left[\frac{h_s}{\mathrm{i}a\omega}\frac{\partial}{\partial x}\left(P^a - Q^a\right)\right]\Big|_{x=X_\pm}. \tag{2.29}$$

The coordinate system in 3D

Later on we will be projecting the equations onto a basis of functions representing the modes of a straight duct. The construction of such a basis is much easier and cleaner with separable boundary conditions in 3D, so here we drop the asymmetry about the centreline to focus on 3D ducts with circular cross-sections[3]: a constraint most brass instruments adhere to. However, as well as bending in the plane, the duct may now twist out of it, complicating the Frenet–Serret frame.

As shown in figure 2.1 (right), we begin once more with a centreline $\mathbf{q}(s)$, but this time have a single radius function $R(s)$. The longitudinal coordinate is s as before, and two more variables span the plane perpendicular to the centreline tangent. The Frenet–Serret frame now has an extra vector and a corresponding extra scalar

$$\frac{\mathrm{d}\mathbf{q}}{\mathrm{d}s} = \mathbf{t}, \qquad \frac{\mathrm{d}\mathbf{t}}{\mathrm{d}s} = \kappa\mathbf{n}, \qquad \frac{\mathrm{d}\mathbf{n}}{\mathrm{d}s} = -\kappa\mathbf{t} + \tau\mathbf{b}, \qquad \frac{\mathrm{d}\mathbf{b}}{\mathrm{d}s} = -\tau\mathbf{n}. \tag{2.30}$$

---

[3] Alternative options that would also be separable include elliptical cross-sections and rectangular cross-sections. The loss of circular symmetry complicates such ducts when they undergo torsion, however: some preliminary work dealing with the resulting complexity for rectangular ducts is presented in appendix B.

Here $\mathbf{b}$ is the *binormal* (satisfying $\mathbf{b} = \mathbf{t} \times \mathbf{n}$) and τ is the *torsion*. We now introduce polar coordinates $r \in [0, R(s)]$ and $\theta \in [0, 2\pi)$ in the transverse plane, but rather than rotating this polar frame in line with the rotation of the basis vectors $\mathbf{n}$ and $\mathbf{b}$, we leave an extra degree of freedom here by also introducing a phase shift, or twist, $\theta_0(s)$, that may vary along the duct [following the work of Germano, 1982], so that any point $\mathbf{x}$ is given in these coordinates by

$$\mathbf{x} = \mathbf{q}(s) + r\cos(\theta - \theta_0)\mathbf{n} + r\sin(\theta - \theta_0)\mathbf{b}. \tag{2.31}$$

Defining $\phi := \theta - \theta_0(s)$, the differential $\mathrm{d}\mathbf{x}$ and the metric $\mathrm{d}\mathbf{x}\cdot\mathrm{d}\mathbf{x}$ are then

$$\begin{aligned} \mathrm{d}\mathbf{x} = \; & \mathbf{t}\Big[(1 - \kappa r\cos\phi)\mathrm{d}s\Big] + \mathbf{n}\Big[\mathrm{d}r\cos\phi - r\mathrm{d}\theta\sin\phi + r\mathrm{d}s(\theta_0' - \tau)\sin\phi\Big] \\ & \qquad + \mathbf{b}\Big[\mathrm{d}r\sin\phi + r\mathrm{d}\theta\cos\phi - r\mathrm{d}s(\theta_0' - \tau)\cos\phi\Big], \end{aligned} \tag{2.32a}$$

$$\mathrm{d}\mathbf{x}\cdot\mathrm{d}\mathbf{x} = \mathrm{d}s^2\Big[1 - \kappa r\cos\phi + r^2(\theta_0' - \tau)^2\Big] + \mathrm{d}r^2 + r^2\mathrm{d}\theta^2 - 2\mathrm{d}s\mathrm{d}\theta r^2(\theta_0' - \tau). \tag{2.32b}$$

An orthogonal coordinate system requires that there be no cross-term differentials in the metric: to achieve this, we utilise the extra degree of freedom we built in earlier, and take $\theta_0' = \tau$. The Lamé coefficients and (s, r, θ) basis vectors can then be written down, and they are

$$h_s = 1 - \kappa r\cos\phi, \qquad h_r = 1, \qquad h_\theta = r, \tag{2.33a}$$

$$\mathbf{e}_s = \mathbf{t}, \qquad \mathbf{e}_r = \mathbf{n}\cos\phi + \mathbf{b}\sin\phi, \qquad \mathbf{e}_\theta = -\mathbf{n}\sin\phi + \mathbf{b}\cos\phi. \tag{2.33b}$$

We decompose the velocity in the same way as before, but now with an extra coordinate, i.e. $\mathbf{U}^a = U^a\mathbf{e}_s + V^a\mathbf{e}_r + W^a\mathbf{e}_\theta$. The basis vectors are now differentiated as

$$\begin{pmatrix} \frac{1}{h_s}\partial_s \\ \frac{1}{h_r}\partial_r \\ \frac{1}{h_\theta}\partial_\theta \end{pmatrix} \begin{pmatrix} \mathbf{e}_s \\ \mathbf{e}_r \\ \mathbf{e}_\theta \end{pmatrix}^{\mathrm{T}} = \begin{pmatrix} \frac{\kappa}{h_s}(\mathbf{e}_r\cos\phi - \mathbf{e}_\theta\sin\phi) & -\frac{\kappa}{h_s}\mathbf{e}_s\cos\phi & \frac{\kappa}{h_s}\mathbf{e}_s\sin\phi \\ 0 & 0 & 0 \\ 0 & \frac{1}{r}\mathbf{e}_\theta & -\frac{1}{r}\mathbf{e}_r \end{pmatrix}, \tag{2.34}$$

so the mass and momentum equations become

$$-\mathrm{i}a\omega P^a + \frac{1}{h_s}\frac{\partial U^a}{\partial s} + \frac{1}{rh_s}\frac{\partial (rh_sV^a)}{\partial r} + \frac{1}{rh_s}\frac{\partial (h_sW^a)}{\partial \theta} = \mathrm{i}a\omega\left(-\beta_0\sum_b P^{a-b}P^b + Q^a\right), \tag{2.35a}$$

$$-\mathrm{i}a\omega U^a + \frac{1}{h_s}\frac{\partial P^a}{\partial s} = \frac{1}{h_s}\frac{\partial Q^a}{\partial s}, \qquad -\mathrm{i}a\omega V^a + \frac{\partial P^a}{\partial r} = \frac{\partial Q^a}{\partial r}, \tag{2.35b}$$

$$-\mathrm{i}a\omega W^a + \frac{1}{r}\frac{\partial P^a}{\partial \theta} = \frac{1}{r}\frac{\partial Q^a}{\partial \theta}. \tag{2.35c}$$

Proceeding as before, we find expressions for V^a and W^a in terms of P^a and U^a:

$$V^a = \frac{1}{\mathrm{i}a\omega}\frac{\partial}{\partial r}(P^a - Q^a), \qquad W^a = \frac{1}{\mathrm{i}a\omega r}\frac{\partial}{\partial \theta}(P^a - Q^a), \tag{2.36}$$

with

$$Q^a = \frac{1}{2}\sum_b\left(P^{a-b}P^b - U^{a-b}U^b + \frac{\nabla_{\mathrm{t}}P^{a-b}\cdot\nabla_{\mathrm{t}}P^b}{(a-b)b\omega^2}\right), \tag{2.37}$$

where we have introduced the *transverse gradient* $\nabla_{\mathrm{t}} = \mathbf{e_r}\partial_r + \frac{1}{r}\mathbf{e}_\theta\partial_\theta$ which acts only in the r, θ plane normal to the centreline. We also define, for any function f, the *Frenet–Serret normal-derivative* (FSND)

$$\frac{\partial f}{\partial \mathbf{n}} = \mathbf{n}\cdot\nabla f = \cos\phi\frac{\partial f}{\partial r} - \frac{\sin\phi}{r}\frac{\partial f}{\partial \theta}. \tag{2.38}$$

This is a useful quantity, since it allows us to commute the transverse gradient with the longitudinal scale factor h_s, as in,

$$\nabla_{\mathrm{t}}\cdot(h_s\nabla_{\mathrm{t}}f) = \left(h_s\nabla_{\mathrm{t}}^2 - \kappa\partial_{\mathbf{n}}\right)f \qquad \text{and} \qquad \nabla_{\mathrm{t}}^2(h_sf) = \left(h_s\nabla_{\mathrm{t}}^2 - 2\kappa\partial_{\mathbf{n}}\right)f. \tag{2.39}$$

This contrasts with the 2D derivation, where both the transverse gradient and the FSND collapse onto the x-derivative (the former as a vector in the $\mathbf{e}_x$ direction, the latter as a scalar). The next step, as before, is to find $O(M)$ expressions for s-derivatives, which in 3D turn out to be

$$\frac{\partial P^a}{\partial s} = \mathrm{i}a\omega h_sU^a + O(M^2), \quad \frac{\partial U^a}{\partial s} = \mathrm{i}a\omega\left[h_s\left(1 + \frac{\nabla_{\mathrm{t}}^2}{a^2\omega^2}\right) - \frac{\kappa}{a^2\omega^2}\frac{\partial}{\partial \mathbf{n}}\right]P^a + O(M^2), \tag{2.40a}$$

$$\frac{\partial V^a}{\partial s} = \frac{1}{\mathrm{i}a\omega}\frac{\partial^2 P^a}{\partial r\partial s} + O(M^2) = \frac{\partial}{\partial r}(h_sU^a) + O(M^2), \tag{2.40b}$$

$$\frac{\partial W^a}{\partial s} = \frac{1}{\mathrm{i}a\omega r}\frac{\partial^2 P^a}{\partial \theta\partial s} + O(M^2) = \frac{1}{r}\frac{\partial}{\partial \theta}(h_sU^a) + O(M^2). \tag{2.40c}$$

Once all of these have been eliminated, the two equations are

$$\begin{aligned}\frac{\partial U^a}{\partial s} - \mathrm{i}a\omega\left[h_s\left(1+\frac{\nabla_\mathrm{t}^2}{a^2\omega^2}\right) - \frac{\kappa}{a^2\omega^2}\frac{\partial}{\partial \mathbf{n}}\right]P^a \\ = \mathrm{i}a\omega\left\{-\beta_0 h_s\sum_b P^{a-b}P^b + \left[h_s\left(1-\frac{\nabla_\mathrm{t}^2}{a^2\omega^2}\right)+\frac{\kappa}{a^2\omega^2}\frac{\partial}{\partial \mathbf{n}}\right]Q^a\right\},\end{aligned} \tag{2.41a}$$

$$\frac{\partial P^a}{\partial s} - \mathrm{i}a\omega h_s U^a = \mathrm{i}\omega h_s \sum_b\left\{U^{a-b}\left[(a-b) - b\left(1+\frac{\nabla_\mathrm{t}^2}{b^2\omega^2}\right)\right]P^b + \frac{\nabla_\mathrm{t}U^{a-b}\cdot\nabla_\mathrm{t}P^b}{b\omega^2}\right\}. \tag{2.41b}$$

Finally, the hard-walled boundary condition in 3D requires the normal $\boldsymbol{\nu}$:

$$\boldsymbol{\nu} = \nabla(r-R)\Big|_{r=R} = (\mathbf{e}_r - R'\mathbf{e}_s/h_s)\Big|_{r=R}. \tag{2.42}$$

Plugging this into $\mathbf{u}\cdot\boldsymbol{\nu}|_{r=R} = 0$ gives

$$R'U^a|_{r=R} = (h_s V^a)|_{r=R} = \left[\frac{h_s}{\mathrm{i}a\omega}\frac{\partial}{\partial r}\left(P^a - Q^a\right)\right]\Bigg|_{r=R}. \tag{2.43}$$

2.1.5 Spatial Modes

At this point, we expand each of P^a and U^a in terms of a basis of straight-duct modes. We will ultimately be solving for the coefficients of the series expansions, which will only depend on s (all transverse variation being contained within the basis functions), so we are in effect exchanging a pair of PDEs for a countably infinite number of coupled ODEs (though when we solve numerically this will be truncated to a finite number).

Spatial modes in 2D

P^a and U^a are expanded as

$$P^a = \sum_{\alpha=0}^{\infty} P^a_\alpha(s)\psi_\alpha(s,x), \qquad U^a = \sum_{\alpha=0}^{\infty} U^a_\alpha(s)\psi_\alpha(s,x), \tag{2.44}$$

with every ψ_α satisfying

- Helmholtz's equation with eigenvalue λ_α in 2D (scaling out the eigenvalue's X-dependence for convenience)

$$\frac{\partial^2\psi_\alpha}{\partial x^2} + \frac{\lambda_\alpha^2}{X^2}\psi_\alpha = 0, \tag{2.45}$$

- a normalisation condition

$$\langle\psi_\alpha,\psi_\beta\rangle = \delta_{\alpha\beta}, \text{ where } \langle\psi_\alpha,\psi_\beta\rangle := \int_{X_-}^{X_+}\psi_\alpha\psi_\beta \,\mathrm{d}x, \tag{2.46}$$

- and a Neumann condition on the duct walls (which ensures that the requisite Sturm–Liouville properties hold, while maintaining consistency with the no-penetration condition)
$$\left.\frac{\partial \psi_\alpha}{\partial x}\right|_{x=X_\pm} = 0. \tag{2.47}$$

Solutions to the Helmholtz equation are quantised by the boundary conditions, giving solutions

$$\psi_\alpha = \frac{C_\alpha}{\sqrt{X}} \cos\left[\frac{\lambda_\alpha (x - X_-)}{X}\right], \qquad \lambda_\alpha = \alpha\pi, \tag{2.48}$$

for $\alpha \in \mathbb{N}_0$ (with the $1/\sqrt{X}$ scaling being deduced from the form of the inner product). Integrating two solutions together determines C_α to be $\sqrt{2 - \delta_{\alpha 0}}$.

Spatial modes in 3D

In 3D, matters are a little more complicated. The expansions are written as

$$P^a = \sum_{\alpha=0}^{\infty} P^a_\alpha(s)\psi_\alpha(s, r, \theta), \qquad U^a = \sum_{\alpha=0}^{\infty} U^a_\alpha(s)\psi_\alpha(s, r, \theta), \tag{2.49}$$

with every ψ_α satisfying

- Helmholtz's equation with eigenvalue λ_α in cylindrical polars (with the eigenvalue's R-dependence scaled out for convenience)
$$\nabla^2_{\mathrm{t}}\psi_\alpha + \frac{\lambda^2_\alpha}{R^2}\psi_\alpha = 0, \tag{2.50}$$
- a normalisation condition
$$\langle \psi_\alpha, \psi_\beta \rangle = \delta_{\alpha\beta}, \qquad \text{where} \qquad \langle \psi_\alpha, \psi_\beta \rangle := \int_{\theta=0}^{2\pi}\int_{r=0}^{R} \psi_\alpha \psi_\beta \; r\mathrm{d}r\mathrm{d}\theta, \tag{2.51}$$
- regularity at $r = 0$,
- periodicity in θ,
- and a Neumann condition on the duct wall (which ensures that the requisite Sturm–Liouville properties hold, while maintaining consistency with the no-penetration condition)
$$\left.\frac{\partial \psi_\alpha}{\partial r}\right|_{r=R} = 0 \quad \forall\theta. \tag{2.52}$$

Performing separation of variables on a general eigenfunction by setting $\psi_\alpha = \psi^r_\alpha(r)\psi^\theta_\alpha(\theta)$ gives Bessel functions of order p with radial wavenumber λ_α/R for $\psi^r_\alpha(r)$, and sinusoidal solutions with azimuthal wavenumber p for $\psi^\theta_\alpha(\theta)$. Periodicity in θ means that $p \in \mathbb{N}_0$.

The Helmholtz equation is second-order in both r and θ, and so requires four conditions for full solution. However, since we are only determining a set of modes here, we have one extra degree of freedom. We apply the first of three conditions by noting that centreline regularity means that we cannot have any Bessel functions of the second kind, so $\psi^r_\alpha(r) \propto \mathrm{J}_p(\lambda_\alpha r/R)$. The degree of freedom is represented by considering $\psi^\theta_\alpha(\theta) = \cos p\theta$ and $\psi^\theta_\alpha(\theta) = \sin p\theta$ to be a pair of different modes for every p. Hence, we have

$$\psi_\alpha = \frac{C_\alpha}{\sqrt{\pi}R}\mathrm{J}_p(\lambda_\alpha r/R)\cos\left(p\phi - \frac{\xi\pi}{2}\right), \tag{2.53}$$

where C_α is a constant to be determined later (the $1/\sqrt{\pi}R$ dependence being deduced dimensionally from the normalisation condition) and $\xi \in \{0,1\}$ encodes the degree of freedom. A property of these eigenfunctions that will be useful later is that their Frenet-Serret normal-derivatives are also eigenfunctions of the transverse Laplacian, i.e. $(\nabla^2_\mathrm{t} + \lambda^2_\alpha/R^2)\partial_\mathbf{n}\psi_\alpha = 0$.

A quick application of the Neumann condition ensures that only countably infinite eigenvalues λ_α satisfy the conditions above: defining j_{pq} to be the q^{th} zero of $\mathrm{J}'_p(x)$, we find that for each α, $\lambda_\alpha = j_{p_\alpha q_\alpha}$ for a pair of indices p_α, q_α. However, changing ξ results in a different mode without changing λ_α; consequently, in order to ensure we have a well-defined map from mode number α to wavenumbers p_α, q_α, we must also specify $\xi = \xi_\alpha$, resulting in a bijection between $\alpha \in \mathbb{N}_0$ and $(p_\alpha, q_\alpha, \xi_\alpha) \in \mathbb{N}_0 \times \mathbb{N}_0 \times \{0,1\}$. A consequence of this method of mode enumeration is that every non-zero eigenvalue λ_α is degenerate with multiplicity 2, except for $p_\alpha = 0$ (since a sine function with an identically zero argument will violate normalisation). The $q = 0$ eigenvalues are not degenerate, as it turns out that all but one of them must be discarded in order to satisfy normalisation

$$\begin{cases} p > 0,\ p \text{ even},\ q = 0, & \mathrm{J}_p(0) = j_{p0} = 0,\ \text{so } \psi_\alpha \equiv 0, \\ p = 0,\ q = 0,\ \xi = 1, & \cos\left(0 - \frac{\pi}{2}\right) = 0,\ \text{ so } \psi_\alpha \equiv 0, \end{cases}$$

so the only remaining zero eigenvalue is $\lambda_0 = j_{00}$, corresponding to a plane wave (odd p is not included in the above cases since there are no $q = 0$ eigenvalues with odd p). Hence, the $p \neq 0$ eigenvalues may be paired such that within each pairing they differ only by ξ (and therefore not by λ_α), with $p = 0$ being unpaired, giving the ordering $0 = \lambda_0 < \lambda_1 = \lambda_2 < \lambda_3 = \lambda_4 < \lambda_5 < \lambda_6 = \lambda_7 < \ldots$ where λ_0 and λ_5 are $p = 0$ eigenvalues.

All that remains is to determine C_α using normalisation. Plugging (B.24) into the norm from (2.51), one finds that

$$\langle\psi_\alpha,\psi_\beta\rangle = \begin{cases} 2(C_\alpha C_\beta/R^2)\int_0^R \mathrm{J}_0\left(j_{0q_\alpha}r/R\right)\mathrm{J}_0\left(j_{0q_\beta}r/R\right)r\mathrm{d}r, & p_\alpha = p_\beta = 0,\\ (C_\alpha C_\beta/R^2)\int_0^R \mathrm{J}_{p_\alpha}\left(j_{p_\alpha q_\alpha}r/R\right)\mathrm{J}_{p_\alpha}(j_{p_\alpha q_\beta}r/R)r\mathrm{d}r, & p_\alpha = p_\beta \neq 0,\\ 0, & p_\alpha \neq p_\beta. \end{cases} \tag{2.54}$$

From here, standard Bessel function orthogonality results in combination with (2.51) determine C_α to be

$$C_\alpha = \begin{cases} \left(|\mathrm{J}_0(j_{0q_\alpha})|\right)^{-1}, & p_\alpha = 0,\\ \left(\sqrt{\frac{1}{2}\left[1 - p_\alpha^2/j_{p_\alpha q_\alpha}^2\right]}\;|\mathrm{J}_{p_\alpha}(j_{p_\alpha q_\alpha})|\right)^{-1}, & p_\alpha \neq 0. \end{cases} \tag{2.55}$$

These (now fully-determined) basis functions will ultimately appear inside analytically insoluble integrals.

2.1.6 Spatial projection and notation

2D

The goal here is to project equations (2.27) onto the basis of spatial modes (2.48). This is achieved by multiplying each equation by a mode ψ_α and integrating over a duct cross-section. If the expansions (2.44) are then employed, the acoustic mode coefficients may then be factored out of the integral, which becomes a matrix with rows in α and columns in the expansion dummy variable β, dependent only on the local geometry. However, the Neumann boundary condition (2.47) prevents us from expanding any first-derivatives of acoustical quantities on the boundary, which means we may not expand second-derivatives of acoustical quantities within integrals, and must instead use integration-by-parts to remove the x-derivatives and then expand once it is safe to so.

If we start with the left-hand side of (2.27a), we get

$$
\begin{aligned}
&\int_{X_-}^{X_+} \psi_\alpha \left\{ \frac{\partial U^a}{\partial s} - \mathrm{i}a\omega \left[h_s \left(1 + \frac{1}{a^2\omega^2}\frac{\partial^2}{\partial x^2}\right) - \frac{\kappa}{a^2\omega^2}\frac{\partial}{\partial x}\right] P^a \right\} \mathrm{d}x = \underbrace{\frac{\mathrm{d}}{\mathrm{d}s}\left(\int_{X_-}^{X_+}\psi_\alpha U^a \mathrm{d}x\right)}_{\boxed{1}} \\
&- \underbrace{\left[X_+' \left(\psi_\alpha U^a\right)\Big|_{X_+} - X_-' \left(\psi_\alpha U^a\right)\Big|_{X_-}\right]}_{\boxed{2}} - \underbrace{\frac{\mathrm{i}a\omega}{a^2\omega^2}\left[\psi_\alpha h_s \frac{\partial P^a}{\partial x} - \frac{\partial(\psi_\alpha h_s)}{\partial x}P^a - \kappa\psi_\alpha P^a\right]_{X_-}^{X_+}}_{\boxed{3}} \\
&\qquad - \int_{X_-}^{X_+} \underbrace{\frac{\partial\psi_\alpha}{\partial s}U^a}_{\boxed{4}} + \underbrace{\mathrm{i}a\omega\left(h_s\psi_\alpha + \frac{1}{a^2\omega^2}\frac{\partial^2(\psi_\alpha h_s)}{\partial x^2} + \frac{\kappa}{a^2\omega^2}\frac{\partial\psi_\alpha}{\partial x}\right)P^a}_{\boxed{5}} \mathrm{d}x.
\end{aligned}
\tag{2.56}
$$

Terms $\boxed{1}$, $\boxed{2}$ and $\boxed{4}$ are the result of bringing the partial s-derivative on the U^a outside of the integral, whereas terms $\boxed{3}$ and $\boxed{5}$ are the result of removing all of the x-derivatives from the P^a via integration-by-parts (in particular, the second-derivative has been removed by a double i-b-p to produce the first two constituent terms of $\boxed{3}$). Term $\boxed{1}$ is an exact s-derivative of the projection of U^a onto the basis, i.e.

$$
\frac{\mathrm{d}}{\mathrm{d}s}\left(\int_{X_-}^{X_+}\psi_\alpha U^a \mathrm{d}x\right) = \frac{\mathrm{d}}{\mathrm{d}s}\left(\int_{X_-}^{X_+}\psi_\alpha \sum_\beta U^a_\beta \psi_\beta \mathrm{d}x\right) = \frac{\mathrm{d}}{\mathrm{d}s}\left(\sum_\beta \delta_{\alpha\beta}U^a_\beta\right) = \frac{\mathrm{d}U^a_\alpha}{\mathrm{d}s},
\tag{2.57}
$$

by mode orthogonality. Term $\boxed{2}$ combines with the first term of $\boxed{3}$ to form the left-hand side of the hard-walled boundary condition (2.29), leaving a term that is $O(M^2)$, while the second two terms of $\boxed{3}$ cancel with one another due to the Neumann condition on the duct modes. Finally, $\boxed{5}$'s second term, by the Leibniz rule, makes -2 lots of $\boxed{5}$'s third term added to a term involving the second-derivative of a spatial mode, which by (2.45) may be turned into multiplication by a squared eigenvalue. Thus, expanding into spatial modes, we have

$$
\begin{aligned}
&\int_{X_-}^{X_+} \psi_\alpha \left\{ \frac{\partial U^a}{\partial s} - \mathrm{i}a\omega \left[h_s \left(1 + \frac{1}{a^2\omega^2}\frac{\partial^2}{\partial x^2}\right) - \frac{\kappa}{a^2\omega^2}\frac{\partial}{\partial x}\right] P^a \right\} \mathrm{d}x \\
&\qquad = \sum_\beta \left(\delta_{\alpha\beta}\frac{\mathrm{d}}{\mathrm{d}s} - \int_{X_-}^{X_+} \frac{\partial\psi_\alpha}{\partial s}\psi_\beta \mathrm{d}x\right) U^a_\beta + \frac{1}{\mathrm{i}a\omega}\left[h_s\psi_\alpha\frac{\partial Q^a}{\partial x}\right]_{X_-}^{X_+} \\
&\qquad\quad - \mathrm{i}a\omega\sum_\beta \left[\left(1 - \frac{\lambda_\alpha^2}{a^2\omega^2X^2}\right)\int_{X_-}^{X_+} h_s\psi_\alpha\psi_\beta \mathrm{d}x - \frac{\kappa}{a^2\omega^2}\int_{X_-}^{X_+}\frac{\partial\psi_\alpha}{\partial x}\psi_\beta \mathrm{d}x\right] P^a_\beta.
\end{aligned}
\tag{2.58}
$$

Apart from the term involving Q^a (which will be dealt with later), we have integrals, with two subscripts α and β, summing over their second subscript with acoustical quantities that have only one subscript, β. In other words, this is standard matrix-vector multiplication, so we may drop the sigmas in employment of the summation convention (for clarity, in all of the expressions henceforth α is the free suffix, while, β, γ and δ are dummy suffices for use in summation). Furthermore, we will define a shorthand for any mode-integral matrices: the integral of two modes is written as Ψ, with Greek-letter subscripts denoting the mode-numbers, while bracketed subscripts denote derivatives of the modes in question (curly brackets are s-derivatives and square brackets are x-derivatives, with a square bracket around all subscripts meaning that this is a boundary term). Finally, any non-mode functions present in the integral appear in square brackets after the subscripts. This notation is the same as was used in McTavish and Brambley [2019]. For example,

$$\Psi_{\{\alpha\}[\beta]}[f(s,x)] \qquad \text{would mean} \qquad \int_{X_-}^{X_+} \frac{\partial\psi_\alpha}{\partial s}\frac{\partial\psi_\beta}{\partial x}f(s,x)\mathrm{d}x. \tag{2.59}$$

With this notation in hand, the projected left-hand side becomes

$$\left(\delta_{\alpha\beta}\frac{\mathrm{d}}{\mathrm{d}s} - \Psi_{\{\alpha\}\beta}\right)U^a_\beta + \frac{1}{\mathrm{i}a\omega}\left[h_s\psi_\alpha\frac{\partial Q^a}{\partial x}\right]_{X_-}^{X_+} \\ - \mathrm{i}a\omega\left[\left(\delta_{\alpha\gamma} - \frac{\Lambda^2_{\alpha\gamma}}{a^2\omega^2X^2}\right)\Psi_{\gamma\beta}[h_s] - \frac{\kappa}{a^2\omega^2}\Psi_{[\alpha]\beta}\right]P^b_\beta = O(M^2). \tag{2.60}$$

where Λ is a matrix with entries given by $\Lambda_{\alpha\gamma} = \lambda_\alpha\delta_{\alpha\gamma}$ (no sum).

We now turn to the right-hand side of (2.27a). Its first term projects very easily, giving

$$\int_{X_-}^{X_+} -\mathrm{i}a\omega\beta_0 h_s\psi_\alpha\sum_b P^{a-b}P^b\mathrm{d}x = -\mathrm{i}a\omega\beta_0\Psi_{\alpha\beta\gamma}[h_s]\sum_b P^{a-b}_\beta P^b_\gamma, \tag{2.61}$$

where the Ψ matrix notation has been naturally extended to third-rank tensors, which contract with acoustical quantities on subscripts 2 and 3. The next term on the right-hand side becomes

$$\mathrm{i}a\omega\int_{X_-}^{X_+}\psi_\alpha\left[h_s\left(1 - \frac{1}{a^2\omega^2}\frac{\partial^2}{\partial x^2}\right) + \frac{\kappa}{a^2\omega^2}\frac{\partial}{\partial x}\right]Q^a\mathrm{d}x \\ = \frac{\mathrm{i}a\omega}{a^2\omega^2}\left[-\psi_\alpha h_s\frac{\partial Q^a}{\partial x} + \frac{\partial(\psi_\alpha h_s)}{\partial x}Q^a + \kappa\psi_\alpha Q^a\right]_{X_-}^{X_+} \\ + \mathrm{i}a\omega\int_{X_-}^{X_+}Q^a\left[\left(1 - \frac{1}{a^2\omega^2}\frac{\partial^2}{\partial x^2}\right)(h_s\psi_\alpha) - \frac{\kappa}{a^2\omega^2}\frac{\partial\psi_\alpha}{\partial x}\right]\mathrm{d}x. \tag{2.62}$$

This is more-or-less the same manipulation as took place on the left-hand side, only now with Q^a in the place of P^a and some sign changes. After the same cancellations have been made, and we switch to the Ψ notation (which requires the terms making up

Q^a to be expanded into spatial modes), we get

$$\begin{aligned}
\mathrm{i}a\omega \int_{X_-}^{X_+} \psi_\alpha \left[h_s \left(1 - \frac{1}{a^2\omega^2} \frac{\partial^2}{\partial x^2} \right) + \frac{\kappa}{a^2\omega^2} \frac{\partial}{\partial x} \right] Q^a \mathrm{d}x &= \frac{1}{\mathrm{i}a\omega} \left[h_s \psi_\alpha \frac{\partial Q^a}{\partial x} \right]_{X_-}^{X_+} \\
&+ \mathrm{i}a\omega \Bigg[\left(\delta_{\alpha\delta} + \frac{\Lambda_{\alpha\delta}^2}{a^2\omega^2 X^2} \right) \Psi_{\delta\beta\gamma}[h_s] + \frac{\kappa}{a^2\omega^2} \Psi_{[\alpha]\beta\gamma} \Bigg] \frac{1}{2} \sum_b P_\beta^{a-b} P_\gamma^b - U_\beta^{a-b} U_\gamma^b \\
&+ \mathrm{i}a\omega \Bigg[\left(\delta_{\alpha\delta} + \frac{\Lambda_{\alpha\delta}^2}{a^2\omega^2 X^2} \right) \Psi_{\delta[\beta][\gamma]}[h_s] + \frac{\kappa}{a^2\omega^2} \Psi_{[\alpha][\beta][\gamma]} \Bigg] \sum_b \frac{P_\beta^{a-b} P_\gamma^b}{2(a-b)b\omega^2}. \qquad (2.63)
\end{aligned}$$

The first term here is exactly the leftover boundary term from the left-hand side; this will therefore cancel when they are combined, meaning the projected mass conservation equation is

$$\begin{aligned}
&\left(\delta_{\alpha\beta} \frac{\mathrm{d}}{\mathrm{d}s} - \Psi_{\{\alpha\}\beta} \right) U_\beta^a - \mathrm{i}a\omega \left[\left(1 - \frac{\lambda_\alpha^2}{a^2\omega^2 X^2} \right) \Psi_{\alpha\beta}[h_s] - \frac{\kappa}{a^2\omega^2} \Psi_{[\alpha]\beta} \right] P_\beta^b \\
&\quad = \mathrm{i}a\omega \sum_b \Bigg\{ - \beta_0 \Psi_{\alpha\beta\gamma}[h_s] P_\beta^{a-b} P_\gamma^b \\
&\qquad + \left[\left(\delta_{\alpha\delta} + \frac{\Lambda_{\alpha\delta}^2}{a^2\omega^2 X^2} \right) \Psi_{\delta\beta\gamma}[h_s] + \frac{\kappa}{a^2\omega^2} \Psi_{[\alpha]\beta\gamma} \right] \frac{P_\beta^{a-b} P_\gamma^b - U_\beta^{a-b} U_\gamma^b}{2} \qquad (2.64) \\
&\qquad + \left[\left(\delta_{\alpha\delta} + \frac{\Lambda_{\alpha\delta}^2}{a^2\omega^2 X^2} \right) \Psi_{\delta[\beta][\gamma]}[h_s] + \frac{\kappa}{a^2\omega^2} \Psi_{[\alpha][\beta][\gamma]} \right] \frac{P_\beta^{a-b} P_\gamma^b}{2(a-b)b\omega^2} \Bigg\}.
\end{aligned}$$

Projecting (2.27b) proves easier, since there are no boundary-term cancellations; care is only needed when dealing with the second x-derivative on the right-hand side. The left-hand side requires no integration-by-parts this time, due to the absence of any x-derivatives, so we simply have

$$\int_{X_-}^{X_+} \psi_\alpha \left(\frac{\partial P^a}{\partial s} - \mathrm{i}a\omega h_s U^a \right) \mathrm{d}x = \left(\delta_{\alpha\beta} \frac{\mathrm{d}}{\mathrm{d}s} + \Psi_{\alpha\{\beta\}} \right) P_\beta^a - \mathrm{i}a\omega \Psi_{\alpha\beta}[h_s] U_\beta^a. \qquad (2.65)$$

The term involving $(a - b)$ on the right-hand side is dealt with very easily, and the final term is effectively a repeat of the final term in (2.63). This leaves only the term with the $\partial^2/\partial x^2$, which must be integrated-by-parts before an expansion of the pressure into spatial modes may take place

$$\begin{aligned}
\int_{X_-}^{X_+} \mathrm{i}\omega h_s \psi_\alpha \sum_b \left[-bU^{a-b} \frac{1}{b^2\omega^2} \frac{\partial^2 P^b}{\partial x^2} \right] \mathrm{d}x &= -\mathrm{i}\omega \left[h_s \psi_\alpha \sum_b \frac{b}{b^2\omega^2} U^{a-b} \frac{\partial P^b}{\partial x} \right]_{X_-}^{X_+} \\
&+ \int_{X_-}^{X_+} \mathrm{i}\omega \sum_b \left[\frac{b}{b^2\omega^2} \frac{\partial \left(h_s \psi_\alpha U^{a-b} \right)}{\partial x} \sum_\gamma P_\gamma^b \frac{\partial \psi_\gamma}{\partial x} \right] \mathrm{d}x. \qquad (2.66)
\end{aligned}$$

We know from the hard-walled boundary condition that the $\partial P^b/\partial x$ in the boundary term must turn into a U^b (i.e. something expansible), and having now (legally) expanded the P^b inside the integral, we may now simply reverse the integration-by-parts (and employ the summation convention over γ), giving

$$\begin{aligned}\int_{X_-}^{X_+} \mathrm{i}\omega h_s \psi_\alpha \sum_b \left(-bU^{a-b} \frac{1}{b^2\omega^2} \frac{\partial^2 P^b}{\partial x^2} \right) \mathrm{d}x &= \left[X_+ \Psi^+_{[\alpha\beta\gamma]} - X_- \Psi^-_{[\alpha\beta\gamma]} \right] \sum_b U_\beta^{a-b} U_\gamma^b \\ &+ \mathrm{i}\omega \sum_b \left[\frac{b}{b^2\omega^2} h_s \psi_\alpha U^{a-b} P_\gamma^b \frac{\partial \psi_\gamma}{\partial x} \right]_{X_-}^{X_+} + \mathrm{i}\omega \sum_b \frac{b\Lambda^2_{\delta\gamma}}{b^2\omega^2 X^2} \Psi_{\alpha\beta\delta}[h_s] U_\beta^{a-b} P_\gamma^b. \end{aligned} \tag{2.67}$$

The $\partial\psi_\gamma/\partial x$ in the second boundary term causes it to vanish, by the Neumann condition on spatial modes. Thus, this term has been dealt with, and the projected momentum equation is

$$\begin{aligned}\left(\delta_{\alpha\beta} \frac{\mathrm{d}}{\mathrm{d}s} + \Psi_{\alpha\{\beta\}} \right) P_\beta^a - \mathrm{i}a\omega \Psi_{\alpha\beta}[h_s] U_\beta^a &= \left[X_+ \Psi^+_{[\alpha\beta\gamma]} - X_- \Psi^-_{[\alpha\beta\gamma]} \right] \sum_b U_\beta^{a-b} U_\gamma^b \\ &+ \mathrm{i}\omega \sum_b \left\{ \Psi_{\alpha\beta\delta}[h_s] \left[(a-b)\delta_{\delta\gamma} - b \left(\delta_{\delta\gamma} - \frac{\Lambda^2_{\delta\gamma}}{b^2\omega^2 X^2} \right) \right] + \frac{1}{b\omega^2} \Psi_{\alpha[\beta][\gamma]}[h_s] \right\} U_\beta^{a-b} P_\gamma^b, \end{aligned} \tag{2.68}$$

where the '+' and '−' superscripts on boundary terms indicate that only a single side of the boundary is being evaluated.

In theory, we have now done all of the work required to turn these equations from PDEs to ODEs and the next step would be to put them into a computer and solve them. However, more work may now be done to these equations in order to make them numerically efficient to solve. At present, we have a countably infinite set of coupled vector ODEs in s with matricial coefficients that also depend on s, meaning that a solver would need to update the value of each matrix at each point along the duct. This is missing a trick, though, since each of these matrices' s-dependence may be factored out into the form of s-dependent scalars such as κ, while the matrices themselves are constant, and thus only need to be defined before solving. This also has the advantage of added clarity, since it will clearly highlight which terms in the equations are responsible for different geometrical irregularities. In 2D, we have s-dependence in the integration limits X_- and X_+, which is removed via the substitution $\xi = (x - X_-)/X$, so that the integration limits are now 0 and 1. Expanding h_s and factoring the κ out then just leaves $1/\sqrt{X}$ in front of the modes, which can also be factored out. If we apply this technique to one of the matrices from (2.68), we get

$$\Psi_{\alpha\beta}[h_s] = \int_{X_-}^{X_+} \frac{C_\alpha C_\beta}{X} h_s \cos\left(\lambda_\alpha \frac{x - X_-}{X}\right) \cos\left(\lambda_\beta \frac{x - X_-}{X}\right) \mathrm{d}x$$
$$= (1 - \kappa X_-)\delta_{\alpha\beta} - \kappa X \int_0^1 C_\alpha C_\beta \xi \cos(\lambda_\alpha \xi) \cos(\lambda_\beta \xi) \mathrm{d}\xi = (1 - \kappa X_-)\delta_{\alpha\beta} - \kappa X \Xi_{\alpha\beta}[\xi] \tag{2.69}$$

where we have adopted a new notation Ξ for the constant matrices, analogous to the Ψ notation but now with different limits and a different integration variable. For clarity, an example is

$$\Xi_{\alpha[\beta]}[f(\xi)] = C_\alpha C_\beta \int_{\xi=0}^{1} \cos(\lambda_\alpha \xi) \frac{\mathrm{d}}{\mathrm{d}\xi} \left[\cos(\lambda_\beta \xi)\right] f(\xi) \mathrm{d}\xi. \tag{2.70}$$

In order to deal with s-derivatives, we note that

$$\frac{\partial \psi_\alpha}{\partial s} = -\frac{X'}{2X}\psi_\alpha - \frac{X'}{X}(x - X_-)\frac{\partial \psi_\alpha}{\partial x} - X'_- \frac{\partial \psi_\alpha}{\partial x} = -\frac{X'}{2X}\left(\psi_\alpha + 2\xi \frac{\partial \psi_\alpha}{\partial \xi}\right) - \frac{X'_-}{X}\frac{\partial \psi_\alpha}{\partial \xi}, \tag{2.71}$$

and a more convenient form may be found for some of the right-hand-side terms involving derivatives on multiple indices, by use of the Leibniz rule. The two relations necessary for this are

$$\Psi_{\alpha[\beta][\gamma]}[h_s] = \frac{\lambda_\beta^2 + \lambda_\gamma^2 - \lambda_\alpha^2}{2X^2}\Psi_{\alpha\beta\gamma}[h_s] - \kappa \Psi_{[\alpha]\beta\gamma} + \frac{\kappa}{2}\Psi_{[\alpha\beta\gamma]}, \tag{2.72a}$$
$$\Psi_{[\alpha][\beta][\gamma]} = \frac{\lambda_\beta^2 + \lambda_\gamma^2 - \lambda_\alpha^2}{2X^2}\Psi_{[\alpha]\beta\gamma} + \frac{\lambda_\alpha^2}{2X^2}\Psi_{[\alpha\beta\gamma]}. \tag{2.72b}$$

We also introduce a compact notation to simplify the form of the projected equations. For each $a \in \mathbb{N}$, let $\boldsymbol{p}^a$ denote the vector of coefficients P_α^a for $\alpha \in \mathbb{N}_0$, and similarly let $\boldsymbol{u}^a$ denote the vector of coefficients U_α^a (recalling that we use Roman letters as superscripts for the temporal Fourier modal decomposition, and Greek letters as subscripts for the spatial modal decomposition). For each of these vectors, matrices M with coefficients $\mathsf{M}_{\alpha\beta}$ act in the normal way,

$$\big(\mathsf{M}\boldsymbol{y}\big)_\alpha = \sum_{\beta=0}^{\infty} \mathsf{M}_{\alpha\beta} y_\beta. \tag{2.73}$$

For the weakly nonlinear terms, we define a quadratic operator $\mathcal{M}$ with coefficients $\mathcal{M}_{\alpha\beta\gamma}$, which acts on vectors $\boldsymbol{y}$ and $\boldsymbol{z}$ as

$$\big(\mathcal{M}\langle \boldsymbol{y}, \boldsymbol{z}\rangle\big)_\alpha = \sum_{\beta=0}^{\infty}\sum_{\gamma=0}^{\infty} \mathcal{M}_{\alpha\beta\gamma} y_\beta z_\gamma. \tag{2.74}$$

We also use the operator shorthand

$$\Big(\mathcal{M}+\mathcal{N}\langle \mathsf{I},\mathsf{A}\rangle\Big)\langle \boldsymbol{y},\boldsymbol{z}\rangle = \mathcal{M}\langle \boldsymbol{y},\boldsymbol{z}\rangle + \mathcal{N}\langle \boldsymbol{y},\mathsf{A}\boldsymbol{z}\rangle. \tag{2.75}$$

In the new notation, (2.64) and (2.68) can be rewritten as

$$\begin{aligned}
&\left[\frac{\mathrm{d}}{\mathrm{d}s}+\frac{X'}{2X}\mathsf{W}+\frac{X'_-}{X}\widetilde{\mathsf{A}}\right]\boldsymbol{u}^a-\mathrm{i}a\omega\left[\left(\mathsf{I}-\frac{\Lambda^2}{a^2\omega^2X^2}\right)\Big((1-\kappa X_-)\mathsf{I}-\kappa X\mathsf{A}\Big)-\frac{\kappa\widetilde{\mathsf{A}}}{a^2\omega^2X}\right]\boldsymbol{p}^a\\
&\quad=\frac{\mathrm{i}a\omega}{\sqrt{X}}\sum_b\Bigg\{-\beta_0\Big((1-\kappa X_-)\mathcal{I}-\kappa X\mathcal{A}\Big)\langle\boldsymbol{p}^{a-b},\boldsymbol{p}^b\rangle\\
&\qquad+\left[\left(\mathsf{I}+\frac{\Lambda^2}{a^2\omega^2X^2}\right)\Big((1-\kappa X_-)\mathcal{I}-\kappa X\mathcal{A}\Big)+\frac{\kappa\widetilde{\mathcal{A}}}{a^2\omega^2X}\right]\frac{\langle\boldsymbol{p}^{a-b},\boldsymbol{p}^b\rangle-\langle\boldsymbol{u}^{a-b},\boldsymbol{u}^b\rangle}{2}\\
&\qquad+\left[\frac{\left(\mathsf{I}+\frac{\Lambda^2}{a^2\omega^2X^2}\right)\Big((1-\kappa X_-)\mathcal{I}^\lambda-\kappa X\mathcal{A}^\lambda\Big)+\frac{\kappa\widetilde{\mathcal{A}}^\lambda}{a^2\omega^2X}}{2(a-b)b\omega^2X^2}\right]\langle\boldsymbol{p}^{a-b},\boldsymbol{p}^b\rangle\Bigg\},
\end{aligned}\tag{2.76a}$$

$$\begin{aligned}
&\left[\frac{\mathrm{d}}{\mathrm{d}s}-\frac{X'}{2X}\mathsf{W}^{\mathrm{T}}-\frac{X'_-}{X}\widetilde{\mathsf{A}}^{\mathrm{T}}\right]\boldsymbol{p}^a-\mathrm{i}a\omega\Big[(1-\kappa X_-)\mathsf{I}-\kappa X\mathsf{A}\Big]\boldsymbol{u}^a\\
&\quad=\frac{1}{\sqrt{X}}\sum_b\Bigg\{\left(\frac{X'_+}{X}\overline{\mathcal{W}}^+-\frac{X'_-}{X}\overline{\mathcal{W}}^-\right)\langle\boldsymbol{u}^{a-b},\boldsymbol{u}^b\rangle\\
&\qquad+\mathrm{i}\omega\Bigg[\Big((1-\kappa X_-)\mathcal{I}-\kappa X\mathcal{A}\Big)\left\langle\mathsf{I},(a-b)\mathsf{I}-b\left(\mathsf{I}-\frac{\Lambda^2}{b^2\omega^2X^2}\right)\right\rangle\\
&\qquad\qquad+\frac{(1-\kappa X_-)\mathcal{I}^\lambda-\kappa X\mathcal{A}^\lambda}{b\omega^2X^2}\Bigg]\langle\boldsymbol{u}^{a-b},\boldsymbol{p}^b\rangle\Bigg\},
\end{aligned}\tag{2.76b}$$

where the constant matrices and tensors have formulae

$$\mathsf{I}=\delta_{\alpha\beta},\qquad \mathsf{W}_{\alpha\beta}=\delta_{\alpha\beta}+2\Xi_{[\alpha]\beta}[\xi],\tag{2.77a}$$

$$\mathsf{A}_{\alpha\beta}=\Xi_{\alpha\beta}[\xi],\qquad \widetilde{\mathsf{A}}_{\alpha\beta}=\Xi_{[\alpha]\beta},\tag{2.77b}$$

$$\mathcal{I}_{\alpha\beta\gamma}=\Xi_{\alpha\beta\gamma},\qquad \mathcal{A}_{\alpha\beta\gamma}=\Xi_{\alpha\beta\gamma}[\xi],\tag{2.77c}$$

$$\widetilde{\mathcal{A}}_{\alpha\beta\gamma}=\Xi_{[\alpha]\beta\gamma},\qquad \overline{\mathcal{A}}_{\alpha\beta\gamma}=\Xi_{[\alpha\beta\gamma]},\tag{2.77d}$$

$$\overline{\mathcal{W}}^+_{\alpha\beta\gamma}=\Xi^+_{[\alpha\beta\gamma]},\qquad \overline{\mathcal{W}}^-_{\alpha\beta\gamma}=\Xi^-_{[\alpha\beta\gamma]},\tag{2.77e}$$

and some are modified by eigenvalue-multiplication

$$\mathcal{I}^\lambda = \mathcal{I}\frac{\langle \mathsf{\Lambda}^2, \mathsf{I}\rangle + \langle \mathsf{I}, \mathsf{\Lambda}^2\rangle - \mathsf{\Lambda}^2}{2}, \tag{2.77f}$$

$$\mathcal{A}^\lambda = \mathcal{A}\frac{\langle \mathsf{\Lambda}^2, \mathsf{I}\rangle + \langle \mathsf{I}, \mathsf{\Lambda}^2\rangle - \mathsf{\Lambda}^2}{2} + \widetilde{\mathcal{A}} - \frac{\overline{\mathcal{A}}}{2}, \tag{2.77g}$$

$$\widetilde{\mathcal{A}}^\lambda = \widetilde{\mathcal{A}}\frac{\langle \mathsf{\Lambda}^2, \mathsf{I}\rangle + \langle \mathsf{I}, \mathsf{\Lambda}^2\rangle - \mathsf{\Lambda}^2}{2} + \frac{\mathsf{\Lambda}^2}{2}\overline{\mathcal{A}}. \tag{2.77h}$$

The names of these matrices have been chosen to represent the geometric irregularities whose influence upon the equations they modulate, i.e. W for 'width', and A for 'annularity' (one matrix, $\widetilde{\mathsf{A}}$ is used for both, so a single name had to be picked). Calligraphic tensors are related to sans-serif matrices with the same name, i.e. $\mathcal{I}_{\alpha\beta 0} = \mathsf{I}_{\alpha\beta}$. The 'building-block' Ξ matrices have definitions listed in appendix A.

3D

Projection of the governing equations is complicated by an extra dimension, though fortunately all boundary terms in θ disappear due to periodicity of the spatial modes. Thus, we only need to worry about boundary terms in r. To help with this, some quick formulae are introduced for integration-by-parts (over a duct cross-section S, with differential $\mathrm{d}S = r\mathrm{d}r\mathrm{d}\theta$) involving the transverse gradient and FSND

$$\begin{aligned}\iint_S f\nabla_\mathrm{t}^2 g\mathrm{d}S &= \int_0^{2\pi}\left[rf\frac{\partial g}{\partial r}\right]_0^R \mathrm{d}\theta - \iint_S \nabla_\mathrm{t} f\cdot\nabla_\mathrm{t} g\mathrm{d}S \\ &= \int_0^{2\pi}\left[r\left(f\frac{\partial g}{\partial r} - \frac{\partial f}{\partial r}g\right)\right]_0^R \mathrm{d}\theta + \iint_S g\nabla_\mathrm{t}^2 f\mathrm{d}S,\end{aligned} \tag{2.78a}$$

$$\iint_S f\frac{\partial g}{\partial \mathbf{n}}\mathrm{d}S = \int_0^{2\pi}\left[r\cos\phi f g\right]_0^R \mathrm{d}\theta - \iint_S g\frac{\partial f}{\partial \mathbf{n}}\mathrm{d}S. \tag{2.78b}$$

Using the formulae above, we can project the left-hand side of (2.41a):

$$\begin{aligned}\iint_S \psi_\alpha\left\{\frac{\partial U^a}{\partial s} - \mathrm{i}a\omega\left[h_s\left(1+\frac{\nabla_\mathrm{t}^2}{a^2\omega^2}\right) - \frac{\kappa}{a^2\omega^2}\frac{\partial}{\partial\mathbf{n}}\right]P^a\right\}\mathrm{d}S &= \underbrace{\frac{\mathrm{d}}{\mathrm{d}s}\left(\iint \psi_\alpha U^a\mathrm{d}S\right)}_{\boxed{1}} \\ - \underbrace{\int_0^{2\pi} R'\left(r\psi_\alpha U^a\right)\Big|_R}_{\boxed{2}} + \underbrace{\frac{\mathrm{i}a\omega}{a^2\omega^2}\left[r\psi_\alpha h_s\frac{\partial P^a}{\partial r} - r\frac{\partial(\psi_\alpha h_s)}{\partial r}P^a - \kappa r\cos\phi\psi_\alpha P^a\right]_0^R}_{\boxed{3}}&\mathrm{d}\theta \\ - \iint_S \underbrace{\frac{\partial\psi_\alpha}{\partial s}U^a}_{\boxed{4}} + \underbrace{\mathrm{i}a\omega\left(h_s\psi_\alpha + \frac{\nabla_\mathrm{t}^2}{a^2\omega^2}(h_s\psi_\alpha) + \frac{\kappa}{a^2\omega^2}\frac{\partial\psi_\alpha}{\partial\mathbf{n}}\right)}_{\boxed{5}}&P^a\,\mathrm{d}S.\end{aligned} \tag{2.79}$$

As in (2.56), we have brought the s-derivative on the U^a outside of the integral, and removed all of the transverse derivatives from the pressure via integration-by-parts, so that all derivatives now act on the ψ_α mode. Once again term $\boxed{2}$ combines with the first bit of term $\boxed{3}$ to form the linear part of the boundary condition (2.43), while the rest of term $\boxed{3}$ cancels, and term $\boxed{5}$ changes after an application of the Leibniz rule, leaving

$$\begin{aligned}\iint_S \psi_\alpha \left\{ \frac{\partial U^a}{\partial s} - \mathrm{i}a\omega \left[h_s \left(1 + \frac{\nabla_{\mathrm{t}}^2}{a^2\omega^2} \right) - \frac{\kappa}{a^2\omega^2} \frac{\partial}{\partial \mathbf{n}} \right] P^a \right\} \mathrm{d}S \\ = \left(\delta_{\alpha\beta} \frac{\mathrm{d}}{\mathrm{d}s} - \iint_S \frac{\partial \psi_\alpha}{\partial s} \psi_\beta \mathrm{d}S \right) U^a_\beta + \frac{1}{\mathrm{i}a\omega} \left[r h_s \psi_\alpha \frac{\partial Q^a}{\partial r} \right]_0^R \\ - \mathrm{i}a\omega \left[\left(1 - \frac{\lambda_\alpha^2}{a^2\omega^2 R^2} \right) \iint_S h_s \psi_\alpha \psi_\beta \mathrm{d}S - \frac{\kappa}{a^2\omega^2} \iint_S \frac{\partial \psi_\alpha}{\partial \mathbf{n}} \psi_\beta \mathrm{d}S \right] P^a_\beta. \qquad (2.80)\end{aligned}$$

We can use the same shorthand for these matrix-integrals as we did earlier, introducing '$|\bullet|$' as a subscript notation for the FSND, and round brackets for θ-derivatives, so that the projected left-hand side of (2.41a) becomes

$$\begin{aligned}\left(\delta_{\alpha\beta} \frac{\mathrm{d}}{\mathrm{d}s} - \Psi_{\{\alpha\}\beta}[r] \right) U^a_\beta + \frac{1}{\mathrm{i}a\omega} \int_0^{2\pi} \left[r h_s \psi_\alpha \frac{\partial Q^a}{\partial r} \right]_0^R \mathrm{d}\theta \\ - \mathrm{i}a\omega \left[\left(\delta_{\alpha\gamma} - \frac{\Lambda_{\alpha\gamma}^2}{a^2\omega^2 R^2} \right) \Psi_{\gamma\beta}[r h_s] - \frac{\kappa}{a^2\omega^2} \Psi_{|\alpha|\beta}[r] \right] P^a_\beta = O(M^2). \qquad (2.81)\end{aligned}$$

Turning now to the right-hand side of (2.41a), we have an easy first term, followed by some derivatives of Q^a, which will removed by integration-by-parts as they just were with the pressure on the left-hand side

$$\begin{aligned}\mathrm{i}a\omega \iint_S \psi_\alpha \left[h_s \left(1 - \frac{\nabla_{\mathrm{t}}^2}{a^2\omega^2} \right) + \frac{\kappa}{a^2\omega^2} \frac{\partial}{\partial \mathbf{n}} \right] Q^a \mathrm{d}S \\ = \int_0^{2\pi} \frac{\mathrm{i}a\omega}{a^2\omega^2} \left[- r h_s \psi_\alpha \frac{\partial Q^a}{\partial r} + r \frac{\partial (h_s \psi_\alpha)}{\partial r} Q^a + \kappa r \cos\phi \psi_\alpha Q^a \right]_0^R \mathrm{d}\theta \\ + \mathrm{i}a\omega \iint_S Q^a \left[\left(1 - \frac{\nabla_{\mathrm{t}}^2}{a^2\omega^2} \right) (h_s \psi_\alpha) - \frac{\kappa}{a^2\omega^2} \frac{\partial \psi_\alpha}{\partial \mathbf{n}} \right] \mathrm{d}S. \qquad (2.82)\end{aligned}$$

Switching to the Ψ notation and making some cancellations, we get

$$\begin{aligned} \mathrm{i}a\omega \iint_S \psi_\alpha \left[h_s \left(1 - \frac{\nabla_{\mathrm{t}}^2}{a^2\omega^2} \right) + \frac{\kappa}{a^2\omega^2} \frac{\partial}{\partial \mathbf{n}} \right] Q^a \mathrm{d}S = \frac{1}{\mathrm{i}a\omega} \int_0^{2\pi} \left[r h_s \psi_\alpha \frac{\partial Q^a}{\partial r} \right]_0^R \mathrm{d}\theta \\ + \mathrm{i}a\omega \Bigg\{ \left[\left(\delta_{\alpha\delta} + \frac{\Lambda_{\alpha\delta}^2}{a^2\omega^2 R^2} \right) \Psi_{\delta\beta\gamma}[r h_s] + \frac{\kappa}{a^2\omega^2} \Psi_{|\alpha|\beta\gamma}[r] \right] \sum_b \frac{P_\beta^{a-b} P_\gamma^b - U_\beta^{a-b} U_\gamma^b}{2} \\ + \left[\left(\delta_{\alpha\delta} + \frac{\Lambda_{\alpha\delta}^2}{a^2\omega^2 R^2} \right) \left(\Psi_{\delta[\beta][\gamma]}[r h_s] + \Psi_{\delta(\beta)(\gamma)}[h_s/r] \right) \right. \\ \left. + \frac{\kappa}{a^2\omega^2} \left(\Psi_{|\alpha|[\beta][\gamma]}[r] + \Psi_{|\alpha|(\beta)(\gamma)}[1/r] \right) \right] \sum_b \frac{P_\beta^{a-b} P_\gamma^b}{2(a-b)b\omega^2} \Bigg\}. \end{aligned} \tag{2.83}$$

Combining this with the left-hand side of (2.41a), the same leftover boundary term vanishes, to give the full projected mass conservation equation,

$$\begin{aligned} \left(\delta_{\alpha\beta} \frac{\mathrm{d}}{\mathrm{d}s} - \Psi_{\{\alpha\}\beta}[r] \right) U_\beta^a - \mathrm{i}a\omega \left[\left(1 - \frac{\lambda_\alpha^2}{a^2\omega^2 R^2} \right) \Psi_{\alpha\beta}[r h_s] - \frac{\kappa}{a^2\omega^2} \Psi_{|\alpha|\beta}[r] \right] P_\beta^a \\ = \mathrm{i}a\omega \sum_b \Bigg\{ - \beta_0 \Psi_{\alpha\beta\gamma}[r h_s] P_\beta^{a-b} P_\gamma^b \\ + \left[\left(\delta_{\alpha\delta} + \frac{\Lambda_{\alpha\delta}^2}{a^2\omega^2 R^2} \right) \Psi_{\delta\beta\gamma}[r h_s] + \frac{\kappa}{a^2\omega^2} \Psi_{|\alpha|\beta\gamma}[r] \right] \frac{P_\beta^{a-b} P_\gamma^b - U_\beta^{a-b} U_\gamma^b}{2} \\ + \left[\left(\delta_{\alpha\delta} + \frac{\Lambda_{\alpha\delta}^2}{a^2\omega^2 R^2} \right) \left(\Psi_{\delta[\beta][\gamma]}[r h_s] + \Psi_{\delta(\beta)(\gamma)}[h_s/r] \right) \right. \\ \left. + \frac{\kappa}{a^2\omega^2} \left(\Psi_{|\alpha|[\beta][\gamma]}[r] + \Psi_{|\alpha|(\beta)(\gamma)}[1/r] \right) \right] \frac{P_\beta^{a-b} P_\gamma^b}{2(a-b)b\omega^2} \Bigg\}. \end{aligned} \tag{2.84}$$

As before, the left-hand side of the momentum conservation equation (2.41b) has no boundary cancellations, so projection is very straightforward

$$\iint_S \psi_\alpha \left(\frac{\partial P^a}{\partial s} - \mathrm{i}a\omega h_s U^a \right) \mathrm{d}S = \left(\delta_{\alpha\beta} \frac{\mathrm{d}}{\mathrm{d}s} + \Psi_{\alpha\{\beta\}}[r] \right) P_\beta^a - \mathrm{i}a\omega \Psi_{\alpha\beta}[r h_s] U_\beta^a. \tag{2.85}$$

Finally, the right-hand side of (2.41b) requires only that we deal carefully with the tranverse Laplacian, which produces a boundary term,

$$\begin{aligned} \iint_S \mathrm{i}\omega h_s \psi_\alpha \sum_b U^{a-b} \left(-b \frac{\nabla_{\mathrm{t}}^2}{b^2\omega^2} P^b \right) \mathrm{d}S = \mathrm{i}\omega \int_0^{2\pi} \left[r h_s \psi_\alpha \sum_b \frac{-b}{b^2\omega^2} U^{a-b} \frac{\partial P^b}{\partial r} \right]_0^R \mathrm{d}\theta \\ - \mathrm{i}\omega \iint_S \sum_b \left(\frac{-b}{b^2\omega^2} \right) \nabla_{\mathrm{t}}(h_s \psi_\alpha U^{a-b}) \cdot \nabla_{\mathrm{t}}(\psi_\gamma) P_\gamma^b \mathrm{d}S. \end{aligned} \tag{2.86}$$

As took place in 2D, the boundary term here becomes a $U^{a-b}U^b$, which can be expanded, and the other term has its integration-by-parts reversed once more, leaving

$$\begin{aligned}\iint_S \mathrm{i}\omega h_s \psi_\alpha \sum_b U^{a-b}\left(-b\frac{\nabla_{\mathrm{t}}^2}{b^2\omega^2}P^b\right)\mathrm{d}S = R'\Psi_{[\alpha\beta\gamma]}\sum_b U_\beta^{a-b}U_\gamma^b \\ -\,\mathrm{i}\omega\int_0^{2\pi}\left[\sum_b \frac{-b}{b^2\omega^2}rh_s\psi_\alpha U^{a-b}\frac{\partial\psi_\gamma}{\partial r}P_\gamma^b\right]_0^R \mathrm{d}\theta + \mathrm{i}\omega\sum_b \frac{b\Lambda_{\delta\gamma}^2}{b^2\omega^2R^2}\Psi_{\alpha\beta\delta}[rh_s]U_\beta^{a-b}P_\gamma^b. \quad (2.87)\end{aligned}$$

The leftover boundary term here cancels due to the Neumann condition on the spatial modes, so the full projected version of (2.41b) is

$$\begin{aligned}\left(\delta_{\alpha\beta}\frac{\mathrm{d}}{\mathrm{d}s}+\Psi_{\alpha\{\beta\}}[r]\right)P_\beta^a - \mathrm{i}a\omega\Psi_{\alpha\beta}[rh_s]U_\beta^a = R'\Psi_{[\alpha\beta\gamma]}\sum_b U_\beta^{a-b}U_\gamma^b \\ +\,\mathrm{i}\omega\sum_b\left\{\Psi_{\alpha\beta\delta}[rh_s]\left[(a-b)\delta_{\delta\gamma}-b\left(\delta_{\delta\gamma}-\frac{\Lambda_{\delta\gamma}^2}{b^2\omega^2R^2}\right)\right]\right. \\ \left.+\,\frac{\Psi_{\alpha[\beta][\gamma]}[rh_s]+\Psi_{\alpha(\beta)(\gamma)}[h_s/r]}{b\omega^2}\right\}U_\beta^{a-b}P_\gamma^b. \quad (2.88)\end{aligned}$$

We now have the same task of rewriting these equations in a more numerically efficient way. The added complication in 3D is that these are double integrals, which means that they must be split into separate radial and azimuthal parts; nonetheless, everything may still be made independent of s just as before. The notation for the split integrals is very similar to that of the Ψ matrices, e.g.

$$\Pi_{\alpha[\beta]}[f(x)] = C_\alpha C_\beta\int_{x=0}^1 \mathrm{J}_{p_\alpha}(\lambda_\alpha x)\frac{\partial}{\partial x}\left[\mathrm{J}_{p_\beta}(\lambda_\beta x)\right]f(x)\mathrm{d}x, \quad (2.89)$$

and

$$\Phi_{\alpha(\beta)}[g(\phi)] = \frac{1}{\pi}\int_{\theta=0}^{2\pi}\cos\!\Big(p_\alpha\phi-\xi_\alpha\frac{\pi}{2}\Big)\frac{\partial}{\partial\theta}\left[\cos\!\Big(p_\beta\phi-\xi_\beta\frac{\pi}{2}\Big)\right]g(\phi)\mathrm{d}\theta. \quad (2.90)$$

Once again, we need to know how s-derivatives of modes work: in 3D, the relevant equation is

$$\frac{\partial\psi_\alpha}{\partial s} = -\frac{R'}{R}\left(\psi_\alpha + r\frac{\partial\psi_\alpha}{\partial r}\right) - \tau\frac{\partial\psi_\alpha}{\partial\theta}, \quad (2.91)$$

while the analogous improved forms of matrices with derivatives on multiple subscripts are

$$\Psi_{\alpha[\beta][\gamma]}[rh_s] + \Psi_{\alpha(\beta)(\gamma)}[h_s/r] = \frac{\lambda_\beta^2 + \lambda_\gamma^2 - \lambda_\alpha^2}{2R^2}\Psi_{\alpha\beta\gamma}[rh_s] - \kappa\Psi_{|\alpha|\beta\gamma}[r] + \frac{\kappa}{2}\Psi_{[\alpha\beta\gamma]}[r\cos\phi], \tag{2.92a}$$

$$\begin{aligned} &\Psi_{|\alpha|[\beta][\gamma]}[r] + \Psi_{|\alpha|(\beta)(\gamma)}[1/r] \\ &\quad = \frac{\lambda_\beta^2 + \lambda_\gamma^2 - \lambda_\alpha^2}{2R^2}\Psi_{|\alpha|\beta\gamma}[r] + \frac{\lambda_\alpha^2 - p_\alpha^2}{2R^2}\Psi_{[\alpha\beta\gamma]}[r\cos\phi] - \frac{1}{2R}\Psi_{[(\alpha)\beta\gamma]}[\sin\phi]. \end{aligned} \tag{2.92b}$$

Equipped with the above, (2.84) and (2.88) become

$$\begin{aligned} &\left(\frac{\mathrm{d}}{\mathrm{d}s} + \frac{R'}{R}\mathsf{W} + \tau\mathsf{H}\right)\boldsymbol{u}^a - \mathrm{i}a\omega\left[\left(\mathsf{I} - \frac{\mathsf{\Lambda}^2}{a^2\omega^2R^2}\right)(\mathsf{I} - \kappa R\mathsf{A}) - \frac{\kappa\widetilde{\mathsf{A}}}{a^2\omega^2R}\right]\boldsymbol{p}^a \\ &\quad = \frac{\mathrm{i}a\omega}{\sqrt{\pi}R}\sum_b\left\{\left[\left(\mathsf{I} + \frac{\mathsf{\Lambda}^2}{a^2\omega^2R^2}\right)(\mathcal{I} - \kappa R\mathcal{A}) + \frac{\kappa\widetilde{\mathcal{A}}}{a^2\omega^2R}\right]\frac{\langle\boldsymbol{p}^{a-b}, \boldsymbol{p}^b\rangle - \langle\boldsymbol{u}^{a-b}, \boldsymbol{u}^b\rangle}{2}\right. \\ &\qquad \left. + \left[\frac{\left(\mathsf{I} + \frac{\mathsf{\Lambda}^2}{a^2\omega^2R^2}\right)(\mathcal{I}^\lambda - \kappa R\mathcal{A}^\lambda) + \frac{\kappa\widetilde{\mathcal{A}}^\lambda}{a^2\omega^2R}}{2(a-b)b\omega^2R^2} - \beta_0(\mathcal{I} - \kappa R\mathcal{A})\right]\langle\boldsymbol{p}^{a-b}, \boldsymbol{p}^b\rangle\right\}, \end{aligned} \tag{2.93a}$$

$$\begin{aligned} &\left(\frac{\mathrm{d}}{\mathrm{d}s} - \frac{R'}{R}\mathsf{W}^{\mathrm{T}} - \tau\mathsf{H}^{\mathrm{T}}\right)\boldsymbol{p}^a - \mathrm{i}a\omega\Big(\mathsf{I} - \kappa R\mathsf{A}\Big)\boldsymbol{u}^a = \frac{1}{\sqrt{\pi}R}\sum_b\left\{\frac{R'}{R}\overline{\mathcal{W}}\langle\boldsymbol{u}^{a-b}, \boldsymbol{u}^b\rangle\right. \\ &\qquad \left. + \mathrm{i}\omega\left[(\mathcal{I} - \kappa R\mathcal{A})\left\langle\mathsf{I}, (a-b)\mathsf{I} - b\left(\mathsf{I} - \frac{\mathsf{\Lambda}^2}{b^2\omega^2R^2}\right)\right\rangle + \frac{\mathcal{I}^\lambda - \kappa R\mathcal{A}^\lambda}{b\omega^2R^2}\right]\langle\boldsymbol{u}^{a-b}, \boldsymbol{p}^b\rangle\right\}, \end{aligned} \tag{2.93b}$$

where the constant matrices and tensors are

$$\mathsf{\Lambda}_{\alpha\beta} = \lambda_\alpha\delta_{\alpha\beta}, \qquad \mathsf{P}_{\alpha\beta} = p_\alpha\delta_{\alpha\beta}, \tag{2.94}$$

$$\mathsf{W}_{\alpha\beta} = \delta_{\alpha\beta} + \Pi_{[\alpha]\beta}[x^2]\Phi_{\alpha\beta}, \qquad \mathsf{H}_{\alpha\beta} = \Pi_{\alpha\beta}[x]\Phi_{(\alpha)\beta}, \tag{2.95}$$

$$\mathsf{A}_{\alpha\beta} = \Pi_{\alpha\beta}[x^2]\Phi_{\alpha\beta}[\cos\phi], \qquad \widetilde{\mathsf{A}}_{\alpha\beta} = \Pi_{[\alpha]\beta}[x]\Phi_{\alpha\beta}[\cos\phi] - \Pi_{\alpha\beta}\Phi_{(\alpha)\beta}[\sin\phi], \tag{2.96}$$

$$\mathcal{I}_{\alpha\beta\gamma} = \Pi_{\alpha\beta\gamma}[x]\Phi_{\alpha\beta\gamma}, \qquad \overline{\mathcal{W}}_{\alpha\beta\gamma} = \Pi_{[\alpha\beta\gamma]}\Phi_{\alpha\beta\gamma}, \tag{2.97}$$

$$\mathcal{A}_{\alpha\beta\gamma} = \Pi_{\alpha\beta\gamma}[x^2]\Phi_{\alpha\beta\gamma}[\cos\phi], \qquad \widetilde{\mathcal{A}}_{\alpha\beta\gamma} = \Pi_{[\alpha]\beta\gamma}[x]\Phi_{\alpha\beta\gamma}[\cos\phi] - \Pi_{\alpha\beta\gamma}\Phi_{(\alpha)\beta\gamma}[\sin\phi], \tag{2.98}$$

$$\overline{\mathcal{A}}_{\alpha\beta\gamma} = \Pi_{[\alpha\beta\gamma]}\Phi_{\alpha\beta\gamma}[\cos\phi], \qquad \overline{\mathcal{A}}^*_{\alpha\beta\gamma} = \Pi_{[\alpha\beta\gamma]}\Phi_{(\alpha)\beta\gamma}[\sin\phi], \tag{2.99}$$

and the eigenvalue-modified matrices $\mathcal{I}^\lambda$, $\mathcal{A}^\lambda$ and $\widetilde{\mathcal{A}}^\lambda$ are defined by

$$\mathcal{I}^\lambda = \mathcal{I}\frac{\langle \Lambda^2, \mathsf{I}\rangle + \langle \mathsf{I}, \Lambda^2\rangle - \Lambda^2}{2}, \tag{2.100}$$

$$\mathcal{A}^\lambda = \mathcal{A}\frac{\langle \Lambda^2, \mathsf{I}\rangle + \langle \mathsf{I}, \Lambda^2\rangle - \Lambda^2}{2} + \widetilde{\mathcal{A}} - \frac{\overline{\mathcal{A}}}{2}, \tag{2.101}$$

$$\widetilde{\mathcal{A}}^\lambda = \widetilde{\mathcal{A}}\frac{\langle \Lambda^2, \mathsf{I}\rangle + \langle \mathsf{I}, \Lambda^2\rangle - \Lambda^2}{2} + \frac{(\Lambda^2 - \mathsf{P}^2)\overline{\mathcal{A}} - \overline{\mathcal{A}}^*}{2}. \tag{2.102}$$

As before, notation has been chosen such that curvature acts through *annularity* matrices (A etc), *width* variation through W, and with the new quantity, torsion, through a *helicity* matrix H. Once more, the 'building-block' Π and Φ matrices have definitions listed in appendix A.

Unified form

The equations have a structure common to both 2D and 3D, and can be written compactly as

$$\frac{\mathrm{d}}{\mathrm{d}s}\begin{pmatrix}\boldsymbol{u}^a\\ \boldsymbol{p}^a\end{pmatrix} = \mathsf{L}^a\begin{pmatrix}\boldsymbol{u}^a\\ \boldsymbol{p}^a\end{pmatrix} + \sum_b \mathcal{N}^{ab}\left\langle \begin{pmatrix}\boldsymbol{u}^{a-b}\\ \boldsymbol{p}^{a-b}\end{pmatrix}, \begin{pmatrix}\boldsymbol{u}^b\\ \boldsymbol{p}^b\end{pmatrix}\right\rangle, \tag{2.103}$$

where in terms of square blocks $\mathsf{L}^a =: \begin{pmatrix}\mathsf{L}_1^a & \mathsf{L}_2^a\\ \mathsf{L}_3^a & \mathsf{L}_4^a\end{pmatrix}$, we have a 2D L^a

$$\mathsf{L}^a = \begin{pmatrix} -\frac{X'}{2X}\mathsf{W} - \frac{X'}{X}\widetilde{\mathsf{A}} & \mathrm{i}a\omega\left[\left(\mathsf{I} - \frac{\Lambda^2}{a^2\omega^2X^2}\right)(\mathsf{I} - \kappa X\mathsf{A}) - \frac{\kappa\widetilde{\mathsf{A}}}{a^2\omega^2X}\right] \\ \mathrm{i}a\omega\Big(\mathsf{I} - \kappa X\mathsf{A}\Big) & \frac{X'}{2X}\mathsf{W}^T + \frac{X'}{X}\widetilde{\mathsf{A}}^T \end{pmatrix}, \tag{2.104}$$

and a 3D L^a

$$\mathsf{L}^a = \begin{pmatrix} -\frac{R'}{R}\mathsf{W} - \tau\mathsf{H} & \mathrm{i}a\omega\left[\left(\mathsf{I} - \frac{\Lambda^2}{a^2\omega^2R^2}\right)(\mathsf{I} - \kappa R\mathsf{A}) - \frac{\kappa\widetilde{\mathsf{A}}}{a^2\omega^2R}\right] \\ \mathrm{i}a\omega\Big(\mathsf{I} - \kappa R\mathsf{A}\Big) & \frac{R'}{R}\mathsf{W}^T + \tau\mathsf{H}^T \end{pmatrix}, \tag{2.105}$$

and in terms of 'cubic blocks'

$$\mathcal{N}^{ab}_{\alpha,\beta,0:\alpha_{\max}} = \begin{pmatrix}\mathcal{N}_1^{ab} & \mathcal{N}_2^{ab}\\ \mathcal{N}_3^{ab} & \mathcal{N}_4^{ab}\end{pmatrix}, \qquad \mathcal{N}^{ab}_{\alpha,\beta,\alpha_{\max}+1:2\alpha_{\max}+1} = \begin{pmatrix}\mathcal{N}_5^{ab} & \mathcal{N}_6^{ab}\\ \mathcal{N}_7^{ab} & \mathcal{N}_8^{ab}\end{pmatrix}, \tag{2.106}$$

we have, in 2D

$$\mathcal{N}_1^{ab} = -\frac{\mathrm{i}a\omega}{2\sqrt{X}}\left[\left(\mathsf{I} + \frac{\Lambda^2}{a^2\omega^2X^2}\right)(\mathcal{I} - \kappa X\mathcal{A}) + \frac{\kappa\widetilde{\mathcal{A}}}{a^2\omega^2X}\right], \tag{2.107}$$

$$\mathcal{N}_3^{ab} = \frac{1}{\sqrt{X}}\left(\frac{X_+'}{X}\overline{\mathcal{W}}^+ - \frac{X_-'}{X}\overline{\mathcal{W}}^-\right), \tag{2.108}$$

$$\mathcal{N}_6^{ab} = -\mathcal{N}_1^{ab} + \frac{\mathrm{i}a\omega}{\sqrt{X}}\left[\frac{\left(\mathsf{I} + \frac{\Lambda^2}{a^2\omega^2X^2}\right)(\mathcal{I}^\lambda - \kappa X\mathcal{A}^\lambda) + \frac{\kappa\widetilde{\mathcal{A}}^\lambda}{a^2\omega^2X}}{2(a-b)b\omega^2X^2} - \beta_0\left(\mathcal{I} - \kappa R\mathcal{A}\right)\right], \tag{2.109}$$

$$\mathcal{N}_7^{ab} = \frac{\mathrm{i}\omega}{\sqrt{X}}\left\{(\mathcal{I} - \kappa X\mathcal{A})\left\langle \mathsf{I}, (a-b)\mathsf{I} - b\left(\mathsf{I} - \frac{\Lambda^2}{b^2\omega^2X^2}\right)\right\rangle + \frac{\mathcal{I}^\lambda - \kappa X\mathcal{A}^\lambda}{b\omega^2X^2}\right\}, \tag{2.110}$$

and in 3D

$$\mathcal{N}_1^{ab} = -\frac{\mathrm{i}a\omega}{2\sqrt{\pi}R}\left[\left(\mathsf{I} + \frac{\Lambda^2}{a^2\omega^2R^2}\right)(\mathcal{I} - \kappa R\mathcal{A}) + \frac{\kappa\widetilde{\mathcal{A}}}{a^2\omega^2R}\right], \tag{2.111}$$

$$\mathcal{N}_3^{ab} = \frac{R'}{\sqrt{\pi}R^2}\overline{\mathcal{W}}, \tag{2.112}$$

$$\mathcal{N}_6^{ab} = -\mathcal{N}_1^{ab} + \frac{\mathrm{i}a\omega}{\sqrt{\pi}R}\left[\frac{\left(\mathsf{I} + \frac{\Lambda^2}{a^2\omega^2R^2}\right)(\mathcal{I}^\lambda - \kappa R\mathcal{A}^\lambda) + \frac{\kappa\widetilde{\mathcal{A}}^\lambda}{a^2\omega^2R}}{2(a-b)b\omega^2R^2} - \beta_0\left(\mathcal{I} - \kappa R\mathcal{A}\right)\right], \tag{2.113}$$

$$\mathcal{N}_7^{ab} = \frac{\mathrm{i}\omega}{\sqrt{\pi}R}\left\{(\mathcal{I} - \kappa R\mathcal{A})\left\langle \mathsf{I}, (a-b)\mathsf{I} - b\left(\mathsf{I} - \frac{\Lambda^2}{b^2\omega^2R^2}\right)\right\rangle + \frac{\mathcal{I}^\lambda - \kappa R\mathcal{A}^\lambda}{b\omega^2R^2}\right\}, \tag{2.114}$$

while in both 2D and 3D $\mathcal{N}_2^{ab} = \mathcal{N}_4^{ab} = \mathcal{N}_5^{ab} = \mathcal{N}_8^{ab} = 0$. We recall that $P_\alpha^{-a} = P_\alpha^{a*}$ and that $P_\alpha^0 = 0$ by our earlier assumptions of real variables and vanishing time-averages. Note that, as expected, the weakly nonlinear terms will mix the effects of different frequencies. We will now work in terms of these quantities, so that everything we do will apply in both 2D and 3D.

In summary, the governing equations are (2.76a) and (2.76b) in 2D and (2.93a) and (2.93b) in 3D, and can be combined and written as (2.103). Greater numerical efficiency has been achieved through the transferral of s-dependence from matrices to the scalars multiplying them (since this allows the matrices to be pre-calculated rather than requiring recalculation at each step). Upper (Roman) indices are Fourier series wavenumbers while lower (Greek) indices are duct mode wavenumbers.

2.1.7 A note on 3D rectangular ducts

Previously, we generalised the 2D duct by removing the width variation of one of the walls, and revolving the entire duct about that wall to create a cylindrical 3D geometry, in which torsion may also be present. This mapping essentially turns the existing x-coordinate into r and introduces θ. Another option is to preserve the asymmetric width variation by retaining an x-coordinate and instead introducing y, thereby creating a duct of rectangular cross-section whose area and aspect ratio may vary with s. In breaking circular symmetry, however, we lose a degree of generality, as the phase shift (previously employed to maintain the coordinate system's orthogonality) will now noticeably rotate the geometry so as to preserve the orientation of the rectangle even in the presence of torsion. In order to generalise properly, we would have to use a phase shift θ_0 with $\theta_0'(s) \neq \tau$ in general; this would allow the rectangular cross section to rotate independently of the centreline's torsion. The resulting non-orthogonal coordinate system is dealt with in appendix B using guidance from Hill and Stokes [2018]. Because this does not optimise well numerically (as described in appendix B), it is not pursued further in this thesis.

2.2 Solution of the Governing Equations

Here, we solve the above governing equations subject to a radiation condition at the duct outlet, inspired by Félix and Pagneux [2001] and McTavish and Brambley [2019]. We first truncate the number of spatial modes to $\alpha_{\max}$ and the number of temporal modes to $a_{\max}$, before introducing the concept of an admittance, which relates velocities to pressures.

2.2.1 Admittance

The *admittance* Y, and its inverse the *impedance* Z, characterise the relationship between acoustic pressure and acoustic velocity. The admittance and impedance are defined here as

$$\boldsymbol{u}^a = \mathsf{Y}^a \boldsymbol{p}^a + \sum_b \mathcal{Y}^{ab} \langle \boldsymbol{p}^{a-b}, \boldsymbol{p}^b \rangle, \qquad \boldsymbol{p}^a = \mathsf{Z}^a \boldsymbol{u}^a + \sum_b \mathcal{Z}^{ab} \langle \boldsymbol{u}^{a-b}, \boldsymbol{u}^b \rangle. \tag{2.115}$$

The first of these relations may be used to eliminate the velocity from the governing equations (2.103). This leaves two equations in terms of $\mathrm{d}\mathsf{Y}^a/\mathrm{d}s$, $\mathrm{d}\boldsymbol{p}^a/\mathrm{d}s$, and $\boldsymbol{p}^a$. Eliminating $\mathsf{Y}^a \mathrm{d}\boldsymbol{p}^a/\mathrm{d}s$ then results in the following, at linear order

$$\mathsf{Y}^a(\mathsf{L}_3^a \mathsf{Y}^a + \mathsf{L}_4^a)\boldsymbol{p}^a = -\frac{\mathrm{d}\mathsf{Y}^a}{\mathrm{d}s}\boldsymbol{p}^a + (\mathsf{L}_1^a \mathsf{Y}^a + \mathsf{L}_2^a)\boldsymbol{p}^a. \tag{2.116}$$

The pressure is a free variable, i.e. can be assigned to be anything depending on our choice of pressure at the inner duct. Therefore, it can be cancelled off,[4], leaving a Riccati-style s-evolution equation for the admittance. The same can be done at weakly

---

[4] If the pressure is zero somewhere in the duct, this results in a singularity in the admittance: section 2.3.3 proposes a mathematical workaround for this eventuality, and section 2.3.6 proposes a numerical one.

nonlinear order, resulting in the following system

$$\frac{\mathrm{d}\mathsf{Y}^a}{\mathrm{d}s} = -\mathsf{Y}^a\mathsf{L}_3^a\mathsf{Y}^a + \mathsf{L}_1^a\mathsf{Y}^a - \mathsf{Y}^a\mathsf{L}_4^a + \mathsf{L}_2^a, \tag{2.117a}$$

$$\begin{aligned}\frac{\mathrm{d}\mathcal{Y}^{ab}}{\mathrm{d}s} =& -\mathsf{Y}^a\mathcal{N}_3^{ab}\langle\mathsf{Y}^{a-b},\mathsf{Y}^b\rangle - \mathsf{Y}^a\mathcal{N}_7^{ab}\langle\mathsf{Y}^{a-b},\mathsf{I}\rangle + \mathcal{N}_1^{ab}\langle\mathsf{Y}^{a-b},\mathsf{Y}^b\rangle + \mathcal{N}_6^{ab}\\ &-\mathcal{Y}^{ab}\left[-\mathsf{L}_1^a + \mathsf{Y}^a\mathsf{L}_3^a + \left\langle\mathsf{L}_4^{a-b} + \mathsf{L}_3^{a-b}\mathsf{Y}^{a-b},\mathsf{I}\right\rangle + \left\langle\mathsf{I},\mathsf{L}_4^b + \mathsf{L}_3^b\mathsf{Y}^b\right\rangle\right].\end{aligned} \tag{2.117b}$$

These equations will be solved to find the admittance, which encodes the acoustic properties of the duct. Once the admittance is known, the acoustic pressure may be solved for by substituting the admittance definition (2.115) back into the governing equations (2.103), giving

$$\frac{\mathrm{d}\boldsymbol{p}^a}{\mathrm{d}s} = \left(\mathsf{L}_3^a\mathsf{Y}^a + \mathsf{L}_4^a\right)\boldsymbol{p}^a + \sum_b\left(\mathsf{L}_3^a\mathcal{Y}^{ab} + \mathcal{N}_3^{ab}\langle\mathsf{Y}^{a-b},\mathsf{Y}^b\rangle + \mathcal{N}_7^{ab}\langle\mathsf{Y}^{a-b},\mathsf{I}\rangle\right)\langle\boldsymbol{p}^{a-b},\boldsymbol{p}^b\rangle, \tag{2.118}$$

with the velocities then given by the known admittance and pressure from the admittance definition (2.115). In order to solve the first order equation (2.117), a known value of the admittance must be given as a boundary condition at some point in the duct, for example, at the outlet. We next investigate special values of the admittance that might be used as boundary conditions for (2.117).

2.2.2 Invariant admittances

We consider admittances that solve (2.117) and are constant in s, therefore having a vanishing s-derivative. Physically, these invariant solutions represent the admittances of ducts for which no position in s is distinguishable from any other. Such a duct would have a constant radius, curvature and torsion, leaving the possibilities of: (a) an infinite straight duct (in 2D or 3D); (b) an annulus (in 2D) or torus (in 3D); and (c) an infinite helical duct (in 3D only). Because of the quadratic term in the evolution equation for Y^a, there is more than one constant solution for a given geometry. Here, a '+' solution will be constructed from the set of eigenvalues that represent waves either decaying or propagating in the positive s-direction, and a '−' solution will be constructed from the eigenvalues representing growth in the positive s-direction or propagation in the negative s-direction. These are respectively the *positive* and *negative characteristic admittances.* We denote by $(\boldsymbol{u}^{a\pm},\boldsymbol{p}^{a\pm})$ disturbances propagating in only the positive + or negative − directions, and define

$$\boldsymbol{u}^{a\pm} = \mathsf{Y}^{a\pm}\boldsymbol{p}^{a\pm} + \sum_b\mathcal{Y}^{ab\pm}\langle\boldsymbol{p}^{(a-b)\pm},\boldsymbol{p}^{b\pm}\rangle, \quad \boldsymbol{p}^{a\pm} = \mathsf{Z}^{a\pm}\boldsymbol{u}^{a\pm} + \sum_b\mathcal{Z}^{ab\pm}\langle\boldsymbol{u}^{(a-b)\pm},\boldsymbol{u}^{b\pm}\rangle. \tag{2.119}$$

The linear characteristic impedances $\mathsf{Z}^{a\pm}$ are the inverses of $\mathsf{Y}^{a\pm}$; the nonlinear characteristic impedances are found by making use of the weakly-nonlinear inversion rule $\mathscr{Z}^{ab\pm} = -\mathsf{Z}^{a\pm}\mathscr{Y}^{ab\pm}\langle \mathsf{Z}^{(a-b)\pm}, \mathsf{Z}^{b\pm}\rangle$.

Straight-duct characteristic admittances

This computation will be done in the general case in order to lay the groundwork for the curvature/torsion cases, where the diagonalisation is less trivial.

For a straight duct, the matrix L^a is constant, and given (across 2D and 3D) by setting $\kappa \equiv \tau \equiv X' \equiv R' \equiv 0$,

$$\overline{\mathsf{L}}^a = \begin{pmatrix} \mathsf{0} & \overline{\mathsf{L}}_2^a \\ \overline{\mathsf{L}}_3^a & \mathsf{0} \end{pmatrix}, \tag{2.120}$$

where $\overline{\mathsf{L}}_2^a$ is diagonal and $\overline{\mathsf{L}}_3^a$ is proportional to the identity. We seek a solution to

$$\frac{\mathrm{d}}{\mathrm{d}s}\begin{pmatrix} \boldsymbol{u}^a \\ \boldsymbol{p}^a \end{pmatrix} = \overline{\mathsf{L}}^a \begin{pmatrix} \boldsymbol{u}^a \\ \boldsymbol{p}^a \end{pmatrix}, \tag{2.121}$$

which takes the form $\boldsymbol{p}^a = \overline{\boldsymbol{c}}^a \exp(\overline{\gamma}^a s)$, with $\overline{\gamma}^a$ an eigenvalue and $\overline{\boldsymbol{c}}^a$ the corresponding eigenvector of $\overline{\mathsf{L}}^a$. We use the fact that for invertible matrices A and D,

$$\det\begin{pmatrix} \mathsf{A} & \mathsf{B} \\ \mathsf{C} & \mathsf{D} \end{pmatrix} = \det\mathsf{A}\det\left(\mathsf{D} - \mathsf{C}\mathsf{A}^{-1}\mathsf{B}\right) = \det\mathsf{D}\det\left(\mathsf{A} - \mathsf{B}\mathsf{D}^{-1}\mathsf{C}\right). \tag{2.122}$$

With this in mind, we know that the characteristic equation reads

$$0 = \det\left[\overline{\mathsf{L}}^a - \overline{\gamma}^a\begin{pmatrix} \mathsf{I} & \mathsf{0} \\ \mathsf{0} & \mathsf{I} \end{pmatrix}\right] = \det\left(\left(\overline{\gamma}^a\right)^2\mathsf{I} - \overline{\mathsf{L}}_3^a\overline{\mathsf{L}}_2^a\right). \tag{2.123}$$

Because $\overline{\mathsf{L}}_3^a\overline{\mathsf{L}}_2^a$ is diagonal (in either 2D or 3D), we may directly read off the eigenvalues. Since we have truncated to $\alpha_{\max}$ spatial modes, and therefore both $\overline{\mathsf{L}}_2^a$ and $\overline{\mathsf{L}}_3^a$ are $\alpha_{\max} \times \alpha_{\max}$, we see that there are precisely $\alpha_{\max}$ solutions for $\overline{\gamma}^{a2}$, of which some are positive and some negative (depending on the frequency ω, since this is determining whether the modes are cut-on or cut-off). None of these solutions are degenerate, since $\overline{\mathsf{L}}_3^a\overline{\mathsf{L}}_2^a$ has $\alpha_{\max}$ distinct diagonal entries. Thus, there will be a set of distinct eigenvalues $\{\overline{\gamma}_\alpha^a\}_{\alpha=0}^{\alpha_{\max}}$ that are exclusively in $\mathbb{R}^-$ or $\mathrm{i}\mathbb{R}^+$, corresponding to forward-decaying or forward-propagating modes respectively. These will be used to build the positive characteristic admittance; each will meanwhile have a mirror image in either $\mathbb{R}^+$ or $\mathrm{i}\mathbb{R}^-$, used to construct the negative characteristic admittance.

We may now partition the eigenvectors into two sets, those corresponding to $\{\overline{\gamma}_\alpha^a\}_{\alpha=0}^{\alpha_{\max}}$ and those corresponding to $\{-\overline{\gamma}_\alpha^a\}_{\alpha=0}^{\alpha_{\max}}$, denoted $\overline{\boldsymbol{c}}^{a\pm}$. Splitting them (as we have split $\overline{\mathsf{L}}^a$) into upper and lower vectors $(\overline{\boldsymbol{c}}_{\alpha,1}^{a\pm}, \overline{\boldsymbol{c}}_{\alpha,2}^{a\pm})$, and eliminating the upper vectors, we get

$$\overline{\mathsf{L}}_3^a\overline{\mathsf{L}}_2^a\overline{\boldsymbol{c}}_{\alpha,2}^{a\pm} = \overline{\gamma}_\alpha^{a\,2}\overline{\boldsymbol{c}}_{\alpha,2}^{a\pm}. \tag{2.124}$$

Because $\overline{\boldsymbol{c}}_{\alpha,2}^{a+}$ and $\overline{\boldsymbol{c}}_{\alpha,2}^{a-}$ satisfy the same equation, we can choose $\overline{\boldsymbol{c}}_{\alpha,2}^{a+} = \overline{\boldsymbol{c}}_{\alpha,2}^{a-} = \overline{\boldsymbol{c}}_{\alpha,2}^{a}$; further to this, we may note that (2.123) implies that $\overline{\mathsf{L}}_3^a\overline{\mathsf{L}}_2^a = \overline{\mathsf{\Gamma}}^{a2}$, where $\overline{\mathsf{\Gamma}}^a$ is a diagonal matrix with entries given by the elements of $\{\overline{\gamma}_\alpha^a\}_{\alpha=0}^{\alpha_{\max}}$. Defining a matrix $\overline{\mathsf{C}}^a$ with each column being a different $\overline{\boldsymbol{c}}_{\alpha,2}^a$ (arranged so as to match the ordering of $\overline{\mathsf{\Gamma}}^a$), we then see that

$$\overline{\mathsf{L}}_3^a\overline{\mathsf{L}}_2^a\overline{\mathsf{C}}^a = \overline{\mathsf{C}}^a\overline{\mathsf{\Gamma}}^{a2} = \overline{\mathsf{C}}^a\overline{\mathsf{L}}_3^a\overline{\mathsf{L}}_2^a. \tag{2.125}$$

Since $\overline{\mathsf{C}}^a$ commutes with a diagonal matrix with unique entries, it too must be diagonal, so having not yet normalised the eigenvectors, we can now simply choose $\overline{\mathsf{C}}^a = \mathsf{I}$. The admittance is then simple to construct from substituting it into the lower block of (2.121), getting $\overline{\mathsf{L}}_3^a\overline{\mathsf{Y}}^{a\pm} = \pm\overline{\mathsf{\Gamma}}^a$. In both 2D and 3D, $\overline{\mathsf{L}}_3^a = \mathrm{i}a\omega\mathsf{I}$, so we have

$$\overline{\mathsf{Y}}^{a\pm} = \pm\frac{1}{\mathrm{i}a\omega}\overline{\mathsf{\Gamma}}^a =: \pm\overline{\mathsf{Y}}^a. \tag{2.126}$$

For clarity, the admittances in 2D have the following explicit expression

$$\overline{\mathsf{Y}}_{\alpha\beta}^{a\pm} = \pm\mathrm{i}\delta_{\alpha\beta}\exp\left\{-\frac{\mathrm{i}\pi}{4}\left[\operatorname{sgn}\left(1-\frac{\lambda_\alpha^2}{a^2\omega^2X^2}\right)+1\right]\right\}\sqrt{\left|1-\frac{\lambda_\alpha^2}{a^2\omega^2X^2}\right|}, \tag{2.127}$$

and the 3D case is identical, only with an R in place of every X. We can then easily write down the definition of the straight-duct cut-off frequency for each mode in 2D and 3D

$$\varpi_\alpha^a(s) = \begin{cases} \frac{\lambda_\alpha}{aX(s)} & \text{2D,} \\ \frac{\lambda_\alpha}{aR(s)} & \text{3D,} \end{cases} \tag{2.128}$$

and note that ϖ_α^a increases with the spatial modenumber, while having the opposite relationship with the temporal modenumber.

In order to calculate the nonlinear characteristic admittances, we substitute the linear characteristic admittances into (2.117b), and look for fixed points

$$0 = -\overline{\mathsf{Y}}^a\overline{\mathcal{N}}_7^{ab}\langle\overline{\mathsf{Y}}^{a-b},\mathsf{I}\rangle + \overline{\mathcal{N}}_1^{ab}\langle\overline{\mathsf{Y}}^{a-b},\overline{\mathsf{Y}}^b\rangle + \overline{\mathcal{N}}_6^{ab} \mp \overline{\mathcal{Y}}^{ab\pm}\Big[\overline{\mathsf{Y}}^a\overline{\mathsf{L}}_3^a + \langle\overline{\mathsf{L}}_3^{a-b}\overline{\mathsf{Y}}^{a-b},\mathsf{I}\rangle + \langle\mathsf{I},\overline{\mathsf{L}}_3^b\overline{\mathsf{Y}}^b\rangle\Big]. \tag{2.129}$$

If we note that the square-bracketed quantity is actually equal to $\overline{\mathsf{\Gamma}}^a + \langle\overline{\mathsf{\Gamma}}^{a-b},\mathsf{I}\rangle + \langle\mathsf{I},\overline{\mathsf{\Gamma}}^b\rangle$, a sum of three diagonal matrices each acting on a different component, then we may simply divide through by this, pointwise, for each entry of $\overline{\mathcal{Y}}^{ab\pm}$, getting

$$\overline{\mathcal{Y}}_{\alpha\beta\gamma}^{ab\pm} = \pm\frac{\left(\overline{\mathcal{N}}_1^{ab}\langle\overline{\mathsf{Y}}^{a-b},\overline{\mathsf{Y}}^b\rangle + \overline{\mathcal{N}}_6^{ab} - \overline{\mathsf{Y}}^a\overline{\mathcal{N}}_7^{ab}\langle\overline{\mathsf{Y}}^{a-b},\mathsf{I}\rangle\right)_{\alpha\beta\gamma}}{\overline{\gamma}_\alpha^a + \overline{\gamma}_\beta^{a-b} + \overline{\gamma}_\gamma^b} =: \pm\overline{\mathcal{Y}}_{\alpha\beta\gamma}^{ab}. \tag{2.130}$$

Note that the linear characteristic *impedance* will have the definition $\mathsf{Z}^{a\pm} := (\mathsf{Y}^{a\pm})^{-1} =$

$\pm(\overline{\mathsf{Y}}^{a})^{-1}$, meaning that the nonlinear inversion rule $\mathcal{Z}^{ab\pm} = -\mathsf{Z}^{a\pm}\mathcal{Y}^{ab\pm}\langle \mathsf{Z}^{(a-b)\pm}, \mathsf{Z}^{b\pm}\rangle$ will result in

$$\mathcal{Z}^{ab\pm} = -\overline{\mathsf{Z}}^{a}\overline{\mathcal{Y}}^{ab}\langle \overline{\mathsf{Z}}^{a-b}, \overline{\mathsf{Z}}^{b}\rangle =: \overline{\mathcal{Z}}^{a-b}. \tag{2.131}$$

The positive and negative characteristic impedances are then $(\overline{\mathsf{Z}}^{a}, \overline{\mathcal{Z}}^{ab})$ and $(-\overline{\mathsf{Z}}^{a}, \overline{\mathcal{Z}}^{ab})$ respectively, with the sign discrepancy being due to the directionality of the velocity; since $\overline{\mathcal{Z}}^{ab}$ contracts with the velocity quadratically, a minus sign to indicate the wave's direction of travel must come from elsewhere.

Obviously we will run into problems if the denominator in 2.130 turns out to be zero: this would constitute a *resonant triad* [Protas et al., 2024, see, e.g.]. Empirically, we do not seem to run into this problem in the straight-duct case, but for the more complicated characteristic admittances that follow there seems to be no such guarantee. We avoid the problem of singular entries in the characteristic admittance by excising them from the matrix when a resonant triad is found, but proper work on the avoidance/physical significance of them should at some point be conducted.

Curved-duct characteristic admittances

When we introduce curvature, the straight-duct operator from equation (2.120) retains its block structure

$$\breve{\mathsf{L}}^{a} = \mathsf{L}^{a}\Big|_{\text{no } \tau,\ X' \text{ or } R'} = \begin{pmatrix} 0 & \breve{\mathsf{L}}^{a}_{2} \\ \breve{\mathsf{L}}^{a}_{3} & 0 \end{pmatrix}, \tag{2.132}$$

with the difference that $\breve{\mathsf{L}}^{a}_{2}$ and $\breve{\mathsf{L}}^{a}_{3}$ are no longer diagonal. They do remain symmetric, however (by inspection in $\breve{\mathsf{L}}^{a}_{3}$'s case, and by a complicated integration-by-parts in $\breve{\mathsf{L}}^{a}_{2}$'s). The eigenvalues $\breve{\gamma}^{a}$ now satisfy (from equation (2.122))

$$0 = \det\left[\breve{\mathsf{L}}^{a} - \breve{\gamma}^{a}\begin{pmatrix} \mathsf{I} & 0 \\ 0 & \mathsf{I} \end{pmatrix}\right] = \det\left((\breve{\gamma}^{a})^{2}\mathsf{I} - \breve{\mathsf{L}}^{a}_{3}\breve{\mathsf{L}}^{a}_{2}\right). \tag{2.133}$$

so they will exhibit the same properties as before (purely real/imaginary and being mirrored either side of the origin). We once again have $\breve{\mathsf{L}}^{a}_{3}\breve{\mathsf{L}}^{a}_{2}\breve{\boldsymbol{c}}^{a\pm}_{\alpha,2} = (\breve{\gamma}^{a}_{\alpha})^{2}\breve{\boldsymbol{c}}^{a\pm}_{\alpha,2}$, so a single lower-eigenvector matrix $\breve{\mathsf{C}}^{a}$ still exists, but this time it is non-diagonal. Substituting the admittance into the lower block this time, we get

$$\breve{\mathsf{L}}^{a}_{3}\breve{\mathsf{Y}}^{a\pm}\breve{\mathsf{C}}^{a} = \pm\breve{\mathsf{C}}^{a}\breve{\mathsf{\Gamma}}^{a}, \qquad \text{so} \qquad \breve{\mathsf{Y}}^{a\pm} = \pm(\breve{\mathsf{L}}^{a}_{3})^{-1}\breve{\mathsf{C}}^{a}\breve{\mathsf{\Gamma}}^{a}(\breve{\mathsf{C}}^{a})^{-1} =: \pm\breve{\mathsf{Y}}^{a}. \tag{2.134}$$

The nonlinear characteristic admittance takes a bit more work this time: the term multiplying $\breve{\mathcal{Y}}^{ab\pm}$ in the nonlinear admittance equation is no longer diagonal. We have already diagonalised $\breve{\mathsf{L}}^{a}_{3}\breve{\mathsf{Y}}^{a\pm}$, but we also need to diagonalise $\breve{\mathsf{Y}}^{a\pm}\breve{\mathsf{L}}^{a}_{3}$. To do this we note that (2.117a) is satisfied by $(\mathsf{Y}^{a})^{\mathrm{T}}$ as well as Y^{a}, so with symmetric $\breve{\mathsf{L}}^{a}_{3}$, we have

$$\breve{\mathsf{Y}}^{a\pm}\breve{\mathsf{L}}^{a}_{3} = (\breve{\mathsf{L}}^{a}_{3}\breve{\mathsf{Y}}^{a\pm})^{\mathrm{T}} = \pm\left(\breve{\mathsf{C}}^{a}\right)^{-\mathrm{T}}\breve{\mathsf{\Gamma}}^{a}\left(\breve{\mathsf{C}}^{a}\right)^{\mathrm{T}}. \tag{2.135}$$

With both diagonalisations, we now have

$$\breve{\mathcal{Y}}^{ab\pm}_{\alpha\beta\gamma} = \pm \sum_{\zeta,\delta,\epsilon} \left(\breve{\mathsf{C}}^{a}\right)^{-1}_{\zeta\alpha} \left(\breve{\mathsf{C}}^{a-b}\right)^{-1}_{\delta\beta} \left(\breve{\mathsf{C}}^{b}\right)^{-1}_{\epsilon\gamma} \\ \times \frac{\left[\left(\breve{\mathsf{C}}^{a}\right)^{\mathrm{T}} \left[\breve{\mathcal{N}}^{ab}_{1}\langle\breve{\mathsf{Y}}^{a-b},\breve{\mathsf{Y}}^{b}\rangle + \breve{\mathcal{N}}^{ab}_{6} - \breve{\mathsf{Y}}^{a}\breve{\mathcal{N}}^{ab}_{7}\langle\breve{\mathsf{Y}}^{a-b},\mathsf{I}\rangle\right] \left\langle\breve{\mathsf{C}}^{a-b},\breve{\mathsf{C}}^{b}\right\rangle\right]_{\zeta\delta\epsilon}}{\breve{\gamma}^{a}_{\zeta} + \breve{\gamma}^{a-b}_{\delta} + \breve{\gamma}^{b}_{\epsilon}} \tag{2.136}$$

Torsional-duct characteristic admittances

The final parameter that we can switch on is torsion, and this is only possible in the 3D case. When we do so, the matrix L^a becomes

$$\widetilde{\mathsf{L}}^{a} = \mathsf{L}^{a}\Big|_{\text{no } R'} = \begin{pmatrix} \widetilde{\mathsf{L}}^{a}_{1} & \widetilde{\mathsf{L}}^{a}_{2} \\ \widetilde{\mathsf{L}}^{a}_{3} & \widetilde{\mathsf{L}}^{a}_{1} \end{pmatrix}, \tag{2.137}$$

where $\widetilde{\mathsf{L}}^{a}_{2}$ and $\widetilde{\mathsf{L}}^{a}_{3}$ remain real and symmetric, and $\widetilde{\mathsf{L}}^{a}_{1}$ is a real antisymmetric matrix (apparent by direct calculation of the matrix H). Since a linear combination of the identity and an antisymmetric matrix is non-singular, we know that the characteristic equation reads

$$0 = \det\left(\left[\widetilde{\mathsf{L}}^{a}_{1} - \widetilde{\gamma}^{a}\mathsf{I}\right]^{2} - \left[\widetilde{\mathsf{L}}^{a}_{1} - \widetilde{\gamma}^{a}\mathsf{I}\right]\widetilde{\mathsf{L}}^{a}_{3}\left[\widetilde{\mathsf{L}}^{a}_{1} - \widetilde{\gamma}^{a}\mathsf{I}\right]^{-1}\widetilde{\mathsf{L}}^{a}_{2}\right), \tag{2.138}$$

but also, from the alternative expression in (2.122), that we have

$$0 = \det\left(\left[\widetilde{\mathsf{L}}^{a}_{1} - \widetilde{\gamma}^{a}\mathsf{I}\right]^{2} - \widetilde{\mathsf{L}}^{a}_{2}\left[\widetilde{\mathsf{L}}^{a}_{1} - \widetilde{\gamma}^{a}\mathsf{I}\right]^{-1}\widetilde{\mathsf{L}}^{a}_{3}\left[\widetilde{\mathsf{L}}^{a}_{1} - \widetilde{\gamma}^{a}\mathsf{I}\right]\right). \tag{2.139}$$

The expression on the right will have the same determinant if we take its transpose. Doing so reverses the signs on every term except those with a $\widetilde{\gamma}^{a}\mathsf{I}$, demonstrating that the eigenvalue mirroring property remains, even if the eigenvalues are no longer necessarily on the real/imaginary axes. We may still partition them into two matched groups, so we define

$$\{\widetilde{\gamma}^{a}_{\alpha}\}^{\infty}_{\alpha=0} = \{\widetilde{\gamma}^{a} : \mathrm{Re}(\widetilde{\gamma}^{a}) < 0\} \cup \{\widetilde{\gamma}^{a} : \mathrm{Re}(\widetilde{\gamma}^{a}) = 0, \mathrm{Im}(\widetilde{\gamma}^{a}) > 0\}, \tag{2.140}$$

a set that we use to construct the positive characteristic admittance. These correspond to purely-forward-propagating waves, as well as forward-decaying waves that may propagate either forwards or backwards.

We must also now keep track of eigenvalue signs when defining eigenvectors. If we define the diagonal $\widetilde{\mathsf{\Gamma}}^{a}$ matrix, and a general acoustic eigenvector $(\widetilde{\boldsymbol{c}}^{a\pm}_{\alpha,1}, \widetilde{\boldsymbol{c}}^{a\pm}_{\alpha,2})$, there will exist matrices $\widetilde{\mathsf{C}}^{a\pm}$, constructed from an ordering of either the '+' lower eigenvectors or the ‘$-$’. The lower-block admittance equation is then

$$(\widetilde{\mathsf{L}}_3^a\widetilde{\mathsf{Y}}^{a\pm}+\widetilde{\mathsf{L}}_1^a)\widetilde{\mathsf{C}}^{a\pm}=\pm\widetilde{\mathsf{C}}^{a\pm}\widetilde{\mathsf{\Gamma}}^a, \quad \text{so} \quad \widetilde{\mathsf{Y}}^{a\pm}=\left(\widetilde{\mathsf{L}}_3^a\right)^{-1}\left[-\widetilde{\mathsf{L}}_1^a\pm\widetilde{\mathsf{C}}^{a\pm}\widetilde{\mathsf{\Gamma}}^a\left(\widetilde{\mathsf{C}}^{a\pm}\right)^{-1}\right], \tag{2.141}$$

from which we deduce that the torsional entries $\widetilde{\mathsf{L}}_1^a$ have caused a symmetry-breaking between the positive and negative characteristic admittances. When it comes to computing the nonlinear admittances, we once again must take a transpose

$$\widetilde{\mathsf{Y}}^{a\pm}\widetilde{\mathsf{L}}_3^a-\widetilde{\mathsf{L}}_1^a=\left(\widetilde{\mathsf{L}}_3^a\widetilde{\mathsf{Y}}^{a\pm}+\widetilde{\mathsf{L}}_1^a\right)^{\mathrm{T}}=\pm\left(\widetilde{\mathsf{C}}^{a\pm}\right)^{-\mathrm{T}}\widetilde{\mathsf{\Gamma}}^a\left(\widetilde{\mathsf{C}}^{a\pm}\right)^{\mathrm{T}}, \tag{2.142}$$

meaning that the nonlinear characteristic admittances are given by

$$\begin{aligned}\widetilde{\mathcal{Y}}^{ab\pm}_{\alpha\beta\gamma}=\pm\sum_{\zeta,\delta,\epsilon}&\left(\widetilde{\mathsf{C}}^{a\pm}\right)^{-1}_{\zeta\alpha}\left(\widetilde{\mathsf{C}}^{(a-b)\pm}\right)^{-1}_{\delta\beta}\left(\widetilde{\mathsf{C}}^{b\pm}\right)^{-1}_{\epsilon\gamma}\\ \times\frac{\left[\left(\widetilde{\mathsf{C}}^{a\pm}\right)^{\mathrm{T}}\left[\widetilde{\mathcal{N}}_1^{ab}\langle\widetilde{\mathsf{Y}}^{(a-b)\pm},\widetilde{\mathsf{Y}}^{b\pm}\rangle+\widetilde{\mathcal{N}}_6^{ab}-\widetilde{\mathsf{Y}}^{a\pm}\widetilde{\mathcal{N}}_7^{ab}\langle\widetilde{\mathsf{Y}}^{(a-b)\pm},\mathsf{I}\rangle\right]\left\langle\widetilde{\mathsf{C}}^{(a-b)\pm},\widetilde{\mathsf{C}}^{b\pm}\right\rangle\right]_{\zeta\delta\epsilon}}{\widetilde{\gamma}^a_\zeta+\widetilde{\gamma}^{a-b}_\delta+\widetilde{\gamma}^b_\epsilon}&.\end{aligned} \tag{2.143}$$

2.2.3 Splitting operators

By using the characteristic admittances defined above, we can split waves into forward- and backward-going parts,

$$\boldsymbol{u}^a=\boldsymbol{u}^{a+}+\boldsymbol{u}^{a-}, \qquad\qquad \boldsymbol{p}^a=\boldsymbol{p}^{a+}+\boldsymbol{p}^{a-}. \tag{2.144}$$

We may perform this decomposition from the total pressure by defining linear and nonlinear *splitting operators* $\mathsf{S}^{a\pm}$ and $\mathcal{S}^{ab\pm}$,

$$\boldsymbol{p}^{a\pm}=\mathsf{S}^{a\pm}\boldsymbol{p}^a+\sum_b\mathcal{S}^{ab\pm}\langle\boldsymbol{p}^{a-b},\boldsymbol{p}^b\rangle; \tag{2.145}$$

a similar procedure could be defined for the velocity. Assuming we have picked a characteristic admittance, we now proceed to calculate these splitting operators in terms of our choice. Restricting ourselves to the linear case for a moment, we have

$$\boldsymbol{p}^{a\pm}=\boldsymbol{p}^a-\boldsymbol{p}^{a\mp}=\boldsymbol{p}^a-\mathsf{Z}^{a\mp}(\boldsymbol{u}^a-\boldsymbol{u}^{a\pm})=(\mathsf{I}-\mathsf{Z}^{a\mp}\mathsf{Y}^a)\boldsymbol{p}^a+\mathsf{Z}^{a\mp}\mathsf{Y}^{a\pm}\boldsymbol{p}^{a\pm}, \tag{2.146}$$

so that

$$\boldsymbol{p}^{a\pm}=(\mathsf{I}-\mathsf{Z}^{a\mp}\mathsf{Y}^{a\pm})^{-1}(\mathsf{I}-\mathsf{Z}^{a\mp}\mathsf{Y}^a)\boldsymbol{p}^a=\mathsf{S}^{a\pm}\boldsymbol{p}^a, \tag{2.147}$$

which may equivalently be written more compactly as

$$\mathsf{S}^{a\pm}=(\mathsf{Y}^{a\pm}-\mathsf{Y}^{a\mp})^{-1}(\mathsf{Y}^a-\mathsf{Y}^{a\mp}). \tag{2.148}$$

If the above equations are expanded to second order in terms of $\mathsf{S}^{a\pm}$, we find $\mathcal{S}^{ab\pm}$ to be

$$\mathcal{S}^{ab\pm} = (\mathsf{Y}^{a\pm} - \mathsf{Y}^{a\mp})^{-1}\Big(\mathcal{Y}^{ab} - \mathcal{Y}^{ab+}\langle \mathsf{S}^{(a-b)+}, \mathsf{S}^{b+}\rangle - \mathcal{Y}^{ab-}\langle \mathsf{S}^{(a-b)-}, \mathsf{S}^{b-}\rangle\Big). \tag{2.149}$$

Consistency of the splitting operators with weak nonlinearity

The decomposition (2.144) may at first sight seem worrying, in that our model is weakly nonlinear but here we assume a linear decomposition, i.e. that $\boldsymbol{p}^a = \boldsymbol{p}^{a+} + \boldsymbol{p}^{a-}$. Note that weak nonlinearity is still accounted for in the decomposition through the $\mathcal{S}^{ab\pm}$ terms in equation (2.145). In fact, this may not be surprising when we consider that the acoustic disturbance is a sum over modes, $p' = \sum_{a,\alpha} P^a_\alpha \psi_\alpha \mathrm{e}^{-\mathrm{i}a\omega t}$, which is necessarily a linear decomposition at each axial duct location, and that the separation into downstream- and upstream-propagating sound just involves rewriting this modal expansion as two sums. Suppose that this decomposition were not assumed, i.e. that $\boldsymbol{p}^{a+}$ and $\boldsymbol{p}^{a-}$ exist, but their sum is not necessarily $\boldsymbol{p}^a$. In this case, we would still have to have definitions (introducing velocity splitting operators $\widetilde{\mathsf{S}}^{a\pm}$ and $\widetilde{\mathcal{S}}^{ab\pm}$)

$$\boldsymbol{p}^{a\pm} = \mathsf{S}^{a\pm}\boldsymbol{p}^a + \sum_b \mathcal{S}^{ab\pm}\langle \boldsymbol{p}^{a-b}, \boldsymbol{p}^b\rangle, \tag{2.150a}$$

$$\boldsymbol{u}^{a\pm} = \widetilde{\mathsf{S}}^{a\pm}\boldsymbol{u}^a + \sum_b \widetilde{\mathcal{S}}^{ab\pm}\langle \boldsymbol{u}^{a-b}, \boldsymbol{u}^b\rangle, \tag{2.150b}$$

since the forward- and backward-going pressures and velocities must respectively be recoverable from the total pressure and velocity alone. If we were to add the forward and backward-going parts of the pressure together, we would get

$$\boldsymbol{p}^{a+} + \boldsymbol{p}^{a-} = (\mathsf{S}^{a+} + \mathsf{S}^{a-})\boldsymbol{p}^a + \sum_b (\mathcal{S}^{ab+} + \mathcal{S}^{ab-})\langle \boldsymbol{p}^{a-b}, \boldsymbol{p}^b\rangle \tag{2.151}$$

from which two things may be deduced. Firstly, we would still have $\mathsf{S}^{a+} + \mathsf{S}^{a-} = \mathsf{I}$ (since the decomposition is always valid at linear order) and secondly, the hypothetical nonlinear correction term making up the difference between $\boldsymbol{p}^a$ and $\boldsymbol{p}^{a+} + \boldsymbol{p}^{a-}$ would act homogeneously across all cross terms, i.e. we would have something of the form

$$\boldsymbol{p}^a = \boldsymbol{p}^{a+} + \boldsymbol{p}^{a-} + \sum_b \mathcal{C}^{ab}\langle \boldsymbol{p}^{a-b}, \boldsymbol{p}^b\rangle \tag{2.152}$$

along with

$$\boldsymbol{u}^a = \boldsymbol{u}^{a+} + \boldsymbol{u}^{a-} + \sum_b \widetilde{\mathcal{C}}^{ab}\langle \boldsymbol{u}^{a-b}, \boldsymbol{u}^b\rangle. \tag{2.153}$$

where

$$\mathcal{S}^{ab+} + \mathcal{S}^{ab-} + \mathcal{C}^{ab} = 0, \quad \text{and} \quad \widetilde{\mathcal{S}}^{ab+} + \widetilde{\mathcal{S}}^{ab-} + \widetilde{\mathcal{C}}^{ab} = 0. \tag{2.154}$$

From the model we have formulated, nothing more can be proven about the relationship between the pressure correction $\mathcal{C}^{ab}$ and splitting operators $\mathcal{S}^{ab\pm}$, or the velocity equivalents of these quantities, therefore we conclude that any arbitrary choice of these correction terms is mathematically consistent, and so here we take them to be zero; indeed, taking the cross-term to be non-zero would break the interpretation of a decomposition into upstream and downstream modes.

Relationship with the reflection matrix

In the linear case, it can be shown that a formulation in terms of the splitting operators is equivalent to one in terms of the reflection matrix R^a, which maps from $\boldsymbol{p}^{a+}$ to $\boldsymbol{p}^{a-}$. The reflection matrix is typically defined as

$$\mathsf{R}^a = (\mathsf{Y}^a - \mathsf{Y}^{a-})^{-1}(\mathsf{Y}^{a+} - \mathsf{Y}^a), \tag{2.155}$$

and, in the notation used here, is given by $\mathsf{S}^{a-}\left(\mathsf{S}^{a+}\right)^{-1}$. Working from the definitions, we find

$$\begin{aligned}
\mathsf{S}^{a-}\left(\mathsf{S}^{a+}\right)^{-1} &= (\mathsf{Y}^{a-} - \mathsf{Y}^{a+})^{-1}(\mathsf{Y}^a - \mathsf{Y}^{a+})(\mathsf{Y}^a - \mathsf{Y}^{a-})^{-1}(\mathsf{Y}^{a+} - \mathsf{Y}^{a-}) \\
&= \Big[(\mathsf{Y}^a - \mathsf{Y}^{a+})^{-1}(\mathsf{Y}^{a-} - \mathsf{Y}^{a+})\Big]^{-1}(\mathsf{Y}^a - \mathsf{Y}^{a-})^{-1}(\mathsf{Y}^a - \mathsf{Y}^{a-} + \mathsf{Y}^{a+} - \mathsf{Y}^a) \\
&= \Big[(\mathsf{Y}^a - \mathsf{Y}^{a+})^{-1}(\mathsf{Y}^a - \mathsf{Y}^{a+} + \mathsf{Y}^{a-} - \mathsf{Y}^a)\Big]^{-1}\Big[\mathsf{I} + (\mathsf{Y}^a - \mathsf{Y}^{a-})^{-1}(\mathsf{Y}^{a+} - \mathsf{Y}^a)\Big] \\
&= \Big[\mathsf{I} + (\mathsf{Y}^a - \mathsf{Y}^{a+})^{-1}(\mathsf{Y}^{a-} - \mathsf{Y}^a)\Big]^{-1}\Big[\mathsf{I} + (\mathsf{Y}^a - \mathsf{Y}^{a-})^{-1}(\mathsf{Y}^{a+} - \mathsf{Y}^a)\Big] \\
&= \Big[\Big\{(\mathsf{Y}^{a-} - \mathsf{Y}^a)^{-1}(\mathsf{Y}^a - \mathsf{Y}^{a+}) + \mathsf{I}\Big\}(\mathsf{Y}^a - \mathsf{Y}^{a+})^{-1}(\mathsf{Y}^{a-} - \mathsf{Y}^a)\Big]^{-1} \\
&\qquad\qquad\qquad\qquad \times \Big[\mathsf{I} + (\mathsf{Y}^a - \mathsf{Y}^{a-})^{-1}(\mathsf{Y}^{a+} - \mathsf{Y}^a)\Big] \\
&= \Big((\mathsf{Y}^a - \mathsf{Y}^{a+})^{-1}(\mathsf{Y}^{a-} - \mathsf{Y}^a)\Big]^{-1} = (\mathsf{Y}^a - \mathsf{Y}^{a-})^{-1}(\mathsf{Y}^{a+} - \mathsf{Y}^a) = \mathsf{R}^a.
\end{aligned} \tag{2.156}$$

In what follows, we will normally work in terms of the splitting operators since they are generally more well-defined than the reflection matrix. For instance, a wholly backward-going pressure field has an everywhere-singular reflection matrix. This is not to say that the splitting operators are well-defined everywhere: as we shall see in section 3.6, nodes in the pressure can occur, where the total pressure is zero but the forward and backward-going pressures are not. However, nodes are isolated points in s where the splitting matrices are singular, as opposed to large intervals in s where the reflection matrix can be singular.

2.2.4 Pressure Boundary Condition

When we come to solve these equations, we prescribe the admittances at the duct's outlet, amounting to a radiation condition, before solving, in order, the equations (2.117a) and (2.117b). After this, we know everything about the global radiative properties of the duct, and correspondingly we have only a first-order ODE (2.118) to solve for the pressure. For musical instruments, the pressure perturbation is prescribed by the musician, who disturbs the internal air column of the instrument at the inlet, meaning that the pressure is specified at the entrance (taken here to be at $s = 0$) and solved forwards from there.

One matter that is not entirely clear from a mathematical point of view is that of the musician's interaction with reflecting waves. Should the musician's playing amount to a prescription of the forward-going pressure only, meaning that waves reflected back impact without consequence on the source? Or should it rather be a prescription of the total pressure, meaning that the musician is adapting to the impact of the reflections they themselves generated? In brass instruments, it is thought that a feedback loop is formed between backward-going waves and the player's lip response to them: however, this complication is avoided here for simplicity, and we generally choose only to specify the forward-going pressure at the inlet, $p^+(\mathbf{x}, t)|_{s=0}$, with corresponding coefficient $\boldsymbol{p}^{a+}(0)$, and convert this (for the purpose of solving the equation) to the total pressure with the inverse splitting operator,

$$\boldsymbol{p}^a(0) = (\mathsf{S}^{a+})^{-1}\left[\boldsymbol{p}^{a+}(0) - \sum_b \mathcal{S}^{ab+}\left\langle (\mathsf{S}^{(a-b)+})^{-1}\boldsymbol{p}^{(a-b)+}(0), (\mathsf{S}^{b+})^{-1}\boldsymbol{p}^{b+}(0)\right\rangle\right]. \tag{2.157}$$

Use of the forward-going pressure is particularly important when dealing with resonances in ducts (as we shall do in section 5.3.3), because duct length can be enough to determine the inlet to be a node of oscillation, for a particular frequency: attempting then to prescribe anything *other* than a node in the total pressure at the node location can result in very unphysical numerical outputs. Nonetheless, we will occasionally prescribe the total pressure for the purpose of validation against previous work that also does so (e.g. in section 3.5, against McTavish and Brambley [2019]).

The simplest boundary condition for the forward-going pressure is that of a sinusoidal piston source at $s = 0$, given by $p^+(\mathbf{x}, t)|_{s=0} = M\sin(\omega t)$ (where we recall M is the perturbation Mach number, introduced in section 2.1.1), and projected onto the coordinate basis as

$$P_\alpha^{a+}(0) = \frac{M\sqrt{A_{\text{cs}}(0)}\operatorname{sgn}(a)\delta^{|a|,1}\delta_{\alpha 0}}{2\mathrm{i}}, \tag{2.158}$$

where $A_{\text{cs}}(0) = X(0)$ in 2D and $\pi R(0)^2$ in 3D. In 2D the piston may be longitudinally offset by an angle θ_1, which has initial condition

$$p^+(\mathbf{x}, t)|_{s=0} = M\sin(\omega t)\left(1 + \frac{2x\tan(\theta_1)}{X}\right), \tag{2.159}$$

translating to a modal coefficient of

$$P_{\alpha}^{a+}(0) = \frac{M\sqrt{A_{\mathrm{cs}}(0)}}{2\mathrm{i}}\delta^{|a|,1}\mathrm{sgn}(a)\left[\left(1 + 2\tan\theta_{\mathrm{l}}\frac{X_{-}(0)}{X(0)}\right)\delta_{\alpha 0} + 2\tan\theta_{\mathrm{l}}\mathsf{A}_{\alpha 0}\right]. \tag{2.160}$$

This can be generalised in 3D, to a piston with longitudinal and transverse offset angles θ_{l} and θ_{t}. We instead use the initial condition

$$p^{+}(\mathbf{x}, t)|_{s=0} = M\sin(\omega t)\left(1 + \frac{r\tan(\theta_{\mathrm{l}})\cos(\theta - \theta_0(0) - \theta_{\mathrm{t}})}{R}\right), \tag{2.161}$$

resulting in an initial modal coefficient of

$$P_{\alpha}^{a+}(0) = \frac{M\sqrt{A_{\mathrm{cs}}(0)}}{2\mathrm{i}}\delta^{|a|,1}\left[\delta_{\alpha 0} + \tan(\theta_{\mathrm{l}})\Pi_{\alpha 0}[x^2]\left(\cos\theta_{\mathrm{t}}\Phi_{\alpha 0}[\cos\phi] + \sin\theta_{\mathrm{t}}\Phi_{\alpha 0}[\sin\phi]\right)\right]; \tag{2.162}$$

in what follows, however, we will always take $\theta_{\mathrm{l}} = \theta_{\mathrm{t}} = 0$.

Another option is to consider non-plane modes. In 2D, for a variable-width straight duct (with width variation symmetric about the centreline), symmetric and antisymmetric modes are uncoupled, so there is a family of pressure distributions inaccessible to the plane-wave inlet condition. The 'fundamental' member of this family is the first antisymmetric mode, so we can consider a variant on condition (2.158) where the $\delta_{\alpha 0}$ is replaced with a $\delta_{\alpha 1}$.

This effect is amplified for any variable-width straight-duct in 3D, where modes of different azimuthal wavenumber are uncoupled, resulting in uncountably many mutually-inaccessible families of pressure distributions. The 'fundamental' of each therefore represents another possible inlet condition, meaning we replace the $\delta_{\alpha 0}$ with a $\delta_{p_\alpha n}\delta_{q_\alpha 1}$ for any n of our choice.

2.3 Numerical method

2.3.1 Truncation

When solving this infinite set of coupled ODEs numerically, we must truncate both the number of spatial and temporal modes used. If we pick maximum values of each, we then have spatial modes ranging from 0 to $\alpha_{\max}$ and temporal modes ranging from $-a_{\max}$ to $a_{\max}$. This would mean that we have $(\alpha_{\max} + 1)(2a_{\max} + 1)$ equations to solve for P_{α}^{a}, $(\alpha_{\max} + 1)^2(2a_{\max} + 1)$ for $\mathsf{Y}_{\alpha\beta}^{a}$ and $(\alpha_{\max} + 1)^3(2a_{\max} + 1)^2$ for $\mathcal{Y}_{\alpha\beta\gamma}^{ab}$. However, by our previous assumptions we are neglecting $a = 0$ modes, and all of our acoustic quantities being real implies that $P_{\alpha}^{-a} = P_{\alpha}^{a*}$ and $U_{\alpha}^{-a} = U_{\alpha}^{a*}$, resulting in $(\alpha_{\max} + 1)a_{\max}$ independent equations for P_{α}^{a} and $(\alpha_{\max} + 1)^2 a_{\max}$ for $\mathsf{Y}_{\alpha\beta}^{a}$.

A slightly messier calculation at this point (taking into account the conjugacy property, the absence of $a = 0$ entries, and also now the absence of $a = b$ entries) puts the number of independent entries of $\mathcal{Y}^{ab}_{\alpha\beta\gamma}$ at $(\alpha_{\max}+1)^3(2a_{\max}-1)a_{\max}$. More entries may yet be discarded though, since discrete convolutions behave strangely upon truncation; if a and b range from $-a_{\max}$ to $a_{\max}$ then $a-b$ ranges from $-2a_{\max}$ to $2a_{\max}$. We need $\boldsymbol{p}^{a-b}$ and $\boldsymbol{p}^{b}$ to calculate $\mathcal{Y}^{ab}$, but cannot know the values of $\boldsymbol{p}^{a-b}$ for $a-b \notin \{-a_{\max},\dots,a_{\max}\}$, so as a consequence, at each timestep, for every triple (α,β,γ), there is an ab matrix $\mathcal{Y}^{ab}_{\alpha\beta\gamma}$ of which the only calculable entries form a *banded* matrix (with bandwidth $a_{\max}$), resulting in $a_{\max}(a_{\max}+1)$ lost entries. Having exploited the conjugacy property already, this means a subtraction of $a_{\max}(a_{\max}+1)/2$ entries from the total, resulting in $3(\alpha_{\max}+1)^3a_{\max}(a_{\max}-1)/2$ independent entries for the nonlinear admittance.

2.3.2 Numerical solver

We use a 4th-order Runge–Kutta method to integrate the admittance and pressure equations in s. Unless otherwise specified, we use the adaptive-step solver `ode45` in MATLAB, although for one case in section 3.5 we use a fixed-step solver, as that proves more accurate in the neighbourhood of a cusp in the duct diameter.

2.3.3 Magnus–Möbius solver

We briefly discuss here an alternative solver to Runge–Kutta. In some geometries, notably when a duct narrows from inlet to outlet (as with the inverse exponential horn seen in section 3.6), there may be nodes in the velocity or pressure. The latter are problematic when solving for the admittance: a point where the velocity is nonzero and the pressure is zero results in a singularity in their ratio. When a Runge-Kutta solver hits a singularity, the computation times out, so we need to use a Magnus–Möbius method.

The Möbius method, aimed specifically at this eventuality (singularities in the solutions to Riccati equations), was devised in Schiff and Shnider [1999]; its name may come from the form of the scheme's resemblance to a Möbius map (see equation (2.168)). This was originally for scalar Riccati equations; Pagneux [2010] combined it with the Magnus method ([Iserles and Nørsett, 1999]) to generalise it to matrix Riccati equations. This was still in the linear case, however: here we present a novel generalisation of the Magnus–Möbius method to *nonlinear* matrix Riccati equations. The use of the Magnus-Möbius method was inspired by Mangin [2023], where it was generalised to higher-order accuracy for use with acoustics in the presence of a mean flow: here, instead, we retain a low order but generalise to nonlinearity.

The linear Magnus–Möbius scheme

The formulation of this scheme requires us to write our system in a particular way. In the linear case, we introduce the *acoustic variable vector* $\boldsymbol{a}^a$ and solve

$$\frac{\mathrm{d}\boldsymbol{a}^a}{\mathrm{d}s} = \mathsf{L}^a \boldsymbol{a}^a, \qquad \boldsymbol{a}^a = \begin{pmatrix} \boldsymbol{u}^a \\ \boldsymbol{p}^a \end{pmatrix}, \tag{2.163}$$

subject to conditions at $s = 0$ and $s = s_\text{o}$. In general, L^a depends on the integration variable s. We discretise the domain into $N + 1$ points $\{s_n\}_{n=0}^N$, chosen so that on each interval $[s_n, s_{n+1}]$ the s-dependence of L^a may be neglected to first order in the local stepsize. We discretise the domain into $N + 1$ points $\{s_n\}_{n=0}^N$, and neglect the s-dependence of L^a within each interval $[s_n, s_{n+1}]$ (an approximation of first order in the local stepsize). Should L^a be constant to begin with, this can mean very few points are needed to find the admittance, provided a fixed point of the admittance equation is the boundary condition. Even in this case however, the pressure calculation will need more points.

Solving over a domain with fixed L^a, we find (specifying $\boldsymbol{a}^a$ at some s_C) that

$$\boldsymbol{a}^a(s) = \exp\Big((s - s_\text{C})\mathsf{L}^a\Big)\boldsymbol{a}^a(s_\text{C}). \tag{2.164}$$

We will need to solve backwards for the admittance: when solving backwards, we find that

$$\boldsymbol{a}^a(s) = \exp\Big(-(s_{n+1} - s)\mathsf{L}^a(\overline{s}_{n+1})\Big)\boldsymbol{a}^a_{n+1} \quad \text{so} \quad \boldsymbol{a}^a_n = \exp\Big(-(\delta s)_{n+1}\mathsf{L}^a(\overline{s}_{n+1})\Big)\boldsymbol{a}^a_{n+1}, \tag{2.165}$$

where $\boldsymbol{a}^a_n = \boldsymbol{a}^a(s_n)$, $\overline{s}_n = \frac{1}{2}(s_n + s_{n-1})$ and $(\delta s)_n = s_n - s_{n-1}$.

The conditions at the endpoints are prescribed by introducing the admittance Y^a: we say

$$\boldsymbol{a}^a = \begin{pmatrix} \mathsf{Y}^a \boldsymbol{p}^a \\ \boldsymbol{p}^a \end{pmatrix}, \qquad \mathsf{Y}^a(s_\text{o}) = \mathsf{Y}^a_\text{o}, \qquad \boldsymbol{p}^a(0) = \boldsymbol{p}^a_\text{i}, \tag{2.166}$$

and solve backwards for Y^a first before solving forwards for $\boldsymbol{p}^a$. Once discretised, this becomes (dividing the matrix exponential $\exp\big((\delta s)_{n+1}\mathsf{L}^a(\overline{s}_{n+1})\big)$ into blocks)

$$\begin{pmatrix} \mathsf{Y}^a_n \boldsymbol{p}^a_n \\ \boldsymbol{p}^a_n \end{pmatrix} = \begin{pmatrix} \mathsf{E}^a_1 & \mathsf{E}^a_2 \\ \mathsf{E}^a_3 & \mathsf{E}^a_4 \end{pmatrix} \begin{pmatrix} \mathsf{Y}^a_{n+1} \boldsymbol{p}^a_{n+1} \\ \boldsymbol{p}^a_{n+1} \end{pmatrix}, \tag{2.167}$$

therefore we have a backward admittance scheme

$$\mathsf{Y}^a_n = (\mathsf{E}^a_1 \mathsf{Y}^a_{n+1} + \mathsf{E}^a_2)(\mathsf{E}^a_3 \mathsf{Y}^a_{n+1} + \mathsf{E}^a_4)^{-1}; \qquad \mathsf{Y}^a_N = \mathsf{Y}^a_\text{o}, \tag{2.168}$$

and then a forward pressure scheme

$$\boldsymbol{p}^a_{n+1} = (\mathsf{E}^a_3 \mathsf{Y}^a_{n+1} + \mathsf{E}^a_4)^{-1} \boldsymbol{p}^a_n; \qquad \boldsymbol{p}^a_0 = \boldsymbol{p}^a_{\mathrm{i}}. \tag{2.169}$$

This is a second-order scheme: the Möbius method has been generalised to higher orders in Schiff and Shnider [1999] and the Magnus expansion in Iserles and Nørsett [1999]; Pagneux [2010] uses a fourth-order Magnus-Möbius scheme based on the higher-order Magnus method.

The nonlinear Magnus–Möbius scheme

Next we outline a possible method for including nonlinear effects while still using the Magnus-Möbius method. Now we are solving

$$\frac{\mathrm{d}\boldsymbol{a}^a}{\mathrm{d}s} = \mathsf{L}^a \boldsymbol{a}^a + \sum_b \mathcal{N}^{ab} \langle \boldsymbol{a}^{a-b}, \boldsymbol{a}^b \rangle. \tag{2.170}$$

Since $\boldsymbol{a}^a$ is $O(M)$ we set

$$\boldsymbol{a}^a(s) = M \hat{\boldsymbol{a}}^a_1(s) + M^2 \hat{\boldsymbol{a}}^a_2(s), \tag{2.171}$$

and first solve, in each $[s_n, s_{n+1}]$

$$\frac{\mathrm{d}\hat{\boldsymbol{a}}^a_1}{\mathrm{d}s} = \mathsf{L}^a(\bar{s}_{n+1}) \hat{\boldsymbol{a}}^a_1, \qquad \hat{\boldsymbol{a}}^a_1\bigg|_{s_{n+1}} = \frac{\boldsymbol{a}^a_{n+1}}{M}, \qquad \text{with} \qquad \hat{\boldsymbol{a}}^a_1\bigg|_{s_N} = \frac{\boldsymbol{a}^a(s_{\mathrm{o}})}{M}, \tag{2.172}$$

so as before we get

$$\hat{\boldsymbol{a}}^a_1(s) = \frac{1}{M} \exp\bigg(-(s_{n+1} - s) \mathsf{L}^a(\bar{s}_{n+1}) \bigg) \boldsymbol{a}^a_{n+1}, \tag{2.173}$$

i.e.

$$\hat{\boldsymbol{a}}^a_1(s_n) = \frac{1}{M} \exp\bigg(-(\delta s)_{n+1} \mathsf{L}^a(\bar{s}_{n+1}) \bigg) \boldsymbol{a}^a_{n+1} = \frac{\mathsf{E}^a \boldsymbol{a}^a_{n+1}}{M}, \tag{2.174}$$

and then this solution is used to solve the next order up

$$\frac{\mathrm{d}\hat{\boldsymbol{a}}^a_2}{\mathrm{d}s} = \mathsf{L}^a(\bar{s}_{n+1}) \hat{\boldsymbol{a}}^a_2 + \sum_b \mathcal{N}^{ab}(\bar{s}_{n+1}) \langle \hat{\boldsymbol{a}}^{a-b}_1, \hat{\boldsymbol{a}}^b_1 \rangle, \quad \hat{\boldsymbol{a}}^a_2\bigg|_{s_{n+1}} = 0, \quad \text{with} \quad \hat{\boldsymbol{a}}^a_2\bigg|_{s_N} = 0. \tag{2.175}$$

If we use an integrating factor of $\exp(-s\mathsf{L}^a)$ then we get (dropping the arguments of L^a and $\mathcal{N}^{ab}$ for brevity, while noting that they are assumed constant throughout this section)

$$\begin{aligned}\frac{\mathrm{d}}{\mathrm{d}s}\left(\exp(-s\mathsf{L}^a)\hat{\boldsymbol{a}}_2^a\right) &= \exp(-s\mathsf{L}^a)\sum_b \mathcal{N}^{ab}\langle \hat{\boldsymbol{a}}_1^{a-b}(s), \hat{\boldsymbol{a}}_1^b(s)\rangle \\ &= \frac{1}{M^2}\sum_b\left\{\exp(-s\mathsf{L}^a)\left\langle \exp\Big(s\mathsf{L}^{a-b}\Big), \exp\Big(s\mathsf{L}^b\Big)\right\rangle\right\} \\ &\quad\times \mathcal{N}^{ab}\left\langle \exp\Big(-s_{n+1}\mathsf{L}^{a-b}\Big)\boldsymbol{a}_{n+1}^{a-b}, \exp\Big(-s_{n+1}\mathsf{L}^b\Big)\boldsymbol{a}_{n+1}^b\right\rangle,\end{aligned} \tag{2.176}$$

so if we integrate up, we have

$$\begin{aligned}\left[\exp(-s\mathsf{L}^a)\hat{\boldsymbol{a}}_2^a\right]_{s_n}^{s_{n+1}} &= -\exp(-s_n\mathsf{L}^a)\hat{\boldsymbol{a}}_2^a(s_n) \\ &= \frac{1}{M^2}\int_{s_n}^{s_{n+1}}\exp(-s\mathsf{L}^a)\left\langle \exp\Big(s\mathsf{L}^{a-b}\Big), \exp\Big(s\mathsf{L}^b\Big)\right\rangle \mathrm{d}s \\ &\quad\times\sum_b \mathcal{N}^{ab}\left\langle \exp\Big(-s_{n+1}\mathsf{L}^{a-b}\Big)\boldsymbol{a}_{n+1}^{a-b}, \exp\Big(-s_{n+1}\mathsf{L}^b\Big)\boldsymbol{a}_{n+1}^b\right\rangle.\end{aligned} \tag{2.177}$$

Note that

$$\begin{aligned}&\int_{s_n}^{s_{n+1}}\exp(-s\mathsf{L}^a)\left\langle \exp\Big(s\mathsf{L}^{a-b}\Big), \exp\Big(s\mathsf{L}^b\Big)\right\rangle \mathrm{d}s \\ &= (\delta s)_{n+1}\exp(-\overline{s}_{n+1}\mathsf{L}^a)\left\langle \exp\Big(\overline{s}_{n+1}\mathsf{L}^{a-b}\Big), \exp\Big(\overline{s}_{n+1}\mathsf{L}^b\Big)\right\rangle + O\left((\delta s)_n^2\right).\end{aligned} \tag{2.178}$$

Therefore, since we have $\overline{s}_{n+1} - s_{n+1} = s_n - \overline{s}_{n+1} = -(\delta s)_{n+1}/2$, we get

$$\begin{aligned}\hat{\boldsymbol{a}}_2^a(s_n) &= -\frac{(\delta s)_{n+1}}{M^2}\exp\left(-\frac{(\delta s)_{n+1}\mathsf{L}^a}{2}\right)\sum_b \mathcal{N}^{ab} \\ &\quad\times\left\langle \exp\left(-\frac{(\delta s)_{n+1}\mathsf{L}^{a-b}}{2}\right), \exp\left(-\frac{(\delta s)_{n+1}\mathsf{L}^b}{2}\right)\right\rangle\left\langle \boldsymbol{a}_{n+1}^{a-b}, \boldsymbol{a}_{n+1}^b\right\rangle + O\left((\delta s)_n^2\right) \\ &= \frac{1}{M^2}\sum_b \mathcal{E}^{ab}\left\langle \boldsymbol{a}_{n+1}^{a-b}, \boldsymbol{a}_{n+1}^b\right\rangle.\end{aligned} \tag{2.179}$$

Putting these together then, we find that

$$\boldsymbol{a}_n^a = \mathsf{E}^a\boldsymbol{a}_{n+1}^a + \sum_b \mathcal{E}^{ab}\left\langle \boldsymbol{a}_{n+1}^{a-b}, \boldsymbol{a}_{n+1}^b\right\rangle, \tag{2.180}$$

so setting

$$\begin{aligned}\begin{pmatrix}\mathsf{Y}_n^a\boldsymbol{p}_n^a + \sum_b \mathcal{Y}_n^{ab}\langle \boldsymbol{p}_n^{a-b}, \boldsymbol{p}_n^b\rangle \\ \boldsymbol{p}_n^a\end{pmatrix} =&\mathsf{E}^a\begin{pmatrix}\mathsf{Y}_{n+1}^a\boldsymbol{p}_{n+1}^a + \sum_b \mathcal{Y}_{n+1}^{ab}\langle \boldsymbol{p}_{n+1}^{a-b}, \boldsymbol{p}_{n+1}^b\rangle \\ \boldsymbol{p}_{n+1}^a\end{pmatrix} \\ &+\sum_b \mathcal{E}^{ab}\left\langle \begin{pmatrix}\mathsf{Y}_{n+1}^{a-b}\boldsymbol{p}_{n+1}^{a-b} \\ \boldsymbol{p}_{n+1}^{a-b}\end{pmatrix}, \begin{pmatrix}\mathsf{Y}_{n+1}^b\boldsymbol{p}_{n+1}^b \\ \boldsymbol{p}_{n+1}^b\end{pmatrix}\right\rangle,\end{aligned} \tag{2.181}$$

we see that it will be necessary to examine orders of magnitude once more. To linear order, we get

$$\begin{pmatrix} \mathsf{Y}_n^a (\hat{\boldsymbol{p}}_1^a)_n \\ (\hat{\boldsymbol{p}}_1^a)_n \end{pmatrix} = \mathsf{E}^a \begin{pmatrix} \mathsf{Y}_{n+1}^a (\hat{\boldsymbol{p}}_1^a)_{n+1} \\ (\hat{\boldsymbol{p}}_1^a)_{n+1} \end{pmatrix} + O(M^2), \tag{2.182}$$

so if we have

$$\mathsf{E}^a = \begin{pmatrix} \mathsf{E}_1^a & \mathsf{E}_2^a \\ \mathsf{E}_3^a & \mathsf{E}_4^a \end{pmatrix}, \quad \mathcal{E}^{ab}_{\alpha,\beta,0:\alpha_{\max}} = \begin{pmatrix} \mathcal{E}_1^{ab} & \mathcal{E}_2^{ab} \\ \mathcal{E}_3^{ab} & \mathcal{E}_4^{ab} \end{pmatrix}, \quad \mathcal{E}^{ab}_{\alpha,\beta,\alpha_{\max}+1:2\alpha_{\max}+1} = \begin{pmatrix} \mathcal{E}_5^{ab} & \mathcal{E}_6^{ab} \\ \mathcal{E}_7^{ab} & \mathcal{E}_8^{ab} \end{pmatrix}, \tag{2.183}$$

then at quadratic order, we find that

$$\begin{aligned} \begin{pmatrix} \mathsf{Y}_n^a (\hat{\boldsymbol{p}}_2^a)_n + \sum_b \mathcal{Y}_n^{ab} \left\langle (\hat{\boldsymbol{p}}_1^{a-b})_n, (\hat{\boldsymbol{p}}_1^b)_n \right\rangle \\ (\hat{\boldsymbol{p}}_2^a)_n \end{pmatrix} &= \begin{pmatrix} \left(\mathsf{E}_1^a \mathsf{Y}_{n+1}^a + \mathsf{E}_2^a\right) (\hat{\boldsymbol{p}}_2^a)_{n+1} \\ \left(\mathsf{E}_3^a \mathsf{Y}_{n+1}^a + \mathsf{E}_4^a\right) (\hat{\boldsymbol{p}}_2^a)_{n+1} \end{pmatrix} \\ &+ \sum_b \begin{pmatrix} \mathsf{E}_1^a \mathcal{Y}_{n+1}^{ab} + \mathcal{E}_1^{ab} \langle \mathsf{Y}_{n+1}^{a-b}, \mathsf{Y}_{n+1}^b \rangle + \mathcal{E}_2^{ab} \langle \mathsf{I}, \mathsf{Y}_{n+1}^b \rangle + \mathcal{E}_5^{ab} \langle \mathsf{Y}_{n+1}^{a-b}, \mathsf{I} \rangle + \mathcal{E}_6^{ab} \\ \mathsf{E}_3^a \mathcal{Y}_{n+1}^{ab} + \mathcal{E}_3^{ab} \langle \mathsf{Y}_{n+1}^{a-b}, \mathsf{Y}_{n+1}^b \rangle + \mathcal{E}_4^{ab} \langle \mathsf{I}, \mathsf{Y}_{n+1}^b \rangle + \mathcal{E}_7^{ab} \langle \mathsf{Y}_{n+1}^{a-b}, \mathsf{I} \rangle + \mathcal{E}_8^{ab} \end{pmatrix} \\ &\times \begin{pmatrix} \left\langle (\hat{\boldsymbol{p}}_1^{a-b})_{n+1}, (\hat{\boldsymbol{p}}_1^b)_{n+1} \right\rangle \\ \left\langle (\hat{\boldsymbol{p}}_1^{a-b})_{n+1}, (\hat{\boldsymbol{p}}_1^b)_{n+1} \right\rangle \end{pmatrix}. \end{aligned} \tag{2.184}$$

This results in the following schemes for Y^a and $\mathcal{Y}^{ab}$:

$$\mathsf{Y}_n^a = (\mathsf{E}_1^a \mathsf{Y}_{n+1}^a + \mathsf{E}_2^a)(\mathsf{E}_3^a \mathsf{Y}_{n+1}^a + \mathsf{E}_4^a)^{-1}; \quad \mathsf{Y}_N^a = \mathsf{Y}_{\mathrm{o}}^a, \tag{2.185a}$$

$$\begin{aligned} \mathcal{Y}_n^{ab} = &\Big[(\mathsf{E}_1^a - \mathsf{Y}_n^a \mathsf{E}_3^a)\, \mathcal{Y}_{n+1}^{ab} + \left(\mathcal{E}_1^{ab} - \mathsf{Y}_n^a \mathcal{E}_3^{ab}\right) \langle \mathsf{Y}_{n+1}^{a-b}, \mathsf{Y}_{n+1}^b \rangle \\ &+ \left(\mathcal{E}_2^{ab} - \mathsf{Y}_n^a \mathcal{E}_4^{ab}\right) \langle \mathsf{I}, \mathsf{Y}_{n+1}^b \rangle + \left(\mathcal{E}_5^{ab} - \mathsf{Y}_n^a \mathcal{E}_7^{ab}\right) \langle \mathsf{Y}_{n+1}^{a-b}, \mathsf{I} \rangle + \left(\mathcal{E}_6^{ab} - \mathsf{Y}_n^a \mathcal{E}_8^{ab}\right) \Big] \\ &\times \left\langle \left(\mathsf{E}_3^{a-b} \mathsf{Y}_{n+1}^{a-b} + \mathsf{E}_4^{a-b}\right)^{-1}, \left(\mathsf{E}_3^b \mathsf{Y}_{n+1}^b + \mathsf{E}_4^b\right)^{-1} \right\rangle; \quad \mathcal{Y}_N^{ab} = \mathcal{Y}_{\mathrm{o}}^{ab}, \end{aligned} \tag{2.185b}$$

and

$$\begin{aligned} \boldsymbol{p}_{n+1}^a = &\left(\mathsf{E}_3^a \mathsf{Y}_{n+1}^a + \mathsf{E}_4^a\right)^{-1} \Big[\boldsymbol{p}_n^a \\ &- \sum_b \left(\mathsf{E}_3^a \mathcal{Y}_{n+1}^{ab} + \mathcal{E}_3^{ab} \langle \mathsf{Y}_{n+1}^{a-b}, \mathsf{Y}_{n+1}^b \rangle + \mathcal{E}_4^{ab} \langle \mathsf{I}, \mathsf{Y}_{n+1}^b \rangle + \mathcal{E}_7^{ab} \langle \mathsf{Y}_{n+1}^{a-b}, \mathsf{I} \rangle + \mathcal{E}_8^{ab} \right) \\ &\times \left\langle \left(\mathsf{E}_3^{a-b} \mathsf{Y}_{n+1}^{a-b} + \mathsf{E}_4^{a-b}\right)^{-1}, \left(\mathsf{E}_3^b \mathsf{Y}_{n+1}^b + \mathsf{E}_4^b\right)^{-1} \right\rangle \langle \boldsymbol{p}_n^{a-b}, \boldsymbol{p}_n^b \rangle \Big]; \quad \boldsymbol{p}_0^a = \boldsymbol{p}_i^a. \end{aligned} \tag{2.186}$$

Since singularities may only be encountered in the admittance, it is not obvious why the Magnus–Möbius method should also be required for the pressure. However, when integrating across a zero in the pressure perturbation, Runge-Kutta methods have been observed to introduce sign errors on the other side, whereas the Magnus–Möbius method remains correct. Thus, when we use it for the admittance, we must also use it for the pressure. In fact, even preserving the method but changing step-size between admittance and pressure calculations can cause sign errors.

This scheme has proved capable of dealing with singularities in the admittance due to the duct geometry (as will be shown in section 3.6) and its nonlinear extension produces accurate results when applied to simple problems (section 3.2.1). However, it is still only first-order accurate, and with a fixed step-size, not always as efficient as `ode45`. The nonlinear extension of the scheme has unfortunately also struggled in the presence of variable-width walls (and also curvature, notably in the case of the 'elephant's trunk' from section 3.7.2); this is perhaps due to the fixed step-size and restriction to first order. Generalisations to higher order or variable step-size are beyond the scope of this work, in which we wish only to introduce it and demonstrate its basic capabilities; for an example of a higher-order nonlinear Magnus scheme, see Casas and Iserles [2006]. For most geometries, the use of a Runge-Kutta method to directly solve equations (2.117a), (2.117b) and (2.118) works very well, and when pressure nodes are encountered, we generally use the method outlined in section 2.3.6.

2.3.4 Numerical Viscosity

One of the pitfalls of truncation is the pooling of energy at higher modes. This can be countered by employing a numerical viscosity, which we do by subtracting a new term E^a from the right-hand-side of the pressure equation (2.118). Here, we take this to be

$$E^a = -\nu_0 \frac{|a|\omega\beta_0 M}{1 + M\beta_0\omega s} \log\left(1 - \frac{|a| - 1}{a_{\text{max}}}\right) P_0^a \sim \nu_0 \frac{|a|^2\omega\beta_0 M}{a_{\text{max}}} P_0^a, \tag{2.187}$$

where ν_0 is a positive scalar determining how great an effect we want the viscosity to have. The second approximation here is in the limit of small s relative to the shock formation distance (given by $1/M\beta_0\omega$), and with $1 \ll |a| \ll a_{\text{max}}$ (where energy pooling starts to occur). This choice of numerical viscosity is informed by the truncation error for a sawtooth plane wave in a 1D duct, and is discussed further in section 3.2.

2.3.5 Physical viscosity

If we instead consider physical viscosity in 1D, the (single) momentum equation picks up an extra term

$$-\mathrm{i}a\omega U^a + \frac{\partial P^a}{\partial s} - \left(\frac{4\mu}{3} + \zeta\right) \frac{\partial^2 U^a}{\partial s^2} = \frac{\partial Q^a}{\partial s}, \tag{2.188}$$

while the mass conservation equation is unchanged. We still wish to use the Riccati-style admittance method, which requires our two equations to be first-order in s; this can be achieved by substituting the $O(M^2)$ expansion of $\partial U^a/\partial s$ from the mass conservation equation here. That substitution results in

$$-\mathrm{i}a\omega U^a + \left(1 - \mathrm{i}a\omega\left(\frac{4\mu}{3} + \zeta\right)\right)\frac{\partial P^a}{\partial s} = \frac{\partial Q^a}{\partial s} - \mathrm{i}a\omega\left(\frac{4\mu}{3} + \zeta\right)\frac{\partial}{\partial s}\left(\sum_b \beta_0 P^{a-b}P^b - Q^a\right). \tag{2.189}$$

The s-derivatives of $O(M^2)$ terms may now have linear terms substituted into them. For notational ease, we define a modified frequency for each temporal index, and absorb both viscosities into a single constant

$$\Omega^a = \frac{\mathrm{i}a\omega}{1 - \mathrm{i}a\omega\tilde{\mu}}, \qquad\qquad \tilde{\mu} = \frac{4\mu}{3} + \zeta, \tag{2.190}$$

so then we have

$$\frac{\partial P^a}{\partial s} - \Omega^a U^a = \frac{\partial Q^a}{\partial s} - \tilde{\mu}\beta_0\Omega^a\frac{\partial}{\partial s}\sum_b P^{a-b}P^b, \tag{2.191}$$

Defining the 1D admittances in the usual way, we end up with the following two equations for them (with a constant cross-sectional area A_{cs} defining the mode ψ_0)

$$\begin{aligned}
\frac{\mathrm{d}\mathsf{Y}^a}{\mathrm{d}s} &= -\Omega^a(\mathsf{Y}^a)^2 + \mathrm{i}a\omega, && (2.192)\\
\frac{\mathrm{d}\mathcal{Y}^{ab}}{\mathrm{d}s} &= -\mathcal{Y}^{ab}\Big(\Omega^a\mathsf{Y}^a + \Omega^{a-b}\mathsf{Y}^{a-b} + \Omega^b\mathsf{Y}^b\Big)\\
&\quad - \frac{1}{\sqrt{A_{\mathrm{cs}}}}\Bigg\{\Big(\Omega^{a-b}\mathsf{Y}^{a-b} + \Omega^b\mathsf{Y}^b\Big)\left(\frac{\mathsf{Y}^a}{2} + \tilde{\mu}\beta_0\Omega^a\right)\\
&\quad + \frac{i\omega}{2}\Big(a\gamma + a\mathsf{Y}^{a-b}\mathsf{Y}^b - b\mathsf{Y}^a\mathsf{Y}^{a-b} - (a-b)\mathsf{Y}^a\mathsf{Y}^b\Big)\Bigg\}. && (2.193)
\end{aligned}$$

Since we are working in 1D, the admittances must be characteristic, and so we have the solutions

$$\begin{aligned}
\overline{\mathsf{Y}}^{a\pm} &= \pm\overline{\mathsf{Y}}^a = \pm\exp\left(-\frac{\mathrm{i}\pi}{4}\left[\mathrm{sgn}(1 - \mathrm{i}a\omega\tilde{\mu}) - 1\right]\right)\sqrt{|1 - \mathrm{i}a\omega\tilde{\mu}|}, && (2.194)\\
\overline{\mathcal{Y}}^{ab\pm} &= \mp\frac{1}{\sqrt{A_{\mathrm{cs}}}}\Bigg\{\Big(\Omega^{a-b}\overline{\mathsf{Y}}^{a-b} + \Omega^b\overline{\mathsf{Y}}^b\Big)\left(\frac{\overline{\mathsf{Y}}^a}{2} \pm \tilde{\mu}\beta_0\Omega^a\right)\\
&\quad + \frac{\mathrm{i}\omega}{2}\Big(a\gamma + a\overline{\mathsf{Y}}^{a-b}\overline{\mathsf{Y}}^b - b\overline{\mathsf{Y}}^a\overline{\mathsf{Y}}^{a-b} - (a-b)\overline{\mathsf{Y}}^a\overline{\mathsf{Y}}^b\Big)\Bigg\}\Big/\Big(\Omega^a\overline{\mathsf{Y}}^a + \Omega^{a-b}\overline{\mathsf{Y}}^{a-b} + \Omega^b\overline{\mathsf{Y}}^b\Big). && (2.195)
\end{aligned}$$

Assuming $\tilde{\mu}$ is small, first-order expansions of these quantities may be found, though the nonlinear admittance only appears in $O(M^2)$ terms to begin with, so its second term here will eventually be $O(M^2\mu)$, and thus discarded. Hence, we have

$$\frac{\mathrm{d}P_0^a}{\mathrm{d}s} \approx \mathrm{i}a\omega P_0^a - \frac{\mathrm{i}a\omega\beta_0}{2\sqrt{A_{\mathrm{cs}}}}\sum_b P_0^{a-b}P_0^b - \frac{a^2\omega^2\tilde{\mu}}{2}P_0^a, \tag{2.196}$$

suggesting that in order to stabilise a truncated sawtooth wave the physical viscosity would need to be around $\tilde{\mu} \approx 2\beta_0 M/a_{\max}\omega$.

2.3.6 Alternative numerical damping

Numerical instabilities can also arise in linear problems. If a node occurs in the pressure (scenarios involving this were discussed in section 2.3.3), this causes a singularity in the admittance. A clever, but difficult-to-implement (and in the nonlinear regime, unreliable) numerical method for dealing with this is the Magnus-Möbius scheme of section 2.3.3; alternatively, such singularities may be avoided (or 'dampened') by the addition of a small imaginary part to the frequency ω, which corresponds to a sound source slowly exponentially growing in time, and therefore a wave pattern that slowly exponentially decays in space away from the source. This technique is borrowed from stability analysis [e.g. Briggs, 1964; Bers, 1983], where adding an imaginary part to the frequency ω is used to guarantee a causal solution. Unless otherwise specified, this method is used for solving in narrowing geometries henceforth.

2.4 Summary

We have formulated a method for calculating the weakly-nonlinear acoustic field within geometrically complicated waveguides in 2D and 3D. This involves prescribing a boundary condition in the admittance at the duct outlet, solving a Riccati-style system (equation 2.117) for the admittance back to the inlet (a process which notably remains independent of the acoustic source), and then prescribing a pressure disturbance at the inlet, forming a boundary condition for solution of the internal acoustic field of the duct (equation 2.158). Characteristic admittances are known in closed form for the straight-duct case, and can easily be numerically calculated for curved or torsional ducts. These correspond, in either direction, to the zero-reflection case, and so are used to separate the acoustic field into forward- and backward-going modes. The method as presented in this chapter can have any admittance boundary condition prescribed at the outlet; in the next chapter we focus on the use of the characteristic admittance itself as a boundary condition, which corresponds to forward propagation only (examples of the resulting numerical calculations are given therein). We also conduct a convergence study into further spatial or temporal modes' effect on accuracy of the solution (section 3.4.1).

Chapter 3

Ducts of infinite length

In this chapter, a number of numerical test cases are given for simple geometries in 2D and 3D. These geometries do not include an open end of the duct, but instead model the duct as being of infinite length. This allows the characteristic admittance to be applied as a boundary condition. The characteristic admittance is the simplest possible admittance to construct, and a useful way to characterise wave propagation; nonetheless, it does not serve as a physically realistic boundary condition, since it effectively corresponds to a duct of infinite length. A more realistic boundary condition is derived in chapter 5, and in fact we make use of the characteristic admittance to do this; for now, we simply use the characteristic admittance as our boundary condition, and focus on *internal* wave propagation. We test against both analytical solutions (e.g. sections 3.2, 3.5, 3.6) or against previously-published numerical results (e.g. sections 3.3, 3.4.1). We also discuss new results concerning the definition of a reflected wave, comparisons of 2D and 3D curved-duct acoustics, and the effective acoustic length of a bend.

This work is under consideration for publication [Jensen and Brambley, 2025]. With the exception of a MATLAB script used to generate zeros of the Bessel function derivative [Carey Smith, 2025], all code used to generate the following results was written by the author.

3.1 Modal resolution

The following test cases require different numbers of modes depending on what physics is being considered. For linear acoustics, spatial modes are the only limiting factor: when comparing with pre-existing linear work, we use the previous resolution as a benchmark (e.g. $\alpha_{\max} = 30$ for figure 3.4), but when comparing with analytical results, we pick a new standard (taking $\alpha_{\max} = 50$ for figures 3.10, 3.11, 3.13, 3.14). In all of these cases the absence of nonlinearity allows us to set $a_{\max} = 1$, and unoptimised MATLAB code run on a standard laptop finishes in the order of seconds.

Where nonlinearity comes in, memory requirements are likely to exceed that of a standard laptop, although all results here have been computed on a single desktop with 128 GiB of memory. For most of these computations (i.e. figures 3.3 and 3.7–3.24) spatial resolution is necessary, so we take $a_{\max} = 10$ and $\alpha_{\max} = 10$, and computations take on the order of tens of minutes. For figure 3.1, we consider only plane waves in a straight duct, so we can take $\alpha_{\max} = 0$ and $a_{\max} = 100$; while this does not exceed the memory limit, the calculation now takes of the order of half a day to compute using a single core.

The numerical procedure converges as the number of temporal and spatial modes is increased, and the truncations above are sufficient for accurate results in all of the cases presented here. A demonstration of the numerical convergence with the number of modes is provided for a constant-curvature bend in 3D in section 3.4.1 below.

3.2 A straight duct of constant diameter

The simplest test geometry in either 2D or 3D is that of a straight duct with constant diameter. For a plane piston source, the equations are simplified greatly, both by the absence of curvature and width-variation terms, and also by the collapsing of the spatial mode vectors onto a single scalar component. The admittance equations are then solved trivially, since the boundary condition is a constant solution, giving

$$\mathsf{Y}^{a}_{00}(s) = 1, \qquad \mathcal{Y}^{ab}_{000}(s) = -\frac{1}{2\sqrt{A_{\mathrm{cs}}}}\left(\beta_0 + \frac{a-2b}{a}\right) \quad \forall s. \tag{3.1}$$

This holds in both 2D and 3D, and we write A_{cs} for the area of the duct cross-section so that we can work in both. Plugging these into the pressure equation, we get (again in both cases, once we substitute the value of $\mathcal{I}_{000}$)

$$\frac{\mathrm{d}P^a_0}{\mathrm{d}s} = \mathrm{i}a\omega P^a_0 + \frac{\mathrm{i}\omega}{2\sqrt{A_{\mathrm{cs}}}}\sum_b \Big[-a\beta_0 + (a-2b)\Big] P^{a-b}_0 P^b_0, \tag{3.2}$$

but if we write the second term in the square bracket here as $(a-b)-b$, we see that it vanishes upon summation. Since the spatial zero-mode ψ_0 does not depend on s for a straight duct, we can multiply through by it, getting an equation for Fourier coefficients

$$\frac{\mathrm{d}P^a}{\mathrm{d}s} = \mathrm{i}a\omega P^a - \frac{\mathrm{i}a\omega\beta_0}{2}\sum_b P^{a-b}P^b. \tag{3.3}$$

This equation was solved up to shock formation by Fubini [1935], for any boundary conditions both periodic and odd in t, resulting in a sine series for the pressure

$$\frac{p}{M} = \sum_a B_a \sin[a\omega(t-s)]; \qquad B_a = \frac{2}{as/s_{\mathrm{sf}}}\mathrm{J}_a(as/s_{\mathrm{sf}}), \tag{3.4}$$

where $s_{\mathrm{sf}} = 1/M\beta_0\omega$ is the shock-formation distance. Fay [1931] found a post-shock-formation solution in the form of a sawtooth wave,

$$B_a = \frac{2}{a(1+s/s_{\mathrm{sf}})}, \tag{3.5}$$

valid for $s \gtrapprox 3s_{\mathrm{sf}}$. Blackstock [1966] matched these two solutions with the following two terms

$$B_a = \frac{2}{a\pi}P_{\mathrm{sh}} + \frac{2}{a\pi s/s_{\mathrm{sf}}}\int_{\Phi_{\mathrm{sh}}}^{\pi} \cos\left[a\left(\Phi - \frac{s}{s_{\mathrm{sf}}}\sin\Phi\right)\right]\mathrm{d}\Phi, \tag{3.6}$$

where the shock amplitude P_{sh} and phase Φ_{sh} satisfy

$$P_{\mathrm{sh}} = \sin\left(\frac{s}{s_{\mathrm{sf}}}P_{\mathrm{sh}}\right), \qquad \Phi_{\mathrm{sh}} = \frac{s}{s_{\mathrm{sf}}}\sin\Phi_{\mathrm{sh}}. \tag{3.7}$$

For $s < s_{\mathrm{sf}}$, the only solution for $(P_{\mathrm{sh}}, \Phi_{\mathrm{sh}})$ is $(0, 0)$, so the first term vanishes and the second becomes the Fubini solution. As s grows greater than s_{sf}, two more solutions appear either side of 0; the relevant solutions here are the positive ones. For $s \gtrapprox 5\pi/2$ more solutions appear; we remain interested from this point in the minimal positive solution for each of P_{sh} and Φ_{sh}. Since Φ_{sh} converges to π from below, the second term tends to 0, while the first term behaves like the Fay solution.

The numerical viscosity used here, described in section 2.3.4 above, is justified by considering the truncation error of a sawtooth wave when substituted into equation (3.3). The sawtooth wave as derived in Fay [1931] has Fourier coefficients given by

$$P^a = \frac{\mathrm{i}Me^{\mathrm{i}a\omega s}}{a(1+s/s_{\mathrm{sf}})} \tag{3.8}$$

so the terms missing if we truncate the nonlinear term in equation (3.3) to a finite sum are then

$$\begin{aligned} E^a &= \frac{\mathrm{i}a\omega\beta_0\sqrt{A_{\mathrm{cs}}}}{2}\sum_{\substack{b=-\infty,\\ b\neq 0,a}}^{\infty} P^{a-b}P^b - \frac{\mathrm{i}a\omega\beta_0\sqrt{A_{\mathrm{cs}}}}{2}\sum_{\substack{b=a-\mathrm{sgn}(a)a_{\max},\\ b\neq 0,a}}^{\mathrm{sgn}(a)a_{\max}} P^{a-b}P^b \\ &= -\frac{\mathrm{i}\omega\beta_0\sqrt{A_{\mathrm{cs}}}M^2e^{\mathrm{i}a\omega s}}{(1+s/s_{\mathrm{sf}})^2}\left(\sum_{\substack{b=-\infty,\\ b\neq 0,a}}^{\infty} - \sum_{\substack{b=a-\mathrm{sgn}(a)a_{\max},\\ b\neq 0,a}}^{\mathrm{sgn}(a)a_{\max}}\right)\frac{a}{2(a-b)b} \end{aligned} \tag{3.9}$$

where the limits on the second sum ensure that for both positive and negative b, $|a-b|$ may never exceed $a_{\max}$. The summand may be split into partial fractions as

$$\frac{a}{2(a-b)b} = \frac{1}{2(a-b)} + \frac{1}{2b} \tag{3.10}$$

and when summed from $-\infty$ to ∞ this becomes $-1/a$. This can be folded into the other sum, so that the error becomes

$$E^a = \frac{\mathrm{i}\omega\beta_0\sqrt{A_{\mathrm{cs}}}M^2 e^{\mathrm{i}a\omega s}}{2(1+s/s_{\mathrm{sf}})^2}\left(\sum_{\substack{b=a-\mathrm{sgn}(a)a_{\max},\\ b\neq a}}^{\mathrm{sgn}(a)a_{\max}} \frac{1}{a-b} + \sum_{\substack{b=a-\mathrm{sgn}(a)a_{\max},\\ b\neq 0}}^{\mathrm{sgn}(a)a_{\max}} \frac{1}{b}\right). \tag{3.11}$$

The first sum is split as

$$\sum_{\substack{b=a-\mathrm{sgn}(a)a_{\max},\\ b\neq a}}^{\mathrm{sgn}(a)a_{\max}} \frac{1}{a-b} = \left(\sum_{b=a-\mathrm{sgn}(a)a_{\max}}^{2a-\mathrm{sgn}(a)(a_{\max}+1)} + \sum_{\substack{2a-\mathrm{sgn}(a)a_{\max},\\ b\neq a}}^{\mathrm{sgn}(a)a_{\max}}\right)\frac{1}{a-b}, \tag{3.12}$$

with the second term vanishing due to symmetric limits and an odd summand about $b = a$. The second sum is treated similarly

$$\sum_{\substack{b=a-\mathrm{sgn}(a)a_{\max},\\ b\neq 0}}^{\mathrm{sgn}(a)a_{\max}} \frac{1}{b} = \left(\sum_{\substack{b=a-\mathrm{sgn}(a)a_{\max},\\ b\neq 0}}^{\mathrm{sgn}(a)a_{\max}-a} + \sum_{\mathrm{sgn}(a)(a_{\max}+1)-a}^{\mathrm{sgn}(a)a_{\max}}\right)\frac{1}{b}, \tag{3.13}$$

and this time the first term vanishes. Both of the remaining sums, with the correct substitution, become

$$\sum_{b=a-\mathrm{sgn}(a)a_{\max}}^{2a-\mathrm{sgn}(a)(a_{\max}+1)} \frac{1}{a-b} = \sum_{\mathrm{sgn}(a)(a_{\max}+1)-a}^{\mathrm{sgn}(a)a_{\max}} \frac{1}{b} = \sum_{b=0}^{|a|-1} \frac{\mathrm{sgn}(a)}{a_{\max}-b}, \tag{3.14}$$

so then the error becomes

$$E^a = \frac{\mathrm{i}\omega\beta_0\sqrt{A_{\mathrm{cs}}}M^2 e^{\mathrm{i}a\omega s}}{(1+s/s_{\mathrm{sf}})^2}\sum_{b=0}^{|a|-1} \frac{\mathrm{sgn}(a)}{a_{\max}-b} = \frac{|a|\omega\beta_0 M P_0^a}{1+s/s_{\mathrm{sf}}}\sum_{b=0}^{|a|-1}\frac{1}{a_{\max}-b}. \tag{3.15}$$

The sum has upper and lower bounds in the form of integrals:

$$\int_0^{|a|-1} \frac{\mathrm{d}x}{a_{\max}-x} < \sum_{b=0}^{|a|-1} \frac{1}{a_{\max}-b} < \int_0^{|a|-1} \frac{\mathrm{d}x}{a_{\max}-(x+1)}. \tag{3.16}$$

We choose the lower bound as the approximation to the sum since the upper bound's integrand is singular at its upper limit. Thus, evaluating the integral and including the viscous scale factor ν_0, we arrive at equation (2.187).

We can compare our numerics with this. This can be done in both 2D and 3D; figure 3.1 compares various modes in the 2D case, for a simulation with 1 spatial mode (since no spatial coupling is induced for this geometry anyway) and 100 temporal modes. As one would expect, good matches are achieved for the lower (dominant) modes, while for higher modes the numerical solutions undershoot at first and over-compensate later on. We have achieved matches of equal quality with the code in 3D.

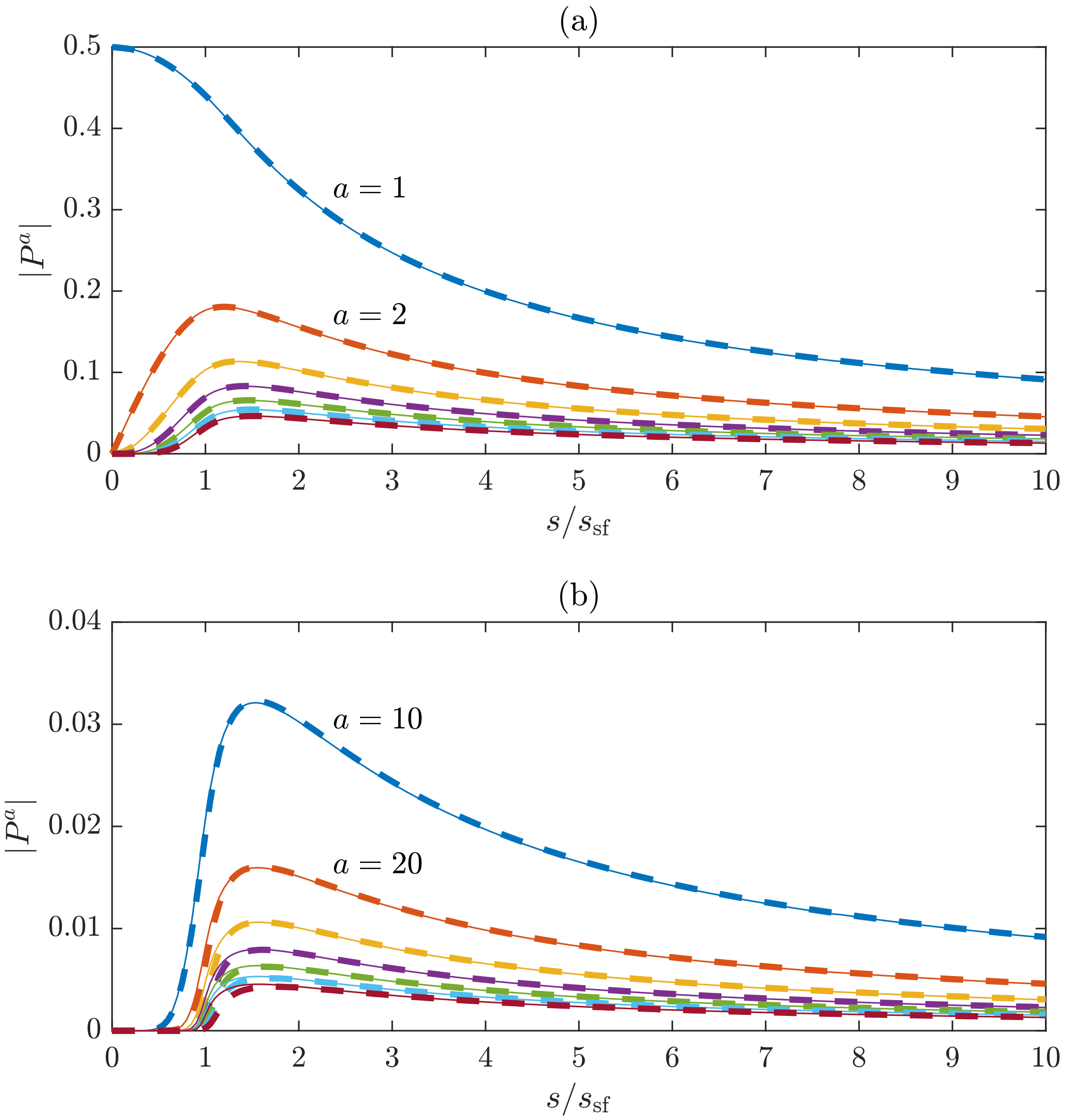

Figure 3.1: Comparison of numerically-calculated (using `ode45`) mode amplitudes (dashed) with those predicted by the Blackstock solution (solid), in 2D. (a) shows modes 1 through 7, while (b) shows 10 through 70. Truncation was taken at $\alpha_{\max} = 0$ and $a_{\max} = 100$.

Eliminating spatial variation in favour of higher temporal modes is a useful special case because it allows for the calibration of the numerical viscosity. Figure 3.1 was created with $\nu_0 = 1$, because higher scale factors than this place far too much damping on the higher modes, while lower factors allow instabilities to build up much more quickly. In light of this, all other nonlinear calculations take $\nu_0 = 1$ as well.

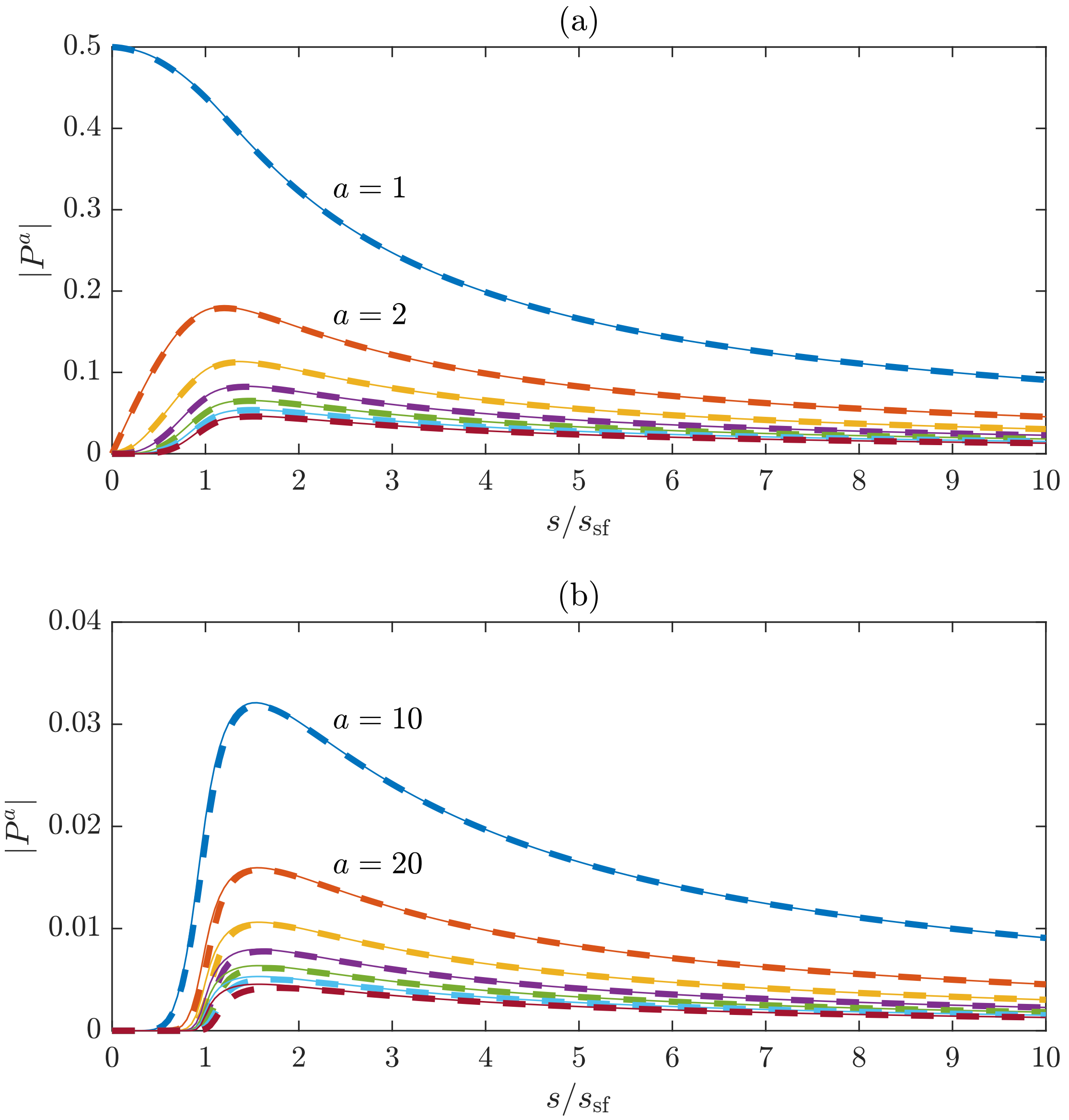

Figure 3.2: Comparison of numerically-calculated (using the nonlinearly-extended Magnus–Möbius scheme) mode amplitudes (dashed) with those predicted by the Blackstock solution (solid), in 2D. (a) shows modes 1 through 7, while (b) shows 10 through 70. Truncation was taken at $\alpha_{\max} = 0$ and $a_{\max} = 100$.

3.2.1 Magnus–Möbius applied to a nonlinear problem

We can also use this problem to check the validity of the nonlinear Magnus–Möbius scheme. While the existence of an analytical solution is very helpful, it should be borne in mind that the plane-wave-only, simplest-possible-geometry case will not necessarily prove the general workability of a method. Nonetheless a very promising match is achieved, as figure 3.2 shows; achieving greater stability on more complicated geometries is the next goal.

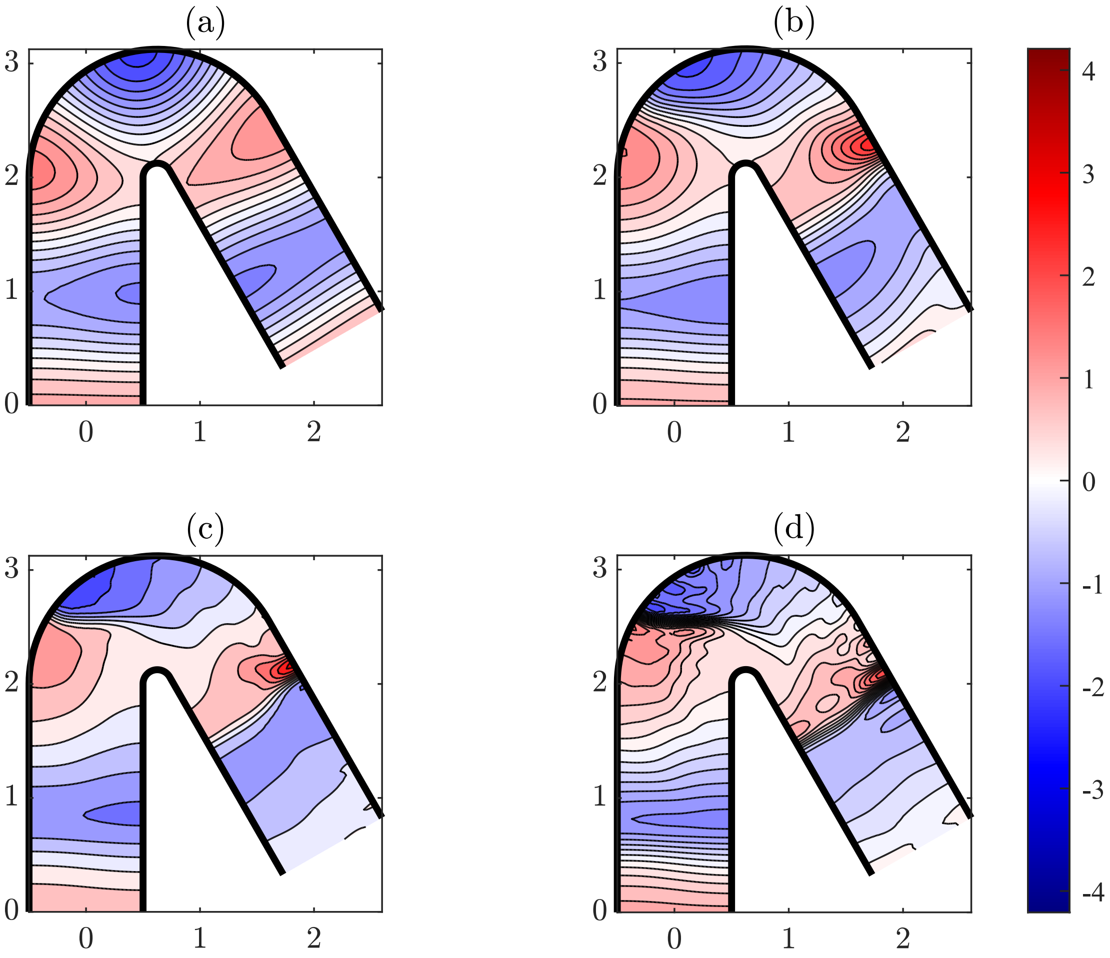

Figure 3.3: Pressure (normalised to the source amplitude) in a bend identical to the one used in McTavish and Brambley [2019], with a plane piston source of frequency $3/X$, for (a) linear, (b) $M = 0.05$, (c) 0.10, and (d) 0.15. Truncation was taken at $\alpha_{\max} = a_{\max} = 10$.

3.3 Constant curvature in 2D

In 2D, McTavish and Brambley [2019] considered linear and nonlinear propagation around a constant-width bend, first computed in the linear case by Félix and Pagneux [2001]. This provides a test case for the combination of curvature and nonlinearity. Figure 3.3 reproduces figure 7 of McTavish and Brambley [2019], with all of the same parameters, i.e. (for constant duct width X) a bend of curvature $8/5X$ located at a distance $2X$ downstream of a plane piston source of frequency $3/X$, with truncation taken at 10 spatial modes and 10 temporal modes, plotted in the linear regime and nonlinearly for $M = 0.05$, 0.10 and 0.15. Good agreement is observed.

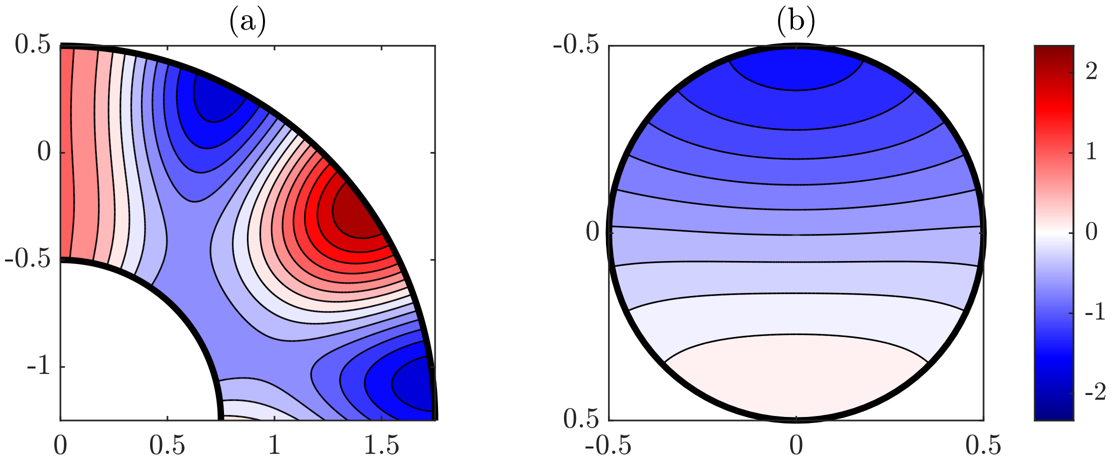

Figure 3.4: Pressure (normalised to the source amplitude) in a bend identical to the one used in Félix and Pagneux [2002], with a plane piston source of frequency $2.4/R$, plotted both through the midplane and across the duct outlet in the linear regime. Truncation was taken at $\alpha_{\max} = 30$ and $a_{\max} = 1$.

3.4 Constant curvature in 3D

3.4.1 General results

Validation in the linear regime

In 3D, no published work exists that can be used to test the combined effects of curvature and nonlinearity, but in the linear case Félix and Pagneux [2002] provides an example that may be tested against. Here, for constant duct radius R, a plane piston source of frequency $2.4/R$ is placed at the mouth of a bend of curvature $4/5R$, and a cross-section through the half-plane is plotted alongside the outlet's circular cross-section. Comparing figure 3.4 with figure 2 of Félix and Pagneux [2002], we again see good agreement. Truncation was taken at 30 spatial modes to match their calculation, with the usual 1 temporal mode in the absence of nonlinearity.

Convergence study

For this geometry, we also follow Félix and Pagneux [2002] in the inclusion of a convergence study for the spatial modes. As well as their two definitions of the error involving integration along a surface, we also calculate a volumetric error, which behaves similarly. The reference solution p_{ref} was calculated here with $\alpha_{\max} = 50$ and $a_{\max} = 1$. Figure 3.5 shows the result. As with Félix and Pagneux [2002], there is uneven behaviour due to the different effects of higher azimuthal or radial resolution; nonetheless, for error metrics ϵ_1 and ϵ_3 the inclusion of more modes never causes the error to grow, and even for error metric ϵ_2 the solution is clearly still converging as more modes are included.

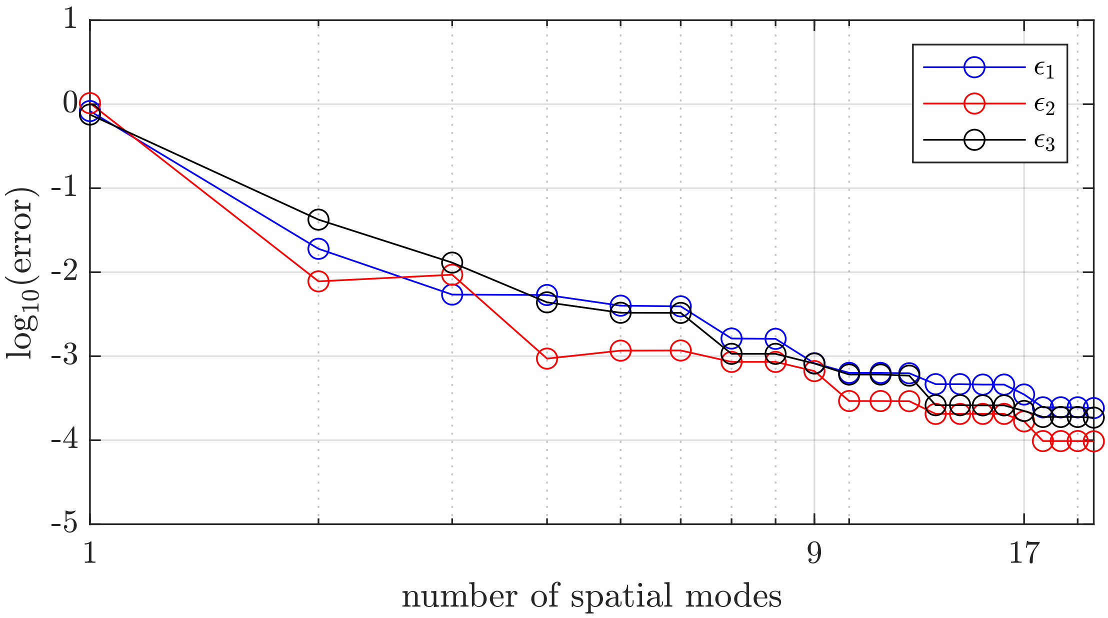

Figure 3.5: Numerical convergence in a 3D planar bend for three definitions of the error, detailed in equation (3.17). $a_{\max} = 1$, and so the number of modes is $\alpha_{\max} + 1$.

The error definitions are

$$\epsilon_1 = \sqrt{\frac{\int_{t=0}^{2\pi/\omega} \int_{s=0}^{s_d} \int_{r=0}^{R} \left[h_s \|p - p_{\text{ref}}\|^2\right]_{\theta=0}^{\pi} \mathrm{d}r\mathrm{d}s\mathrm{d}t}{\int_{t=0}^{2\pi/\omega} \int_{s=0}^{s_d} \int_{r=0}^{R} \left[h_s \|p_{\text{ref}}\|^2\right]_{\theta=0}^{\pi} \mathrm{d}r\mathrm{d}s\mathrm{d}t}}, \tag{3.17a}$$

$$\epsilon_2 = \sqrt{\frac{\int_{t=0}^{2\pi/\omega} \int_{\theta=0}^{2\pi} \int_{r=0}^{R} r\|p - p_{\text{ref}}\|^2|_{s=s_d} \mathrm{d}r\mathrm{d}\theta\mathrm{d}t}{\int_{t=0}^{2\pi/\omega} \int_{\theta=0}^{2\pi} \int_{r=0}^{R} r\|p_{\text{ref}}\|^2|_{s=s_d} \mathrm{d}r\mathrm{d}\theta\mathrm{d}t}}, \tag{3.17b}$$

$$\epsilon_3 = \sqrt{\frac{\int_{t=0}^{2\pi/\omega} \int_{\theta=0}^{2\pi} \int_{r=0}^{R} \int_{s=0}^{s_d} r h_s\|p - p_{\text{ref}}\|^2|_{s=s_d} \mathrm{d}s\mathrm{d}r\mathrm{d}\theta\mathrm{d}t}{\int_{t=0}^{2\pi/\omega} \int_{\theta=0}^{2\pi} \int_{r=0}^{R} \int_{s=0}^{s_d} r h_s\|p_{\text{ref}}\|^2|_{s=s_d} \mathrm{d}r\mathrm{d}s\mathrm{d}\theta\mathrm{d}t}}. \tag{3.17c}$$

Having added nonlinearity to the problem, we also conduct a convergence study of the temporal modes, using the same error definitions and the same geometry (figure 3.6). The convergence study is conducted for $M = 0.05$, and 10 temporal modes are used for the reference solution. This corresponds to 168dB, i.e. a reasonable assumption for the mouthpiece of a trombone being played loudly. In contrast to the spatial modes, the curves are now monotonic, and also an increasingly rapid decrease is observed.

Nonlinear regime

In figure 3.7 the same geometry has a plane piston source of frequency $\omega = 2.4/R$ prescribed in the total pressure at the top left, for various Mach numbers. We see good agreement both with the published linear work of Félix and Pagneux [2002], where evenly-spaced peaks and troughs travel around the outside of the bend, and also with

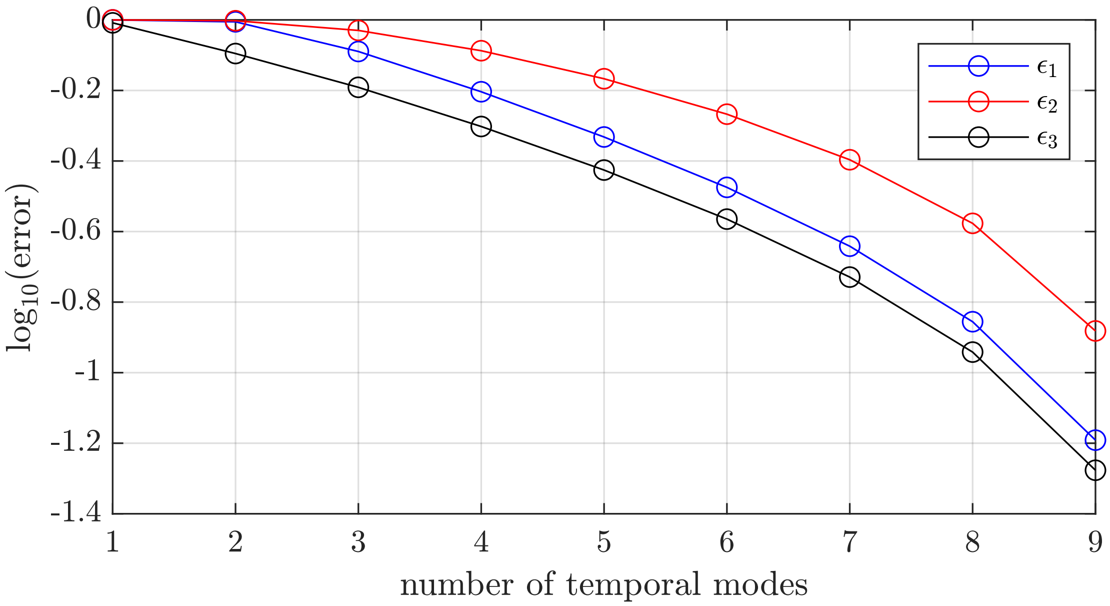

Figure 3.6: Numerical convergence with increasing temporal modes in a 3D planar bend for three definitions of the error, detailed in equation (3.17). A Mach number $M = 0.05$ was used; $\alpha_{\max} = 10$, and so the number of modes is $11a_{\max}$.

the unpublished nonlinear work of McTavish [2018], where the contours are deformed by the steepening of the peaks as the Mach number is increased. To match the latter calculation, 10 spatial modes and 10 temporal modes were used.

3.4.2 Reflections

We can use a curved-duct geometry to demonstrate an ambiguity in the definition of the forward- and backward-pressure decomposition. We consider the bend from the previous examples, but with the addition of straight sections before and after the bend, and use a plane-wave condition for the forward-going pressure.

Linear regime

For the linear regime, the result is shown in plot (a) of figure 3.8.

When we decompose into forward- and backward-going pressures, we need splitting matrices, which depend on the characteristic admittance. If we use the curved-duct characteristic admittance $\check{\mathsf{Y}}$ from section 2.2.2 (which reduces to the straight-duct admittance $\overline{\mathsf{Y}}$ in the non-curved sections), we get (c) for the forward-going pressure and (d) for the backward. This takes full account of the geometry of the duct, but since there is a discontinuous parameter in this geometry (namely the curvature, as shown in (b)) the splitting matrices, and therefore the decomposed pressures, are also discontinuous. Since these decompositions are only mathematical constructions and not physical quantities unto themselves, non-continuity may not be a problem; however, if

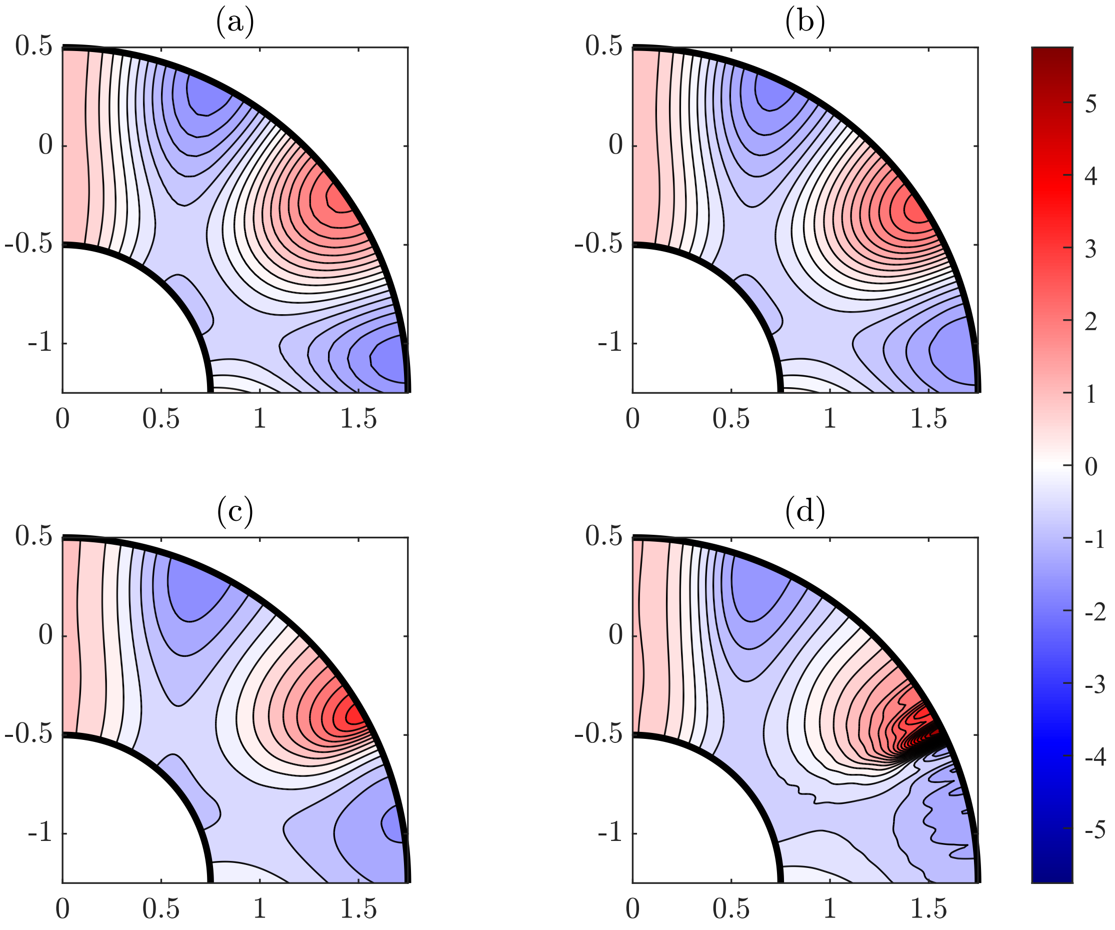

Figure 3.7: Pressure (normalised to the source amplitude) in a bend identical to the one used in Félix and Pagneux [2002], with a plane piston source of frequency $2.4/R$, for (a) linear, (b) $M = 0.02$, (c) 0.05, and (d) 0.10. Truncation was taken at $\alpha_{\max} = a_{\max} = 10$.

we wanted a continuous decomposition, we could instead use the straight-duct characteristic admittance $\overline{\mathsf{Y}}$ from section 2.2.2. This results in plots (e) and (f). As well as being continuous, this also has the advantage of comparing the reflective properties of the bend more directly with those of a straight duct (since the splitting operators used for analysis of a straight duct are those used for this).

When animated, plot (d) exhibits much more straightforward backward motion in the bend than plot (f), whose pressure instead travels backwards along the outside while travelling forwards along the inside. It is conceivable that a backward-going wave could *appear* to be travelling forwards, if the source generating it (in this case the reflection from the duct walls) is itself travelling forwards. It is unclear whether or not this is happening here; in any case it is another difference between the two decompositions. Two general points to note about both decompositions are (i) that the forward-going pressure is entirely made up of plane waves prior to the bend, since no reflection takes place at this point, and (ii) that there is no backward-going pressure at all post-bend, due to the forward-going admittance condition at the outlet.

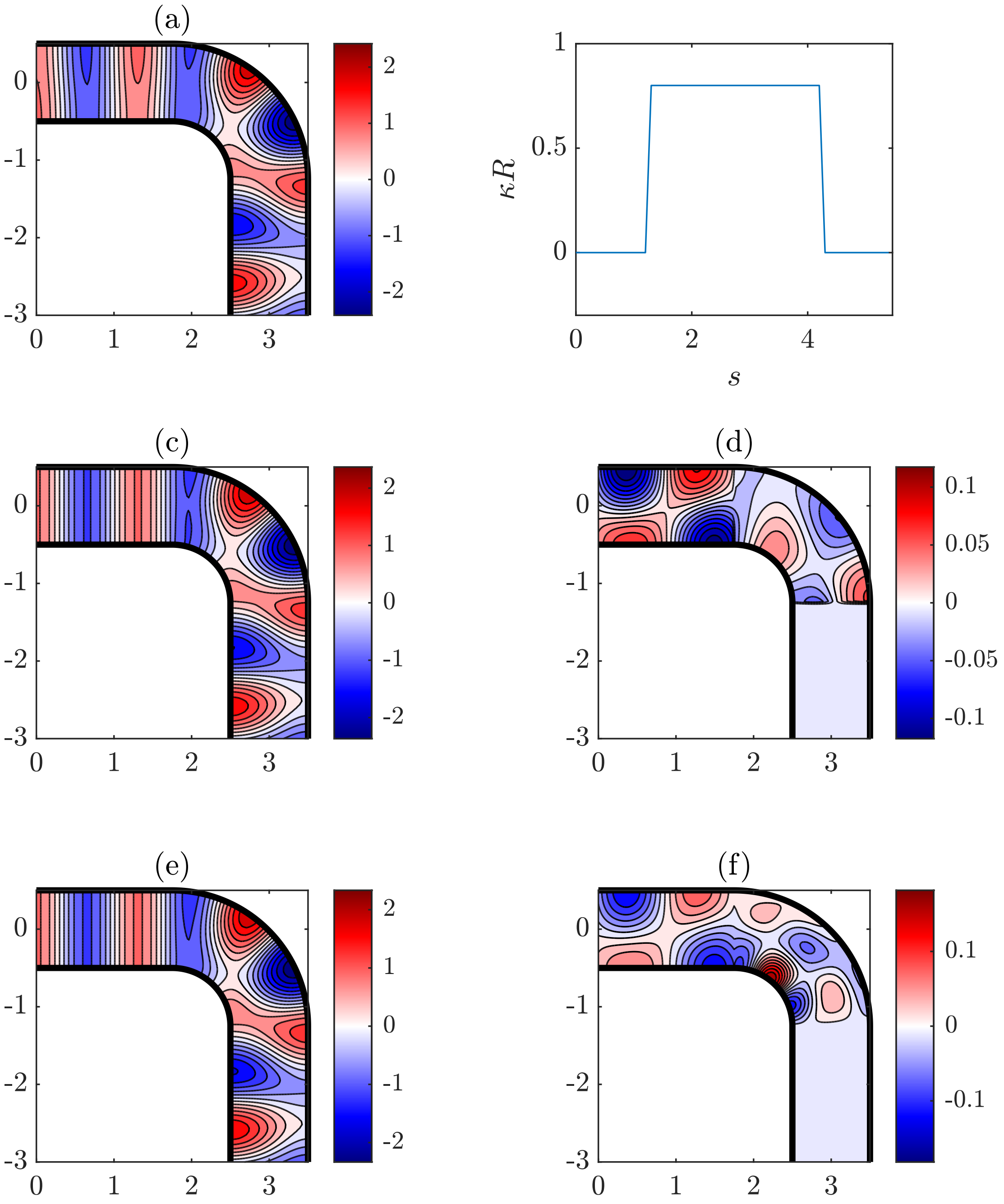

Figure 3.8: Pressure (normalised to the source amplitude) in an extended form of the bend used previously, with a plane piston source of frequency $2.4/R$, in the linear regime. (a) shows the total pressure, (b) shows the curvature variation for this geometry, (c) and (d) the forward- and backward-going pressures according to the curved-duct admittance $\check{\mathsf{Y}}$ and (e) and (f) those according to the straight-duct admittance $\overline{\mathsf{Y}}$. Truncation was taken at $\alpha_{\max} = a_{\max} = 10$.

A broader question concerning the ambiguity here is as follows: for the geometry used here, do we expect that waves will be constantly reflected by the curved portion of the duct, or reflected suddenly by the sudden changes in curvature? This is in fact a philosophical question rather than a mathematical one, in that both definitions are equally mathematically valid: in fact, the existence of two separate viable mathematical definitions giving substantially different results when computed, shows that the concept of transmitted and reflected waves is more subtle than may previously have been imagined.

Nonlinear regime

An equivalent result with $M = 0.10$ may also be obtained. Results are shown in figure 3.9. Once more it is demonstrated that the decomposition may either take account of the curvature discontinuity or disregard it in favour of a uniformly straight-duct admittance benchmark. Plots (d) and (f) in this example also exhibit straightforward backward motion and mixed forward-inside, backward-outside motion respectively, as in figure 3.8. We also have no backward-going pressure post-bend, as before; however, the plane-wave-only condition pre-bend is not met in the nonlinear case. This is because nonlinearity results in the inclusion of higher temporal harmonics' forward-going components in this region, and these are not necessarily plane waves.

3.5 An exponential horn

The exponential horn is a convenient geometry: if an approximation is made allowing only plane waves to propagate, an analytical solution [Webster, 1919] exists, with the growth rate of the horn acting to dampen oscillations. The geometry is best parametrised across both 2D and 3D by specifying the growth exponent of the horn's cross-sectional area, i.e. by setting

$$A_{\mathrm{cs}}(s) = \begin{cases} A_{\mathrm{cs}}(0)\exp(2ms) & s \in [0, s_{\mathrm{o}}], \\ A_{\mathrm{cs}}(0)\exp(2ms_{\mathrm{o}}) & s > s_{\mathrm{o}}. \end{cases} \tag{3.18}$$

so that the radial growth factor in 2D is doubled relative to that in 3D. The section of duct with $s > s_{\mathrm{o}}$ forms the infinite straight duct providing the characteristic admittance boundary condition $\mathsf{Y}^a = \mathsf{Y}^{a+}$ at the outlet $s = s_0$. Since we are only interested in plane waves, the (scalar) linear admittance equation (in the variable radius region) becomes

$$\frac{\mathrm{d}Y^a}{\mathrm{d}s} = -\mathrm{i}a\omega(Y^a)^2 - 2mY^a + \mathrm{i}a\omega, \tag{3.19}$$

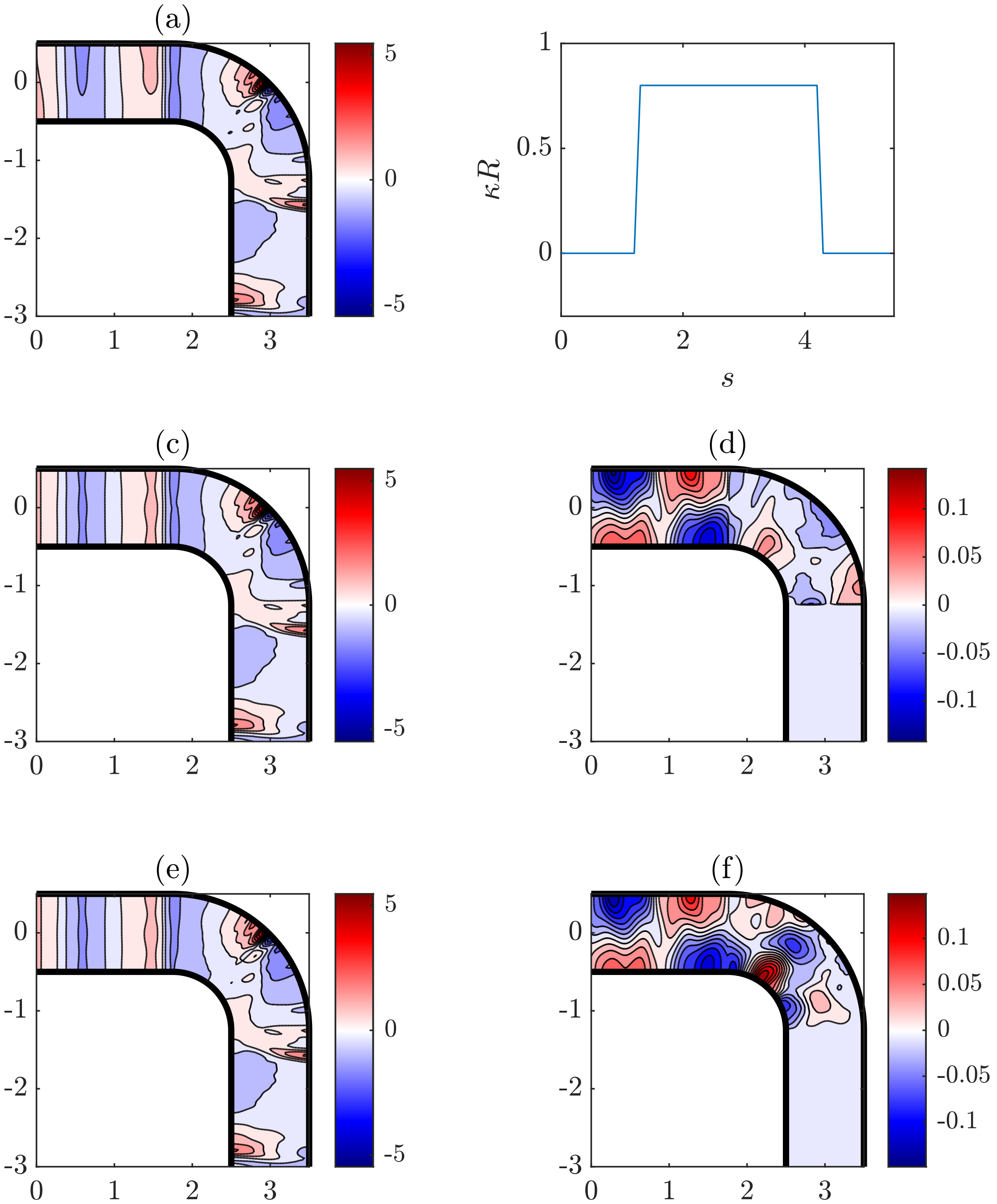

Figure 3.9: Pressure (normalised to the source amplitude) in an extended form of the bend used previously, with a plane piston source of frequency $2.4/R$, for $M = 0.10$. (a) shows the total pressure, (b) shows the curvature variation for this geometry, (c) and (d) the forward- and backward-going pressures according to the curved-duct admittance $\check{\mathsf{Y}}$ and (e) and (f) those according to the straight-duct admittance $\overline{\mathsf{Y}}$. Truncation was taken at $\alpha_{\max} = a_{\max} = 10$.

with the outlet condition at $s = s_\mathrm{o}$ being $Y^a = 1$ (which also holds for all $s > s_\mathrm{o}$). This ODE has solution

$$Y^a = \frac{n_a \cos n_a(s_\mathrm{o} - s) - (\mathrm{i}a\omega - m)\sin n_a(s_\mathrm{o} - s)}{n_a \cos n_a(s_\mathrm{o} - s) - (\mathrm{i}a\omega + m)\sin n_a(s_\mathrm{o} - s)}, \tag{3.20}$$

for $s \leq s_\mathrm{o}$. Here n_a is a quantity satisfying $n_a^2 = a^2\omega^2 - m^2$, which is real in the case of cut-on modes and imaginary otherwise. Having found Y^a, it may now be plugged into the equation for the pressure, which in the plane-wave case reduces to

$$\frac{\mathrm{d}P_0^a}{\mathrm{d}s} = \begin{cases} (m + \mathrm{i}a\omega Y^a)P_0^a & s \leq s_\mathrm{o}, \\ \mathrm{i}a\omega P_0^a & s > s_\mathrm{o}, \end{cases} \tag{3.21}$$

with our inlet condition being

$$P_0^a = \frac{M\sqrt{A_\mathrm{cs}(0)}}{2\mathrm{i}}\delta^{|a|1}\mathrm{sgn}(a), \tag{3.22}$$

or alternatively

$$P_0^a = \frac{M\sqrt{A_\mathrm{cs}(0)}}{2\mathrm{i}}\delta^{|a|1}\mathrm{sgn}(a)\frac{n_a \cos n_a s_\mathrm{o} - (\mathrm{i}a\omega + m)\sin n_a s_\mathrm{o}}{n_a \cos n_a s_\mathrm{o} - \mathrm{i}a\omega \sin n_a s_\mathrm{o}} \tag{3.23}$$

if we wish to specify only the forward-going pressure. Solving this equation, with condition (3.22), the pressure is

$$P_0^a(s) = \frac{M\mathrm{sgn}(a)\delta^{|a|,1}}{2\mathrm{i}}\sqrt{A_\mathrm{cs}(0)}\frac{n_a \cos n_a(s_\mathrm{o} - s) - (\mathrm{i}a\omega + m)\sin n_a(s_\mathrm{o} - s)}{n_a \cos n_a s_\mathrm{o} - (\mathrm{i}a\omega + m)\sin n_a s_\mathrm{o}}, \tag{3.24}$$

and if we specify the forward-going pressure instead, the m disappears from the bracketed term in the denominator.

To test our code on this geometry, we follow McTavish and Brambley [2019] in considering a 2D horn of inlet width X_i, length $4.5X_\mathrm{i}$ and width increase ratio of 16, and a plane piston source of frequency of $0.95\overline{\omega}_1^1(s_\mathrm{o}) = 0.95\pi/X(s_\mathrm{o})$ for the inlet condition on the total pressure (where we recall the definition of the cutoff frequency from equation (2.128)). With 50 spatial modes and 1 temporal mode (since with no nonlinearity there is no temporal coupling) a good match is observed with their results in the linear case (figure 3.10).

Further to this, a more direct comparison with Webster's analytical approximation is shown in figure 3.11, where the RMS pressure at the centreline is plotted (in contrast to McTavish and Brambley [2019], the analytical solution is calculated for the whole domain, including the straight-duct section post-outlet). We achieve a very good match by restricting our calculation to plane waves only: this is achieved with a fixed (and very small)-stepsize method, since the discontinuity in X' at the outlet is severe enough to cause errors in a variable stepsize solver like `ode45`. In contrast, the 50-mode

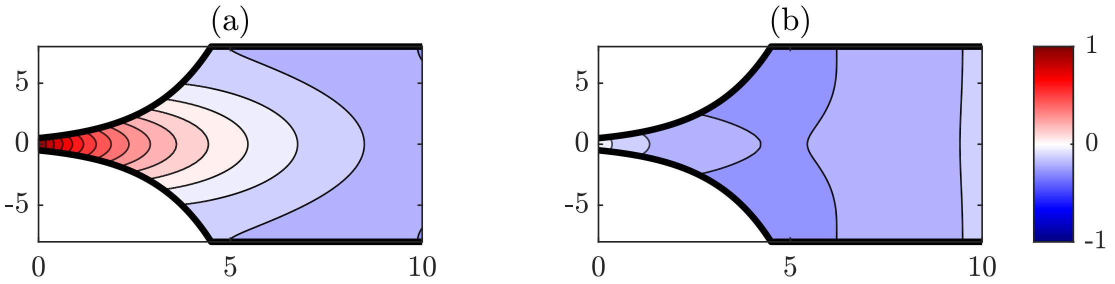

Figure 3.10: Pressure (normalised to the source amplitude) in an exponential horn identical to the one used in McTavish and Brambley [2019], with a plane piston source of frequency $0.95\overline{\omega}_1^1(s_o) = 0.95\pi/X(s_o)$, for (a) linear, (b) linear, quarter of a cycle later. Truncation was taken at $\alpha_{\max} = 50$ and $a_{\max} = 1$.

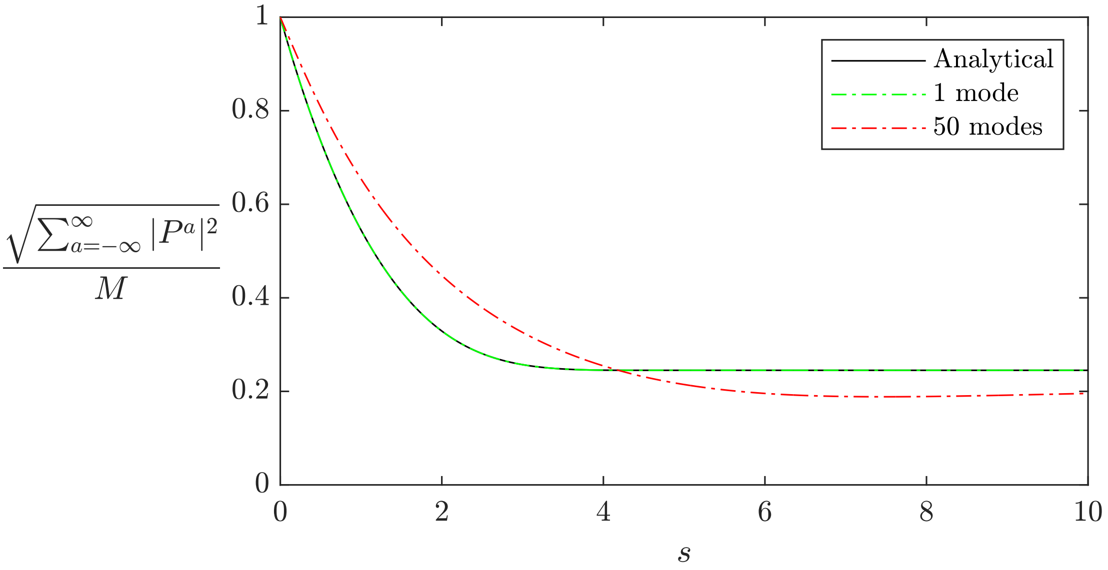

Figure 3.11: RMS pressure along the centreline of the exponential horn for two different modal resolutions, compared with the plane-wave approximation [Webster, 1919]. Mode coupling induced by the variation in duct width causes the plane-wave approximation to be an inaccurate one for this geometry.

calculation disagrees very obviously with the Webster approximation, showing that the Webster approximation will necessarily fail to capture the spatial coupling effects of a duct bell.

3.6 An inverse exponential horn in 2D

If we consider an 'inverse' exponential horn, i.e. one that narrows rather than widening, we introduce the possibility of nodes. This is because waves are now reflecting backwards to a much greater degree, so cancellations can occur. This effect is most readily observed with antisymmetric waves (and in fact cannot occur in a straight duct when considering only plane waves). Since antisymmetric waves are uncoupled from symmetric ones in a straight duct, there are grounds to consider the derivation of an analogous Webster-like solution to the first antisymmetric mode. We will solve only the 2D problem here, since the 3D problem is complicated by a greater number of ways to break azimuthal symmetry. As with the Webster solution, this discussion also covers only linear acoustics in this geometry.

When the Webster solution is derived, we consider a single-mode truncation of equation (2.103) for straight ducts of variable width (whose centreline is always in the middle of the duct, so $X_+ = -X_- = X/2$) in the linear regime. As such, we have no $\mathcal{N}^{ab}$, and L^a (which for $a = 1$ we call L) reads

$$\mathsf{L} = \begin{pmatrix} -\frac{X'}{2X}\left(\mathsf{W} - \widetilde{\mathsf{A}}\right) & \mathrm{i}\omega\left(\mathsf{I} - \frac{\mathsf{\Lambda}^2}{\omega^2 X^2}\right) \\ \mathrm{i}\omega\mathsf{I} & \frac{X'}{2X}\left(\mathsf{W}^T - \widetilde{\mathsf{A}}^T\right) \end{pmatrix}. \tag{3.25}$$

The non-coupling between symmetric and antisymmetric waves is encoded here by the fact that the matrix $\mathsf{W} - \widetilde{\mathsf{A}}$ has non-zero entries only where the column index and row index are either both even (antisymmetric) or both odd (symmetric). In particular, this results in the following 2-mode truncation of equation (2.103)

$$\frac{\mathrm{d}}{\mathrm{d}s}\begin{pmatrix} u_0 \\ u_1 \\ p_0 \\ p_1 \end{pmatrix} = \begin{pmatrix} -\frac{X'}{2X}\begin{pmatrix} 1 & 0 \\ 0 & 2 \end{pmatrix} & \mathrm{i}\omega\begin{pmatrix} 1 & 0 \\ 0 & 1 - \frac{\pi^2}{\omega^2 X^2} \end{pmatrix} \\ \mathrm{i}\omega\begin{pmatrix} 1 & 0 \\ 0 & 1 \end{pmatrix} & \frac{X'}{2X}\begin{pmatrix} 1 & 0 \\ 0 & 2 \end{pmatrix} \end{pmatrix}\begin{pmatrix} u_0 \\ u_1 \\ p_0 \\ p_1 \end{pmatrix}. \tag{3.26}$$

Solving the symmetric problem (u_0, p_0) results in the Webster Horn Equation, while solving the *uncoupled* antisymmetric problem (u_1, p_1) results in the following equation for p_1 (from which we henceforth drop the subscript 1, as with u_1)

$$\frac{\mathrm{d}^2 p}{\mathrm{d}s^2} - \left[4m^2 - \omega^2 + \frac{\pi^2}{X_\mathrm{i}^2}\mathrm{e}^{4|m|s}\right]p = 0, \tag{3.27}$$

where for inlet width X_i we have now substituted in the 2D inverse exponential horn definition $X := X_\mathrm{i}\mathrm{e}^{-2|m|s}$. If we use the substitution $\varsigma = \pi\mathrm{e}^{2|m|s}/2|m|X_\mathrm{i}$, this reduces to the modified Bessel equation

$$\varsigma^2\frac{\mathrm{d}^2 p}{\mathrm{d}\varsigma^2} + \varsigma\frac{\mathrm{d}p}{\mathrm{d}\varsigma} - (\nu^2 + \varsigma^2)p = 0, \tag{3.28}$$

where ν is defined by $\nu^2 = 1 - \omega^2/4m^2$, and takes purely real values or purely imaginary values, depending on whether ω exceeds $2|m|$. If ν is not a real integer, then the solution is given by

$$p(\varsigma) = c_1\mathrm{I}_\nu(\varsigma) + c_2\mathrm{K}_\nu(\varsigma). \tag{3.29}$$

The velocity was eliminated in the derivation of equation (3.27), but can be retrieved from the fourth row of equation (3.26), since we have

$$\frac{\mathrm{d}p}{\mathrm{d}s} = \mathrm{i}\omega u + \frac{X'}{X}p \qquad \Longrightarrow \qquad u(\varsigma) = \frac{2|m|}{\mathrm{i}\omega}\left[\varsigma p'(\varsigma) + p(\varsigma)\right], \tag{3.30}$$

thus the velocity is given by

$$u(\varsigma) = \frac{2|m|}{\mathrm{i}\omega}\left[c_1\tilde{\mathrm{I}}_\nu(\varsigma) + c_2\tilde{\mathrm{K}}_\nu(\varsigma)\right], \quad \text{where} \quad \tilde{\mathrm{I}}_\nu(\varsigma) := \varsigma\mathrm{I}'_\nu(\varsigma) + \mathrm{I}_\nu(\varsigma). \tag{3.31}$$

and $\tilde{\mathrm{K}}_\nu(\varsigma)$ is defined similarly. We then have an admittance given by

$$Y(\varsigma) = \frac{u(\varsigma)}{p(\varsigma)} = \frac{2|m|}{\mathrm{i}\omega}\frac{c_1\tilde{\mathrm{I}}_\nu(\varsigma) + c_2\tilde{\mathrm{K}}_\nu(\varsigma)}{c_1\mathrm{I}_\nu(\varsigma) + c_2\mathrm{K}_\nu(\varsigma)}. \tag{3.32}$$

Applying the boundary condition $Y(\varsigma_\mathrm{o}) = \overline{Y}_\mathrm{o}$, we get

$$Y(\varsigma) = \frac{2|m|}{\mathrm{i}\omega}\frac{\left[\tilde{\mathrm{K}}_\nu(\varsigma_\mathrm{o}) - \frac{\mathrm{i}\omega\overline{Y}_\mathrm{o}}{2|m|}\mathrm{K}_\nu(\varsigma_\mathrm{o})\right]\tilde{\mathrm{I}}_\nu(\varsigma) - \left[\tilde{\mathrm{I}}_\nu(\varsigma_\mathrm{o}) - \frac{\mathrm{i}\omega\overline{Y}_\mathrm{o}}{2|m|}\mathrm{I}_\nu(\varsigma_\mathrm{o})\right]\tilde{\mathrm{K}}_\nu(\varsigma)}{\left[\tilde{\mathrm{K}}_\nu(\varsigma_\mathrm{o}) - \frac{\mathrm{i}\omega\overline{Y}_\mathrm{o}}{2|m|}\mathrm{K}_\nu(\varsigma_\mathrm{o})\right]\mathrm{I}_\nu(\varsigma) - \left[\tilde{\mathrm{I}}_\nu(\varsigma_\mathrm{o}) - \frac{\mathrm{i}\omega\overline{Y}_\mathrm{o}}{2|m|}\mathrm{I}_\nu(\varsigma_\mathrm{o})\right]\mathrm{K}_\nu(\varsigma)}, \tag{3.33}$$

where the characteristic admittance $\overline{Y}_\mathrm{o}$ is given by plugging the definition of X_o into equation (2.127)

$$\overline{Y}_\mathrm{o} = \overline{Y}(\varsigma_\mathrm{o}) = \exp\left\{-\frac{\mathrm{i}\pi}{4}\left[\operatorname{sgn}\left(1 - \frac{4m^2\varsigma_\mathrm{o}^2}{\omega^2}\right) - 1\right]\right\}\sqrt{\left|1 - \frac{4m^2\varsigma_\mathrm{o}^2}{\omega^2}\right|}. \tag{3.34}$$

Specifying the total pressure at the inlet, we match the overall remaining constant with equation (2.158) to get

$$p(\varsigma) = \frac{M\sqrt{X_\mathrm{i}}}{2\mathrm{i}}\frac{\left[\tilde{\mathrm{K}}_\nu(\varsigma_\mathrm{o}) - \frac{\mathrm{i}\omega\overline{Y}_\mathrm{o}}{2|m|}\mathrm{K}_\nu(\varsigma_\mathrm{o})\right]\mathrm{I}_\nu(\varsigma) - \left[\tilde{\mathrm{I}}_\nu(\varsigma_\mathrm{o}) - \frac{\mathrm{i}\omega\overline{Y}_\mathrm{o}}{2|m|}\mathrm{I}_\nu(\varsigma_\mathrm{o})\right]\mathrm{K}_\nu(\varsigma)}{\left[\tilde{\mathrm{K}}_\nu(\varsigma_\mathrm{o}) - \frac{\mathrm{i}\omega\overline{Y}_\mathrm{o}}{2|m|}\mathrm{K}_\nu(\varsigma_\mathrm{o})\right]\mathrm{I}_\nu(\varsigma_\mathrm{i}) - \left[\tilde{\mathrm{I}}_\nu(\varsigma_\mathrm{o}) - \frac{\mathrm{i}\omega\overline{Y}_\mathrm{o}}{2|m|}\mathrm{I}_\nu(\varsigma_\mathrm{o})\right]\mathrm{K}_\nu(\varsigma_\mathrm{i})}. \tag{3.35}$$

The boundary condition at the duct outlet ς_o can be rewritten as a vector orthogonality condition in 2D, i.e.

$$\begin{pmatrix} c_1 \\ c_2 \end{pmatrix} \cdot \left[\varsigma_\mathrm{o}\begin{pmatrix} \mathrm{I}'_\nu(\varsigma_\mathrm{o}) \\ \mathrm{K}'_\nu(\varsigma_\mathrm{o}) \end{pmatrix} + \left(1 - \frac{\mathrm{i}\omega\overline{Y}_\mathrm{o}}{2|m|}\right)\begin{pmatrix} \mathrm{I}_\nu(\varsigma_\mathrm{o}) \\ \mathrm{K}_\nu(\varsigma_\mathrm{o}) \end{pmatrix}\right] = 0. \tag{3.36}$$

$\mathrm{I}_\nu(\varsigma)$ and $\mathrm{I}'_\nu(\varsigma)$ are exponentially-growing functions, while $\mathrm{K}_\nu(\varsigma)$ and $\mathrm{K}'_\nu(\varsigma)$ exponentially decay. Unscaled, these functions will therefore be of very different orders of magnitude at the outlet. This relation, however, effectively sets the vector (c_1, c_2) to be 'asymptotically orthogonal' to the Bessel function vector, meaning that the two terms in both the velocity and the pressure are instead of comparable order at the outlet. If we then move backwards from the outlet, the K functions will grow rapidly while the

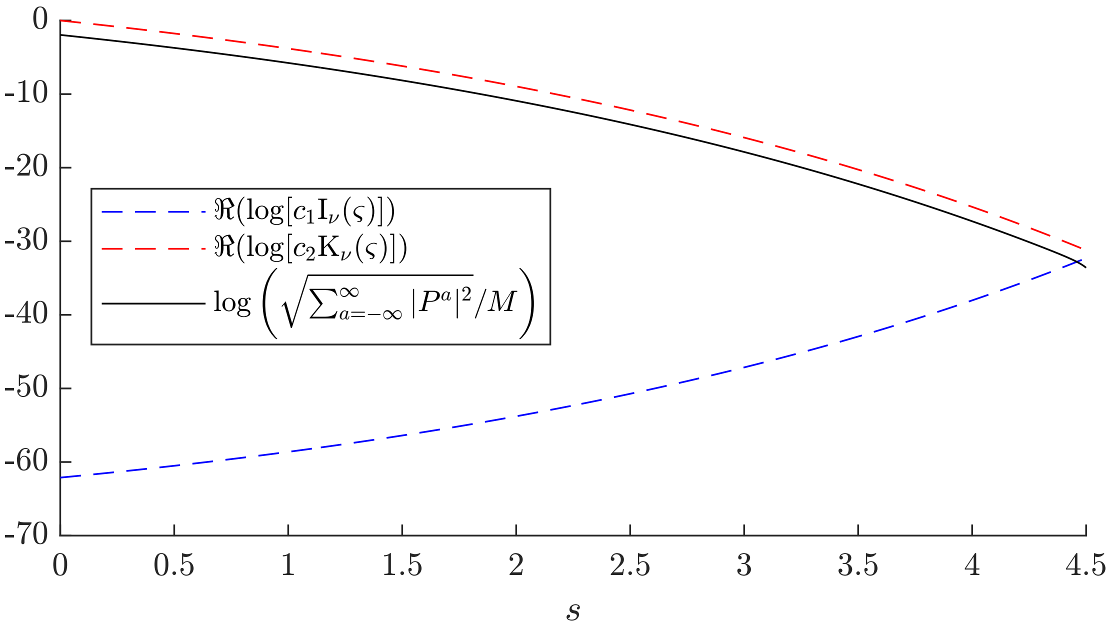

Figure 3.12: Figure comparing the (real parts of the) logarithmically plotted modified Bessel functions ($\mathrm{I}_\nu(\varsigma)$ in blue, $\mathrm{K}_\nu(\varsigma)$ in red), along an inverse exponential horn of length $4.5X_i$ and width decrease ratio of 4, for a frequency of $0.5/X_i$. RMS pressure (according to this analytical solution) normalised by Mach number is logarithmically plotted in black.

I functions decay, so for most of the duct the K functions will dominate. For higher frequencies, ν can become imaginary, causing K to oscillate towards the inlet: these oscillations will pass through zero, resulting in pressure nodes, which cause singularities in the admittance. Figure 3.12 shows these relationships in more detail, for a frequency low enough that oscillations do not yet occur. We note that for the inverse exponential horn, the lowest-mode admittance singularities correspond approximately to roots s of $\mathrm{K}_{\mathrm{i}\sqrt{\omega^2/4m^2-1}}(\pi \mathrm{e}^{2|m|s}/2|m|X_\mathrm{i})$.

Another feature of this geometry (or any geometry with width variation) is that *turning points* can occur, i.e. points where a mode can go from being cut-on to cut-off. These are significant because they correspond mathematically to the eigenvalue $\overline{\gamma}_\alpha^a$ for that particular mode passing from the real axis to the imaginary axis, and therefore necessarily passing through zero. Since the splitting operators then involve the inverse of a matrix with a zero eigenvalue, this results in singularities in the forward and backward-going pressures at this point. By inverting equation (2.128) for $\omega = \overline{\varpi}_\alpha^a$, $\lambda_\alpha = \alpha\pi$, and $X = X_\mathrm{i}\mathrm{e}^{2|m|s}$, we note that the location of the turning point for mode (a, α) is

$$s_\mathrm{tp} = \frac{1}{2|m|} \log\left(\frac{a\omega X_\mathrm{i}}{\alpha\pi}\right). \tag{3.37}$$

We can test our code on this geometry as well. To form a good physical picture of where the admittance singularities are, we may exploit the lack of coupling between symmet-

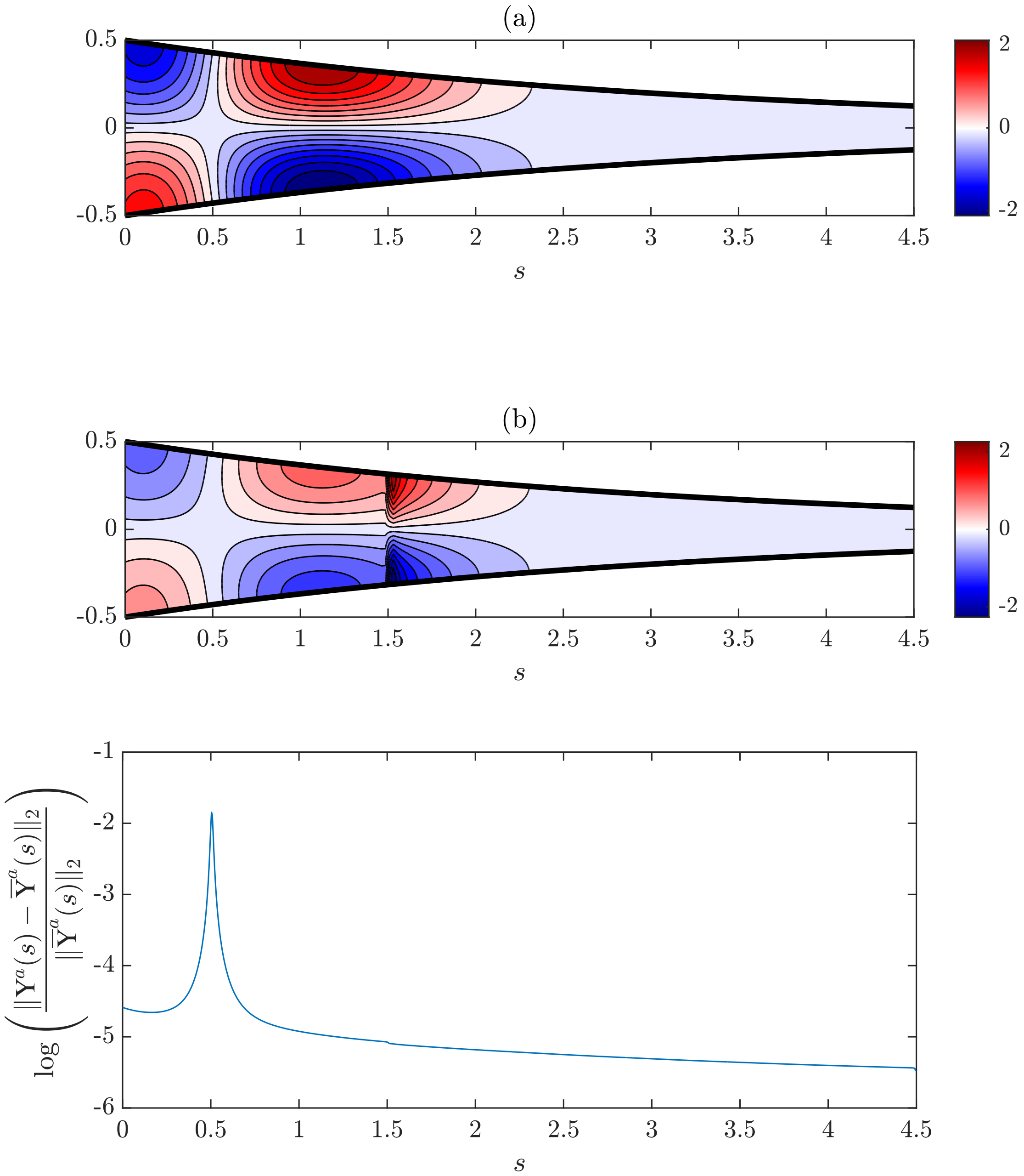

Figure 3.13: Pressure (total in (a), forward-going in (b), both normalised to the source amplitude) inside an inverse exponential horn, with an antisymmetric source of frequency $(5+0.01\mathrm{i})/X_{\mathrm{i}}$, together with the normalised deviation of the admittance from the characteristic admittance. Truncation was taken at $\alpha_{\max}=50$ and $a_{\max}=1$, and `ode45` was used.

ric and antisymmetric modes in this geometry to eliminate the plane-wave component from the solution altogether. To do this we make use of the alternative inlet condition mentioned in section 2.2.4. Figure 3.13 shows the pressure distribution lined up with a demonstration of the admittance singularity in this geometry. This was calculated with 50 spatial modes and 1 temporal mode (since we are testing just linearity here), for a

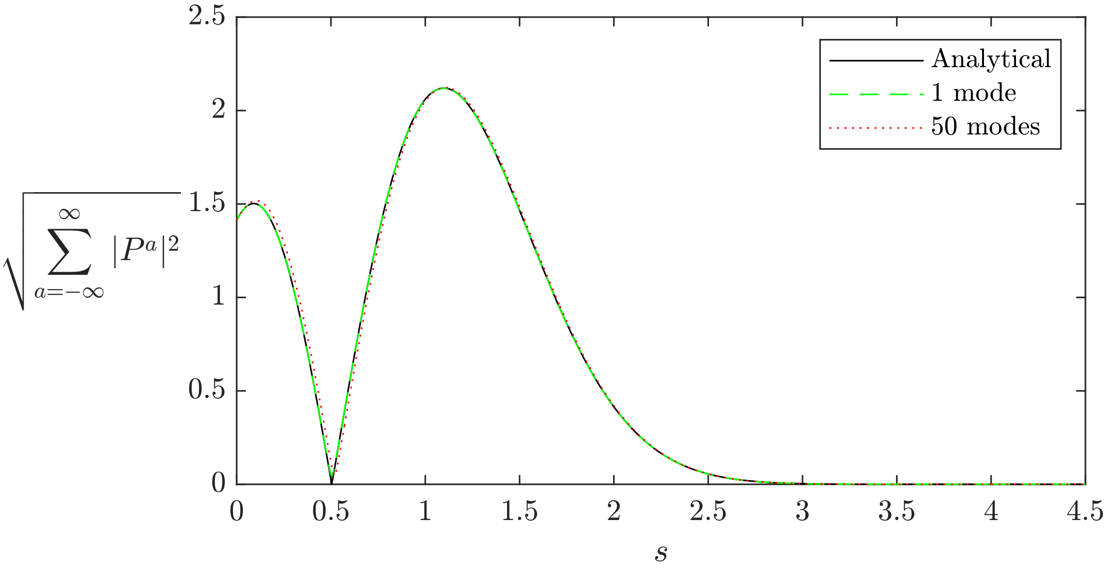

Figure 3.14: RMS pressure along the wall of the inverse exponential horn for two different modal resolutions, compared with the analytical solution.

duct of length $4.5X_\mathrm{i}$ and decrease ratio of 4. As mentioned in section 2.3.6 we add a small imaginary part to the frequency to 'dampen' any singularities. The frequency is then $(5+0.01\mathrm{i})/X_\mathrm{i}$, resulting in a value of $\mathrm{Im}(\nu)$ high enough that the first root of $\mathrm{K}_\nu(\varsigma)$ is within the duct domain, causing a node in the pressure, observable a little beyond $s = 0.5$. We also plot the forward-going pressure, allowing us to see a turning point at $s \approx 1.5$. Waves to the left of this are propagating, while waves to the right decay; the turning point is also visible as a small kink in the admittance plot.

Figure 3.14 compares the results of a single-spatial-mode calculation with the 50-mode calculation (the same frequency, and therefore the same stabilising imaginary part, were used on the single-mode calculation). We find that the coupling is very minimal: while the 1-mode line matches the analytical solution exactly, the 50-mode line is a lot closer than it was in the case of the Webster plane-wave solution.

Magnus–Möbius applied to admittance singularities

This is an ideal geometry on which to test the Magnus–Möbius solver, because of the presence of nodes. Figure 3.15 shows the result of such a calculation and compares the admittance calculation with the one from before. We see that the dampening effect of the imaginary frequency makes both the turning-point singularity in p^+ and the node singularity in Y^a less extreme: we know from the mathematical analysis that these are both 'authentic' singularities, so this is an argument for the Magnus–Möbius scheme's use.

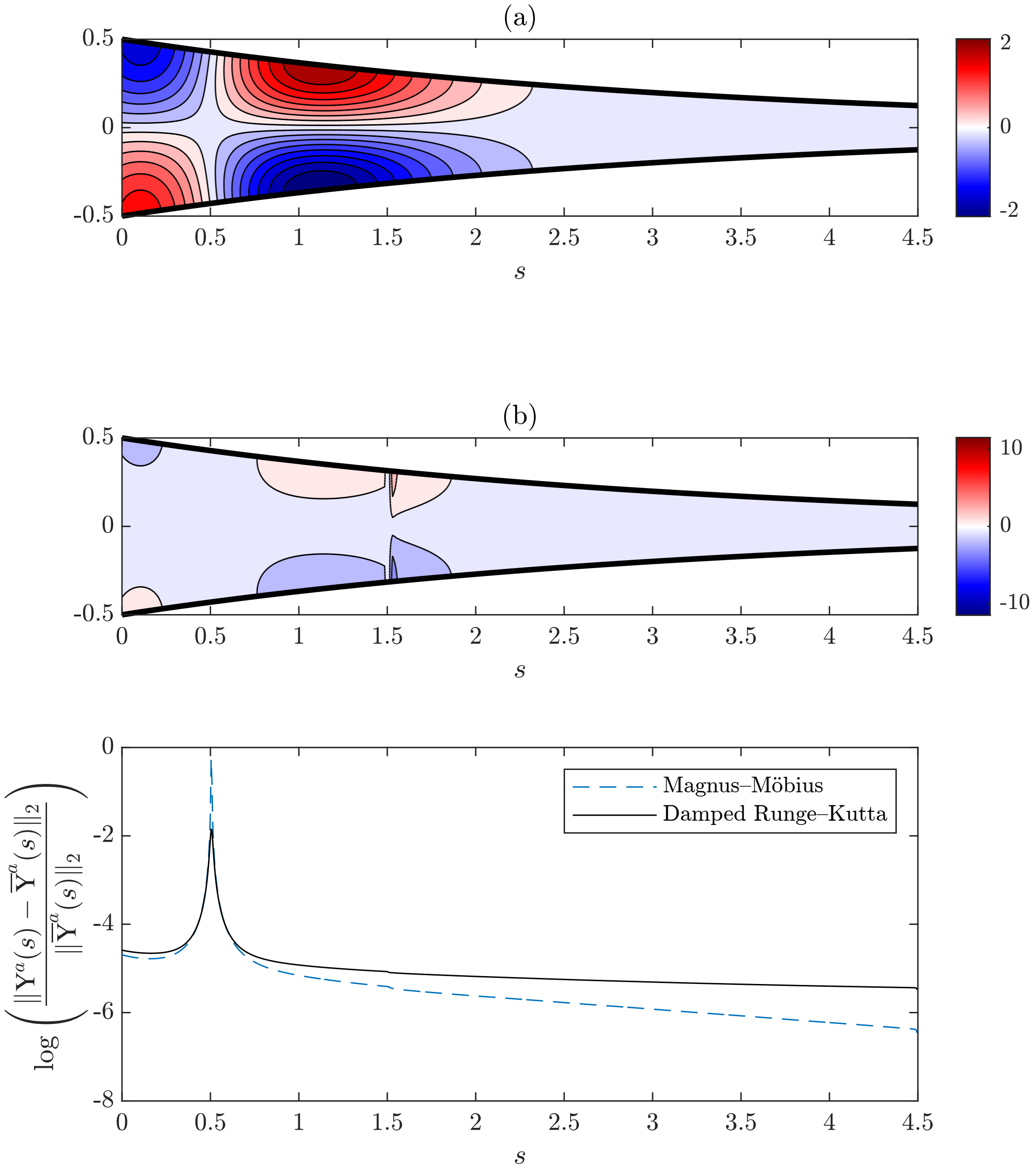

Figure 3.15: Pressure (total in (a), forward-going in (b), both normalised to the source amplitude) inside an inverse exponential horn, with an antisymmetric source of frequency $5/X_{\mathrm{i}}$, together with the normalised deviation of the admittance from the characteristic admittance. Truncation was taken at $\alpha_{\max} = 50$ and $a_{\max} = 1$, and the Magnus–Möbius solver was used (the Runge-Kutta admittance is shown for comparison).

3.7 Curvature and width variation combined

3.7.1 Plane wave tunnelling

We can use the inverse exponential horn to demonstrate mode coupling. In the linear case, if we send in an antisymmetric source and the duct is straight, only antisymmetric modes will be excited. This symmetry can be broken in multiple ways. If nonlinearity is included, higher-order temporal harmonics will be coupled, and these can include symmetric modes (a physical argument for this is that the nonlinear terms are quadratic in the pressure, so two odd pressure modes will multiply to create an even one). Alternatively symmetric modes of the same temporal order can be picked up if the originally-straight duct is bent. Symmetric modes can include plane waves, which have the property of always being cut-on, so we see that for an antisymmetric source of a certain frequency, propagating waves will only 'escape' the duct if a) they are allowed to steepen or b) the duct is bent.

Figure 3.16 displays this phenomenon of 'acoustic leakage', for the same inverse exponential horn as in figure 3.13. An antisymmetric inlet source of frequency $1/X_\mathrm{i}$ is used: this ensures that all non-plane waves are cut-off at the outlet. We see plane-wave tunnelling induced both for a straight duct with Mach number 0.05, or in the linear regime with a curvature of $0.2/X_\mathrm{i}$. Truncation was taken at 10 spatial modes and 10 temporal modes for each of these calculations.

While acoustic leakage from an inverse exponential horn does not bear particular application to brass instruments, it is an interesting object of study in its own right given the potential wider scope of duct acoustics beyond musical applications. It is included here as example of a phenomenon that can now be analysed owing to the present framework.

3.7.2 The 'elephant's trunk' geometry

As well as looking at mode coupling, we also compare results to those obtained by McTavish and Brambley [2019] in modelling a duct of constant curvature and decreasing width (this problem was originally examined in Félix and Pagneux [2001] but only in the linear case). In such a geometry, the same problems of singular admittance are encountered as in 3.6; McTavish and Brambley [2019] chose to deal with this by adding a small imaginary part to the frequency (or wavenumber, in their case). We follow this method here, and observe transverse oscillations for higher Mach numbers, likely due to the complex frequency placing more stringent demands on the spatial and temporal resolution. Simulations were performed with 15 spatial modes and 10 temporal modes (sufficient for the other geometries considered).

The geometry considered is an 'elephant's trunk' duct, of curvature $4/5X_\mathrm{i}$ and

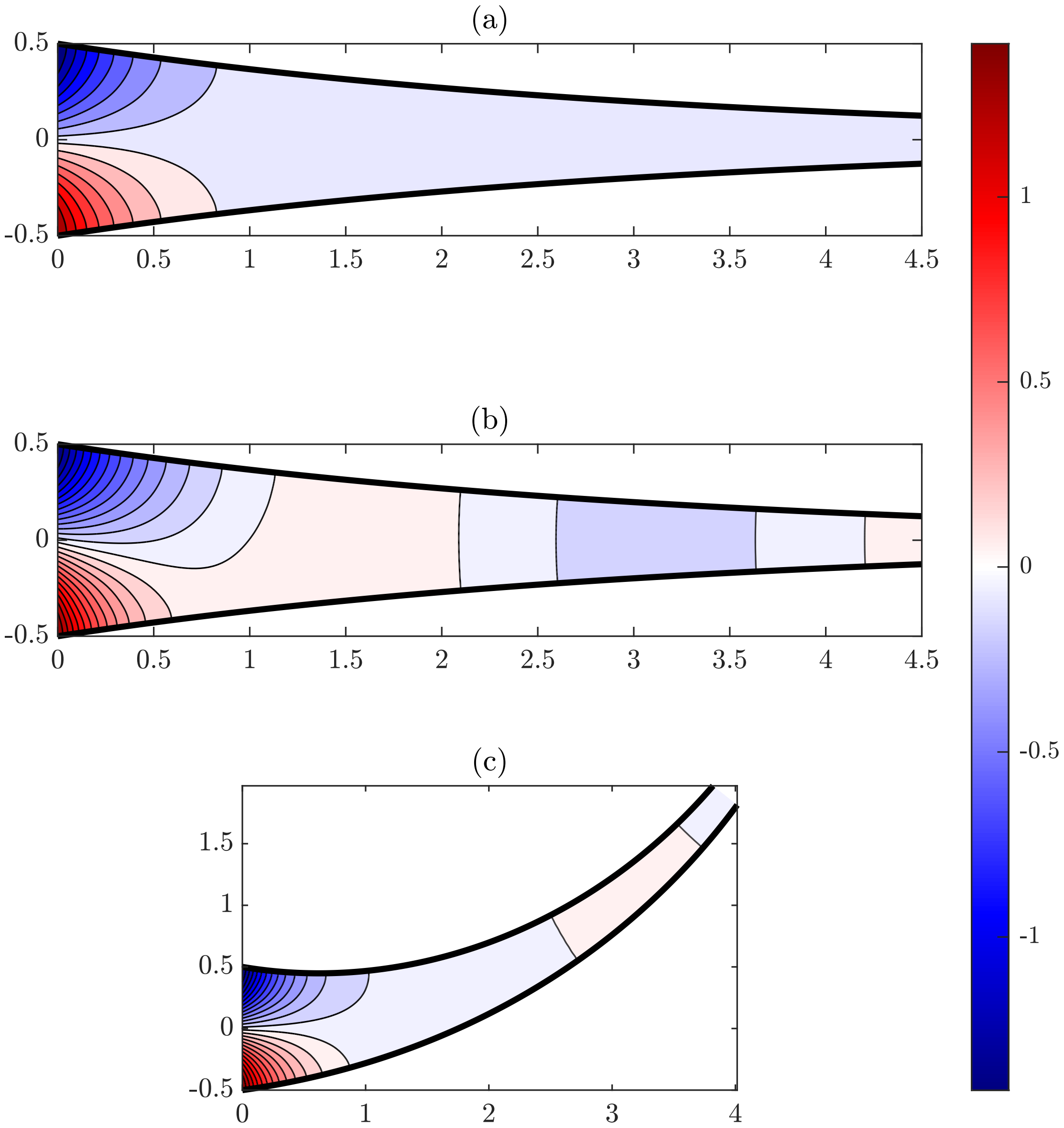

Figure 3.16: Pressure (normalised to the source amplitude) for an antisymmetric source of frequency $1/X_\mathrm{i}$ in an inverse exponential horn for (a) linear, straight, (b) $M = 0.05$, straight, and (c) linear, $\kappa = 0.2/X_\mathrm{i}$. Truncation was taken at $\alpha_\mathrm{max} = a_\mathrm{max} = 10$.

arclength $s_\mathrm{o} = 3.275X_\mathrm{i}$, with a cubically-varying width given by

$$X = X_\mathrm{i}\left(\frac{3}{4}\left(\frac{s}{s_\mathrm{o}}\right)^2\left(\frac{2s}{s_\mathrm{o}} - 3\right) + 1\right), \tag{3.38}$$

resulting in an inlet-outlet width ratio of 4. The result is shown in figure 3.17: aside from the transverse oscillations visible in the contours near the duct outlet, a good match with figure 8 from McTavish and Brambley [2019] is achieved.

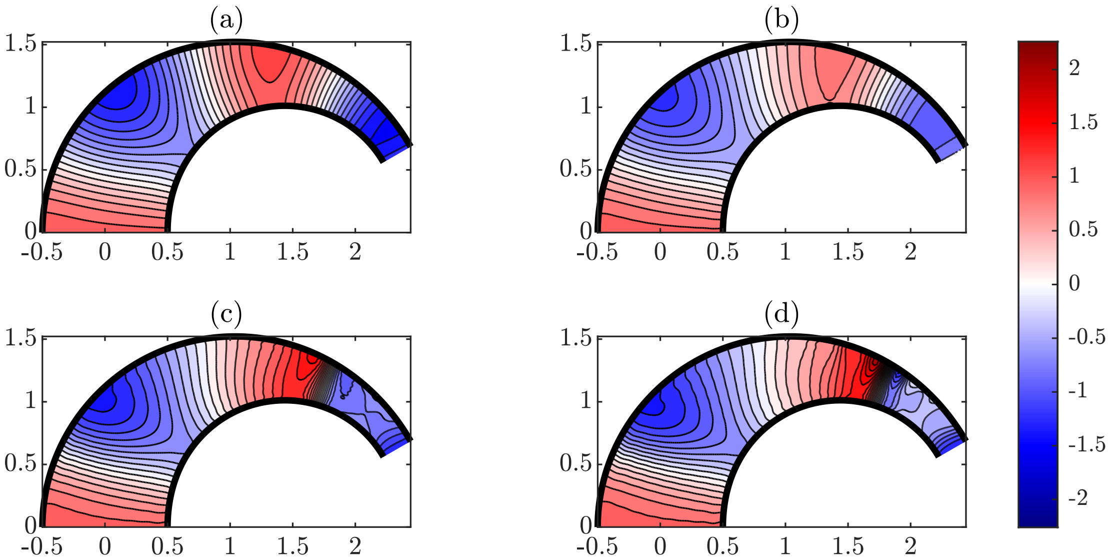

Figure 3.17: Pressure (normalised to the source amplitude) in an 'elephant's trunk' duct, for (a) linear, (b) $M = 0.05$, (c) $M = 0.10$, (d) $M = 0.15$.

3.8 Torsion

Our framework allows us to investigate the effects of torsion on both linear and nonlinear acoustics. To this end, we examine helical ducts of constant wall radius R and curvature κ, with various torsions τ. For each helix, we have a duct centreline given by

$$\mathbf{q}(s) = (a \cos \tilde{s}, a \sin \tilde{s}, b\tilde{s}), \tag{3.39}$$

where a is the helical radius, $2\pi b$ is the *pitch* of the helix, and $\tilde{s}$ is a transformed arclength. These are given in terms of κ and τ by

$$a = \frac{\kappa}{\kappa^2 + \tau^2}, \qquad b = \frac{\tau}{\kappa^2 + \tau^2}, \qquad \tilde{s} = \sqrt{\kappa^2 + \tau^2} s. \tag{3.40}$$

The binormal is calculated as $\mathbf{b} = \sqrt{\kappa^2 + \tau^2}(b \sin \tilde{s}, -b \cos \tilde{s}, a)$. At each point along the centreline, this vector points upward with a degree of backward tilt parallel to the centreline to make it perpendicular to the tangent vector. The angle between $\mathbf{b}$ and the vertical is calculated with the dot product to be

$$\cos \theta_{\mathbf{b}} = \mathbf{b} \cdot \mathbf{e}_z = a\sqrt{\kappa^2 + \tau^2}, \tag{3.41}$$

so if we wish to know the vertical distance from a point $\tilde{s}_0$ to the duct wall above, we consider the hypotenuse of a right-angled triangle with adjacent side of length R and an angle of $\theta_{\mathbf{b}}$ between. This distance is therefore

$$\frac{R}{\cos \theta_{\mathbf{b}}} = \frac{R\sqrt{\kappa^2 + \tau^2}}{\kappa}. \tag{3.42}$$

We also know from the definition of the helix that the vertical distance between point $\tilde{s}_0$ and point $\tilde{s}_0 + 2\pi$ (where the centreline next passes over it) is $2\pi b$. Therefore, for non-self-intersection, we require that $2\pi b$ be greater than twice the vertical centreline-to-wall distance calculated above. This constraint yields the following condition for the helical duct

$$0 > (\tau R)^6 + 3(\kappa R)^2(\tau R)^4 + \left(3(\kappa R)^2 - \pi^2\right)(\kappa R)^2(\tau R)^2 + (\kappa R)^6. \qquad (3.43)$$

All of the helical ducts we consider have curvature given by $\kappa R = 2/3$. We consider three torsions: $\tau R = 0.16$ (just large enough to avoid self-intersection), $\tau R = 0.2$, and $\tau R = 1$. All are compared in the linear case in figure 3.18, while each is held fixed for varying Mach number in figures 3.19, 3.20 and 3.21. We use a frequency of $\omega = 0.95\overline{\omega}_1^1 = 0.95 \times 1.8412/R$; truncation for all helical calculations is taken at 10 spatial modes and 10 temporal modes.

Each of these examples shows how torsional coupling causes a planar source to become non-planar at the duct outlet. It is also clear from figure 3.18 that (for all of the torsions we consider) the highest peaks and lowest troughs in the pressure occur on the outside of the helix, which is consistent with what was observed both in 2D and 3D planar bends. Figure 3.20 shows that when the amplitude is high enough, the peaks and troughs then lose their even spacing as the wave steepens along the outside of the helix. The effect of the $\theta_0(s)$ coordinate twisting due to the helical coordinate system is less visible in the static images shown in figures 3.18 and 3.20, but is more evident when the figures are animated; the wave at the outlet is seen to spin as it propagates due to the helical nature of the duct.

3.9 Comparison of 2D and 3D

Width variation should not, by itself, produce significantly different effects between 2D and 3D, since the same symmetry is being broken in each case. Torsion is only possible in 3D, so does not invite comparison. Therefore, we will concentrate here on the difference between the effects of curvature in 2D and 3D. We consider a duct of width $X_\mathrm{i} = 1$ in 2D, and radius $R_\mathrm{i} = 0.5$ in 3D. In each case, there are straight sections of length 7/4 either side of a right-angled bend with bend radius 5/4. We prescribe a piston source of frequency 9/2: figure 3.22 compares the pressure fields in the linear case with those of Mach number 0.1. In figure 3.23, we plot the spatially-averaged outlet pressures against time, as a means of demonstrating the bend's effect on a piston source. Truncation was taken at 10 spatial modes and 10 temporal modes for each calculation.

We note that while the two cases seem to steepen equally, the effective acoustic length of the bend differs between them. The 3D outlet pressure is consistently 'ahead' of the 2D outlet pressure in both the linear and nonlinear regimes, suggesting that the

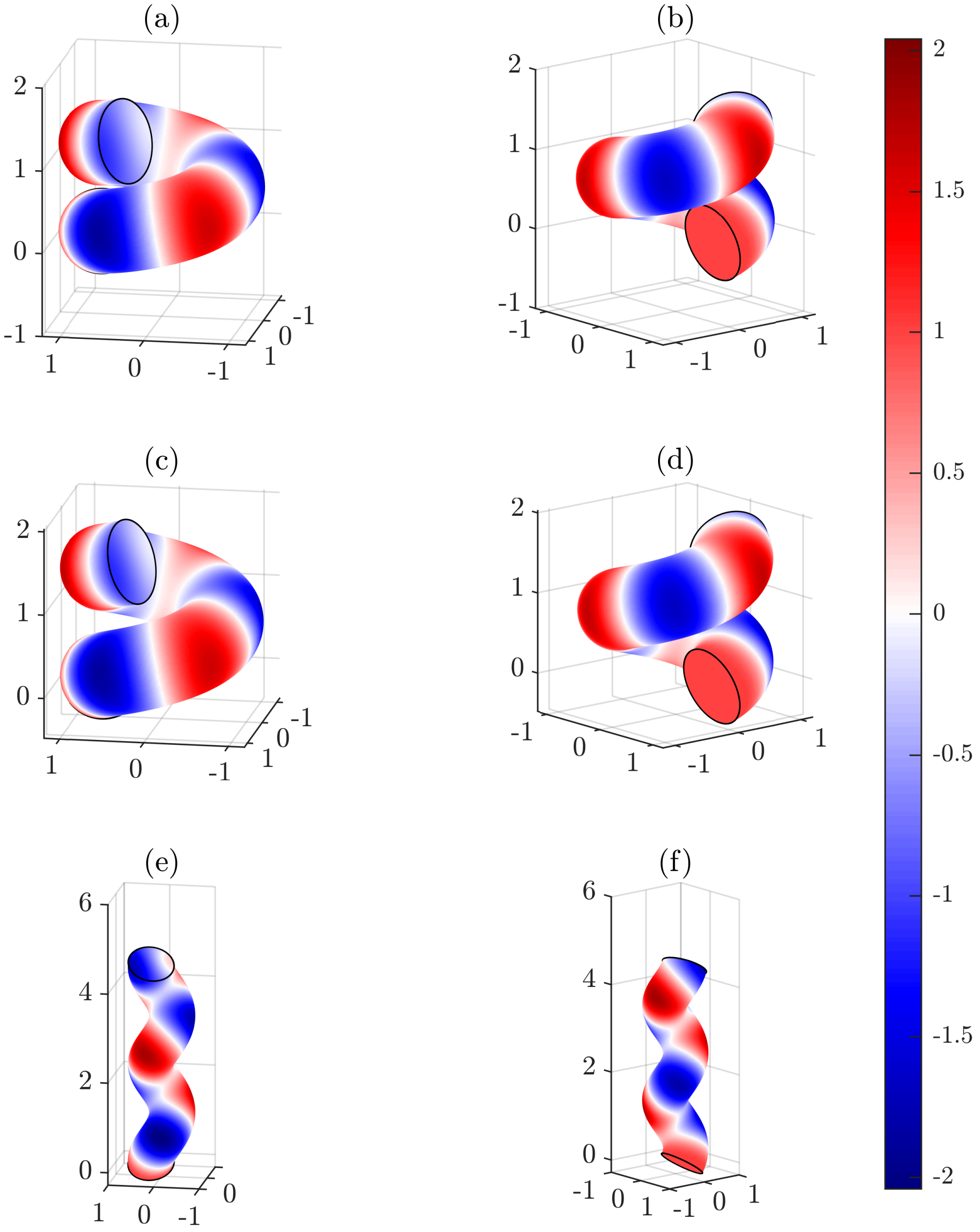

Figure 3.18: Linear pressure field (normalised by the Mach number) on the walls of a helical duct for the three torsions $\tau R = 0.16$, 0.20 and 1.00, with a plane piston source of frequency $\omega = 0.95\overline{\omega}_1^1 = 0.95 \times 1.8412/R$, viewed from two different angles in each case. Truncation was taken at $\alpha_{\max} = a_{\max} = 10$.

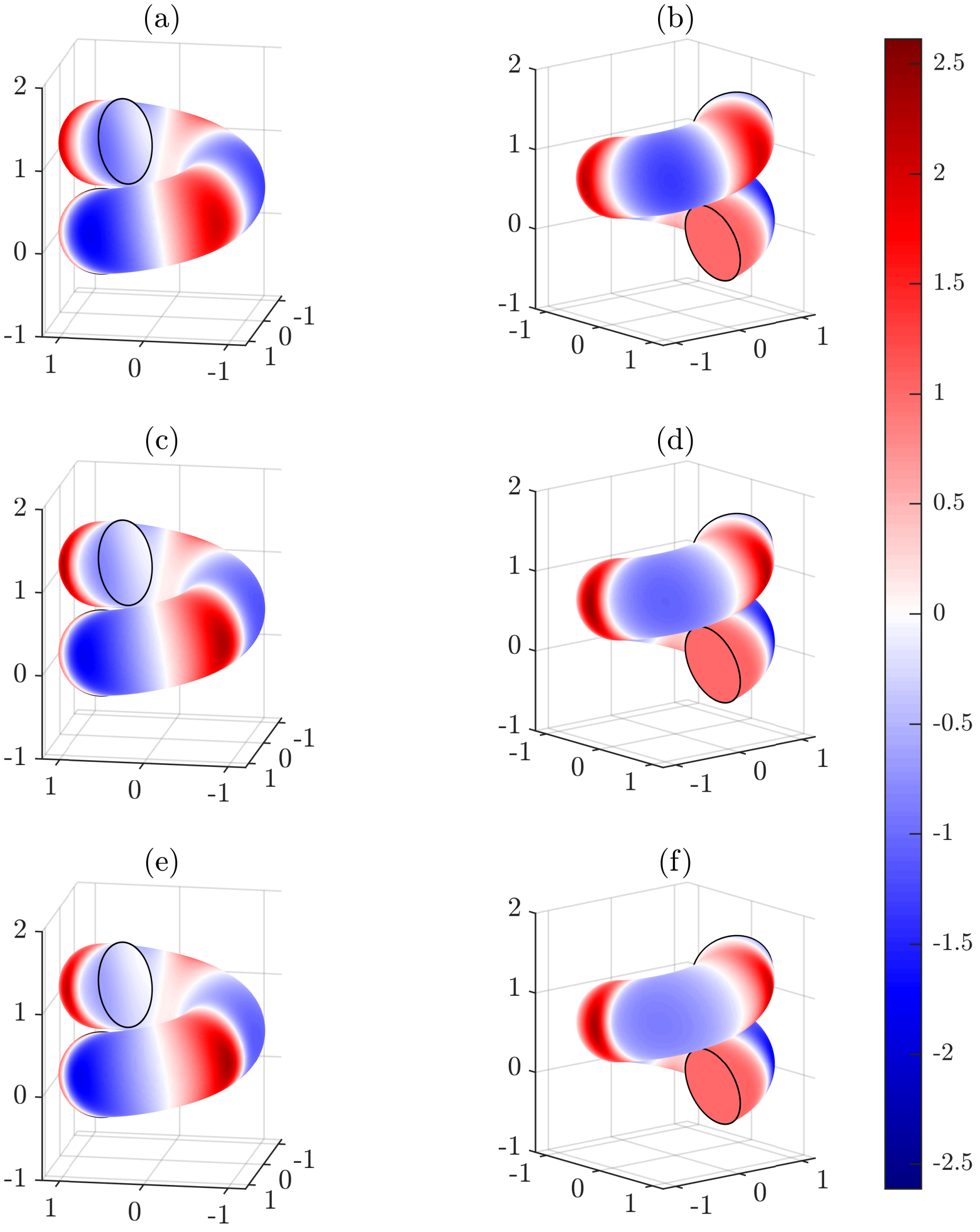

Figure 3.19: Pressure field (normalised by the Mach number) on the walls of a helical duct with torsion $\tau R = 0.16$, for $M = 0.05$ (a,b), 0.10 (c,d), and 0.15 (e,f), with a plane piston source of frequency $\omega = 0.95\overline{\omega}_1^1 = 0.95 \times 1.8412/R$. Truncation was taken at $\alpha_{\max} = a_{\max} = 10$.

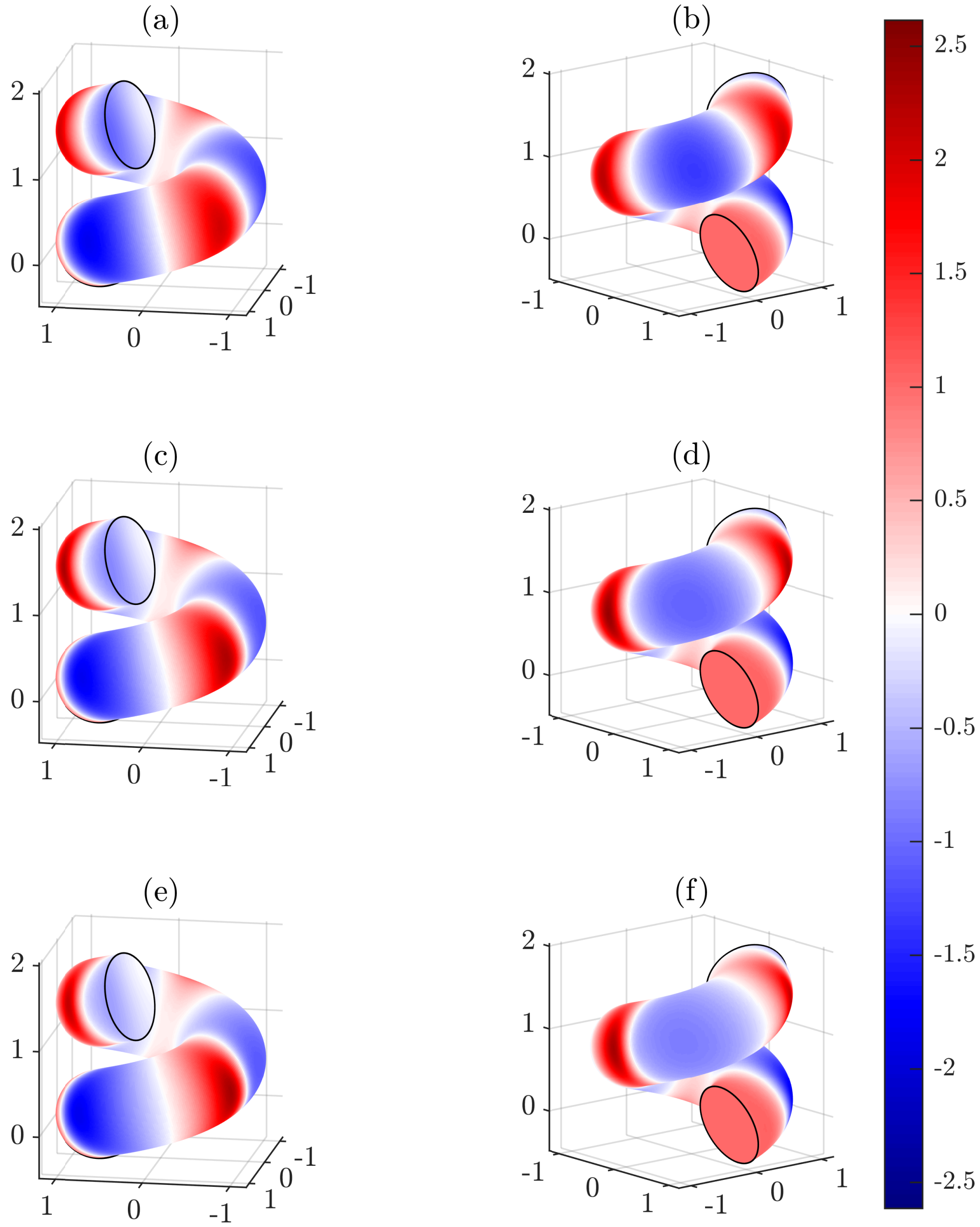

Figure 3.20: Pressure field (normalised by the Mach number) on the walls of a helical duct with torsion $\tau R = 0.20$, for $M = 0.05$ (a,b), 0.10 (c,d), and 0.15 (e,f), with a plane piston source of frequency $\omega = 0.95\overline{\omega}_1^1 = 0.95 \times 1.8412/R$. Truncation was taken at $\alpha_{\max} = a_{\max} = 10$.

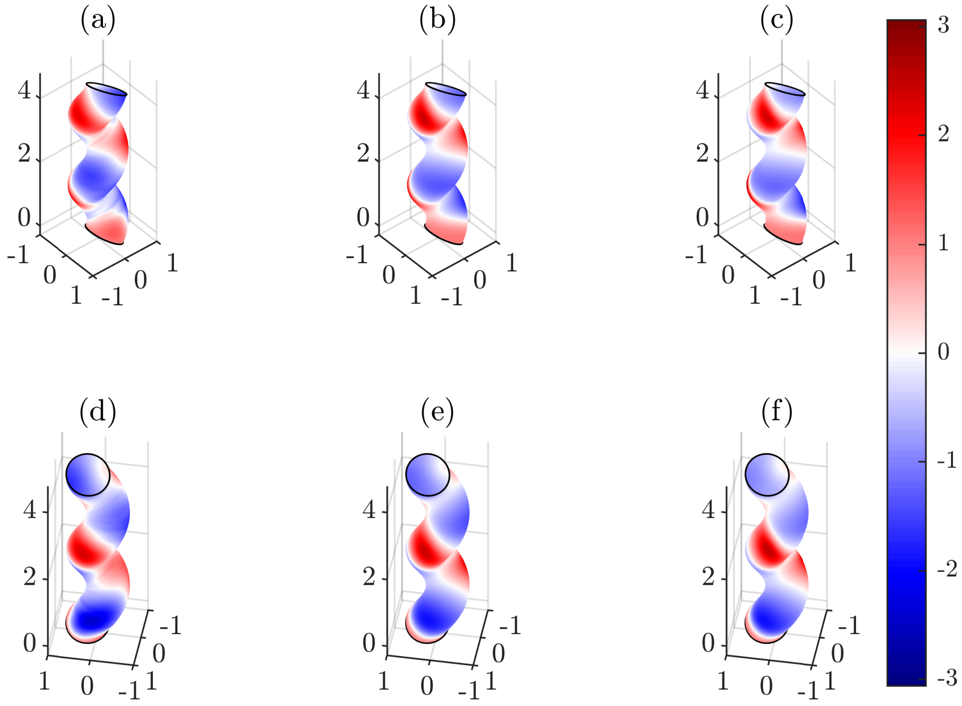

Figure 3.21: Pressure field (normalised by the Mach number) on the walls of a helical duct with torsion $\tau R = 1.00$, for $M = 0.05$ (a,b), 0.10 (c,d), and 0.15 (e,f), with a plane piston source of frequency $\omega = 0.95\overline{\omega}_1^1 = 0.95 \times 1.8412/R$. Truncation was taken at $\alpha_{\max} = a_{\max} = 10$.

effective bend length is longer in 2D. It may also be observed that the 2D calculations exhibit more transverse oscillations than in 3D: this is unsurprising, since that is the only possible plane of oscillation in 2D, whereas in 3D there is an entire circular surface of oscillation at each s.

3.10 Effective acoustic length of a bend

We can also examine the competing effects of curvature and nonlinearity. We calculate the cross-sectional average of the pressure two wavelengths along the centreline from the inlet, for a range of different bend angles and Mach numbers, while keeping the arclength along the centre of the bend constant. The boundary condition at the inlet ensures that the average pressure across the inlet will pass upwardly through zero at $t = \pi/\omega$, and downwardly at $t = \pi/2\omega$. In a straight duct, the average pressure across a surface two wavelengths along would match this, but curvature causes a deviation of these upstroke and downstroke crossings, which we call Δt. We then define a *bend correction factor* $B := 2c\Delta t/\Delta x$, where Δx is the difference in arclength between the outer wall of the duct and the centreline for that particular bend angle. This parameter

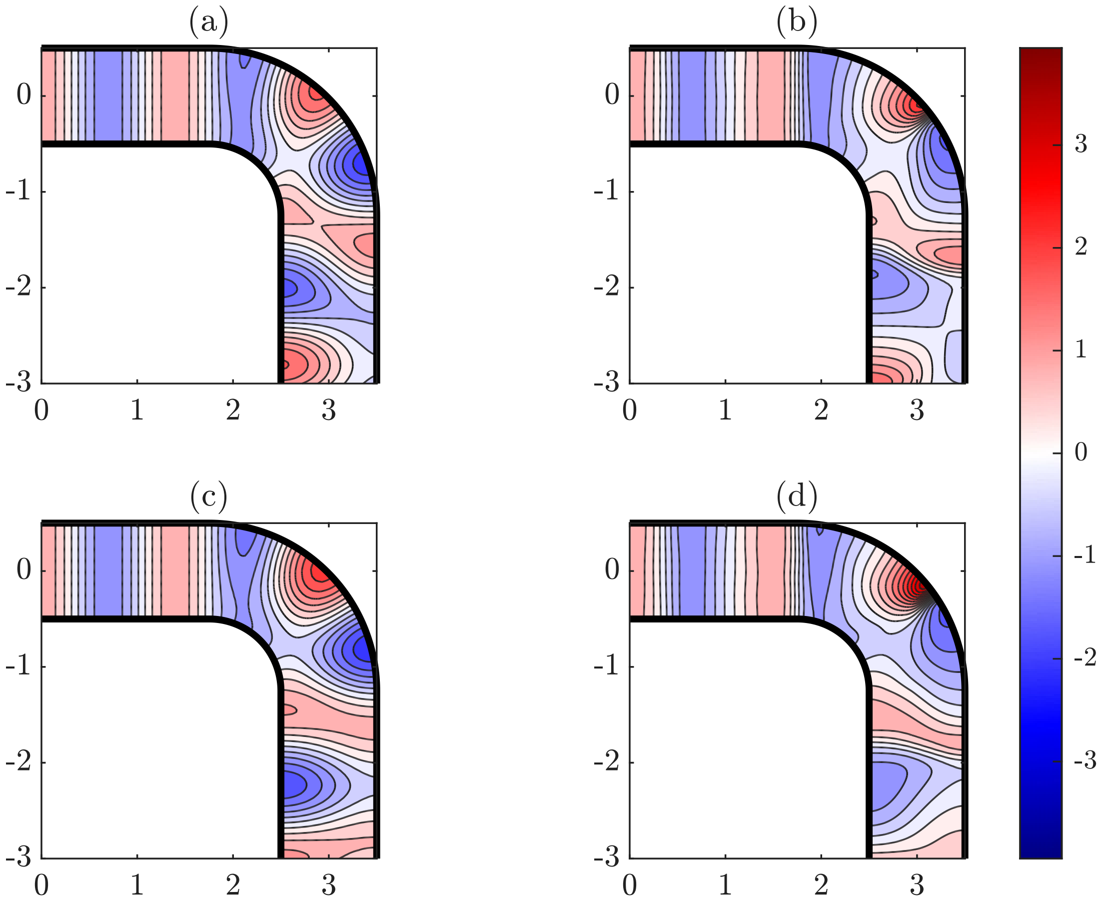

Figure 3.22: Forward-going pressure (normalised to the source amplitude) in an extended bend with a plane piston source of 9/2, for (a) linear, 2D, (b) nonlinear, 2D, (c) linear, 3D and (d) nonlinear, 3D. Truncation was taken at $\alpha_{\max} = a_{\max} = 10$.

is equal to 1 for a wave travelling along the outside of the bend, and -1 for the inside. We can also choose whether to use the deviation time Δt for the upstroke of the wave, or the downstroke. Figure 3.24 shows upstroke and downstroke values of B for three duct radii in 2D. Each data point on these contour plots is the result of a calculation with 10 spatial modes and 10 temporal modes.

From the upstroke plots we see that for greater bend angles (and correspondingly tighter bends), nonlinearity plays a bigger role in forcing the wave around the outside of the bend, whereas for smaller bend angles, the bend angle takes over as the determining parameter. The downstroke plots are less conclusive, but they do exhibit the emergence of a local minimum in B as the radius is varied.

3.11 Summary

In this chapter, the mathematical framework from chapter 2 and its numerical implementation have been validated where possible against existing work [Blackstock, 1966;

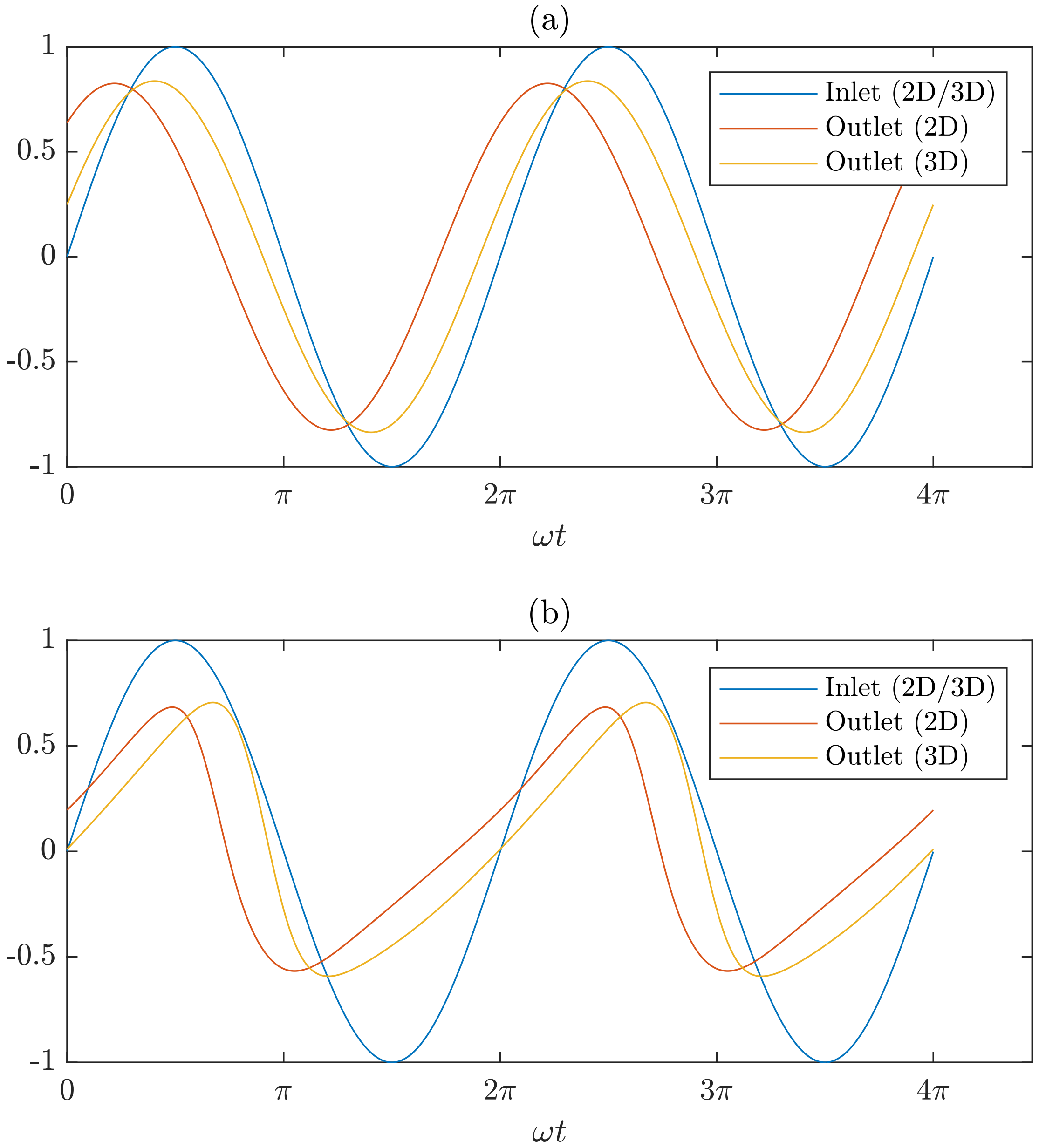

Figure 3.23: Forward-going pressure (normalised to the source amplitude), averaged over the inlet, the outlet in 2D, and the outlet in 3D, in the linear regime (a) and for $M = 0.10$ (b). Truncation was taken at $\alpha_{\max} = a_{\max} = 10$.

Webster, 1919; Félix and Pagneux, 2002; McTavish and Brambley, 2019]. After gaining confidence in the model as a result, we have produced novel results to do with acoustic leakage due to spatial or temporal mode coupling (section 3.7.1), qualitative comparison of acoustic behaviour in 2D vs 3D (section 3.9), and the effective acoustic length of a bend taking nonlinearity into account (section 3.10). We have also seen in section 3.4.2 that there is some ambiguity in the definition of reflected waves, and that this affects our interpretation of how varying geometry (such as a bend in a duct) leads to wave reflection. Extensive testing of the code has also confirmed the model's gains in compu-

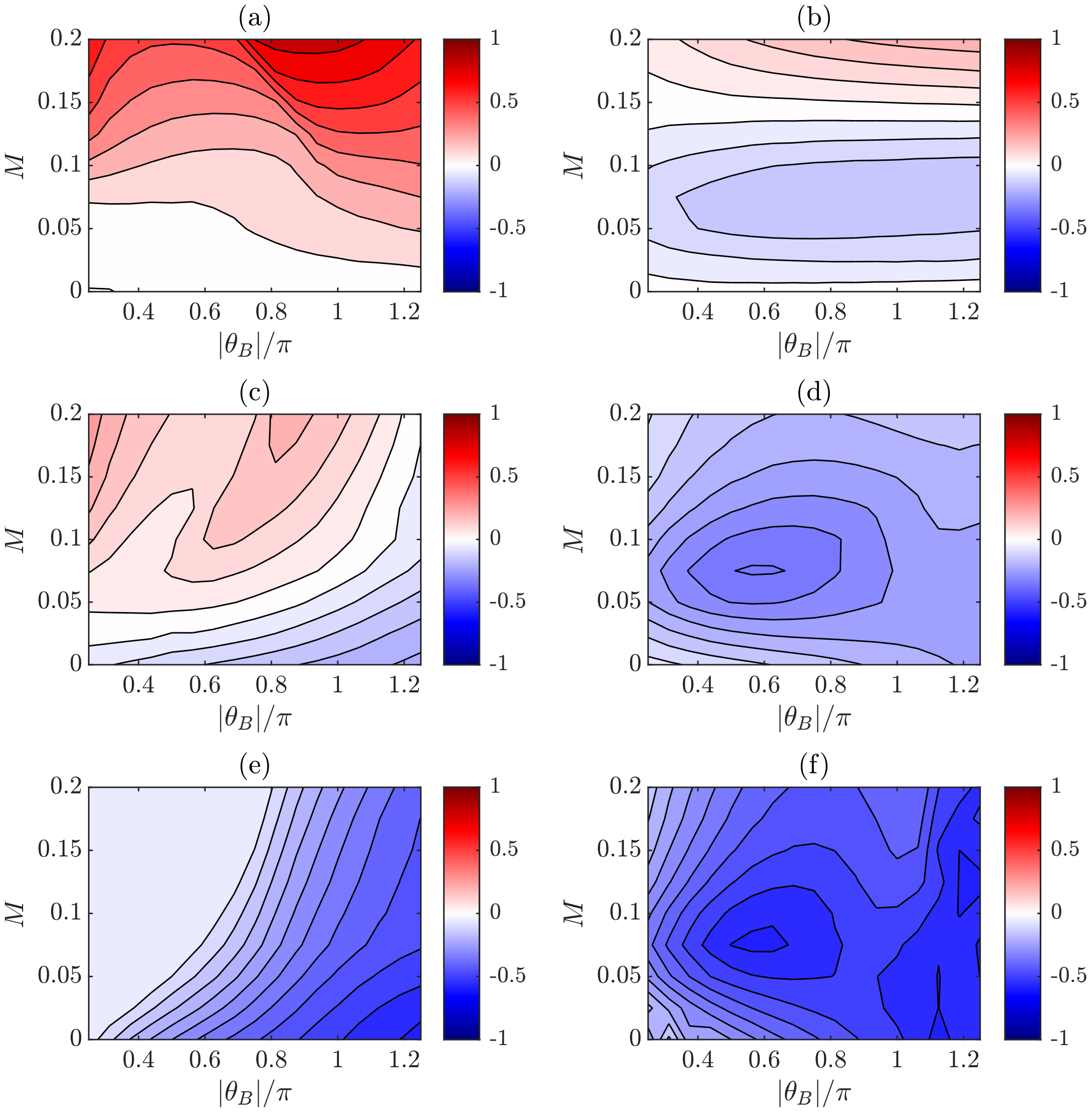

Figure 3.24: Upstroke (left) and downstroke (right) values of the bend correction parameter B in 2D, for $\omega X = 3$ (a,b), 3/2 (c,d) and 3/4 (e,f). Truncation was taken at $\alpha_{\max} = a_{\max} = 10$.

tational efficiency over previous multi-modal models such as in McTavish and Brambley [2019]: for instance, the model and implementation in that paper took tens of minutes running a calculation with 5 spatial / 5 temporal modes, whereas here that runtime has been reduced by a factor of ten.

All of the above results, while helpful for analysis of internal duct acoustics, reveal very little about the external radiation from ducts or their resonating properties, due to the use of the simplified characteristic admittance boundary condition. In the next chapter we consider a linear semi-analytical model of the duct exit; we then generalise our unrelated weakly nonlinear duct acoustics model to include the duct exit in chapter 5, and compare the two models' results in the linear regime.

Chapter 4

Linear acoustics at a duct exit

This chapter takes a break from the multi-modal method to focus on analytical modelling of the duct exit condition in the linear regime. Instead of explicitly calculating the pressure field outside the duct (as will be done in chapter 5), we focus here on the *end-correction* problem. This is a problem in musical acoustics whereby the pressure node at the end of an open duct is not found precisely at the duct exit but rather a small distance beyond it. As a result, the length of the resonating air column differs from the physical length of the tube, and thus the instrument is out-of-tune relative to a naïve prediction of its pitch. Naturally, musical instrument designers (e.g. organ builders) are aware of this discrepancy and allow for it; however, theoretical study of the end-correction has rarely gone beyond plane waves [see, e.g. Snakowska et al., 2011, for an example with which we compare later] or dealt with nonlinearity.

After reproducing the model for the known linear plane-wave case, we carry out a derivation (borrowing heavily from Noble [1958]) of a solution to the problem of general (non-planar) linear sound radiating from a duct outlet into free space. This solution makes use of the Wiener–Hopf technique. It is analytical in 2D and semi-analytical in 3D, and provides a means of analytically determining the end-correction length in the linear regime. This work forms part of a paper [Jensen et al., 2025], recently submitted to the Journal of Fluid Mechanics.

4.1 The end correction

4.1.1 Plane wave case

If we first consider plane waves in the linear regime, the pressure within the inner duct is given by the superposition of an incident plane wave propagating towards the exit and a reflected plane wave propagating back towards the entrance with complex reflection coefficient R,

$$p = \mathrm{Re}\left[p_0\left(\mathrm{e}^{\gamma s - \mathrm{i}\omega t} - |R|\mathrm{e}^{-\gamma s - \mathrm{i}\omega t + \mathrm{i}\arg(-R)}\right)\right], \tag{4.1}$$

with $-\mathrm{i}\gamma > 0$ (since plane waves are always cut-on). Assuming that a node in the pressure occurs at some point $\hat{s}$, and taking the node to be a point where the incident and reflected waves are in phase and so maximally cancel, we get

$$\mathrm{Im}\Big[\gamma\hat{s} - \mathrm{i}\omega t\Big] = \mathrm{Im}\big[-\gamma\hat{s} - \mathrm{i}\omega t + \mathrm{i}\arg(-R)\big] \qquad \Rightarrow \qquad \hat{s} = \frac{\arg(-R)}{2\mathrm{Im}(\gamma)}. \tag{4.2}$$

4.1.2 Linear generalisation

Attempting to generalise the above for non-plane-wave duct modes, we express the pressure as an expansion in the straight duct modes at a single frequency (effectively setting $a = 1$ in the language of chapter 2):

$$p = \mathrm{Re}\left[\mathrm{e}^{-\mathrm{i}\omega t}\sum_\alpha \psi_\alpha(\mathbf{x})\left(\mathrm{e}^{\gamma_\alpha s}A_\alpha^+ + \mathrm{e}^{-\gamma_\alpha s}A_\alpha^-\right)\right], \tag{4.3}$$

where γ_α is the straight-duct eigenvalue $\overline{\gamma}_\alpha$ from section 2.2.2, given e.g. in 3D by

$$\gamma_\alpha = \begin{cases} \mathrm{i}\omega\sqrt{1-\lambda_\alpha^2/\omega^2R^2} & \mathrm{Re}(\omega) \geq \lambda_\alpha/R, \\ -\omega\sqrt{\lambda_\alpha^2/\omega^2R^2 - 1} & \mathrm{Re}(\omega) < \lambda_\alpha/R, \end{cases} \tag{4.4}$$

and A_α^+ and A_α^- are vectors of constants. The reflection matrix is given (as in equation 2.155) by

$$\mathsf{R} = \left(\mathsf{Y} + \overline{\mathsf{Y}}\right)^{-1}\left(\overline{\mathsf{Y}} - \mathsf{Y}\right), \tag{4.5}$$

and maps from the forward-going pressure to the backward, i.e. $\boldsymbol{p}^- = \mathsf{R}\boldsymbol{p}^+$ (its equivalence to the splitting operators that we normally use was shown in section 2.2.3: for end-correction modelling it proves a more important quantity, so we work in terms of it in this chapter and the next). From the definition of the reflection matrix at the duct outlet, we may write the reflected waves in terms of the outgoing waves,

$$A_\alpha^-\mathrm{e}^{-\gamma_\alpha s_\mathrm{o}} = P_\alpha^-(s_\mathrm{o}) = \sum_\beta \mathsf{R}_{\alpha\beta}(s_\mathrm{o})A_\beta^+\mathrm{e}^{\gamma_\beta s_\mathrm{o}}. \tag{4.6}$$

Writing $\hat{s} = s - s_\mathrm{o}$, and factoring out the A_β^+ vector, we have an expression equivalent to (4.1),

$$p = \mathrm{Re}\left[\mathrm{e}^{-\mathrm{i}\omega t}\sum_{\alpha,\beta}\psi_\alpha(\mathbf{x})\left(\mathrm{e}^{\gamma_\alpha\hat{s}}\delta_{\alpha\beta} - |\mathsf{R}_{\alpha\beta}(s_\mathrm{o})|\mathrm{e}^{-\gamma_\alpha\hat{s}+\mathrm{i}\arg(-\mathsf{R}_{\alpha\beta}(s_\mathrm{o}))}\right)A_\beta^+\mathrm{e}^{\gamma_\beta s_\mathrm{o}}\right]; \tag{4.7}$$

since we do not have a sensible definition of the end correction for cut-off waves, we restrict ourselves to the cut-on case. Further to this, because we are comparing the arguments of entries in the reflection matrix to those of the matrix $\mathrm{e}^{2\gamma_\alpha\hat{s}}\delta_{\alpha\beta}$, which is diagonal, we correspondingly only consider the reflection matrix's diagonal entries. This results in a different end correction $\hat{s}_\alpha$ for each mode α that is cut-on (with $\mathrm{Im}(\gamma_\alpha) \neq 0$), given by

$$\hat{s}_\alpha = \frac{\arg(-\mathsf{R}_{\alpha\alpha}(s_{\mathrm{o}}))}{2\mathrm{Im}(\gamma_\alpha)}. \tag{4.8}$$

4.2 The end correction calculated using the Wiener–Hopf technique

We now present a derivation (borrowing heavily from Noble [1958]) of a solution to the problem of linear sound radiating from a duct outlet into free space. The solution is analytical in 2D and semi-analytical in 3D, and provides a helpful comparison for use in section 5.3.1.

4.2.1 Wiener–Hopf technique in 2D

Here we consider the case of a semi-infinite waveguide in $s < 0$ with walls at $x = \pm X/2$ containing an incident wave consisting of multiple duct modes, opening into free space at $s = 0$. We impose a forward-going pressure

$$p^+(s,x,t) = \mathrm{Re}\left[\sum_{\alpha=0}^{\infty} \psi_\alpha(x) A_\alpha^+ \exp\{-\mathrm{i}\omega t + \gamma_\alpha s\}\right], \tag{4.9}$$

with $\psi_\alpha(x) = (C_\alpha/\sqrt{X})\cos\left(\lambda_\alpha\left[\frac{x}{X}+\frac{1}{2}\right]\right)$, where

$$\lambda_\alpha = \alpha\pi, \quad C_\alpha = \sqrt{2-\delta_{\alpha 0}}, \quad \text{and} \quad \gamma_\alpha = \begin{cases} \mathrm{i}\omega\sqrt{1-\lambda_\alpha^2/\omega^2X^2}, & \mathrm{Re}(\omega) \geq \lambda_\alpha/X, \\ -\omega\sqrt{\lambda_\alpha^2/\omega^2X^2-1}, & \mathrm{Re}(\omega) < \lambda_\alpha/X. \end{cases} \tag{4.10}$$

These are the 2D spatial modes ψ_α and straight-duct eigenvalues $\overline{\gamma}_\alpha$ (with the overline dropped here for clarity). The standard boundary condition introduced in chapter 2 and used throughout chapters 3 and 5 is $A_\alpha^+ = \mathrm{i}M\sqrt{X}\delta_{\alpha 0}$, i.e. a piston condition of $p^+ = M\sin\omega t$ at $s = 0$ in the inner duct; equation (4.9) is a generalisation. We take ω to have a small positive imaginary part: this ensures that γ_α always has a negative real part, meaning that a later Fourier transform will converge.

We can express the equivalent coefficient of the *total* pressure within the duct in terms of the reflection matrix $\mathsf{R}_{\alpha\beta}(s)$

$$\begin{aligned} p &= \mathrm{Re}\left[\mathrm{e}^{-\mathrm{i}\omega t}\sum_\alpha \psi_\alpha(x)\left(A_\alpha^+\mathrm{e}^{\gamma_\alpha s} + \sum_\beta \mathsf{R}_{\alpha\beta}(s)A_\beta^+\mathrm{e}^{\gamma_\beta s}\right)\right] \\ &= \mathrm{Re}\left[\mathrm{e}^{-\mathrm{i}\omega t}\sum_{\alpha,\beta}\psi_\alpha(x)\left(\delta_{\alpha\beta}\mathrm{e}^{\gamma_\alpha s} + \left\{\mathsf{R}_{\alpha\beta}(s)\mathrm{e}^{[\gamma_\alpha+\gamma_\beta]s}\right\}\mathrm{e}^{-\gamma_\alpha s}\right)A_\beta^+\right], \end{aligned} \tag{4.11}$$

where we have rearranged in the manner of equation (4.1). Since this is a linear problem, we may omit taking the real part and the common $\mathrm{e}^{-\mathrm{i}\omega t}$ factor in what follows (this is equivalent to working in terms of the $a = 1$ Fourier coefficient P^1, whose superscript we drop for simplicity). We then apply the Wiener–Hopf technique in order to calculate the reflection matrix. In the language of this method, we say that we have an *incident* Fourier pressure coefficient given by

$$P_{\mathrm{inc}} = \begin{cases} \frac{1}{2}\sum_\alpha \psi_\alpha(x) A_\alpha^+ \mathrm{e}^{\gamma_\alpha s} & |x| < \frac{X}{2}, \\ 0 & |x| > \frac{X}{2}. \end{cases} \tag{4.12}$$

The total pressure $P = P_{\mathrm{inc}} + P_{\mathrm{ref}}$ (where P_{ref} is the *reflected* pressure) must satisfy the Helmholtz equation

$$\frac{\partial^2 P}{\partial s^2} + \frac{\partial^2 P}{\partial x^2} + \omega^2 P = 0, \tag{4.13}$$

and be continuous everywhere except at the duct walls, where it must satisfy a Neumann condition. Applying the linearity of these conditions and considering the boundary behaviour of P_{inc}, we then have the following system for P_{ref}

$$\left[\frac{\partial^2}{\partial s^2} + \frac{\partial^2}{\partial x^2} + \omega^2\right] P_{\mathrm{ref}} = 0, \tag{4.14a}$$

$$\begin{cases} \left.\dfrac{\partial P_{\mathrm{ref}}}{\partial x}\right|_{x=\pm X/2} = 0 & s < 0, \\ \Big[P_{\mathrm{ref}}\Big]_{x=(\pm X/2)^\mp}^{(\pm X/2)^\pm} = \dfrac{1}{2\sqrt{X}} \sum_\alpha C_\alpha (\mp 1)^\alpha A_\alpha^+ \mathrm{e}^{\gamma_\alpha s} \quad \left[\dfrac{\partial P_{\mathrm{ref}}}{\partial x}\right]_{x=(\pm X/2)^\mp}^{(\pm X/2)^\pm} = 0 & s > 0. \end{cases} \tag{4.14b}$$

We then take a Fourier transform $s \mapsto \sigma$. The wave equation transforms to

$$\frac{\partial^2 \hat{P}_{\mathrm{ref}}}{\partial x^2} - (\sigma^2 - \omega^2)\hat{P}_{\mathrm{ref}} = 0, \tag{4.15}$$

meaning that, defining $\mu(\sigma) := \sqrt{\sigma^2 - \omega^2}$ with branch cuts chosen such that $\mathrm{Re}(\mu) > 0$, we must have

$$\hat{P}_{\mathrm{ref}} = \begin{cases} B(\sigma)\exp(-\mu(\sigma)x) & x > X/2, \\ C(\sigma)\cosh(\mu(\sigma)x) + D(\sigma)\sinh(\mu(\sigma)x) & x \in [-X/2, X/2], \\ E(\sigma)\exp(\mu(\sigma)x) & x < -X/2, \end{cases} \tag{4.16}$$

since the system is symmetric in x and waves at infinity may only be outgoing. The Fourier transform is then split as follows

$$\hat{P}_{\mathrm{ref}}(\sigma, x) = \hat{P}^-_{\mathrm{ref}}(\sigma, x) + \hat{P}^+_{\mathrm{ref}}(\sigma, x) = \int_{s=-\infty}^{0} P_{\mathrm{ref}}(s, x)\ \mathrm{e}^{\mathrm{i}\sigma s}\mathrm{d}s + \int_{s=0}^{\infty} P_{\mathrm{ref}}(s, x)\ \mathrm{e}^{\mathrm{i}\sigma s}\mathrm{d}s, \tag{4.17}$$

and the boundary conditions become (taking a Fourier transform of the discontinuity in P_{ref} outside of the duct, with the small positive imaginary part of ω ensuring that γ_α always has a negative real part, so the first condition on $\hat{P}^+_{\mathrm{ref}}$ converges)

$$\left.\frac{\partial \hat{P}^-_{\mathrm{ref}}}{\partial x}\right|_{x=\pm\frac{X}{2}} = 0, \quad \left[\hat{P}^+_{\mathrm{ref}}\right]^{\left(\pm\frac{X}{2}\right)^\pm}_{x=\left(\pm\frac{X}{2}\right)^\mp} = \frac{\mathrm{i}}{2\sqrt{X}}\sum_\alpha \frac{C_\alpha(\mp 1)^\alpha A^+_\alpha}{\sigma - \mathrm{i}\gamma_\alpha} \quad \text{and} \quad \left[\frac{\partial \hat{P}^+_{\mathrm{ref}}}{\partial x}\right]^{\left(\pm\frac{X}{2}\right)^\pm}_{x=\left(\pm\frac{X}{2}\right)^\mp} = 0. \tag{4.18}$$

Between these conditions, the derivative must always be continuous at the boundary between the inner and outer domains; applying the continuous derivative condition to eliminate constants, we get

$$\hat{P}_{\mathrm{ref}} = \begin{cases} \left[\tilde{C}(\sigma)\sinh\left(\frac{\mu X}{2}\right) + \operatorname{sgn}(x)\tilde{D}(\sigma)\cosh\left(\frac{\mu X}{2}\right)\right]\exp(-\mu|x|) & |x| > \frac{X}{2}, \\ -\exp\left(-\frac{\mu X}{2}\right)\left[\tilde{C}(\sigma)\cosh(\mu x) + \tilde{D}(\sigma)\sinh(\mu x)\right] & |x| < \frac{X}{2}. \end{cases} \tag{4.19}$$

This results in

$$\tilde{C}(\sigma) \pm \tilde{D}(\sigma) = \left[\hat{P}_{\mathrm{ref}}\right]^{\left(\pm\frac{X}{2}\right)^\pm}_{x=\left(\pm\frac{X}{2}\right)^\mp} = \frac{\mathrm{i}}{2\sqrt{X}}\sum_\alpha \frac{C_\alpha(\mp 1)^\alpha A^+_\alpha}{\sigma - \mathrm{i}\gamma_\alpha} + \left[\hat{P}^-_{\mathrm{ref}}\right]^{\left(\pm\frac{X}{2}\right)^\pm}_{x=\left(\pm\frac{X}{2}\right)^\mp}. \tag{4.20}$$

The Neumann condition reduces to

$$\begin{aligned} \left.\frac{\partial \hat{P}^+_{\mathrm{ref}}}{\partial x}\right|_{x=\pm\frac{X}{2}} &= \left.\frac{\partial \hat{P}_{\mathrm{ref}}}{\partial x}\right|_{x=\pm\frac{X}{2}} \\ &= -\mu(\sigma)\mathrm{e}^{-\frac{\mu(\sigma)X}{2}}\left[\pm\tilde{C}(\sigma)\sinh\left(\frac{\mu(\sigma)X}{2}\right) + \tilde{D}(\sigma)\cosh\left(\frac{\mu(\sigma)X}{2}\right)\right] \qquad (4.21) \\ &=: \mp\mu(\sigma)^2 X\tilde{C}(\sigma)L(\sigma) - \mu(\sigma)\tilde{D}(\sigma)K(\sigma), \qquad (4.22) \end{aligned}$$

where $L(\sigma)$ and $K(\sigma)$ are defined [equivalently to their definitions in Noble, 1958] for notational ease later on. Eliminating $\tilde{C}(\sigma)$ and $\tilde{D}(\sigma)$ yields symmetric and antisymmetric Wiener–Hopf equations

$$\frac{\frac{\partial \hat{P}^+_{\mathrm{ref}}}{\partial x}\left(\Big|_{x=\frac{X}{2}} - \Big|_{x=-\frac{X}{2}}\right)}{\mu(\sigma)^2 X L(\sigma)} + \left[\hat{P}^-_{\mathrm{ref}}\right]\left(\Big|^{\left(\frac{X}{2}\right)^+}_{x=\left(\frac{X}{2}\right)^-} + \Big|^{\left(-\frac{X}{2}\right)^+}_{x=\left(-\frac{X}{2}\right)^+}\right) = -\frac{\mathrm{i}}{\sqrt{X}}\sum_{\alpha\ \text{even}} \frac{C_\alpha A^+_\alpha}{\sigma - \mathrm{i}\gamma_\alpha}, \tag{4.23a}$$

$$\frac{\frac{\partial \hat{P}^+_{\mathrm{ref}}}{\partial x}\left(\Big|_{x=\frac{X}{2}} + \Big|_{x=-\frac{X}{2}}\right)}{\mu(\sigma) K(\sigma)} + \left[\hat{P}^-_{\mathrm{ref}}\right]\left(\Big|^{\left(\frac{X}{2}\right)^+}_{x=\left(\frac{X}{2}\right)^-} - \Big|^{\left(-\frac{X}{2}\right)^+}_{x=\left(-\frac{X}{2}\right)^+}\right) = -\frac{\mathrm{i}}{\sqrt{X}}\sum_{\alpha\ \text{odd}} \frac{C_\alpha A^+_\alpha}{\sigma - \mathrm{i}\gamma_\alpha}x. \tag{4.23b}$$

If we can multiplicatively decompose (i.e. factorise) $L(\sigma)$ and $K(\sigma)$ into two functions each, two which are analytic in the upper-half plane ($L^+(\sigma)$, $K^+(\sigma)$) and another two which are analytic in the lower-half plane ($L^-(\sigma)$, $K^-(\sigma)$), then we can arrange the Wiener–Hopf equations as

$$\begin{aligned}
&\frac{\frac{\partial \hat{P}^+_{\text{ref}}}{\partial x}\left(\big|_{x=\frac{X}{2}} - \big|_{x=-\frac{X}{2}}\right)}{(\sigma+\omega)XL^+(\sigma)} + \frac{\mathrm{i}}{\sqrt{X}}\sum_{\alpha\text{ even}} \frac{C_\alpha A^+_\alpha(\mathrm{i}\gamma_\alpha - \omega)L^-(\mathrm{i}\gamma_\alpha)}{\sigma - \mathrm{i}\gamma_\alpha} \\
&\qquad = -(\sigma-\omega)L^-(\sigma)\left[\hat{P}^-_{\text{ref}}\right]\left(\big|^{\left(\frac{X}{2}\right)^+}_{x=\left(\frac{X}{2}\right)^-} + \big|^{\left(-\frac{X}{2}\right)^+}_{x=\left(-\frac{X}{2}\right)^+}\right) \\
&\qquad\quad - \frac{\mathrm{i}}{\sqrt{X}}\sum_{\alpha\text{ even}} \frac{C_\alpha A^+_\alpha\Big((\sigma-\omega)L^-(\sigma) - (\mathrm{i}\gamma_\alpha - \omega)L^-(\mathrm{i}\gamma_\alpha)\Big)}{\sigma - \mathrm{i}\gamma_\alpha},
\end{aligned} \tag{4.24a}$$

$$\begin{aligned}
&\frac{\frac{\partial \hat{P}^+_{\text{ref}}}{\partial x}\left(\big|_{x=\frac{X}{2}} + \big|_{x=-\frac{X}{2}}\right)}{\sqrt{\sigma+\omega}K^+(\sigma)} - \frac{\mathrm{i}}{\sqrt{X}}\sum_{\alpha\text{ odd}} \frac{C_\alpha A^+_\alpha\sqrt{\mathrm{i}\gamma_\alpha - \omega}K^-(\mathrm{i}\gamma_\alpha)}{\sigma - \mathrm{i}\gamma_\alpha} \\
&\qquad = -\sqrt{\sigma-\omega}K^-(\sigma)\left[\hat{P}^-_{\text{ref}}\right]\left(\big|^{\left(\frac{X}{2}\right)^+}_{x=\left(\frac{X}{2}\right)^-} - \big|^{\left(-\frac{X}{2}\right)^+}_{x=\left(-\frac{X}{2}\right)^+}\right) \\
&\qquad\quad + \frac{\mathrm{i}}{\sqrt{X}}\sum_{\alpha\text{ odd}} \frac{C_\alpha A^+_\alpha\Big(\sqrt{\sigma-\omega}K^-(\sigma) - \sqrt{\mathrm{i}\gamma_\alpha - \omega}K^-(\mathrm{i}\gamma_\alpha)\Big)}{\sigma - \mathrm{i}\gamma_\alpha}.
\end{aligned} \tag{4.24b}$$

In each case, the left-hand side is analytic in the upper-half plane and the right-hand side is analytic in the lower-half plane. Therefore, both sides are analytic everywhere, and so we follow Noble [1958] in setting them to zero (corresponding physically to a choice of the smoothest possible solution at the scattering point, i.e. the outlet corners). As such, we determine $\tilde{C}(\sigma)$ and $\tilde{D}(\sigma)$ to be

$$\tilde{C}(\sigma) = \frac{\mathrm{i}\exp\left(\frac{\mu(\sigma)X}{2}\right)(\sigma+\omega)L^+(\sigma)}{4\sqrt{X}\mu(\sigma)\sinh\left(\frac{\mu(\sigma)X}{2}\right)}\sum_{\alpha\text{ even}}\frac{C_\alpha A^+_\alpha(\mathrm{i}\gamma_\alpha-\omega)L^-(\mathrm{i}\gamma_\alpha)}{\sigma-\mathrm{i}\gamma_\alpha}, \tag{4.25a}$$

$$\tilde{D}(\sigma) = -\frac{\mathrm{i}\exp\left(\frac{\mu(\sigma)X}{2}\right)\sqrt{\sigma+\omega}K^+(\sigma)}{2\sqrt{X}\mu(\sigma)\cosh\left(\frac{\mu(\sigma)X}{2}\right)}\sum_{\alpha\text{ odd}}\frac{C_\alpha A^+_\alpha\sqrt{\mathrm{i}\gamma_\alpha-\omega}K^-(\mathrm{i}\gamma_\alpha)}{\sigma-\mathrm{i}\gamma_\alpha}. \tag{4.25b}$$

Substituting these formulae into the expression for $\hat{P}_{\mathrm{ref}}$ and inverting, we find

$$P_{\mathrm{ref}} = \begin{cases} \dfrac{\mathrm{i}}{4\pi\sqrt{X}} \displaystyle\int_{\sigma=-\infty}^{\infty} \frac{\mathrm{e}^{-\mu(\sigma)\left(|x|-\frac{X}{2}\right)-\mathrm{i}\sigma s}}{\mu(\sigma)} \Bigg[\sum_{\alpha \text{ even}} \frac{C_\alpha A_\alpha^+ (\sigma+\omega)(\mathrm{i}\gamma_\alpha-\omega) X L^+(\sigma) L^-(\mathrm{i}\gamma_\alpha)}{2(\sigma-\mathrm{i}\gamma_\alpha)} \\ \qquad -\operatorname{sgn}(x) \displaystyle\sum_{\alpha \text{ odd}} \frac{C_\alpha A_\alpha^+ \sqrt{(\sigma+\omega)(\mathrm{i}\gamma_\alpha-\omega)} K^+(\sigma) K^-(\mathrm{i}\gamma_\alpha)}{\sigma-\mathrm{i}\gamma_\alpha} \Bigg] \mathrm{d}\sigma \qquad |x| > \dfrac{X}{2}, \\ \\ \dfrac{\mathrm{i}}{4\pi\sqrt{X}} \displaystyle\int_{\sigma=-\infty}^{\infty} \mathrm{e}^{-\mathrm{i}\sigma s} \Bigg[-\sum_{\alpha \text{ even}} \frac{C_\alpha A_\alpha^+ (\sigma+\omega)(\mathrm{i}\gamma_\alpha-\omega) X L^+(\sigma) L^-(\mathrm{i}\gamma_\alpha) \cosh(\mu(\sigma)x)}{2(\sigma-\mathrm{i}\gamma_\alpha)\mu(\sigma)\sinh\left(\frac{\mu(\sigma)X}{2}\right)} \\ \qquad + \displaystyle\sum_{\alpha \text{ odd}} \frac{C_\alpha A_\alpha^+ \sqrt{(\sigma+\omega)(\mathrm{i}\gamma_\alpha-\omega)} K^+(\sigma) K^-(\mathrm{i}\gamma_\alpha) \frac{\sinh \mu(\sigma)x}{\mu(\sigma)}}{(\sigma-\mathrm{i}\gamma_\alpha)\cosh\left(\frac{\mu(\sigma)X}{2}\right)} \Bigg] \mathrm{d}\sigma \qquad |x| < \dfrac{X}{2}. \end{cases} \tag{4.26}$$

In order to calculate these integrals, the contour of integration can be deformed either into the lower or upper-half plane, depending on the sign of s. There are two possible signs of $|x| - X/2$, each with two possible signs of s, so altogether there are four cases.

We know that $L^+(\sigma)$ and $K^+(\sigma)$ are analytic in the upper-half plane. In the lower-half plane they must contain all of the singularities of $L(\sigma)$ and $K(\sigma)$, i.e. a branch cut downward from $\sigma = -\omega$. For $|x| > X/2$, we have a branch cut in the upper-half-plane anyway due to the factors of μ, meaning that this integral will be deformed around a branch cut for both $s > 0$ and $s < 0$ (cases 1 and 2). For $|x| < X/2$ and $s > 0$, the integral may only be deformed into the lower-half plane, where there is a branch cut (case 3). However, for $|x| < X/2$ and $s < 0$, because the series expansion of the integrand contains only μ^2 (not μ), and L^+ and K^+ are analytic in the upper-half plane, we can deform upwards and encounter only poles, whose residues become duct modes (case 4, corresponding to the duct interior). This has the following result

$$\begin{aligned} P_{\mathrm{ref}} = -\frac{1}{2X} \Bigg(& \sum_{\substack{\alpha \text{ even}, \\ \beta \text{ even}}} \frac{C_\alpha A_\alpha^+ \mathrm{e}^{-\gamma_\beta s} L^+(-\mathrm{i}\gamma_\beta) L^-(\mathrm{i}\gamma_\alpha) C_\beta \psi_\beta(x)}{(\gamma_\alpha+\gamma_\beta)\gamma_\beta} \\ & + \sum_{\substack{\alpha \text{ odd}, \\ \beta \text{ odd}}} \frac{C_\alpha A_\alpha^+ \mathrm{e}^{-\gamma_\beta s} K^+(-\mathrm{i}\gamma_\beta) K^-(\mathrm{i}\gamma_\alpha) C_\beta \psi_\beta(x)}{(\gamma_\alpha+\gamma_\beta)\gamma_\beta} \Bigg). \end{aligned} \tag{4.27}$$

This is substituted into the total pressure with the α and β labels flipped, and upon comparison with equation (4.11) we get the following expression

$$
\mathsf{R}_{\alpha\beta}(s) = \begin{cases} -\dfrac{C_\alpha C_\beta L^+(-\mathrm{i}\gamma_\alpha)L^-(\mathrm{i}\gamma_\beta)(\gamma_0+\gamma_\alpha)(\gamma_0+\gamma_\beta)}{2\gamma_\alpha(\gamma_\alpha+\gamma_\beta)X\mathrm{e}^{(\gamma_\alpha+\gamma_\beta)s}} & \alpha \text{ even, } \beta \text{ even,} \\ -\dfrac{C_\alpha C_\beta K^+(-\mathrm{i}\gamma_\alpha)K^-(\mathrm{i}\gamma_\beta)\sqrt{-\mathrm{i}(\gamma_0+\gamma_\alpha)}\sqrt{\mathrm{i}(\gamma_0+\gamma_\beta)}}{\gamma_\alpha(\gamma_\alpha+\gamma_\beta)X\mathrm{e}^{(\gamma_\alpha+\gamma_\beta)s}} & \alpha \text{ odd, } \beta \text{ odd,} \\ 0 & \text{otherwise,} \end{cases} \tag{4.28}
$$

so then

$$
\mathsf{R}_{\alpha\alpha}(0) = \begin{cases} -\dfrac{C_\alpha^2 L^+(-\mathrm{i}\gamma_\alpha)L^-(\mathrm{i}\gamma_\alpha)(\gamma_0+\gamma_\alpha)^2}{4(\gamma_\alpha)^2X} & \alpha \text{ even,} \\ -\dfrac{\mathrm{i}C_\alpha^2 K^+(-\mathrm{i}\gamma_\alpha)K^-(\mathrm{i}\gamma_\alpha)|\gamma_0+\gamma_\alpha|}{2(\gamma_\alpha)^2X} & \alpha \text{ odd.} \end{cases} \tag{4.29}
$$

Further analytical expressions

A more precise expression may be found for the reflection matrix: for particular ranges of ω, this can lead to elegant closed-form expressions for the end correction itself. From Noble [1958], we have analytical expressions for L^+ and K^+ as follows

$$
\begin{aligned} \left\{\begin{matrix} L^+(\sigma) \\ K^+(\sigma) \end{matrix}\right\} &= \exp\left(\frac{\mathrm{i}\sigma X}{2\pi}\left(1 - C + \log\frac{\{4,1\}\pi}{\omega X}\right) - \frac{\sigma X}{4} - \frac{\mu(\sigma)X}{2\pi}\cos^{-1}\frac{\sigma}{\omega}\right) \\ &\times \prod_{\beta>0,\{\text{even,odd}\}}^{\infty} \left(\frac{X}{\beta\pi}\right)(-\gamma_\beta - \mathrm{i}\sigma)\exp\left(\frac{\mathrm{i}\sigma X}{\beta\pi}\right), \end{aligned} \tag{4.30}
$$

with $L^-(\sigma) = L^+(-\sigma)$ and $K^-(\sigma) = K^+(-\sigma)$, and C being the Euler-Mascheroni constant. We then have

$$
\arg\left(-\mathsf{R}_{\alpha\alpha}(0)\right) = \begin{cases} \arg(L^+(-\mathrm{i}\gamma_\alpha))^2 & \alpha \text{ even,} \\ \arg(K^+(-\mathrm{i}\gamma_\alpha))^2 - \frac{\pi}{2} & \alpha \text{ odd.} \end{cases} \tag{4.31}
$$

$(L^+(-\mathrm{i}\gamma_\alpha))^2$ may be written in a way that makes taking the argument easier, i.e.

$$
\begin{aligned} (L^+(-\mathrm{i}\gamma_\alpha))^2 &= \exp\left(\frac{\mathrm{i}|\gamma_\alpha|X}{\pi}\left(1 - C + \log\frac{4\pi}{\omega X}\right) - \frac{|\gamma_\alpha|X}{2} - \mathrm{i}\alpha\cos^{-1}\frac{|\gamma_\alpha|}{\omega}\right) \\ &\times \prod_{\substack{\beta>0,\\ \text{even}}}^{2\lfloor\frac{\omega X}{2\pi}\rfloor} \left\{\left(\frac{X}{\beta\pi}\right)^2 \mathrm{e}^{-\mathrm{i}\pi}\,(|\gamma_\beta| + |\gamma_\alpha|)^2\exp\left(\frac{2\mathrm{i}|\gamma_\alpha X}{\beta\pi}\right)\right\} \\ &\times \prod_{\substack{\beta>2\lfloor\frac{\omega X}{2\pi}\rfloor,\\ \text{even}}}^{\infty} \left\{\left(\frac{X}{\beta\pi}\right)^2 (|\gamma_\beta| - \mathrm{i}|\gamma_\alpha|)^2\exp\left(\frac{2\mathrm{i}|\gamma_\alpha X}{\beta\pi}\right)\right\}, \end{aligned} \tag{4.32}
$$

so that after a bit of manipulation we find the expression for even modes to be

$$\begin{aligned}\arg(-\mathsf{R}_{\alpha\alpha}(0)) = \frac{|\gamma_\alpha|X}{\pi}\Bigg\{&1 - C + \log\frac{4\pi}{\omega X} + H_{\lfloor \omega X/2\pi\rfloor}\\ &+ \sum_{n=\lfloor \omega X/2\pi\rfloor+1}^{\infty}\left[\frac{1}{n} - \frac{2\pi}{|\gamma_\alpha|X}\tan^{-1}\frac{|\gamma_\alpha|X}{2\pi n\sqrt{1-\frac{\omega^2X^2}{4n^2\pi^2}}}\right]\Bigg\}\\ &- \alpha\left(\frac{\pi}{2} - \cos^{-1}\frac{|\gamma_\alpha|}{\omega}\right) - \pi\left(\left\lfloor\frac{\omega X}{2\pi}\right\rfloor - \frac{\alpha}{2}\right).\end{aligned} \tag{4.33}$$

Doing the same for odd modes, we get

$$\begin{aligned}\arg(-\mathsf{R}_{\alpha\alpha}(0)) = \frac{|\gamma_\alpha|X}{\pi}\Bigg\{&1 - C + \log\frac{\pi}{\omega X} + 2H_{2\lfloor \omega X/2\pi+1/2\rfloor} - H_{\lfloor \omega X/2\pi+1/2\rfloor}\\ &+ \sum_{n=\lfloor \omega X/2\pi+1/2\rfloor+1}\left[\frac{1}{n-\frac{1}{2}} - \frac{2\pi}{|\gamma_\alpha|X}\tan^{-1}\frac{|\gamma_\alpha|X}{2(n-\frac{1}{2})\pi\sqrt{1-\frac{\omega^2X^2}{4(n-1/2)^2X^2}}}\right]\Bigg\}\\ &- \alpha\left(\frac{\pi}{2} - \cos^{-1}\frac{|\gamma_\alpha|}{\omega}\right) - \pi\left(\left\lfloor\frac{\omega X}{2\pi}+\frac{1}{2}\right\rfloor - \frac{\alpha+1}{2}\right),\end{aligned} \tag{4.34}$$

where H_n is the n^{th} harmonic number. For $\omega \in (\overline{\omega}_\alpha, \overline{\omega}_{\alpha+2})$, if α is even we have

$$\begin{aligned}\frac{\hat{s}_\alpha}{X} = \frac{1}{2\pi}\Bigg\{&1 - C + \log\frac{4\pi}{\omega X} + H_{\alpha/2} + \sum_{n=\alpha/2+1}^{\infty}\left[\frac{1}{n} - \frac{2\pi}{|\gamma_\alpha|X}\tan^{-1}\frac{|\gamma_\alpha|X}{2\pi n\sqrt{1-\frac{\omega^2X^2}{4n^2\pi^2}}}\right]\Bigg\}\\ &- \frac{\alpha}{2|\gamma_\alpha|X}\left(\frac{\pi}{2} - \cos^{-1}\frac{|\gamma_\alpha|}{\omega}\right),\end{aligned} \tag{4.35}$$

and if α is odd we have

$$\begin{aligned}\frac{\hat{s}_\alpha}{X} = \frac{1}{2\pi}\Bigg\{&1 - C + \log\frac{\pi}{\omega X} + 2H_{\alpha+1} - H_{(\alpha+1)/2}\\ &+ \sum_{n=(\alpha+1)/2+1}\left[\frac{1}{n-\frac{1}{2}} - \frac{2\pi}{|\gamma_\alpha|X}\tan^{-1}\frac{|\gamma_\alpha|X}{2(n-\frac{1}{2})\pi\sqrt{1-\frac{\omega^2X^2}{4(n-1/2)^2X^2}}}\right]\Bigg\}\\ &- \frac{\alpha}{2|\gamma_\alpha|X}\left(\frac{\pi}{2} - \cos^{-1}\frac{|\gamma_\alpha|}{\omega}\right),\end{aligned} \tag{4.36}$$

and in particular if $\omega < \overline{\omega}_1$, we can use $\sin^{-1}(z) = \tan^{-1}(z/\sqrt{1-z^2})$ to get

$$\frac{\hat{s}_0}{X} = \frac{1}{2\pi}\left\{1 - C + \log\frac{4\pi}{\omega X} + \sum_{n=1}^{\infty}\left[\frac{1}{n} - \frac{2\pi}{\omega X}\sin^{-1}\frac{\omega X}{2\pi n}\right]\right\}, \tag{4.37}$$

as derived in Noble [1958]. Note that this gives a logarithmic singularity as $\omega X \to 0$, but that $\hat{s}_0 \sim X \log \frac{1}{X}$ as $X \to 0$: this means the end correction *does* tend to zero, just sublinearly with duct width.

4.2.2 Wiener–Hopf technique in 3D

In order to prescribe an incident pressure of the same form as in 2D, we set our incident pressure to be

$$P_{\text{inc}} = \begin{cases} \frac{1}{2}\sum_\alpha \psi_\alpha(r,\theta) A_\alpha^+ \exp(\gamma_\alpha s) & r < R, \\ 0 & r > R. \end{cases} \tag{4.38}$$

The spatial modes in 3D are $\psi_\alpha(r,\theta) = (C_\alpha/\sqrt{\pi}R)\mathrm{J}_{p_\alpha}(\lambda_\alpha r/R)\cos(p_\alpha\theta - \xi_\alpha\pi/2)$, where modenumbers, constants and eigenvalues are defined by

$$\lambda_\alpha = j_{p_\alpha q_\alpha}, \qquad C_\alpha = \begin{cases} \left|\mathrm{J}_0(\lambda_\alpha)\right|^{-1}, & p_\alpha = 0, \\ \left(\sqrt{\frac{1}{2}\left[1 - \frac{{p_\alpha}^2}{{\lambda_\alpha}^2}\right]}\left|\mathrm{J}_{p_\alpha}(\lambda_\alpha)\right|\right)^{-1}, & p_\alpha \neq 0, \end{cases} \tag{4.39a}$$

$$\xi_\alpha \in \{0,1\} \qquad \text{and} \qquad \gamma_\alpha = \begin{cases} \mathrm{i}\omega\sqrt{1 - \lambda_\alpha^2/\omega^2R^2}, & \mathrm{Re}(\omega) \geq \lambda_\alpha/R, \\ -\omega\sqrt{\lambda_\alpha^2/\omega^2R^2 - 1}, & \mathrm{Re}(\omega) < \lambda_\alpha/R, \end{cases} \tag{4.39b}$$

where $j'_{p_\alpha q_\alpha}$ is the q_α-th zero of the Bessel function of order p_α. Once again, taking $A_\alpha^+ = \mathrm{i}M\sqrt{\pi}R\delta_{\alpha 0}$ results in a piston condition of $p^+ = M\sin\omega t$ at $s = 0$ in the inner duct. Taking a Fourier transform and solving the Helmholtz equation results in a solution for the reflected pressure (dropping the superscript once more)

$$\hat{P}_{\text{ref}} = \begin{cases} \sum_{p=0}^\infty \mathrm{I}_p(\mu(\sigma)r)\left[A_p(\sigma)\cos p\theta + B_p(\sigma)\sin p\theta\right] & r < R, \\ \sum_{p=0}^\infty \mathrm{K}_p(\mu(\sigma)r)\left[C_p(\sigma)\cos p\theta + D_p(\sigma)\sin p\theta\right] & r > R, \end{cases} \tag{4.40}$$

where again we have $\mu^2 := \sigma^2 - \omega^2$. In writing down this solution, we have already applied the conditions of periodicity in θ, regularity at $r = 0$ and decay in the far field. Defining the split Fourier transform as before, we then have duct wall and continuity conditions

$$\begin{cases} \left.\dfrac{\partial \hat{P}_{\text{ref}}^-}{\partial r}\right|_{r=R} = 0, \\ \left[\hat{P}_{\text{ref}}^+\right]_{R^-}^{R^+} = \dfrac{\mathrm{i}}{2\sqrt{\pi}R}\displaystyle\sum_\alpha \dfrac{C_\alpha \mathrm{J}_{p_\alpha}(\lambda_\alpha)\cos\left(p_\alpha\theta - \frac{\xi_\alpha\pi}{2}\right)A_\alpha^+}{\sigma - \mathrm{i}\gamma_\alpha}, \quad \left[\dfrac{\partial \hat{P}_{\text{ref}}^+}{\partial r}\right]_{R^-}^{R^+} = 0. \end{cases} \tag{4.41}$$

Applying the continuous derivative condition reduces the number of constants to two, giving

$$\hat{P}_{\mathrm{ref}} = \begin{cases} \displaystyle\sum_{p=0}^{\infty} \frac{\mathrm{I}_p(\mu(\sigma)r)}{\mathrm{I}_p'(\mu(\sigma)R)} \left[\widetilde{A}_p(\sigma)\cos p\theta + \widetilde{B}_p(\sigma)\sin p\theta\right] & r < R, \\ \displaystyle\sum_{p=0}^{\infty} \frac{\mathrm{K}_p(\mu(\sigma)r)}{\mathrm{K}_p'(\mu(\sigma)R)} \left[\widetilde{A}_p(\sigma)\cos p\theta + \widetilde{B}_p(\sigma)\sin p\theta\right] & r > R. \end{cases} \tag{4.42}$$

We can apply the jump condition to this expression, getting

$$\left[\hat{P}_{\mathrm{ref}}\right]_{R^-}^{R^+} = \sum_{p=0}^{\infty} \left(\frac{\mathrm{K}_p(\mu(\sigma)R)}{\mathrm{K}_p'(\mu(\sigma)R)} - \frac{\mathrm{I}_p(\mu(\sigma)R)}{\mathrm{I}_p'(\mu(\sigma)R)} \right) \left(\widetilde{A}_p(\sigma)\cos p\theta + \widetilde{B}_p(\sigma)\sin p\theta\right), \tag{4.43}$$

where the bracketed quantity on the left may be re-expressed in terms of the Wronskian $W\left\{\mathrm{K}_p(z), \mathrm{I}_p(z)\right\} = 1/z$, i.e.

$$\begin{aligned} \frac{\mathrm{K}_p(\mu(\sigma)R)}{\mathrm{K}_p'(\mu(\sigma)R)} - \frac{\mathrm{I}_p(\mu(\sigma)R)}{\mathrm{I}_p'(\mu(\sigma)R)} &= \frac{W\left\{\mathrm{K}_p(\mu(\sigma)R), \mathrm{I}_p(\mu(\sigma)R)\right\}}{\mathrm{K}_p'(\mu(\sigma)R)\mathrm{I}_p'(\mu(\sigma)R)} \\ &= \frac{1}{\mu(\sigma)R\mathrm{K}_p'(\mu(\sigma)R)\mathrm{I}_p'(\mu(\sigma)R)} =: -\frac{2}{L_p(\sigma)}. \end{aligned} \tag{4.44}$$

Here we have defined $L_p(\sigma)$ as we did with $L(\sigma)$ and $K(\sigma)$ in the 2D case. Integrating the jump condition over a period in θ allows us to find $\widetilde{A}_p(\sigma)$ and $\widetilde{B}_p(\sigma)$

$$-\frac{2}{L_p(\sigma)} \begin{Bmatrix} \widetilde{A}_p(\sigma) \\ \widetilde{B}_p(\sigma) \end{Bmatrix} = \left[\frac{1}{\pi} \int_0^{2\pi} \left[\hat{P}_{\mathrm{ref}}^-\right]_{R^-}^{R^+} \begin{Bmatrix} \cos p\theta \\ \sin p\theta \end{Bmatrix} \mathrm{d}\theta + \frac{\mathrm{i}}{2\sqrt{\pi}R} \sum_{\substack{\alpha: p_\alpha = p, \\ \xi_\alpha = \{0,1\}}} \frac{C_\alpha \mathrm{J}_{p_\alpha}(\lambda_\alpha) A_\alpha^+}{\sigma - \mathrm{i}\gamma_\alpha} \right]. \tag{4.45}$$

The Fourier transform of the continuity condition here was previously a sum of modes, but the orthogonality of these modes has been exploited through integration over a period, hence the new limits on the sum. We may also find $\widetilde{A}_p(\sigma)$ and $\widetilde{B}_p(\sigma)$ in terms of the derivative on the boundary, by noting that we have

$$\left.\frac{\partial \hat{P}_{\mathrm{ref}}^+}{\partial r}\right|_{r=R} = \left.\frac{\partial \hat{P}_{\mathrm{ref}}}{\partial r}\right|_{r=R} = \mu(\sigma) \sum_{p=0}^{\infty} \left(\widetilde{A}_p(\sigma)\cos p\theta + \widetilde{B}_p(\sigma)\sin p\theta\right), \tag{4.46}$$

and integrating similarly. Eliminating $\widetilde{A}_p(\sigma)$ and $\widetilde{B}_p(\sigma)$ results in

$$\begin{aligned} -\frac{L_p(\sigma)}{2} \left[\frac{1}{\pi} \int_0^{2\pi} \left[\hat{P}_{\mathrm{ref}}^-\right]_{R^-}^{R^+} \begin{Bmatrix} \cos p\theta \\ \sin p\theta \end{Bmatrix} \mathrm{d}\theta + \frac{\mathrm{i}}{2\sqrt{\pi}R} \sum_{\substack{\alpha: p_\alpha = p, \\ \xi_\alpha = \{0,1\}}} \frac{C_\alpha \mathrm{J}_{p_\alpha}(\lambda_\alpha) A_\alpha^+}{\sigma - \mathrm{i}\gamma_\alpha} \right] \\ = \frac{1}{\pi\mu(\sigma)} \int_0^{2\pi} \left[\frac{\partial \hat{P}_{\mathrm{ref}}^+}{\partial r}\right]_{r=R} \begin{Bmatrix} \cos p\theta \\ \sin p\theta \end{Bmatrix} \mathrm{d}\theta. \end{aligned} \tag{4.47}$$

Taking the decomposition $L_p(\sigma) = L_p^+(\sigma)L_p^-(\sigma)$, we can write this as an equality between an UHP-analytic function and a LHP-analytic one

$$\begin{aligned}
&-\frac{2}{\pi\mu^+(\sigma)L_p^+(\sigma)}\int_0^{2\pi}\left[\frac{\partial\hat{P}^+_{\text{ref}}}{\partial r}\right]_{r=R}\begin{Bmatrix}\cos p\theta\\ \sin p\theta\end{Bmatrix}\mathrm{d}\theta\\
&\qquad\qquad -\frac{\mathrm{i}}{2\sqrt{\pi}R}\sum_{\substack{\alpha:p_\alpha=p,\\ \xi_\alpha=\{0,1\}}}\frac{C_\alpha \mathrm{J}_{p_\alpha}(\lambda_\alpha)A_\alpha^+\mu^-(\mathrm{i}\gamma_\alpha)L_p^-(\mathrm{i}\gamma_\alpha)}{\sigma-\mathrm{i}\gamma_\alpha}\\
&\quad=\frac{\mu^-(\sigma)L_p^-(\sigma)R}{\pi}\int_0^{2\pi}\left[\hat{P}^-_{\text{ref}}\right]_{R^-}^{R^+}\begin{Bmatrix}\cos p\theta\\ \sin p\theta\end{Bmatrix}\mathrm{d}\theta\\
&\qquad\qquad +\frac{\mathrm{i}}{2\sqrt{\pi}R}\sum_{\substack{\alpha:p_\alpha=p,\\ \xi_\alpha=\{0,1\}}}\frac{C_\alpha \mathrm{J}_{p_\alpha}(\lambda_\alpha)A_\alpha^+\left[\mu^-(\sigma)L_p^-(\sigma)-\mu^-(\mathrm{i}\gamma_\alpha)L_p^-(\mathrm{i}\gamma_\alpha)\right]}{\sigma-\mathrm{i}\gamma_\alpha}.
\end{aligned} \tag{4.48}$$

Assuming that both sides are equal to zero as before, we can eliminate $\left[\partial\hat{P}^+_{\text{ref}}/\partial r\right]_{r=R}$ and $\left[\hat{P}^-_{\text{ref}}\right]_{R^-}^{R^+}$ to find expressions for $\widetilde{A}_p(\sigma)$ and $\widetilde{B}_p(\sigma)$; these are substituted into $\hat{P}_{\text{ref}}$ to give an inner-duct result (in which we have turned the addition of $\widetilde{A}_p(\sigma)$ and $\widetilde{B}_p(\sigma)$ into a sum over ξ)

$$\hat{P}_{\text{ref}} = -\sum_{p=0}^{\infty}\frac{\mathrm{i}\mu^+(\sigma)L_p^+(\sigma)\mathrm{I}_p(\mu r)}{4\sqrt{\pi}R\mu(\sigma)\mathrm{I}_p'(\mu R)}\sum_{\xi=0}^{1}\sum_{\substack{\alpha:\\ p_\alpha=p,\\ \xi_\alpha=\xi}}\frac{C_\alpha \mathrm{J}_{p_\alpha}(\lambda_\alpha)A_\alpha^+\mu^-(\mathrm{i}\gamma_\alpha)L_p^-(\mathrm{i}\gamma_\alpha)\cos\left(p_\alpha\theta-\frac{\xi\pi}{2}\right)}{\sigma-\mathrm{i}\gamma_\alpha}, \tag{4.49}$$

and an outer-duct result with K_p in place of I_p. A power-series calculation verifies that only factors of μ^2 appear in the inner-duct expression for $s < 0$ (as before) so we can calculate the residue at each pole, getting

$$\begin{aligned}
\mathrm{i}\ \mathrm{res}_{\sigma=-\mathrm{i}\gamma_\beta}\hat{P}_{\text{ref}}\,\mathrm{e}^{-\mathrm{i}\sigma s} &= -\frac{\mathrm{e}^{-\gamma_\beta s}\mu^+(-\mathrm{i}\gamma_\beta)L_{p_\beta}^+(-\mathrm{i}\gamma_\beta)C_\beta \mathrm{J}_{p_\beta}(\lambda_\beta)\psi_\beta}{4(2-\delta_{p_\beta 0})\gamma_\beta}\\
&\quad\times\sum_{\xi=0}^{1}\frac{C_\beta \mathrm{J}_{p_\beta}(\lambda_\beta r/R)\cos\left(p_\beta\theta-\frac{\xi\pi}{2}\right)}{\pi R}\sum_{\substack{\alpha:\\ p_\alpha=p_\beta\\ \xi_\alpha=\xi}}\frac{C_\alpha \mathrm{J}_{p_\alpha}(\lambda_\alpha)A_\alpha^+\mu^-(\mathrm{i}\gamma_\alpha)L_{p_\beta}^-(\mathrm{i}\gamma_\alpha)}{\gamma_\alpha+\gamma_\beta},
\end{aligned} \tag{4.50}$$

where the sum over ξ accounts for the fact that modes with $p_\alpha \neq 0$ are degenerate with multiplicity 2. Since we have $P_{\text{ref}} = 2\pi\mathrm{i}\sum_\beta \mathrm{res}_{\sigma=-\mathrm{i}\gamma_\beta}\hat{P}_{\text{ref}}\mathrm{e}^{-\mathrm{i}\sigma s}/2\pi$, this results in a sum of all duct modes, which can be rephrased in the manner of equation (4.27): the reflection matrix is then calculated to be

$$\mathsf{R}_{\alpha\beta}(s) = -\frac{C_\alpha C_\beta \mathrm{J}_{p_\alpha}(\lambda_\alpha)\mathrm{J}_{p_\beta}(\lambda_\beta)\mu^+(-\mathrm{i}\gamma_\alpha)\mu^-(\mathrm{i}\gamma_\beta)L_{p_\alpha}^+(-\mathrm{i}\gamma_\alpha)L_{p_\beta}^-(\mathrm{i}\gamma_\beta)}{2(2-\delta_{p_\alpha 0})\gamma_\alpha(\gamma_\alpha+\gamma_\beta)\exp\left((\gamma_\alpha+\gamma_\beta)s\right)}\delta_{p_\alpha p_\beta}\delta_{\xi_\alpha\xi_\beta}, \tag{4.51}$$

so we have

$$\mathsf{R}_{\alpha\alpha}(0) = -\frac{\mathrm{i}C_\alpha^2 |\mathrm{J}_{p_\alpha}(\lambda_\alpha)|^2 \, |\gamma_0 + \gamma_\alpha| \, L_{p_\alpha}^+(-\mathrm{i}\gamma_\alpha) L_{p_\beta}^-(\mathrm{i}\gamma_\beta)}{4(2-\delta_{p_\alpha 0}) \, |\gamma_\alpha|^2}. \tag{4.52}$$

Multiplicative decomposition

We wish to multiplicatively decompose $L_p(\sigma)$. The form of L_p was chosen because of the asymptotic expansions

$$\mathrm{I}_p'(\mu R) \sim \frac{e^{\mu R}}{\sqrt{2\pi\mu R}} \left[1 + O\left(\frac{1}{\mu R}\right)\right] \quad \text{and} \quad \mathrm{K}_p'(\mu R) \sim -\sqrt{\frac{\pi}{2\mu R}} e^{-\mu R} \left[1 + O\left(\frac{1}{\mu R}\right)\right], \tag{4.53}$$

as $\mu \to \infty$. From this we have $L_p(\sigma) \to 1$ as $\sigma \to \pm\infty$, which is useful because it means that $\log(L_p(\sigma))$ will converge at these limits. Because $\mu(\sigma) := \sqrt{\sigma^2 - \omega^2}$ will necessarily involve branch cuts, we will need a multiplicative decomposition of $\mu(\sigma)$. We write

$$\mu(\sigma) = \mu^+(\sigma)\mu^-(\sigma) := \sqrt{-\mathrm{i}(\sigma+\omega)}\sqrt{\mathrm{i}(\sigma-\omega)}, \tag{4.54}$$

so that $\mu^+(\sigma)$ has a branch cut vertically downwards from $\sigma = -\omega$, and $\mu^-(\sigma)$ has a branch cut vertically upwards from $\sigma = \omega$. Therefore $L_p(\sigma)$ is analytic, and also nonzero, in the strip between $\mathrm{Im}(\sigma) = -\mathrm{Im}(\omega)$ and $\mathrm{Im}(\sigma) = \mathrm{Im}(\omega)$. Thus if we take $\log(L_p(\sigma))$, this function is analytic in the same region. Cauchy's integral formula then says that for $Y \in \mathbb{R}^+$ and $\delta < \mathrm{Im}(\omega)$ we can write

$$2\pi\mathrm{i} L_p(\sigma) = \left(\int_{-Y-\mathrm{i}\delta}^{Y-\mathrm{i}\delta} + \int_{Y-\mathrm{i}\delta}^{Y+\mathrm{i}\delta} + \int_{Y+\mathrm{i}\delta}^{-Y+\mathrm{i}\delta} + \int_{-Y+\mathrm{i}\delta}^{-Y-\mathrm{i}\delta}\right) \frac{\log(L_p(\tilde\sigma))}{\tilde\sigma - \sigma} \mathrm{d}\tilde\sigma. \tag{4.55}$$

Taking $Y \to \infty$ and assuming the end integrals converge, we then have

$$2\pi\mathrm{i} \log(L_p(\sigma)) = \int_{-\infty-\mathrm{i}\delta}^{\infty-\mathrm{i}\delta} \frac{\log(L_p(\tilde\sigma))}{\tilde\sigma - \sigma} \mathrm{d}\tilde\sigma - \int_{-\infty+\mathrm{i}\delta}^{\infty+\mathrm{i}\delta} \frac{\log(L_p(\tilde\sigma))}{\tilde\sigma - \sigma} \mathrm{d}\tilde\sigma. \tag{4.56}$$

The first integral is analytic for $\mathrm{Im}(\sigma) > -\delta$ and the second integral is analytic for $\mathrm{Im}(\sigma) < \delta$. Therefore we write

$$\log(L_p(\sigma)) = \log\bigl(L_p^+(\sigma)\bigr) + \log\bigl(L_p^-(\sigma)\bigr), \tag{4.57}$$

and have the definitions

$$L_p^\pm(\sigma) = \exp\left(\pm\frac{1}{2\pi\mathrm{i}} \int_{-\infty}^{\infty} \frac{\log L_p(\tilde\sigma)}{\tilde\sigma - \sigma} \mathrm{d}\tilde\sigma\right). \tag{4.58}$$

It is evident from these definitions that $L_p^-(\sigma) = L_p^+(-\sigma)$, therefore

$$\begin{aligned} \arg(-\mathsf{R}_{\alpha\alpha}(0)) &= 2\arg(L_{p_\alpha}^+(-\mathrm{i}\gamma_\alpha)) + \frac{\pi}{2} \\ &= -\frac{1}{\pi}\mathrm{Re}\left(\int_{-\infty}^{\infty} \frac{\log L_p(\tilde{\sigma})}{\tilde{\sigma} - \sigma}\mathrm{d}\tilde{\sigma}\right) + \frac{\pi}{2}. \end{aligned} \tag{4.59}$$

While we require ω to have a small positive imaginary part for the above calculation to work, we would ideally like it to be real. Thus we define a factorising contour $\mathcal{C}_\sigma$ with equation

$$\sigma = \omega\left(\xi - \mathrm{i}h\frac{4(\xi/q)}{3 + (\xi/q)^4}\right), \qquad \xi \in \mathbb{R}, \tag{4.60}$$

which ensures we can bend around the point ω on the real axis, as well as any cut-on poles that now lie on it. In our calculations, we took $h = 0.01$ and $q = 1$, with ω having an imaginary part of $\mathrm{i} \times 10^{-5}$ added to it.

4.2.3 Plotting the end correction coefficients against frequency

Here we plot the end correction coefficients $\hat{s}_\alpha$ as frequency is increased, using the results of the Wiener–Hopf calculation in this chapter.

End correction coefficients in 3D

Figure 4.1 plots the $p_\alpha = 0$ end-correction coefficients $\hat{s}_{(0,q_\alpha,\xi_\alpha)}$ as frequency is increased (using the equivalence from section 2.1.5 between the mode α and the triple $(p_\alpha, q_\alpha, \xi_\alpha)$. Here we recover the classical end correction distance of $\hat{s}_0 = \hat{s}_{(0,0,0)} \approx 0.6R$ at low frequencies, and then a sharp reduction as the frequency is increased before new modes cut on. In contrast to Snakowska et al. [2011], modes are seen to cut-on with a nonzero end-correction, before eventually, as the frequency increases further, collapsing onto the mode-zero curve. It should not be concluded from this that continuous variation of ωR results in discontinuous variation of $\hat{s}_\alpha/R$: if the definition of $\hat{s}_\alpha/R$ could be analytically extended to account for evanescent modes, continuous results would be seen. Future work on the end correction could aim towards this.

Figure 4.2 shows the end-correction coefficients $\hat{s}_{(p_\alpha,q_\alpha,\xi_\alpha)}$ corresponding to higher-modal azimuthal excitations symmetric across $\theta = 0$ (in terms of section 2.1.5, higher values of p_α for varying q_α and $\xi_\alpha = 0$). We see similar behaviour to the $p_\alpha = 0$ case, but with no low-frequency cut-on, as expected.

End correction coefficients in 2D

Figure 4.3(a) shows the end-correction coefficients for a 2D duct with a symmetric source. Here, the end correction once again decays with increasing Helmholtz number, and its coefficients exhibit a cusp every time a new duct mode cuts on; this is in

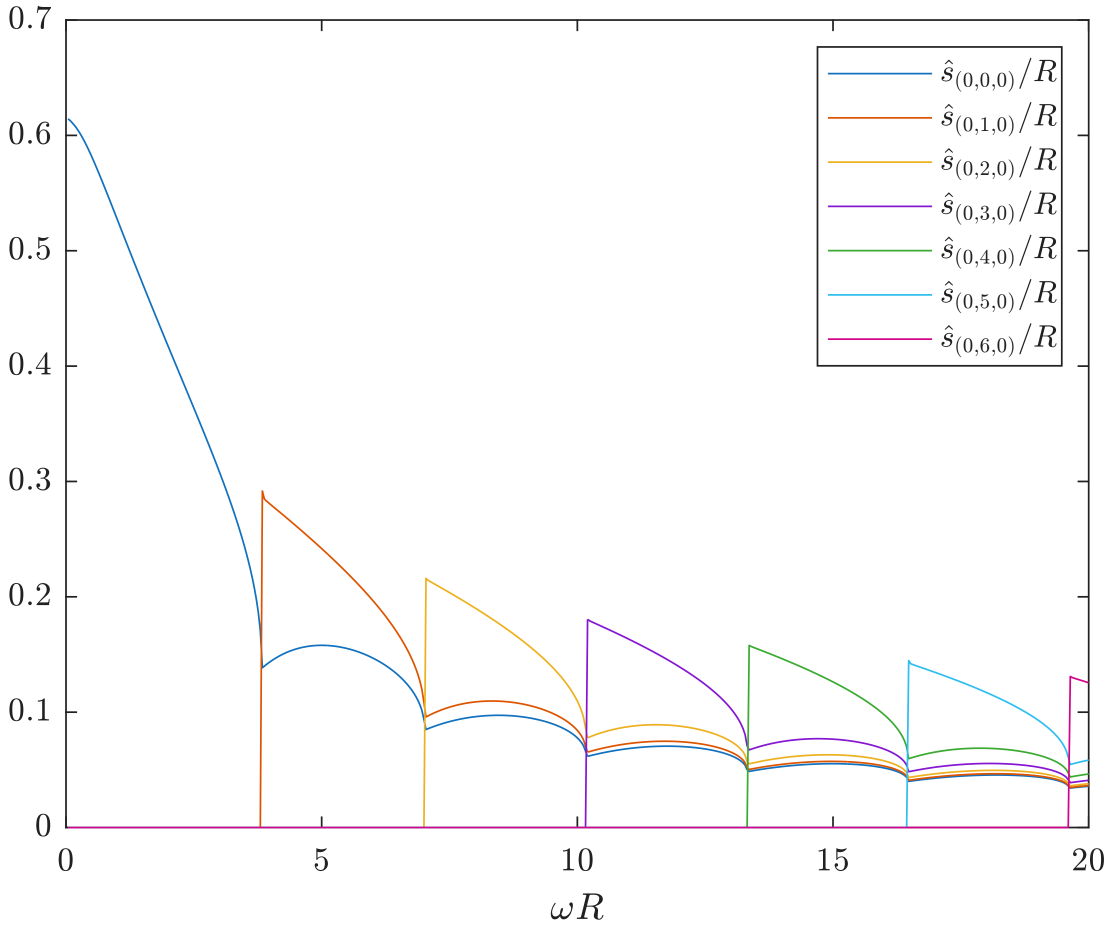

Figure 4.1: End-correction coefficients for a 3D duct, calculated using the Wiener–Hopf technique. These are the coefficients with the azimuthal modenumber $p = 0$, corresponding to no azimuthal variation.

qualitative agreement with the 3D results presented above. However, in contrast to the well-known low-frequency end correction figure of $\hat{s}_0 \approx 0.6R$ for 3D ducts [Rayleigh, 1871], in 2D the end correction exhibits a logarithmic singularity at low frequencies, and so is unbounded as the frequency tends to zero, or equivalently, as the duct width X tends to zero. This is not an indication that the end correction *itself* diverges in practice, but rather that its convergence is sublinear with the duct width X, and so it diverges when plotted using the nondimensional scaling used here. For more detail, see equation (4.37).

Figure 4.3(b) shows the end-correction coefficients for an antisymmetric source. We see that these antisymmetric modes exhibit the same behaviour as was seen in the symmetric case (from which they are totally uncoupled), but with no singularities since there are no cut-on antisymmetric modes at low frequencies.

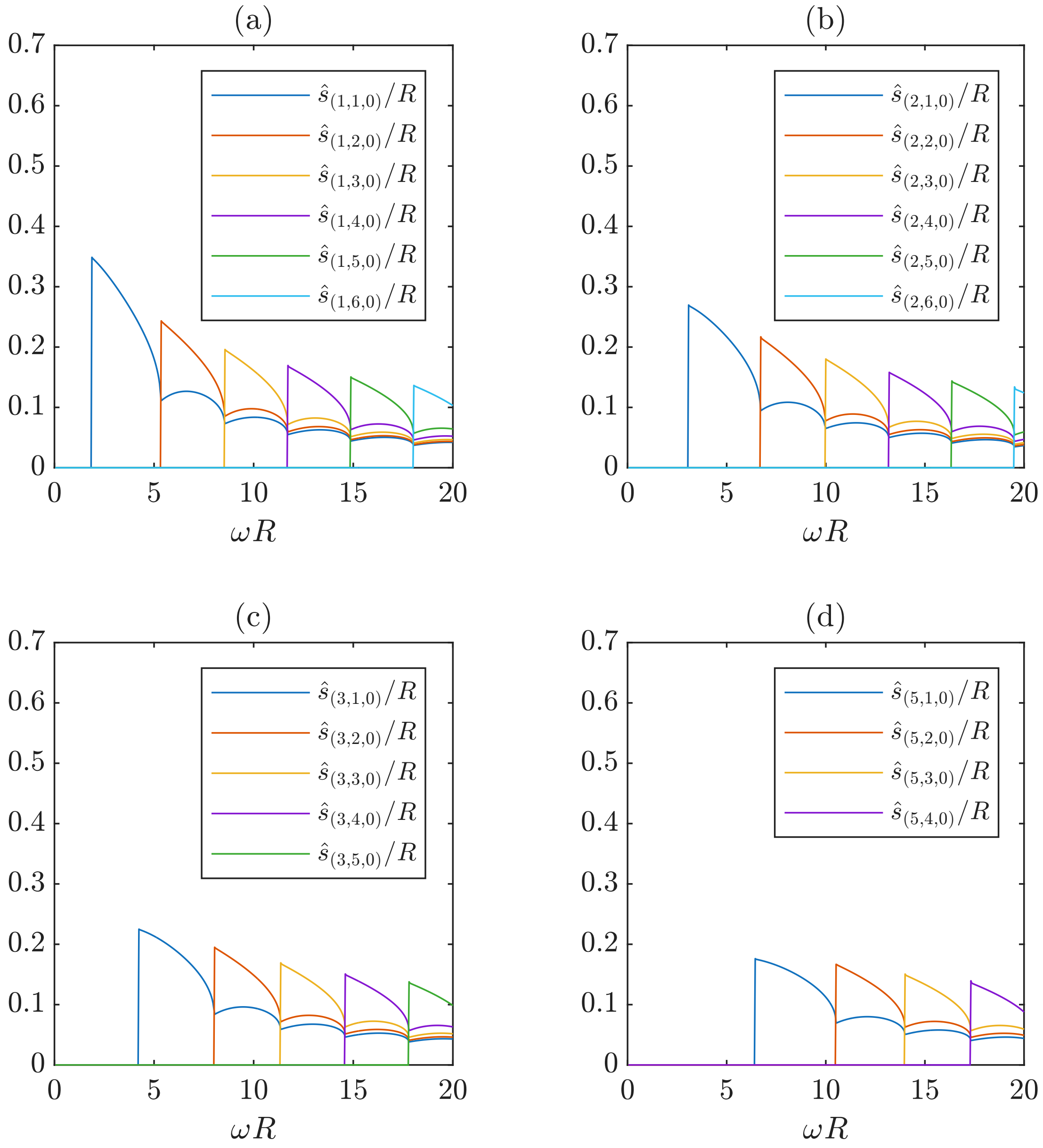

Figure 4.2: End-correction coefficients for a 3D duct for multiples values of azimuthal modenumber p, calculated using the Wiener–Hopf technique. (a) shows $p = 1$, (b) shows $p = 2$, (c) shows $p = 3$ and (d) shows $p = 5$; these correspond to sources of different azimuthal symmetry.

4.3 Summary

In this chapter we have formulated the end-correction problem in the linear regime and presented a derivation of a solution using the Wiener–Hopf technique. Unfortunately, this technique is only valid in the linear regime and does not generalize to weak non-linearity, so an alternative method for deriving the end correction is required: this will be developed in chapter 5. The Wiener–Hopf calculation of the end-correction was also plotted here, which will be used for validation of the model we develop in chapter 5.

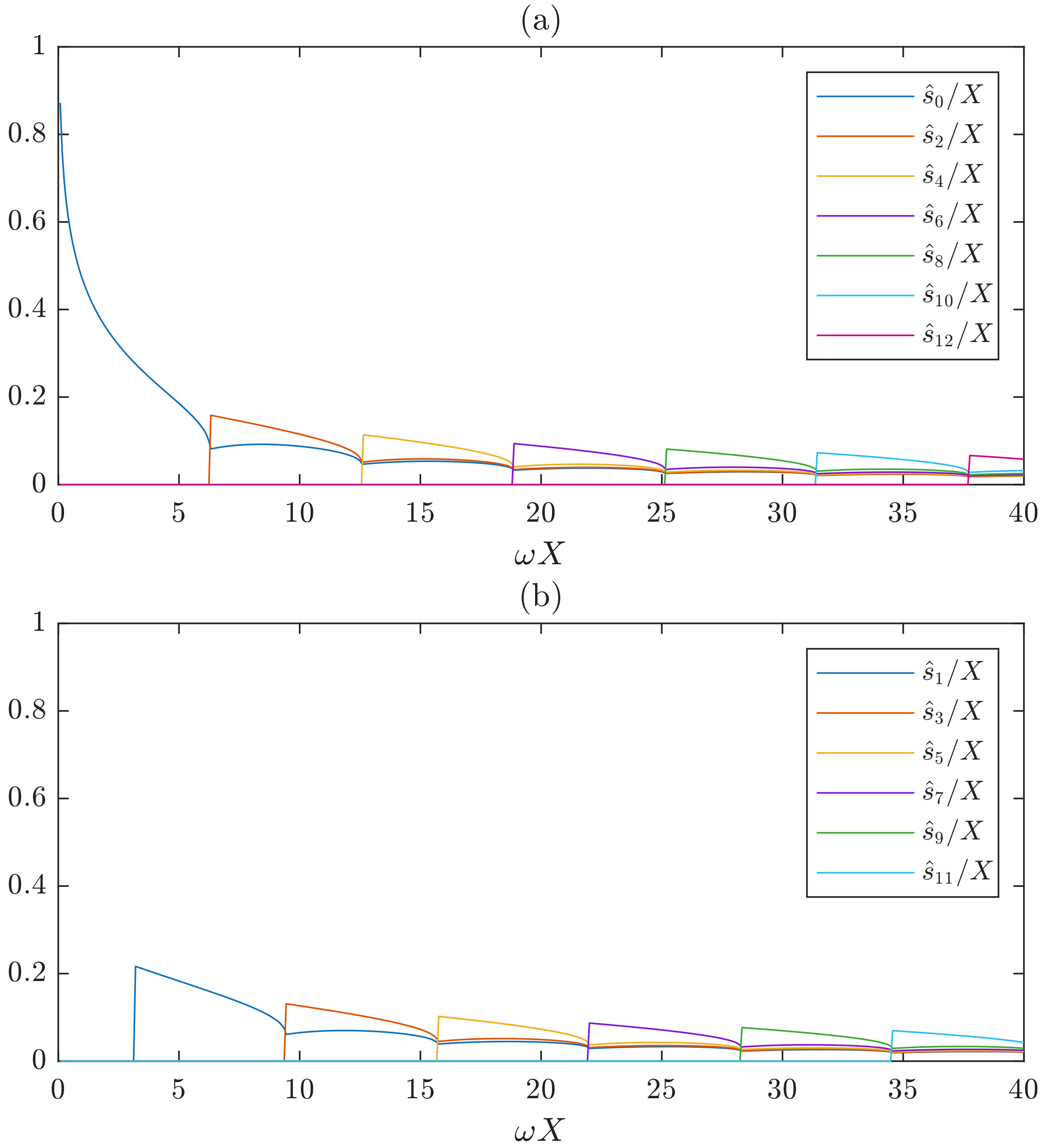

Figure 4.3: End-correction coefficients for a 2D duct, calculated using the Wiener–Hopf technique. (a) Even-modenumber coefficients, corresponding to a symmetric source. (b) Odd-modenumber coefficients, corresponding to an antisymmetric source.

Chapter 5

Ducts of finite length

This chapter develops a weakly nonlinear duct exit condition by introducing into the duct-acoustic model a larger, concentric ‘outer duct’ into which the original duct emits its sound: this approximates free space as the outer duct’s walls are widened. The condition itself is derived in terms of the admittance, before a pressure condition linking the inner duct to the outer duct is derived. A novel nonlinear end-correction coefficient is introduced, and once the outer-duct model has been validated against the linear end-correction results from chapter 4, the nonlinear end-correction coefficient is calculated for various parameter choices. After a discussion of resonance, a number of numerical examples are shown. This chapter forms the rest of Jensen et al. [2025] (of which the first part was presented in chapter 4).

5.1 Formulation of the exit condition and solution in the outer duct

5.1.1 The duct outlet as an acoustic source

Here we wish to model the propagation of sound from a duct outlet, in order to inform our choice of radiation condition for the duct itself. Rather than a duct radiating sound into free space, we consider an inner duct positioned within an outer duct several times larger, i.e. ‘approximately free’ space. A schematic of this model in depicted in figure 5.1. The inner duct exit, shown in green in figure 5.1, is modelled as an acoustic source within the outer-duct at arclength $s = 0$, with its width being a fraction $\eta < 1$ of the outer duct’s width. The right (positive s-facing) side of the source then emanates sound into the outer duct, while the left side (shown in red in figure 5.1) will have an acoustic absorption condition to be specified later: since sound entering this surface departs forever from the domain of computation, we term this the ‘acoustic wormhole’. This is obviously a somewhat idealised situation, as the body of the inner duct is not present in the outer domain, but the expectation is as follows: of the sound leaving the bell of a trumpet, only a relatively small proportion will emanate backwards; a yet

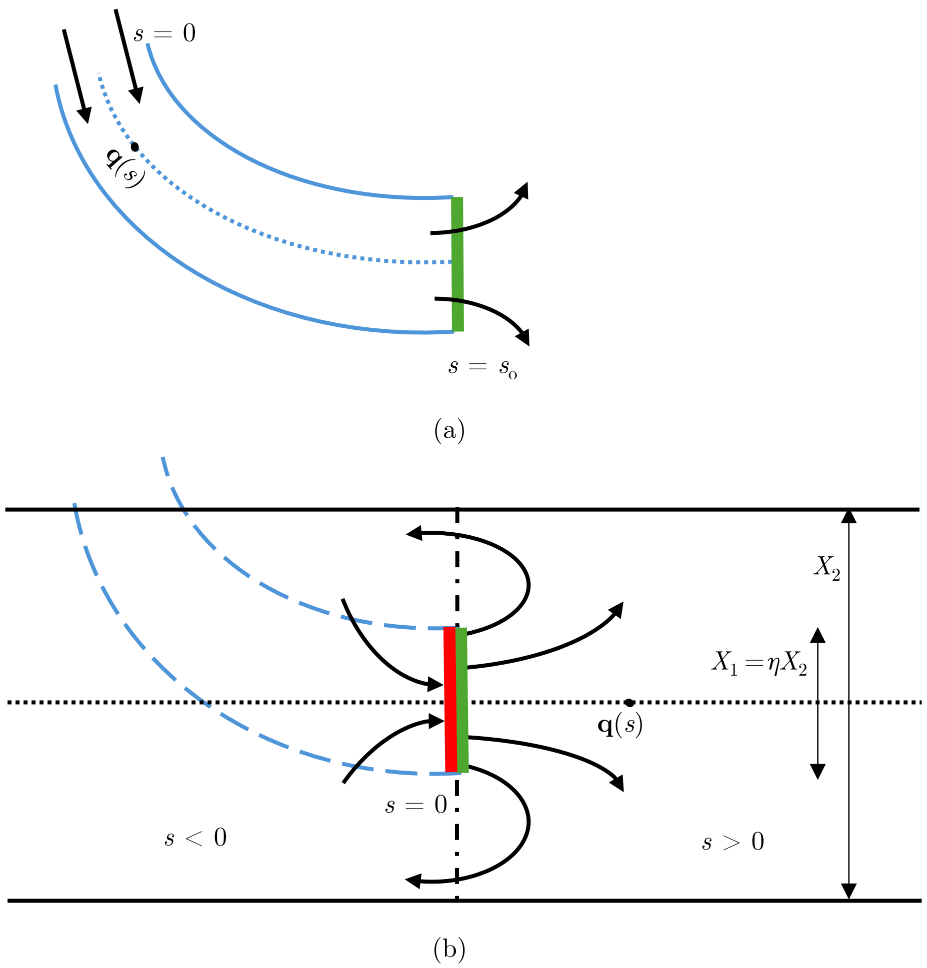

Figure 5.1: A schematic depicting the inner and outer ducts. (a) The inner duct, with centreline $\mathbf{q}(s)$, inlet ($s = 0$), and the outlet boundary/surface of emission ($s = s_{\mathrm{o}}$) depicted in green. (b) The outer duct, with centreline $\mathbf{q}(s)$, relative duct widths X_1 and X_2, the acoustic source/surface of emission ($s = 0+$) depicted in green, the absorbing boundary or 'acoustic wormhole' ($s = 0-$) depicted in red, and the two domains of propagation $s > 0$ and $s < 0$, with acoustic variables continuous across the dash-dotted line. Note that the outer duct domain $s < 0$ intersects with the inner duct domain, shown by the blue dashed lines, but this intersection is ignored in this model. Outer and inner widths X_2 and X_1 use the 2D notation.

smaller proportion of this will reflect off the body of the trumpet; and this small fraction of reflected sound's contribution is unlikely to have a significant influence on the inner duct's acoustics.

We define $p^R(\mathbf{x}, t)$ and $u^R(\mathbf{x}, t)$ to be the pressure and longitudinal velocity to the right of the source ($s > 0$), while $p^L(\mathbf{x}, t)$ and $u^L(\mathbf{x}, t)$ are the equivalent quantities to the left of the source ($s < 0$). These quantities are all expanded in the same way as described in section 2.1.5, although being within the outer duct they are all expanded in terms of the outer-duct modes: taking $p^R(\mathbf{x},t)$ as an example, we have

$$p^R(\mathbf{x},t) = \sum_{a=-\infty}^{\infty}\sum_{\alpha=0}^{\infty} \mathrm{e}^{-\mathrm{i}a\omega t}\psi_\alpha^2(\mathbf{x})P_{\alpha,2}^{a,R}(s), \tag{5.1}$$

where $\psi_\alpha^2(\mathbf{x})$ are the outer-duct modes given by (2.48) in 2D and (2.53) in 3D (using the outer-duct width in these equations). Note that the definition of the coefficient $P_{\alpha,2}^{a,R}(s)$ is

$$P_{\alpha,2}^{a,R}(s) = \frac{\omega}{2\pi}\int_{t=0}^{2\pi}\iint_{S_2(s)} p_2^R(\mathbf{x},t)\mathrm{e}^{\mathrm{i}a\omega t}\psi_\alpha^2(\mathbf{x})\mathrm{d}S\mathrm{d}t, \tag{5.2}$$

where $S_2(s)$ is the outer-duct cross section at s.

As in chapter 2, we then treat $P_{\alpha,2}^{a,R}(s)$ as a set of vectors with α-coefficients, $\{\boldsymbol{p}_2^{a,R}(s) : a \in \mathbb{Z}\}$; in this section, however, we perform a further bit of shorthand and refer to these with the notation $\boldsymbol{p}_2^R(s)$ (similarly $\boldsymbol{u}_2^R(s)$, $\boldsymbol{p}_2^L(s)$ and $\boldsymbol{u}_2^L(s)$). Dropping the temporal indices means that sums over b become implicit; for example, we write the admittance relation

$$U_\alpha^a = \sum_{\beta=0}^{\infty}\mathsf{Y}_{\alpha\beta}^a P_\beta^a + \sum_{b=-\infty}^{\infty}\sum_{\beta,\gamma=0}^{\infty}\mathcal{Y}_{\alpha\beta\gamma}^{ab}P_\beta^{a-b}P_\gamma^b, \tag{5.3}$$

using the shorthand $\boldsymbol{u} = \mathsf{Y}\boldsymbol{p} + \mathcal{Y}\langle\boldsymbol{p},\boldsymbol{p}\rangle$, where $\boldsymbol{u}$ and $\boldsymbol{p}$ are vectors of velocity and pressure modal coefficients U_α^a and P_α^a, Y is a block-diagonal matrix performing matrix multiplication on each frequency harmonic independently, and angle brackets denote the quadratic convolution operation

$$\boldsymbol{q} = \mathcal{N}\langle\boldsymbol{v},\boldsymbol{w}\rangle \qquad\Longleftrightarrow\qquad q_\alpha^a = \sum_{b=-\infty}^{\infty}\sum_{\beta,\gamma=0}^{\infty}\mathcal{N}_{\alpha\beta\gamma}^{ab}\,v_\beta^{a-b}\,w_\gamma^b. \tag{5.4}$$

To avoid repetition of complicated arguments, we will also use the shorthand notation $\mathcal{N}\langle\boldsymbol{v},\boldsymbol{v}\rangle \equiv \mathcal{N}\langle\boldsymbol{v},\cdots\rangle$; as in chapter 2 we also use the notation that $\mathcal{A} = \mathcal{B}\langle\mathsf{C},\mathsf{D}\rangle$ defines a nonlinear operator such that $\mathcal{A}\langle\boldsymbol{v},\boldsymbol{w}\rangle = \mathcal{B}\langle\mathsf{C}\boldsymbol{v},\mathsf{D}\boldsymbol{w}\rangle$.

We can then introduce linear and nonlinear admittances to the right of the source ($s > 0$), $\mathsf{Y}_{\alpha\beta}^{a,R}(s)$ and $\mathcal{Y}_{\alpha\beta\gamma}^{ab,R}(s)$, defined as in section 2.2.1, and similarly for $s < 0$, giving $\mathsf{Y}_{\alpha\beta}^{a,L}(s)$ and $\mathcal{Y}_{\alpha\beta\gamma}^{ab,L}(s)$. Equipped with these radiative quantities, we then stipulate that sound to the right of the source must only travel rightward in the outer duct, and sound to the left must only travel leftward; equivalently, we are taking the outer duct admittances ($\mathsf{Y}_2^R(s)$, $\mathcal{Y}_2^R(s)$) to be *positive characteristic* ($\overline{\mathsf{Y}}_2$, $\overline{\mathcal{Y}}_2$) for $s > 0$, and $\mathsf{Y}_2^L(s)$, $\mathcal{Y}_2^L(s)$ to be *negative characteristic* ($-\overline{\mathsf{Y}}_2$, $-\overline{\mathcal{Y}}_2$) for $s < 0$. Note that the impedances in these regions will then be $(\overline{\mathsf{Z}}_2, \overline{\mathcal{Z}}_2)$ and $(-\overline{\mathsf{Z}}_2, \overline{\mathcal{Z}}_2)$[1] respectively, where $\overline{\mathsf{Z}}_2 = \overline{\mathsf{Y}}_2^{\,-1}$ and $\overline{\mathcal{Z}}_2 = -\overline{\mathsf{Z}}_2\overline{\mathcal{Y}}_2\langle\overline{\mathsf{Z}}_2, \overline{\mathsf{Z}}_2\rangle$. This notation is taken from section 2.2.2, where explicit formulae

---

[1] The non-matching signs here are due to reflection in $s = 0$ giving a sign change of longitudinal velocity u' but not of pressure p', and the linear and weakly-nonlinear parts of the impedance being either linear or quadratic in this sign change. A discussion of this may also be found in section 2.2.2.

and a derivation of the characteristic admittance is given.

5.1.2 Restriction and zero-extension

Before we derive the outlet condition, it will first prove helpful to consider how modal expansions using the outer-duct modes $\psi_\alpha^2(\mathbf{x})$ are related to modal expansions using the inner-duct modes; inner duct modes are denoted here as $\psi_\alpha^1(\mathbf{x})$, and are similarly given by (2.48) using the inner-duct width X_1 in 2D and by (2.53) using the inner duct radius R_1 in 3D. Expanding using the inner-duct modes would result in a different set of coefficients $\boldsymbol{p}_1^R(s)$, $\boldsymbol{u}_1^R(s)$, $\boldsymbol{p}_1^L(s)$ and $\boldsymbol{u}_1^L(s)$, and is valid only for $|x| < X_1$ in 2D and $r < R_1$ in 3D. We now relate the outer-duct coefficients to the inner-duct ones. For example,

$$\sum_{\beta=0}^{\infty} \psi_\beta^1(\mathbf{x}) P_{\beta,1}^{a,R}(s) = \sum_{\beta=0}^{\infty} \psi_\beta^2(\mathbf{x}) P_{\beta,2}^{a,R}(s) \qquad \text{provided} \quad \mathbf{x} \in S_1(s). \tag{5.5}$$

Multiplying both sides by $\psi_\alpha^1(\mathbf{x})$ and integrating both sides over an inner-duct cross section $S_1(s)$ gives (by orthogonality of the modes)

$$P_{\alpha,1}^{a,R}(s) = \sum_{\beta=0}^{\infty} \int_{S_1(s)} \psi_\alpha^1(\mathbf{x}) \psi_\beta^2(\mathbf{x}) \mathrm{d}S \; P_{\beta,2}^{a,R}(s) =: \sum_\beta \mathsf{F}_{\alpha\beta}(s) P_{\beta,2}^{a,R}(s), \tag{5.6}$$

where we term F the *restriction operator*. We utilise the vector notation here and write $\boldsymbol{p}_1^R = \mathsf{F}\boldsymbol{p}_2^R$. Technically, all of these quantities depend on s, but as we shall see in a moment, all restrictions will be taken at $s = 0$, so henceforth we write F for $\mathsf{F}(0)$, S_1 for $S_1(0)$ and S_2 for $S_2(0)$.

Since restriction is a one-way operation (in that information for $\mathbf{x} \in S_2 \setminus S_1$ is lost), we cannot define an inverse operation, but we can still map from the inner duct to the outer duct if we think carefully about what this lost information can be replaced with. While we expect a jump in the pressure and velocity as we move from one side of the source to the other, we do not expect this discontinuity to hold above and below the source. We therefore define acoustic jump variables $u^*(\mathbf{x}, t)$ and $p^*(\mathbf{x}, t)$ as

$$u^*(\mathbf{x}, t) = u^R(\mathbf{x}, t)|_{s=0^+} - u^L(\mathbf{x}, t)|_{s=0^-}, \quad p^*(\mathbf{x}, t) = p^R(\mathbf{x}, t)|_{s=0^+} - p^L(\mathbf{x}, t)|_{s=0^-}, \tag{5.7}$$

in the expectation that these will be nonzero only on the region S_1. Finding the outer-duct coefficients of one of these jump variables, we have

$$U_{\alpha,2}^{a,*} = \frac{\omega}{2\pi} \int_{t=0}^{2\pi} \iint_{S_2} u^*(\mathbf{x}, t) \mathrm{e}^{\mathrm{i}a\omega t} \psi_\alpha^2(\mathbf{x}) \mathrm{d}S \mathrm{d}t, \tag{5.8}$$

but the integral over S_2 here may equivalently be performed over S_1, since u^* is zero outside S_1. Making this change, and expanding $u^*(\mathbf{x},t)$ in terms of the inner-duct modes, we get

$$U^{a,*}_{\alpha,2} = \iint_{S_1} \psi^2_\alpha(\mathbf{x})\psi^1_\beta(\mathbf{x})\mathrm{d}S \; U^{a,*}_{\alpha,1}, \tag{5.9}$$

or in other words

$$\boldsymbol{u}^*_2 = \mathsf{F}^{\mathrm{T}}\boldsymbol{u}^*_1, \qquad \text{and by the same property,} \qquad \boldsymbol{p}^*_2 = \mathsf{F}^{\mathrm{T}}\boldsymbol{p}^*_1. \tag{5.10}$$

From this, we deduce that taking the transpose of the restriction operator results in a *zero-extension* operator. Note that while $\mathsf{F}\mathsf{F}^{\mathrm{T}} = \mathsf{I}$ (because zero-extending and then restricting returns the original), in general $\mathsf{F}^{\mathrm{T}}\mathsf{F} \neq \mathsf{I}$ (since restricting and then zero-extending essentially sets the original to zero for $\mathbf{x} \in S_2 \setminus S_1$).

For the mode definitions (2.48) and (2.53), the restriction operator is given in 2D by

$$\mathsf{F}_{\alpha\beta} = \begin{cases} \frac{C_\alpha C_\beta}{\pi}\frac{\eta^{3/2}\beta}{\alpha^2-\eta^2\beta^2}\left[\sin\left(\frac{1-\eta}{2}\beta\pi\right) - (-1)^\alpha \sin\left(\frac{1+\eta}{2}\beta\pi\right)\right] & \text{if } \alpha \neq \eta\beta, \\ \frac{C_\alpha C_\beta}{2}\sqrt{\eta}\cos\left(\frac{\alpha\pi}{2}\left[1-\frac{1}{\eta}\right]\right) & \text{if } \alpha = \eta\beta \neq 0, \\ C_\alpha C_\beta\sqrt{\eta} & \text{if } \alpha = \eta\beta = 0, \end{cases} \tag{5.11}$$

and in 3D by

$$\mathsf{F}_{\alpha\beta} = \begin{cases} (1+\delta_{m_\alpha 0})\eta C_\alpha C_\beta \dfrac{\lambda_\alpha \mathrm{J}_{m_\alpha-1}(\lambda_\alpha)\mathrm{J}_{m_\alpha}(\eta\lambda_\beta) - \eta\lambda_\beta \mathrm{J}_{m_\alpha}(\lambda_\alpha)\mathrm{J}_{m_\alpha-1}(\eta\lambda_\beta)}{\eta^2\lambda_\beta^2 - \lambda_\alpha^2} & \\ & \text{if } m_\alpha = m_\beta,\ \xi_\alpha = \xi_\beta,\ \eta\lambda_\beta \neq \lambda_\alpha, \\ \eta & \text{if } m_\alpha = m_\beta,\ \xi_\alpha = \xi_\beta,\ \eta\lambda_\beta = \lambda_\alpha, \\ 0 & \text{otherwise.} \end{cases} \tag{5.12}$$

5.1.3 Derivation of the outlet admittance

We now go on to derive the open-end admittance boundary condition, using the restriction and zero-extension operators F and F^{T} from the previous section, applied at $s = 0$. Specifically, we aim to derive a condition relating pressure and axial velocity at the exit of the smaller duct as it enters the larger duct (shown in green in figures 5.1(a) and (b)); i.e. a relation between $\boldsymbol{p}^R_1$ and $\boldsymbol{u}^R_1$ at $s = 0$. To do so, we will assume: (i) a known relation between $\boldsymbol{p}^L_1$ and $\boldsymbol{u}^L_1$ (i.e. the condition on the red 'acoustic wormhole' surface in figure 5.1(b)); (ii) that waves in the larger duct are only outgoing for both $s > 0$ and $s < 0$; and (iii) that the acoustic variables are continuous at the duct exit (across $s = 0$) in the larger duct outside the smaller duct (for $\mathbf{x} \in S_2 \setminus S_1$). This last condition means that the jump in velocity and pressure when crossing $s = 0$, given by u^* and p^* in (5.7), is only nonzero for $\mathbf{x} \in S_1$. The entirety of this section is evaluated within the outer duct at $s = 0$. We start by using the acoustic jump variables in the outer duct to eliminate $\boldsymbol{u}_2^L = \boldsymbol{u}_2^R - \boldsymbol{u}_2^*$ and $\boldsymbol{p}_2^L = \boldsymbol{p}_2^R - \boldsymbol{p}_2^*$; in particular, the outer-left-duct admittance equation becomes

$$\boldsymbol{u}_2^R - \boldsymbol{u}_2^* = -\overline{\mathsf{Y}}_2\big(\boldsymbol{p}_2^R - \boldsymbol{p}_2^*\big) - \overline{\mathcal{Y}}_2\langle \boldsymbol{p}_2^R - \boldsymbol{p}_2^*, \boldsymbol{p}_2^R - \boldsymbol{p}_2^* \rangle, \tag{5.13a}$$

$$\text{or equivalently,}\quad \boldsymbol{p}_2^R - \boldsymbol{p}_2^* = -\overline{\mathsf{Z}}_2\big(\boldsymbol{u}_2^R - \boldsymbol{u}_2^*\big) + \overline{\mathcal{Z}}_2\langle \boldsymbol{u}_2^R - \boldsymbol{u}_2^*, \boldsymbol{u}_2^R - \boldsymbol{u}_2^* \rangle. \tag{5.13b}$$

At linear order, this may be rearranged for $\boldsymbol{u}_2^R$ using the identities $\boldsymbol{u}_2^R = \overline{\mathsf{Y}}_2 \boldsymbol{p}_2^R$ and $\boldsymbol{p}_2^R = \overline{\mathsf{Z}}_2 \boldsymbol{u}_2^R$ to give

$$\boldsymbol{u}_2^R = \frac{1}{2}\big(\boldsymbol{u}_2^* + \overline{\mathsf{Y}}_2 \boldsymbol{p}_2^*\big) + O(M^2), \quad \text{or equivalently} \quad \boldsymbol{p}_2^R = \frac{1}{2}\big(\boldsymbol{p}_2^* + \overline{\mathsf{Z}}_2 \boldsymbol{u}_2^*\big) + O(M^2). \tag{5.14}$$

These two expressions may be substituted into the nonlinear terms in (5.13) (recall we are neglecting $O(M^3)$ and smaller terms), resulting in

$$\boldsymbol{u}_2^R = \frac{1}{2}\big(\boldsymbol{u}_2^* + \overline{\mathsf{Y}}_2 \boldsymbol{p}_2^*\big) + \frac{1}{8}\overline{\mathcal{Y}}_2\Big(\big\langle \boldsymbol{p}_2^* + \overline{\mathsf{Z}}_2\boldsymbol{u}_2^*, \boldsymbol{p}_2^* + \overline{\mathsf{Z}}_2\boldsymbol{u}_2^* \big\rangle - \big\langle \boldsymbol{p}_2^* - \overline{\mathsf{Z}}_2\boldsymbol{u}_2^*, \boldsymbol{p}_2^* - \overline{\mathsf{Z}}_2\boldsymbol{u}_2^* \big\rangle\Big), \tag{5.15a}$$

$$\boldsymbol{p}_2^R = \frac{1}{2}\big(\boldsymbol{p}_2^* + \overline{\mathsf{Z}}_2 \boldsymbol{u}_2^*\big) + \frac{1}{8}\overline{\mathcal{Z}}_2\Big(\big\langle \boldsymbol{u}_2^* + \overline{\mathsf{Y}}_2\boldsymbol{p}_2^*, \boldsymbol{u}_2^* + \overline{\mathsf{Y}}_2\boldsymbol{p}_2^* \big\rangle + \big\langle \boldsymbol{u}_2^* - \overline{\mathsf{Y}}_2\boldsymbol{p}_2^*, \boldsymbol{u}_2^* - \overline{\mathsf{Y}}_2\boldsymbol{p}_2^* \big\rangle\Big). \tag{5.15b}$$

By outer-duct continuity at $s = 0$, both u^* and p^* are zero outside $\mathbf{x} \in S_1$, and so we can use (5.10) to replace all outer-duct quantities on the right-hand sides with inner-duct ones. Applying F to both sides then gives

$$\begin{aligned}\boldsymbol{u}_1^R =& \frac{1}{2}\Big(\boldsymbol{u}_1^* + \mathsf{F}\overline{\mathsf{Y}}_2\mathsf{F}^{\mathrm{T}}\boldsymbol{p}_1^*\Big) \\ &+ \frac{1}{8}\mathsf{F}\overline{\mathcal{Y}}_2\Big(\big\langle \mathsf{F}^{\mathrm{T}}\boldsymbol{p}_1^* + \overline{\mathsf{Z}}_2\mathsf{F}^{\mathrm{T}}\boldsymbol{u}_1^*, \mathsf{F}^{\mathrm{T}}\boldsymbol{p}_1^* + \overline{\mathsf{Z}}_2\mathsf{F}^{\mathrm{T}}\boldsymbol{u}_1^* \big\rangle - \big\langle \mathsf{F}^{\mathrm{T}}\boldsymbol{p}_1^* - \overline{\mathsf{Z}}_2\mathsf{F}^{\mathrm{T}}\boldsymbol{u}_1^*, \mathsf{F}^{\mathrm{T}}\boldsymbol{p}_1^* - \overline{\mathsf{Z}}_2\mathsf{F}^{\mathrm{T}}\boldsymbol{u}_1^* \big\rangle\Big),\end{aligned} \tag{5.16a}$$

$$\begin{aligned}\boldsymbol{p}_1^R =& \frac{1}{2}\Big(\boldsymbol{p}_1^* + \mathsf{F}\overline{\mathsf{Z}}_2\mathsf{F}^{\mathrm{T}}\boldsymbol{u}_1^*\Big) \\ &+ \frac{1}{8}\mathsf{F}\overline{\mathcal{Z}}_2\Big(\big\langle \mathsf{F}^{\mathrm{T}}\boldsymbol{u}_1^* + \overline{\mathsf{Y}}_2\mathsf{F}^{\mathrm{T}}\boldsymbol{p}_1^*, \mathsf{F}^{\mathrm{T}}\boldsymbol{u}_1^* + \overline{\mathsf{Y}}_2\mathsf{F}^{\mathrm{T}}\boldsymbol{p}_1^* \big\rangle + \big\langle \mathsf{F}^{\mathrm{T}}\boldsymbol{u}_1^* - \overline{\mathsf{Y}}_2\mathsf{F}^{\mathrm{T}}\boldsymbol{p}_1^*, \mathsf{F}^{\mathrm{T}}\boldsymbol{u}_1^* - \overline{\mathsf{Y}}_2\mathsf{F}^{\mathrm{T}}\boldsymbol{p}_1^* \big\rangle\Big).\end{aligned} \tag{5.16b}$$

The inner-duct admittances to the right of the source, Y_1^R and $\mathcal{Y}_1^R$, are what we wish to determine; those to the left of the source, Y_1^L and $\mathcal{Y}_1^L$, will be prescribed. For the remainder of this section, we will suppress indices on radiative quantities and (unless otherwise specified) take $(\mathsf{Y}^R, \mathcal{Y}^R)$ to be $(\mathsf{Y}_1^R, \mathcal{Y}_1^R)$, $(\mathsf{Y}^L, \mathcal{Y}^L)$ to be $(\mathsf{Y}_1^L, \mathcal{Y}_1^L)$, and $(\overline{\mathsf{Y}}, \overline{\mathcal{Y}})$ to be $(\overline{\mathsf{Y}}_2, \overline{\mathcal{Y}}_2)$ (with similar shorthand for all impedances). We then have the acoustic wormhole's impedance equation in terms of the jump and outlet quantities

$$\boldsymbol{p}_1^* - \boldsymbol{p}_1^R = \mathsf{Z}^L\Big(\boldsymbol{u}_1^* - \boldsymbol{u}_1^R\Big) - \mathcal{Z}^L\Big\langle \boldsymbol{u}_1^* - \boldsymbol{u}_1^R, \boldsymbol{u}_1^* - \boldsymbol{u}_1^R \Big\rangle. \tag{5.17}$$

Substituting $\boldsymbol{p}_1^*$ from this expression into (5.16a), at linear order we may rearrange to find

$$\boldsymbol{u}_1^* = (\mathsf{I}+\mathsf{Q})\boldsymbol{u}_1^R - (\mathsf{I}-\mathsf{Q})\mathsf{Y}^L\boldsymbol{p}_1^R + O\big(M^2\big), \tag{5.18}$$

where $\mathsf{Q} := \big(\mathsf{I}+\mathsf{F}\overline{\mathsf{Y}}\mathsf{F}^{\mathrm{T}}\mathsf{Z}^L\big)^{-1}$ is a shorthand quantity. This expression can be substituted back into (5.17) to gain an expression for $\boldsymbol{p}_1^*$, again at linear order

$$\boldsymbol{p}_1^* = \mathsf{Z}^L\mathsf{Q}\Big(\boldsymbol{u}_1^R + \mathsf{Y}^L\boldsymbol{p}_1^R\Big) + O\big(M^2\big). \tag{5.19}$$

We may now perform the same two steps, but including the quadratic quantities, making use of these linear identities within the nonlinear terms (since the error introduced by doing so is $O\big(M^3\big)$, i.e. comparable with the magnitude of other neglected terms). This results in

$$\begin{aligned}\boldsymbol{u}_1^* = {} & (\mathsf{I}+\mathsf{Q})\boldsymbol{u}_1^R - (\mathsf{I}-\mathsf{Q})\mathsf{Y}^L\boldsymbol{p}_1^R + (\mathsf{I}-\mathsf{Q})\mathsf{Y}^L\mathcal{Z}^L\Big\langle\mathsf{Q}\boldsymbol{u}_1^R - (\mathsf{I}-\mathsf{Q})\mathsf{Y}^L\boldsymbol{p}_1^R, \cdots\Big\rangle \qquad (5.20\text{a})\\ & + \frac{1}{4}\mathsf{Q}\mathsf{F}\overline{\mathsf{Y}}\overline{\mathcal{Z}}\Big(-\Big\langle\overline{\mathsf{Y}}\mathsf{F}^{\mathrm{T}}\mathsf{Z}^L\mathsf{Q}\left(\boldsymbol{u}_1^R + \mathsf{Y}^L\boldsymbol{p}_1^R\right) - \mathsf{F}^{\mathrm{T}}\big[(\mathsf{I}+\mathsf{Q})\boldsymbol{u}_1^R - (\mathsf{I}-\mathsf{Q})\mathsf{Y}^L\boldsymbol{p}_1^R\big], \cdots\Big\rangle\\ & \qquad + \Big\langle\overline{\mathsf{Y}}\mathsf{F}^{\mathrm{T}}\mathsf{Z}^L\mathsf{Q}\left(\boldsymbol{u}_1^R + \mathsf{Y}^L\boldsymbol{p}_1^R\right) + \mathsf{F}^{\mathrm{T}}\big[(\mathsf{I}+\mathsf{Q})\boldsymbol{u}_1^R - (\mathsf{I}-\mathsf{Q})\mathsf{Y}^L\boldsymbol{p}_1^R\big], \cdots\Big\rangle\Big),\\ \boldsymbol{p}_1^* = {} & \mathsf{Z}^L\mathsf{Q}\left(\boldsymbol{u}_1^R + \mathsf{Y}^L\boldsymbol{p}_1^R\right) - \mathsf{Z}^L\mathsf{Q}\mathsf{Y}^L\mathcal{Z}^L\Big\langle\mathsf{Q}\boldsymbol{u}_1^R - (\mathsf{I}-\mathsf{Q})\mathsf{Y}^L\boldsymbol{p}_1^R, \cdots\Big\rangle \qquad (5.20\text{b})\\ & + \frac{1}{4}\mathsf{Z}^L\mathsf{Q}\mathsf{F}\overline{\mathsf{Y}}\overline{\mathcal{Z}}\Big(-\Big\langle\overline{\mathsf{Y}}\mathsf{F}^{\mathrm{T}}\mathsf{Z}^L\mathsf{Q}\left(\boldsymbol{u}_1^R + \mathsf{Y}^L\boldsymbol{p}_1^R\right) - \mathsf{F}^{\mathrm{T}}\big[(\mathsf{I}+\mathsf{Q})\boldsymbol{u}_1^R - (\mathsf{I}-\mathsf{Q})\mathsf{Y}^L\boldsymbol{p}_1^R\big], \cdots\Big\rangle\\ & \qquad + \Big\langle\overline{\mathsf{Y}}\mathsf{F}^{\mathrm{T}}\mathsf{Z}^L\mathsf{Q}\left(\boldsymbol{u}_1^R + \mathsf{Y}^L\boldsymbol{p}_1^R\right) + \mathsf{F}^{\mathrm{T}}\big[(\mathsf{I}+\mathsf{Q})\boldsymbol{u}_1^R - (\mathsf{I}-\mathsf{Q})\mathsf{Y}^L\boldsymbol{p}_1^R\big], \cdots\Big\rangle\Big),\end{aligned}$$

where we recall that '$\cdots$' indicates the left argument of the $\langle\bullet,\bullet\rangle$ operation being repeated on the right. Since we have not yet used (5.16b), we may now do so, and so we substitute (5.20b) and (5.20a) into it. At linear order, this results in

$$\boldsymbol{p}_1^R = \frac{1}{2}\big[\mathsf{F}\overline{\mathsf{Z}}\mathsf{F}^{\mathrm{T}}(\mathsf{I}+\mathsf{Q}) + \mathsf{Z}^L\mathsf{Q}\big]\boldsymbol{u}_1^R + \frac{1}{2}\big[-\mathsf{F}\overline{\mathsf{Z}}\mathsf{F}^{\mathrm{T}}(\mathsf{I}-\mathsf{Q}) + \mathsf{Z}^L\mathsf{Q}\big]\mathsf{Y}^L\boldsymbol{p}_1^R + O\big(M^2\big). \tag{5.21}$$

This may be rearranged, using another shorthand quantity $\widetilde{\mathsf{Q}} := \big(\mathsf{I}+\mathsf{Y}^L\mathsf{F}\overline{\mathsf{Z}}\mathsf{F}^{\mathrm{T}}\big)^{-1}$, into the form $\boldsymbol{p}_1^R = \mathsf{Z}^R\boldsymbol{u}_1^R + O\big(M^2\big)$, where

$$\mathsf{Z}^R = -\mathsf{Z}^L\big[\mathsf{I}+\widetilde{\mathsf{Q}}^{-1}(\mathsf{I}-\mathsf{Q})\big]^{-1}\big[\mathsf{I}-\widetilde{\mathsf{Q}}^{-1}(\mathsf{I}+\mathsf{Q})\big]. \tag{5.22}$$

As before, we now carry out the same steps, but including the quadratic quantities, and making use of linear identities within the nonlinear terms. The full nonlinear substitution of (5.20b) and (5.20a) into (5.16b) is then $\boldsymbol{p}_1^R = \mathsf{Z}^R\boldsymbol{u}_1^R + \mathcal{Z}^R\big\langle\boldsymbol{u}_1^R,\boldsymbol{u}_1^R\big\rangle$, where

$$\begin{aligned}\mathcal{Z}^R = \mathsf{Z}^L\big[\mathsf{I}+\widetilde{\mathsf{Q}}^{-1}(\mathsf{I}-\mathsf{Q})\big]^{-1}\Big\{ &-\big[\mathsf{I}-\widetilde{\mathsf{Q}}^{-1}(\mathsf{I}-\mathsf{Q})\big]\mathsf{Y}^L\mathcal{Z}^L\Big\langle \mathsf{Q}-(\mathsf{I}-\mathsf{Q})\mathsf{Y}^L\mathsf{Z}^R,\cdots\Big\rangle \\ &+\frac{1}{4}\Big(\mathsf{Y}^L\mathsf{F}-\widetilde{\mathsf{Q}}^{-1}\mathsf{Q}\mathsf{F}\overline{\mathsf{Y}}\Big)\overline{\mathcal{Z}}\Big\langle\overline{\mathsf{Y}}\mathsf{F}^{\mathrm{T}}\mathsf{Z}^L\mathsf{Q}\big(\mathsf{I}+\mathsf{Y}^L\mathsf{Z}^R\big)-\mathsf{F}^{\mathrm{T}}\big[(\mathsf{I}+\mathsf{Q})-(\mathsf{I}-\mathsf{Q})\mathsf{Y}^L\mathsf{Z}^R\big],\cdots\Big\rangle \\ &+\frac{1}{4}\Big(\mathsf{Y}^L\mathsf{F}+\widetilde{\mathsf{Q}}^{-1}\mathsf{Q}\mathsf{F}\overline{\mathsf{Y}}\Big)\overline{\mathcal{Z}}\Big\langle\overline{\mathsf{Y}}\mathsf{F}^{\mathrm{T}}\mathsf{Z}^L\mathsf{Q}\big(\mathsf{I}+\mathsf{Y}^L\mathsf{Z}^R\big)+\mathsf{F}^{\mathrm{T}}\big[(\mathsf{I}+\mathsf{Q})-(\mathsf{I}-\mathsf{Q})\mathsf{Y}^L\mathsf{Z}^R\big],\cdots\Big\rangle\Big\},\end{aligned} \tag{5.23}$$

and we recall the notation that $\mathcal{A}=\mathcal{B}\langle\mathsf{C},\mathsf{D}\rangle$ defines a nonlinear operator such that $\mathcal{A}\langle\boldsymbol{v},\boldsymbol{w}\rangle=\mathcal{B}\langle\mathsf{C}\boldsymbol{v},\mathsf{D}\boldsymbol{w}\rangle$. Using the nonlinear inversion rule from section 2.2.2, we may invert the impedances Z^R and $\mathcal{Z}^R$ to get the admittances

$$\mathsf{Y}^R = -\big[\mathsf{I}-\widetilde{\mathsf{Q}}^{-1}(\mathsf{I}+\mathsf{Q})\big]^{-1}\big[\mathsf{I}+\widetilde{\mathsf{Q}}^{-1}(\mathsf{I}-\mathsf{Q})\big]\mathsf{Y}^L, \tag{5.24a}$$

$$\begin{aligned}\mathcal{Y}^R = \big[\mathsf{I}-\widetilde{\mathsf{Q}}^{-1}(\mathsf{I}+\mathsf{Q})\big]^{-1}\Big\{&\big[\mathsf{I}-\widetilde{\mathsf{Q}}^{-1}(\mathsf{I}-\mathsf{Q})\big]\mathcal{Y}^L\Big\langle\mathsf{I}-\mathsf{Z}^L\mathsf{Q}\left(\mathsf{Y}^L+\mathsf{Y}^R\right),\cdots\Big\rangle \\ &-\frac{1}{4}\Big(\mathsf{Y}^L\mathsf{F}\overline{\mathsf{Z}}-\widetilde{\mathsf{Q}}^{-1}\mathsf{Q}\mathsf{F}\Big)\overline{\mathcal{Y}}\Big\langle\mathsf{F}^{\mathrm{T}}\mathsf{Z}^L\mathsf{Q}\big(\mathsf{Y}^L+\mathsf{Y}^R\big)-\overline{\mathsf{Z}}\mathsf{F}^{\mathrm{T}}\big[(\mathsf{I}+\mathsf{Q})\mathsf{Y}^R-(\mathsf{I}-\mathsf{Q})\mathsf{Y}^L\big],\cdots\Big\rangle \\ &-\frac{1}{4}\Big(\mathsf{Y}^L\mathsf{F}\overline{\mathsf{Z}}+\widetilde{\mathsf{Q}}^{-1}\mathsf{Q}\mathsf{F}\Big)\overline{\mathcal{Y}}\Big\langle\mathsf{F}^{\mathrm{T}}\mathsf{Z}^L\mathsf{Q}\big(\mathsf{Y}^L+\mathsf{Y}^R\big)+\overline{\mathsf{Z}}\mathsf{F}^{\mathrm{T}}\big[(\mathsf{I}+\mathsf{Q})\mathsf{Y}^R-(\mathsf{I}-\mathsf{Q})\mathsf{Y}^L\big],\cdots\Big\rangle\Big\}.\end{aligned} \tag{5.24b}$$

It finally remains to choose the boundary condition to apply on the acoustic wormhole (left of the discontinuity) by specifying the admittance Y^L and $\mathcal{Y}^L$. This boundary is somewhat artificial, as we have here neglected the outer walls of the inner duct, and this boundary sits within the region that should be inaccessible to sound from outside the inner duct (see figure 5.1(b) for a corresponding schematic). In order to avoid spurious reflections from this artificial boundary, we here choose the left-hand side admittances to be perfectly absorbing, i.e. $\mathsf{Y}^L=\overline{\mathsf{Y}}_1$ and $\mathcal{Y}^L=\overline{\mathcal{Y}}_1$, and hence sound may enter the 'acoustic wormhole' but no sound leaves from it. This, in combination with (5.24a) and (5.24b), fully determines the admittance at the inner duct's open end, which may be used as an initial condition to solve the Riccati-style system (2.117) in $(\mathsf{Y}_1(s),\mathcal{Y}_1(s))$ within the inner duct from arclength s_{o} to 0, so that the admittance is then known everywhere throughout the system, and can then be used to calculate acoustic variables such as the pressure.

5.1.4 Pressure continuity conditions

Once the admittance has been calculated in the inner duct, the pressure in the inner duct $\boldsymbol{p}_1^R(s)$ may be computed (subject to an inlet condition such as in equation (2.158)). Details of this calculation are the subject of chapter 2. For the examples that follow, we will specify the inlet condition in terms of the incoming (forward-going) acoustics only; that is, we assume that acoustics travelling backwards along the duct away from the open end may leave the duct at the inlet unimpeded. While this is a helpful inlet condition to use for studying duct resonances, as we will do later, we note in passing that it is equally possible to use this framework for any inlet condition, or indeed for a duct open at both ends with a suitable sound source located in its interior.

In this section, we derive the relations needed for transforming the computed pressure at the outlet of the inner duct into a boundary condition for computation of the pressure *field* in the outer duct. We start by imposing continuity of acoustic velocity at $s = 0$ outside the smaller duct, so that the velocity discontinuity is zero-extended from the outlet,

$$\boldsymbol{u}_2^R - \boldsymbol{u}_2^L = \mathsf{F}^{\mathrm{T}}\big(\boldsymbol{u}_1^R - \boldsymbol{u}_1^L\big). \tag{5.25}$$

In terms of the pressure, using the outer-duct admittance gives

$$\begin{aligned}\overline{\mathsf{Y}}\left(\boldsymbol{p}_2^R + \boldsymbol{p}_2^L\right) + \overline{\mathcal{Y}}\left(\langle \boldsymbol{p}_2^R, \boldsymbol{p}_2^R\rangle + \langle \boldsymbol{p}_2^L, \boldsymbol{p}_2^L\rangle\right) \\ = \mathsf{F}^{\mathrm{T}}\big(\mathsf{Y}^R\boldsymbol{p}_1^R - \mathsf{Y}^L\boldsymbol{p}_1^L + \mathcal{Y}^R\langle \boldsymbol{p}_1^R, \boldsymbol{p}_1^R\rangle - \mathcal{Y}^L\langle \boldsymbol{p}_1^L, \boldsymbol{p}_1^L\rangle\big)\,,\end{aligned} \tag{5.26}$$

from which $\boldsymbol{p}_2^L$ may be eliminated by imposing continuity of pressure in the outer duct away from the outlet; that is, by using the zero-extension of the pressure discontinuity,

$$\boldsymbol{p}_2^L = \boldsymbol{p}_2^R + \mathsf{F}^{\mathrm{T}}\big(\boldsymbol{p}_1^L - \boldsymbol{p}_1^R\big), \tag{5.27}$$

resulting in the equation for $\boldsymbol{p}_2^R$ in terms of $\boldsymbol{p}_1^R$ and $\boldsymbol{p}_1^L$,

$$\begin{aligned}\boldsymbol{p}_2^R =& \frac{1}{2}\overline{\mathsf{Z}}\mathsf{F}^{\mathrm{T}}\left(\mathsf{Y}^R\boldsymbol{p}_1^R - \mathsf{Y}^L\boldsymbol{p}_1^L\right) + \frac{1}{2}\mathsf{F}^{\mathrm{T}}\left(\boldsymbol{p}_1^R - \boldsymbol{p}_1^L\right) \\ &+ \frac{1}{2}\overline{\mathsf{Z}}\Bigg\{\mathsf{F}^{\mathrm{T}}\left(\mathcal{Y}^R\langle \boldsymbol{p}_1^R, \boldsymbol{p}_1^R\rangle - \mathcal{Y}^L\langle \boldsymbol{p}_1^L, \boldsymbol{p}_1^L\rangle\right) \\ &\qquad - \frac{1}{4}\overline{\mathcal{Y}}\bigg(\Big\langle \overline{\mathsf{Z}}\mathsf{F}^{\mathrm{T}}(\mathsf{Y}^R\boldsymbol{p}_1^R - \mathsf{Y}^L\boldsymbol{p}_1^L) + \mathsf{F}^{\mathrm{T}}\left(\boldsymbol{p}_1^R - \boldsymbol{p}_1^L\right), \ldots\Big\rangle \\ &\qquad\qquad + \Big\langle \overline{\mathsf{Z}}\mathsf{F}^{\mathrm{T}}(\mathsf{Y}^R\boldsymbol{p}_1^R - \mathsf{Y}^L\boldsymbol{p}_1^L) - \mathsf{F}^{\mathrm{T}}\left(\boldsymbol{p}_1^R - \boldsymbol{p}_1^L\right), \ldots\Big\rangle\bigg)\Bigg\}\end{aligned} \tag{5.28}$$

Taking the restriction of both sides maps $\boldsymbol{p}_2^R$ to $\boldsymbol{p}_1^R$; we then rearrange for $\boldsymbol{p}_1^L$, getting

$$\boldsymbol{p}_1^L = \mathsf{C}\boldsymbol{p}_1^R + \big(\mathsf{I} + \mathsf{F}\overline{\mathsf{Z}}\mathsf{F}^{\mathrm{T}}\mathsf{Y}^L\big)^{-1}\mathsf{F}\mathcal{C}\langle \boldsymbol{p}_1^R, \boldsymbol{p}_1^R\rangle, \tag{5.29}$$

where C and $\mathcal{C}$ are defined as

$$\mathsf{C} = -\big(\mathsf{I} + \mathsf{F}\overline{\mathsf{Z}}\mathsf{F}^{\mathrm{T}}\mathsf{Y}^L\big)^{-1}\Big(\mathsf{I} - \mathsf{F}\overline{\mathsf{Z}}\mathsf{F}^{\mathrm{T}}\mathsf{Y}^R\Big), \tag{5.30a}$$

$$\mathcal{C} = \overline{\mathsf{Z}}\Big[\mathsf{F}^{\mathrm{T}}\left(\mathcal{Y}^R - \mathcal{Y}^L\langle \mathsf{C}, \mathsf{C}\rangle\right) - \frac{1}{2}\overline{\mathcal{Y}}\Big(\langle \overline{\mathsf{Z}}\mathsf{F}^{\mathrm{T}}(\mathsf{Y}^R - \mathsf{Y}^L\mathsf{C}), \cdots\rangle + \langle \mathsf{F}^{\mathrm{T}}(\mathsf{I} - \mathsf{C}), \cdots\rangle\Big)\Big]. \tag{5.30b}$$

Substituting this into the original equation (5.28) for $\boldsymbol{p}_2^R$, we get

$$\begin{aligned}\boldsymbol{p}_2^R = \frac{1}{2}\Big[\big(\overline{\mathsf{Z}}\mathsf{F}^{\mathrm{T}}\mathsf{Y}^R + \mathsf{F}^{\mathrm{T}}\big) - \big(\overline{\mathsf{Z}}\mathsf{F}^{\mathrm{T}}\mathsf{Y}^L + \mathsf{F}^{\mathrm{T}}\big)\mathsf{C}\Big]\boldsymbol{p}_1^R \\ + \frac{1}{2}\Big[\mathsf{I} - \big(\overline{\mathsf{Z}}\mathsf{F}^{\mathrm{T}}\mathsf{Y}^L + \mathsf{F}^{\mathrm{T}}\big)\big(\mathsf{I} + \mathsf{F}\overline{\mathsf{Z}}\mathsf{F}^{\mathrm{T}}\mathsf{Y}^L\big)^{-1}\mathsf{F}\Big]\mathcal{C}\langle \boldsymbol{p}_1^R, \boldsymbol{p}_1^R\rangle, \end{aligned} \tag{5.31}$$

and then using (5.27) gives

$$\begin{aligned}\boldsymbol{p}_2^L = \frac{1}{2}\Big[\big(\overline{\mathsf{Z}}\mathsf{F}^{\mathrm{T}}\mathsf{Y}^R - \mathsf{F}^{\mathrm{T}}\big) - \big(\overline{\mathsf{Z}}\mathsf{F}^{\mathrm{T}}\mathsf{Y}^L - \mathsf{F}^{\mathrm{T}}\big)\mathsf{C}\Big]\boldsymbol{p}_1^R \\ + \frac{1}{2}\Big[\mathsf{I} - \big(\overline{\mathsf{Z}}\mathsf{F}^{\mathrm{T}}\mathsf{Y}^L - \mathsf{F}^{\mathrm{T}}\big)\big(\mathsf{I} + \mathsf{F}\overline{\mathsf{Z}}\mathsf{F}^{\mathrm{T}}\mathsf{Y}^L\big)^{-1}\mathsf{F}\Big]\mathcal{C}\langle \boldsymbol{p}_1^R, \boldsymbol{p}_1^R\rangle. \end{aligned} \tag{5.32}$$

Equations (5.31) and (5.32) give the pressure at $s = 0^+$ and $s = 0^-$ as boundary conditions from which the pressure within the outer duct for $s > 0$ and $s < 0$ can be solved, respectively. The method of solution is the same as for the inner duct (again as described in chapter 2). This allows the acoustic field within the outer duct, modelling free space, to be plotted and visualized. Examples of this will be given below.

5.1.5 Numerical Method

In this section we describe details of our numerical implementation of the open end exit calculation outlined in section 5.1.3, and the subsequent pressure matching described in section 5.1.4. For details of the numerical method for calculating propagation along either the inner or outer ducts, and a demonstration of its convergence as more modes are added, the reader is referred to sections 2.3 and 3.4.1.

When calculating the duct exit condition the infinite series of modes must be truncated during numerical implementation. Regarding truncation, it should be noted that the decision (taken in section 5.1.3) to set $\mathsf{Y}_1^L = \overline{\mathsf{Y}}_1$ and $\mathcal{Y}_1^L = \overline{\mathcal{Y}}_1$ on the acoustic wormhole has a numerical justification as well as a physical one. The natural alternative to characteristic admittances to the left of the outlet would be to take a zero admittance (corresponding to a hard wall and allowing no sound to propagate through): this causes numerical difficulties with the definitions of Q and $\widetilde{\mathsf{Q}}$, and even when the equations are reformulated to avoid these problems, numerical difficulties still arise as a result of the non-invertibility of $\mathsf{F}\overline{\mathsf{Z}}\mathsf{F}^{\mathrm{T}}$ and $\mathsf{F}\overline{\mathsf{Y}}\mathsf{F}^{\mathrm{T}}$ when truncated. In contrast, for the perfectly-absorbing characteristic admittance used here, no such numerical difficulties arise.

Choosing modenumbers and the width ratio

When truncating, we generally follow the rule of thumb set by McTavish [2018] that $\alpha^2_{\max} \geq \alpha^1_{\max}/\eta$, where $\alpha^1_{\max}$ and $\alpha^2_{\max}$ are the maximum modenumbers in the inner and outer ducts respectively. As well as choosing modenumbers carefully, it is also important that η be small enough to approximate free space; there is therefore a tradeoff between needing small η, large $\alpha^2_{\max}$, and manageable runtime. The computations we perform with this framework are not always of the same complexity, since we will focus on different parts of the solution depending on what we wish to calculate. While the number of modes in the inner duct $\alpha^1_{\max}$ always remains around 10, $\alpha^2_{\max}$ and η can vary much more.

When only a single computation of the linear-regime exit condition at a given location is required (for example, when calculating the linear end correction described in section 4.1, or when calculating resonances in section 5.3.3), with no need to solve any ODEs in the outer duct, large numbers of modes can be used. In such cases, we will typically take on the order of a thousand modes for $\alpha^2_{\max}$, meaning that we can take η down to $1/40$ without under-resolving the duct exit. Such computations will only require tens of megabytes of memory in the linear case. These memory requirements apply in either 2D or 3D, but the calculation can take much longer in 3D than 2D, since the 3D calculation involves integration of millions of Bessel function products: a 3D calculation will often last hours on a standard desktop computer using a single core, whereas a 2D one will be done in seconds. Figures 5.2 and 5.3 provide a means of calibrating η and $\alpha^2_{\max}$ by validating against results from the Wiener–Hopf technique, as discussed further in section 5.3.1 below. We may still solve ODEs in the inner duct (i.e. in section 5.3.3) using this large value of $\alpha^2_{\max}$, since the number of modes in the inner duct $\alpha^1_{\max}$ remains quite small, and linearity requires only a single temporal mode, so this does not present a time or memory constraint.

When nonlinearity becomes involved, memory requirements are a greater concern due to the presence of third-rank tensors. Using thousands of modes for a nonlinear calculation of the exit condition at a single location would require more than 128 GB of memory, so the number of modes was reduced in this case. It is demonstrated for the linear regime in section 5.3.1 that the parameters $(\eta, \alpha^1_{\max}, \alpha^2_{\max}) = (1/10, 10, 200)$ still provide a reasonable approximation to the semi-analytical Wiener–Hopf solution: this requires on the order of 10 MB of memory even in the nonlinear case (provided that the reasonable benchmark of $a_{\max} = 10$ is used).

Computational time is also more of a limiting factor in the nonlinear regime (such as in sections 5.3.2 and 5.3.6), especially since we will see in section 5.2 that the nonlinear exit condition cannot be considered in isolation without also solving for the acoustic field within the inner duct. In contrast to the linear regime, despite the number of spatial modes in the inner duct still being low, temporal modes are also required, and the ODEs are coupled in more ways than in the linear case. Performing a single computation for a simple duct geometry in the nonlinear case will thus take on the order of tens of minutes, meaning that the data for plots like figure 5.5 and 5.6 can take days to generate.

Moreover, even when calculating just the linear acoustic field in the outer duct, we also need to reduce the number of modes relative to a single exit-condition calculation: using the number of modes from section 5.3.1 would cause calculations to run very slowly. In order to compute in the outer duct in a reasonable computation time, the choices of $(\alpha^1_{\text{max}}, \alpha^2_{\text{max}}, \eta) = (10, 200, 1/10)$ are therefore maintained, resulting in calculations that take on the order of tens of seconds. This is further compunded in the nonlinear case: even with this more modest number of modes, combination with the ~ 10 temporal modes required for an accurate nonlinear calculation is beyond the memory and time constraints of our MATLAB code on a standard desktop computer: we therefore restrict modelling of the nonlinear regime here to the inner-duct domain. While the emphasis in this thesis is on the theoretical derivation and some proof-of-concept numerical examples to showcase possible behaviours, future work could focus on implementing the model in a more memory-efficient language than MATLAB, or parallelising the code to run on a distributed-memory cluster, either of which would potentially make nonlinear outer-duct computations possible.

In summary, we use the numerical paramaters $(\alpha^1_{\text{max}}, \alpha^2_{\text{max}}, \eta) = (10, 200, 1/10)$ for the examples that follow, unless indicated otherwise. This is shown in section 5.3.1 to give sufficiently accurate results, although higher resolutions are used in a few special cases where they are needed for accuracy, as noted in the text.

5.2 The end correction with weak nonlinearity

Before we move on to giving some numerical examples using the nonlinear theory above, we first introduce an application of it: a novel nonlinear generalisation of the end correction. The standard plane-wave end correction problem was introduced along with its higher-frequency generalisation in section 4.1, to which the reader is referred in order to lay the groundwork for what follows here.

It is not obvious how best to introduce nonlinearity to the end-correction problem. The reflection matrix R may be generalised to weak nonlinearity exactly as for the admittance or impedance, giving $\boldsymbol{p}^- = \mathsf{R}\boldsymbol{p}^+ + \mathcal{R}\langle \boldsymbol{p}^+, \cdots \rangle$, but this extra nonlinearity reflects incoming modes into *different* reflected modes, and so does not *directly* affect the end correction; instead, these other reflected modes feed back on the initial mode through weakly-nonlinear propagation along the inner duct. Here, we consider a different nonlinear correction to the reflection matrix that includes both nonlinear scattering at the open end and nonlinear interactions within the duct; this alternative nonlinear reflection matrix then facilitates the calculation of a nonlinear end correction. The linear reflection matrix at the open end, as given above in terms of the admittance (equation 4.5), may also be obtained directly from the acoustic pressure in the duct if a single duct mode (a, α) is excited at the inlet, so that $P^{b+}_{\beta} = A^{a+}_{\alpha}\delta_{\alpha\beta}\delta^{ab}$. We always take $a = 1$ in order to see how a source at the fundamental excites higher harmonics.

In this case, at $s = s_{\rm o}$, we have

$$\frac{\sum_{b=1}^{\infty}\sum_{\beta}(P_{\beta}^{b+})^{*}P_{\beta}^{b-}}{\sum_{b=1}^{\infty}\sum_{\beta}|P_{\beta}^{b+}|^{2}} = \frac{\sum_{b=1}^{\infty}\sum_{\beta,\gamma}(P_{\beta}^{1+})^{*}\mathsf{R}_{\beta\gamma}^{b}P_{\gamma}^{b+}}{\sum_{\beta}|P_{\beta}^{1+}|^{2}} + O(M) = \mathsf{R}_{\alpha\alpha}^{1} + O(M), \qquad (5.33)$$

where '$*$' denotes a complex conjugate and the nonlinear reflection tensor $\mathcal{R}$ is contained within the $O(M)$ term. We may therefore instead define a matricial reflection coefficient $\tilde{\mathsf{R}}$ that includes both the nonlinear propagation in the duct and the nonlinear reflection at the open end by taking

$$\tilde{\mathsf{R}}_{\alpha\alpha}^{1} := \frac{\sum_{b=1}^{\infty}\sum_{\beta}(P_{\beta}^{b+})^{*}P_{\beta}^{b-}}{\sum_{b=1}^{\infty}\sum_{\beta}|P_{\beta}^{b+}|^{2}}, \qquad \Rightarrow \qquad \tilde{s}_{\alpha} = \frac{\arg(-\tilde{\mathsf{R}}_{\alpha\alpha}^{1})}{2\mathrm{Im}(\gamma_{\alpha}^{1})}. \qquad (5.34)$$

where $\tilde{s}_{\alpha}$ is a modified, nonlinear end correction. Note that this definition only holds if the fundamental $a = 1$ is the only mode excited at the inlet, as the vector P_{β}^{b+} must select only a single value of $\tilde{\mathsf{R}}$ and make all others zero upon summation.

An important difference between this calculation and the linear one is that the length and geometry of the duct now matter (since these affect the pressure at the outlet). The amount of steepening that a wave can undergo within the duct will influence its behaviour at the outlet, so the previously 1D parameter space (frequency only) is now 3D (frequency, Mach number and duct length). We choose to fix the frequency and study the 2D relationship between Mach number and duct length for the fundamental frequency ($a = 1$) plane-wave ($\alpha = 0$) coefficient $\tilde{s}_0$: results from this calculation will be shown in section 5.3.2.

5.3 Results

We now make use of the framework described above to compute some numerical examples. These examples are intended to demonstrate a range of different behaviours. While one motivation for this work was investigating the acoustics of musical instruments, we instead concentrate here on basic examples that aid fundamental understanding, which may or may not be relevant to musical instruments. A thorough analysis of musical instruments in particular is left to future studies.

5.3.1 Prediction of the linear end-correction coefficient

We first consider the exit condition in isolation, without needing to solve for the acoustics either inside or outside the duct. We do this by investigating the end correction, introduced in section 4.1, beginning with the linear case. This allows comparison with existing methods, and in particular, with the Wiener–Hopf solution [Noble, 1958], a derivation of which was given in section 4.2. A discussion of the results' physical interpretation is given in section 4.2.3; here we simply focus on validation of the outer-duct

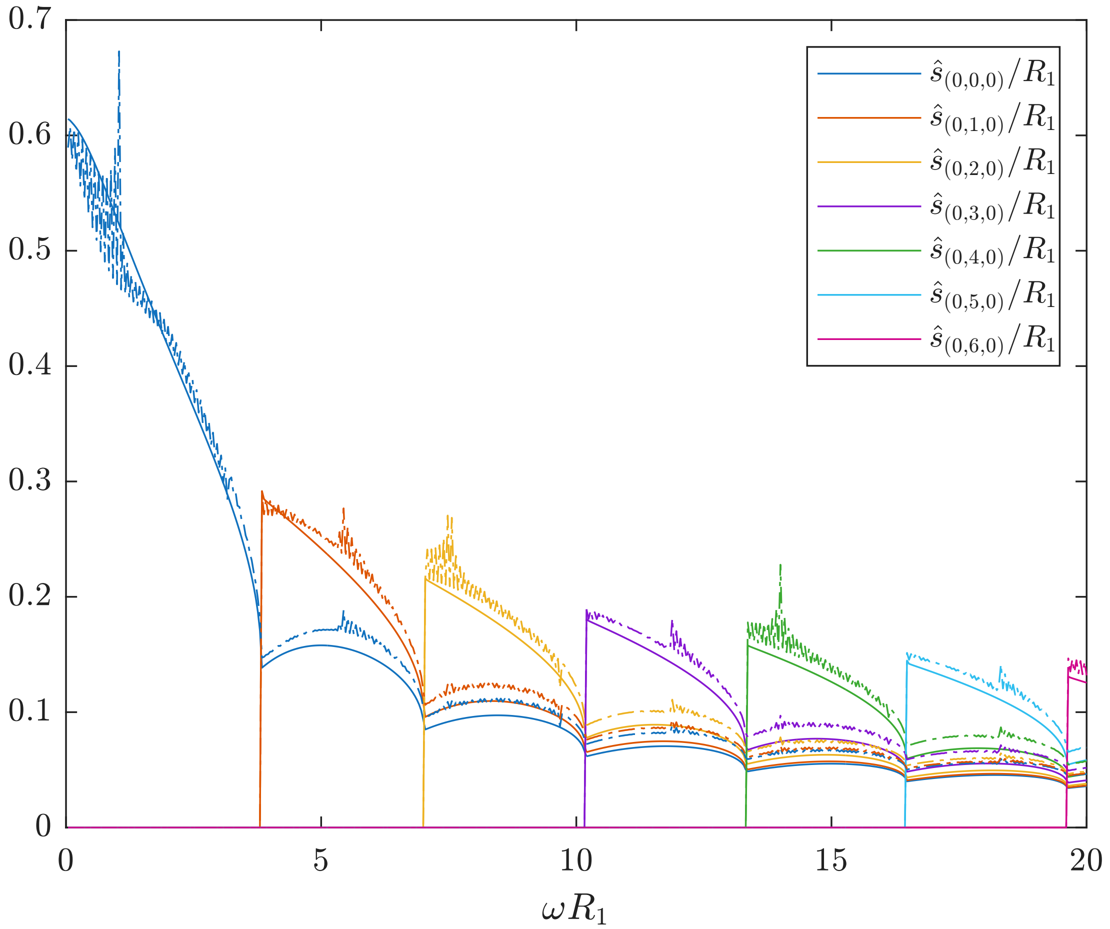

Figure 5.2: End-correction coefficients for a 3D duct with an azimuthally invariant source, calculated using the Wiener–Hopf technique (solid line) and our outlet condition (dash-dotted line). 8 modes were used in the inner duct and 1200 in the outer duct, with a duct width ratio of 1/40.

method.

The end correction in 3D

Figure 5.2 plots the end correction for various modes as a function of nondimensionalised frequency (the Helmholtz number, ωR_1) for a 3D duct exit. Convergence will be studied further in the 2D case below; taking inspiration from it in the meantime, results here are produced with a width ratio of $\eta = 1/40$, with 8 modes used in the inner duct. As the modal basis in 3D is more complicated than in 2D (and requires lots of numerical integration of Bessel function products) only 1200 modes were used in the outer duct: a valid mode ratio, given that $\eta = 1/40$ is still considerably larger than 8/1200. This proves a reasonable parameter choice, with relatively good agreement between the numerics and the Wiener–Hopf solution, and with the numerical solution's oscillations being of lower amplitude than for a more moderate modenumber ratio. Once more the

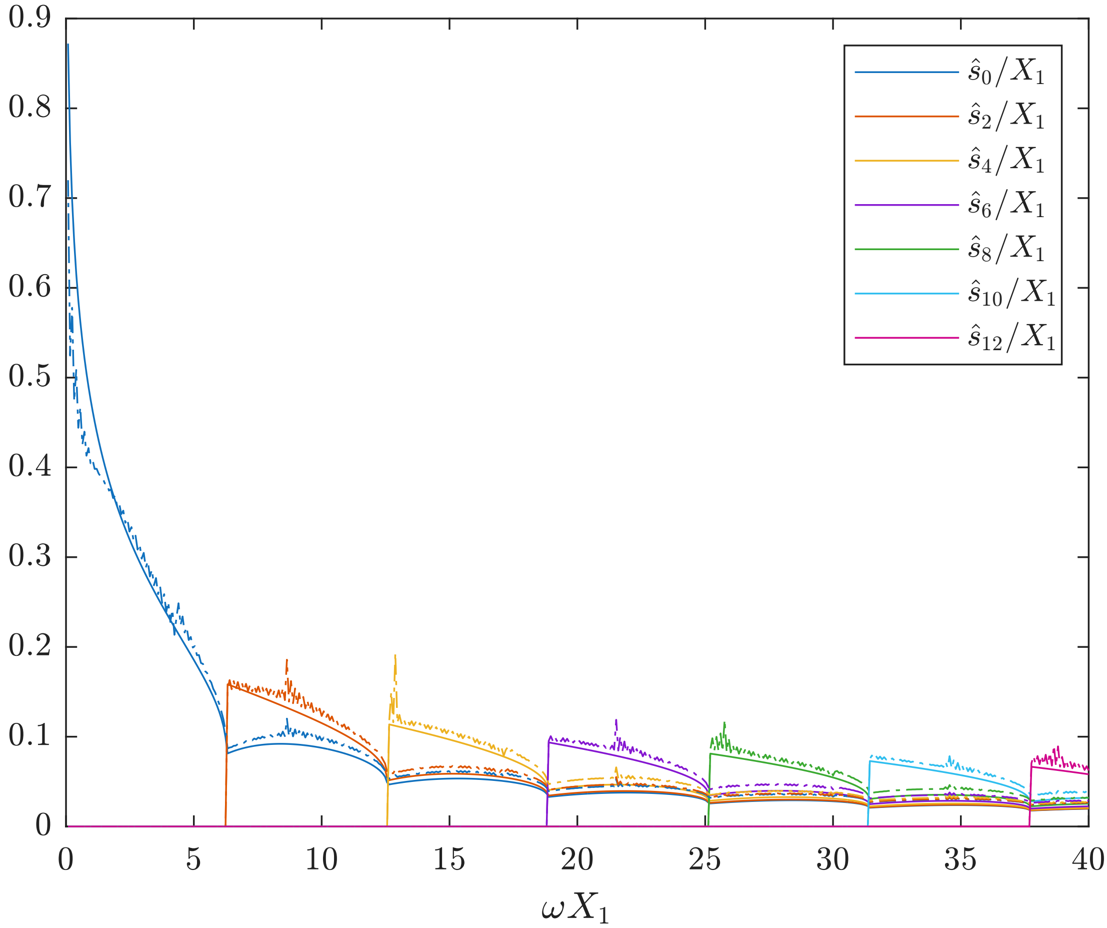

Figure 5.3: End-correction coefficients for a 2D duct with a symmetric source, calculated using the Wiener–Hopf technique (solid line) and our outlet condition (dash-dotted line). 13 modes were used in the inner duct and 2000 in the outer duct, with a width ratio of 1/40.

end correction curves show sharp cusps as the modes cut on, unlike those in Snakowska et al. [2011]; having verified that the Wiener–Hopf solution and our own method agree on this, we conclude that this is physical and not a numerical artefact (a conclusion which also agrees with the 2D case below).

The end correction in 2D

Figure 5.3 plots the end correction for various modes as a function of the Helmholtz number ωX_1 for a 2D duct. This is again in agreement with the analytical Wiener–Hopf solution (also plotted in figure 5.3), as it shows sharp increases at mode cut-ons, and a logarithmic singularity as the frequency tends to zero (physical implications of this singularity were discussed in section 4.2.3).

The end correction as a convergence study

This example (i.e. the end-correction coefficients in 2D) is useful for validating the above modelling and its numerical implementation, at least in the linear regime, and is also useful as a yardstick for parameter choices later on. In figure 5.3, at least 13 spatial modes were required in the inner duct in order to show which will go from cut-off to cut-on for the chosen frequency range. A reasonable, not-too-computationally-intensive choice for the outer duct is to use $\alpha^2_{\text{max}} = 2000$ modes, since the 2000 modes will only be used for calculating admittances at one location, and we do not need to solve 2000 coupled ODEs for any propagation away from this location. According to the $\eta \geq \alpha^1_{\text{max}}/\alpha^2_{\text{max}}$ rule, this makes the most extreme possible width ratio $\eta = 13/2000 (\approx 0.0065)$. Using this value, however, our calculation noticeably overshoots the Wiener–Hopf solution to a large degree, and so we will choose our parameters more cautiously. The other extreme is when the inner and outer ducts are too similar in size and there is too much reflection from the outer duct walls. For the end-correction this manifests as large oscillations as the frequency is increased, due to modes cutting on in the outer duct. We can calculate the wavelength of the oscillations as follows: for the fundamental frequency $a = 1$, the cut-on frequency of mode α in the outer duct is $\alpha\pi/X_2 = \eta\alpha\pi/X_1$, so in figure 5.3, where only even modes are excited, a new outer-duct mode cuts on each time the frequency is increased by $2\eta\pi$ (≈ 0.16 in figure 5.3). The amplitude of the oscillations seems to increase as this frequency increment increases, and presents a problem even for ratios as low as $\eta = 1/20$; thus, we opt for a lower ratio of $\eta = 1/40$, which is seen in figures 5.2 and 5.3 to give reasonable results.

To further demonstrate the appropriateness of our choice of numerical parameters, we plot the end-correction coefficient $\hat{s}_2$ as calculated for various values of α^2_{max} and η in figure 5.4, alongside the Wiener–Hopf solution in black. This is a zoomed-in section of figure 5.3, focussing only on Helmholtz numbers between the $\alpha = 2$ mode's cut-on and that of the next mode up (i.e. between 2π and 4π).

We see that the option we chose ($\eta = 1/40$ and $\alpha^2_{\text{max}} = 2000$, shown by the dashed orange line) is the closest to the Wiener–Hopf solution. We also see that if we restrict α_{max} to 200 (while keeping $\alpha^1_{\text{max}} = 10$), the $\eta = 1/10$ option (solid, orange), while oscillating much more than the $\eta = 1/40$ option (dotted, orange), actually has an average value much closer to the Wiener–Hopf one, and never exceeds the $\eta = 1/40$ value in its inaccuracy, thus making more moderate values of η a better choice for more moderate modenumber ratios. This is because smaller values of η correspond to a smaller duct exit on the scale of the outer duct width, and therefore require higher resolution in the outer duct to correctly resolve. This phenomenon is also demonstrated when comparing values of η for fixed $\alpha^2_{\text{max}} = 2000$: the $\eta = 1/40$ line (dashed, orange) from figure 5.3 is consistently closer to the Wiener–Hopf value than the $\eta = 1/100$ line (dot-dashed, orange), proving the same point.

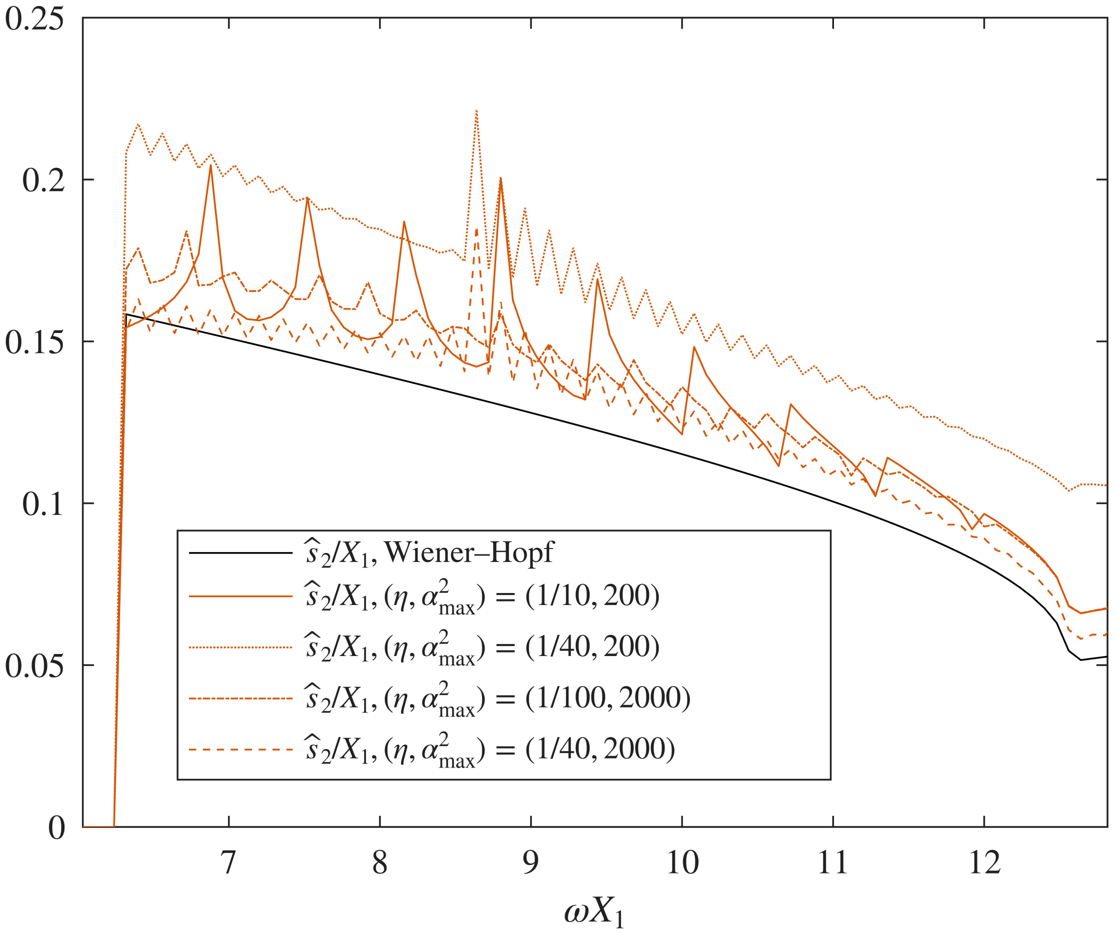

Figure 5.4: Comparison of different numerical parameter choices for a segment of figure 5.3 between 2π and 4π, with only the $\alpha^1 = 2$ mode shown. The Wiener–Hopf solution is plotted in black, and the original parameter choice $(\eta, \alpha^2_{\mathrm{max}}) = (1/40, 2000)$ from figure 5.3 is shown plotted with a orange dashed line as before. All of these take $\alpha^1_{\mathrm{max}} = 10$.

5.3.2 The generalised nonlinear end-correction coefficient

Since the analysis here involves not only linear but also weakly-nonlinear effects, we may investigate the effect of changing the amplitude on the position of the end correction using the results of section 5.2. Two examples are provided here: a low-frequency example in 3D and an intermediate-frequency example in 2D.

Low frequency in 3D

Figure 5.5 shows values of the generalised nonlinear end correction coefficient $\tilde{s}_0/R_1$ (given by equation 5.34) for a fixed low frequency of $\omega R_1 = 0.05$, while the duct length and Mach number are varied. In order to capture the effects of nonlinearity 10 temporal modes were used; for an accurate calculation in the inner duct this was paired with $\alpha^1_{\mathrm{max}} = 8$. Nonlinearity also requires third-rank tensors, which in the outer duct can become expensive memory-wise: as such, we used only 200 modes in the outer duct,

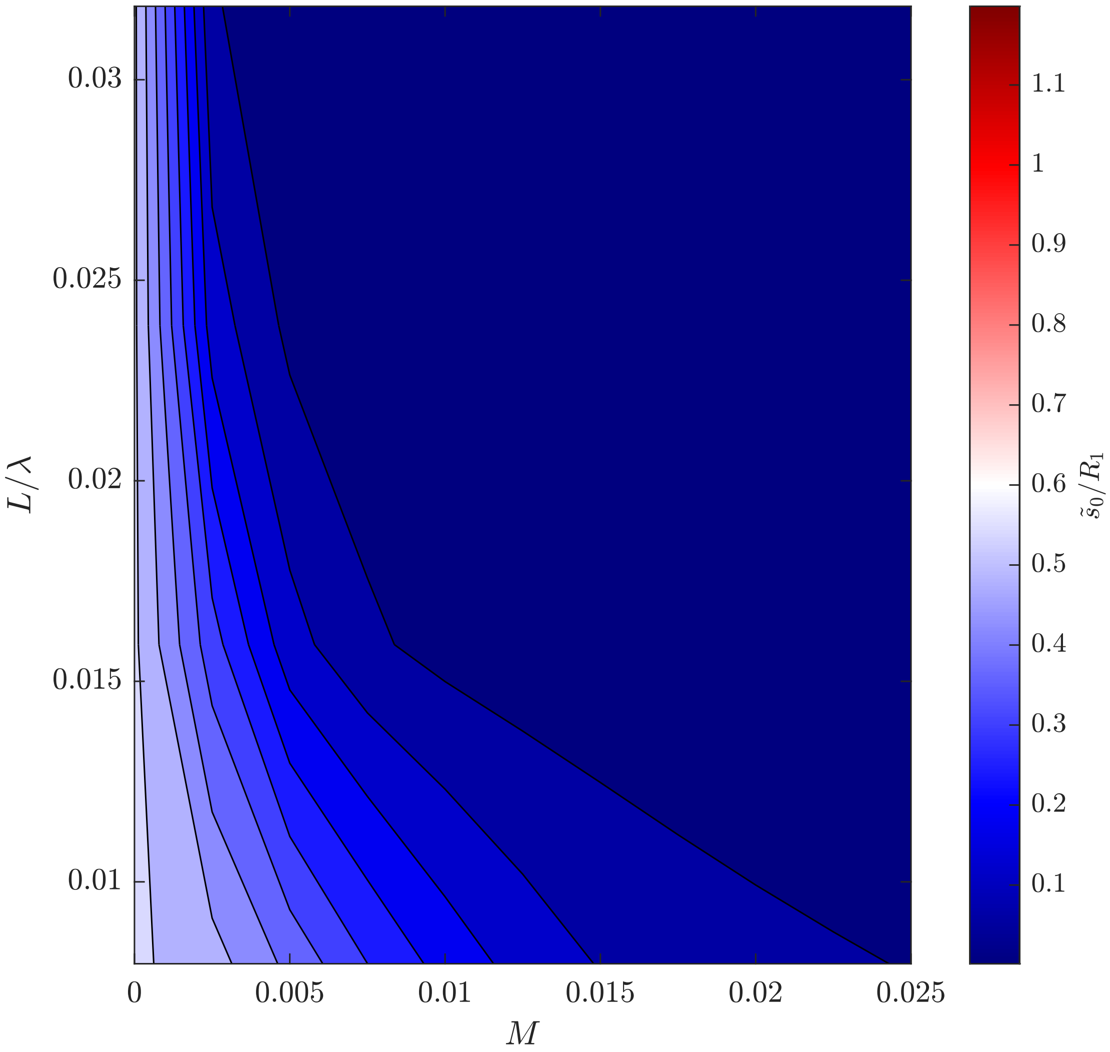

Figure 5.5: The nonlinear generalised end correction coefficient $\tilde{s}_0/R_1$ for fixed Helmholtz number $\omega R_1 = 0.05$ and a range of duct lengths (scaled by source wavelength $\lambda = 2\pi/\omega$) and Mach numbers, in 3D. Nonlinearity is shown to have a dampening effect on the discrepancy between duct length and resonant length for low frequencies, and the longer the duct the stronger this effect will be. 8 modes were used in the inner duct and 200 in the outer duct, with 10 temporal modes and a width ratio of 1/10.

making $\eta = 1/10$ a good intermediate width ratio choice (although the linear value of $\tilde{s}_0 \approx 0.6R_1$ is slightly undershot). We see that in the linear case, the duct length plays no role as expected; once the Mach number is increased, however, the end correction quickly decays to zero. For longer ducts, the wave has steepened more by the outlet, so zero is reached for smaller Mach number. Loosely, this suggests that if an instrument is played close to its resonant frequency, higher volume means a shorter resonating length, i.e. higher frequency and a correspondingly sharper pitch.

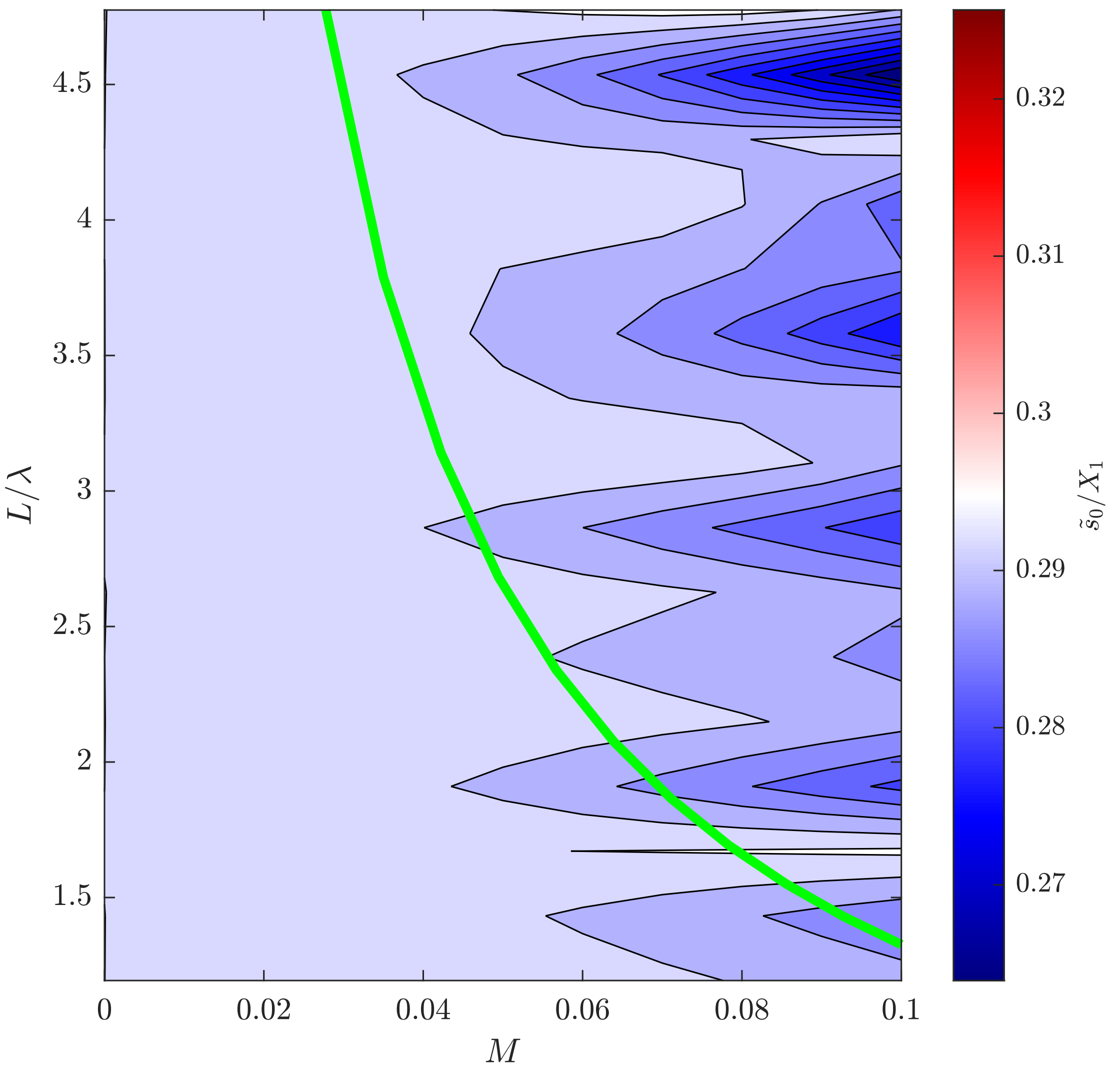

Figure 5.6: The nonlinear generalised end correction coefficient $\tilde{s}_0/X_1$ for fixed Helmholtz number $\omega X_1 = 3$ and a range of duct lengths (scaled by source wavelength $\lambda = 2\pi/\omega$) and Mach numbers, in 2D. We see that for an intermediate frequency, the end correction remains the same or decreases depending on the duct length. 8 modes were used in the inner duct and 200 in the outer duct, with 10 temporal modes and a width ratio of 1/10. The shock formation distance, given by $L_{\mathrm{sf}} = 1/M\beta_0\omega$, for β_0 the coefficient of nonlinearity, is shown in green (and has also been normalised by X_1 here).

Intermediate frequency in 2D

Figure 5.6 shows values of the generalised nonlinear end correction coefficient $\tilde{s}_0/X_1$ for a fixed intermediate frequency of $\omega X_1 = 3$ while the duct length and Mach number are varied. As with the previous example, here $(\alpha^1_{\max}, \alpha^2_{\max}, \eta) = (8, 200, 1/10)$. Once again, the linear value is length-independent, but this time as the Mach number is increased the end correction decays for certain duct lengths and remains constant for others. For ducts as long as three wavelengths or more, we start to see that the end correction decreases more sharply if the duct length is an odd multiple of a half-wavelength, i.e.

there is a pressure node at one end and an antinode at the other. This is consistent with the fact that when a sine wave steepens into a sawtooth, the antinodes get much closer to the half-wavelength nodes, while remaining far away from the full-wavelength nodes: thus, a small deviation from the former position results in vast pressure variation (something that might drive resistance to the end-correction phenomenon) whereas a deviation from the latter position results in roughly linear-acoustic behaviour.

5.3.3 Resonances in a finite-length duct in 3D

We next consider the effect of the open duct exit on the resonances of the inner duct. There are multiple ways to calculate the resonances in a duct of finite length. One method is to consider the impedance at the duct inlet. Physical instruments can have either one or two openings (described as 'closed' or 'open' ducts respectively). If the duct is 'closed', we expect a minimum in the velocity at the inlet, corresponding to a very high impedance. Conversely, if it is open, the free-space condition at the inlet will result in a pressure minimum, i.e. a low impedance. Here, we define a scalar impedance as

$$|Z| = \sqrt{\frac{\sum_{a=-\infty}^{\infty}\sum_{\alpha=0}^{\infty}|P_\alpha^a|^2}{\sum_{a=-\infty}^{\infty}\sum_{\alpha=0}^{\infty}|U_\alpha^a|^2}}, \tag{5.35}$$

and calculate it at the inlet for a range of frequencies, driven by a plane-wave source at the same location. Using this, we can infer information about the tone and harmonic series of the duct in question.

In figure 5.7, these calculations are performed for 3D ducts of varying aspect ratio, taking $(\alpha^1_{\max}, \alpha^2_{\max}, \eta) = (8, 1200, 1/40)$. The maxima occur (roughly) at odd-integer frequency multiples of the first maximum (or *closed-duct fundamental*), consistent with the harmonic series of a 'closed' instrument admitting oscillations of a quarter-wavelength and all odd multiples thereof. The minima, meanwhile, occur (roughly) at integer multiples of the first minimum (or *open-duct fundamental)*, consistent with the harmonic series of an 'open' instrument admiting integer multiples of a half-wavelength.

Also notable are the variations in the magnitude of the maxima/minima across different aspect ratios. More pronounced maxima/minima occur for more extreme aspect ratios; this agrees with the fact that broad organ pipes have a tone much more fundamental-dominated than slender ones. Between plots (c) and (d) in figure 5.7 we are able to assess the difference that a bent duct makes: the slightly split resonance at the 8th peak in (c) is much more clearly split in (d), and peaks beyond that point have lower amplitude in (d). Figure 5.8 shows the duct geometries used to generate figure 5.7, together with the acoustics within each duct at the third closed resonant frequency in each case (corresponding to the third maximum in figure 5.7). It is notable that the largely plane-wave oscillations are disrupted only at the outlet, where particularly in (a) the characteristic 'cap' causing the end-correction effect may be seen.

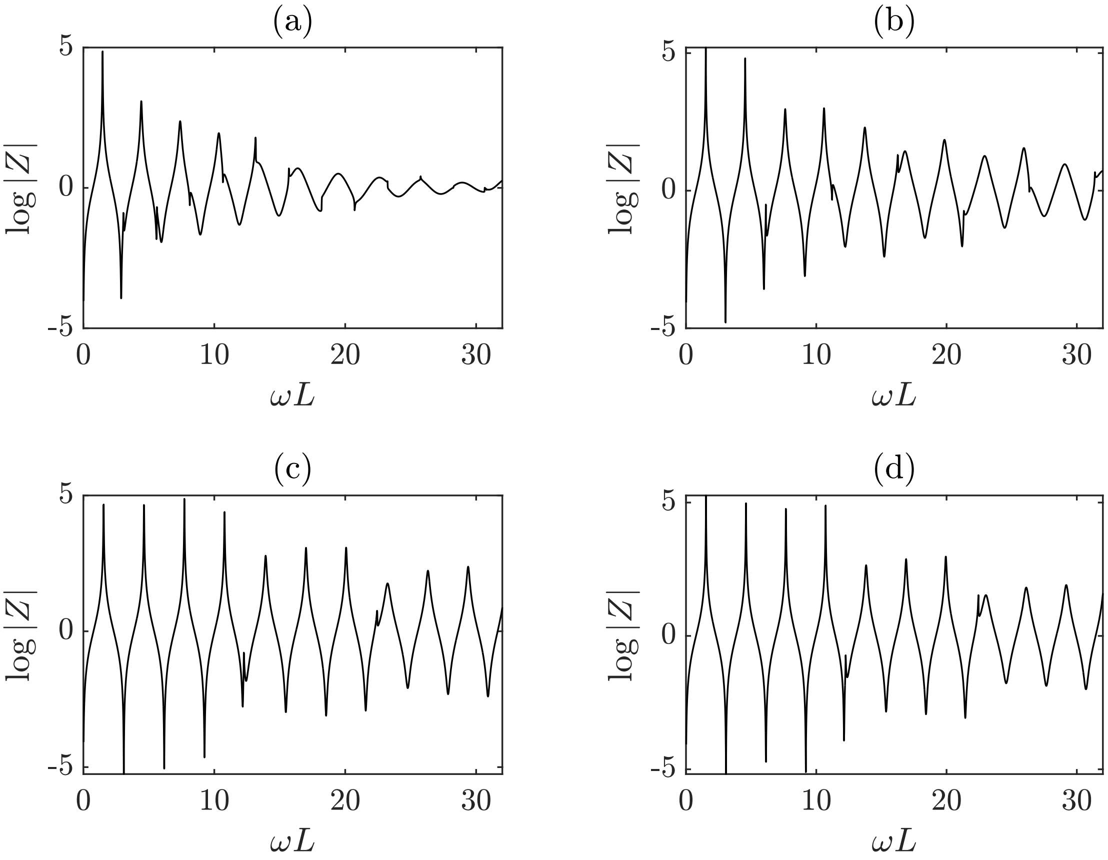

Figure 5.7: Inlet scalar impedance plots using (5.35) for a range of frequencies in 3D, for (a) a straight duct of aspect ratio 1/4; (b) a straight duct of aspect ratio 1/8; (c) a straight duct of aspect ratio 1/16; and (d) a duct of aspect ratio 1/16 undergoing a constant-curvature bend of angle $\pi/2$. 8 modes were used in the inner duct, 1200 in the outer duct, and the width ratio was 1/40.

5.3.4 Linear radiation from an acoustic source

Having until now considered the admittance in the inner duct without calculating in the outer duct, here we calculate the acoustic field in the outer duct without considering the inner duct's acoustics. The pressure field in the outer duct due to a plane-wave sound source located at the inner-duct exit in 2D is plotted in figure 5.9. In order to obey the conditions mentioned in section 5.3.1 while also having few enough modes to allow for solution of the governing equations in the outer duct, this figure was generated using $(\alpha^1_{\text{max}}, \alpha^2_{\text{max}}, \eta) = (10, 200, 1/10)$. We see that the absorbing boundary condition on the 'acoustic wormhole' surface has resulted in radiation travelling predominantly rightward from the outlet: this suggests that the absorbing condition is a reasonable workaround for the problem of the intersecting inner-duct and outer-duct geometries. The effect of the hard outer-duct walls is clearly present to the right of the source, giving the typical interference pattern, which is also the cause of the rapid oscillations in the end correction seen in figures 5.2 and 5.3, although the expected circular wave-fronts

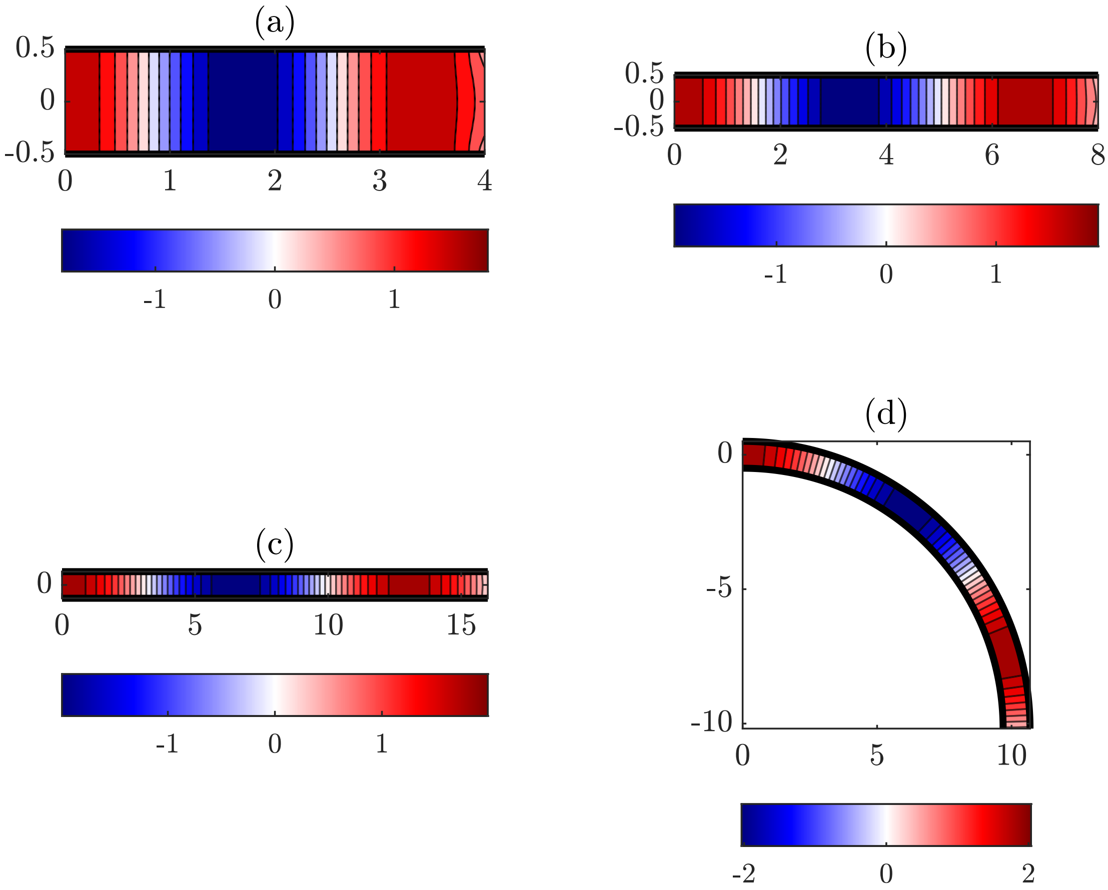

Figure 5.8: Linear acoustic field within a duct opening into another duct 10 times larger, in 3D, for (a) a straight duct of aspect ratio 1/4; (b) a straight duct of aspect ratio 1/8; (c) a straight duct of aspect ratio 1/16; and (d) a duct of aspect ratio 1/16 undergoing a bend of angle $\pi/2$. Each duct has a source at the inlet of frequency equal to that of the duct in question's third closed resonance (as calculated in figure 5.7). 8 modes were used in the inner duct, 1200 in the outer duct, and the width ratio was 1/40.

emanating from the source are clearly visible despite this.

5.3.5 Linear radiation from a straight duct

In contrast to the previous section, we can also choose to calculate the inner-duct acoustic field to see how sound generated by a plane-wave source within the duct subsequently exits from the duct outlet. This is shown in 2D in figure 5.10, and in 3D in figure 5.11, both with the same width ratios and numbers of modes as the previous example in figure 5.9.

Comparing the 2D duct (figure 5.10) with a 2D source (figure 5.9), we unsurprisingly see great similarity. Comparing the 2D duct (figure 5.10) with the 3D duct (figure 5.11), it is clear that, compared with the duct interior, the radiation from the outlet in 3D has a much lower amplitude than in 2D, as the decay rate in 3D is $1/r$ with distance from the exit while it is $1/\sqrt{x}$ in 2D. However, the acoustics within the

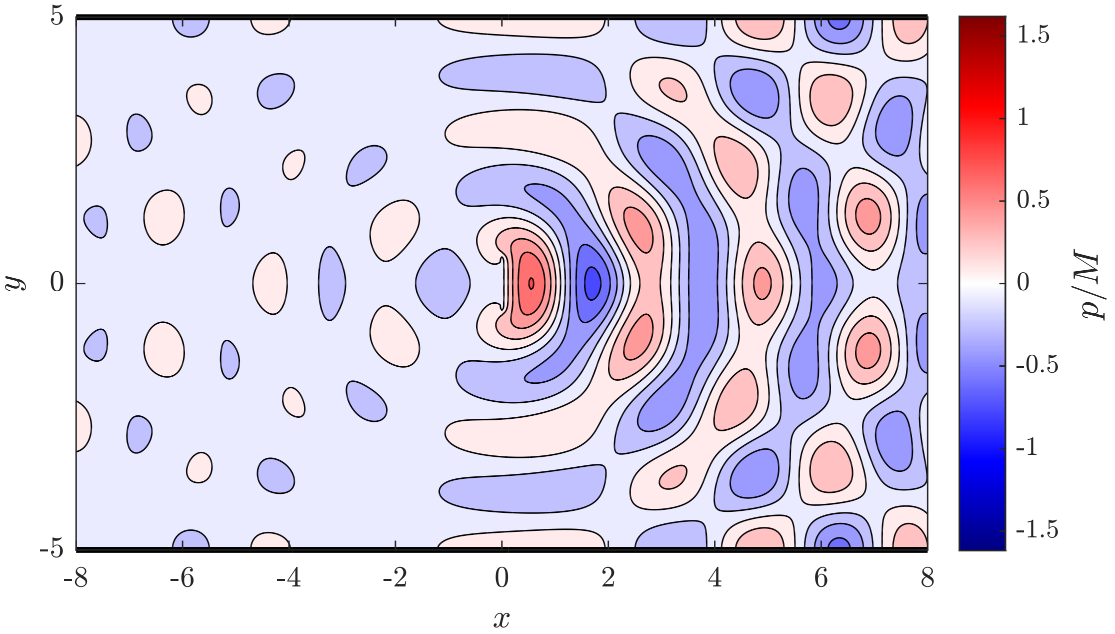

Figure 5.9: Linear acoustic field emanating from a 1D acoustic source into a 2D duct 10 times larger. 10 modes were used in the inner calculation and 200 modes in the outer, with $\omega X_1 = 3$ for X_1 the inner width.

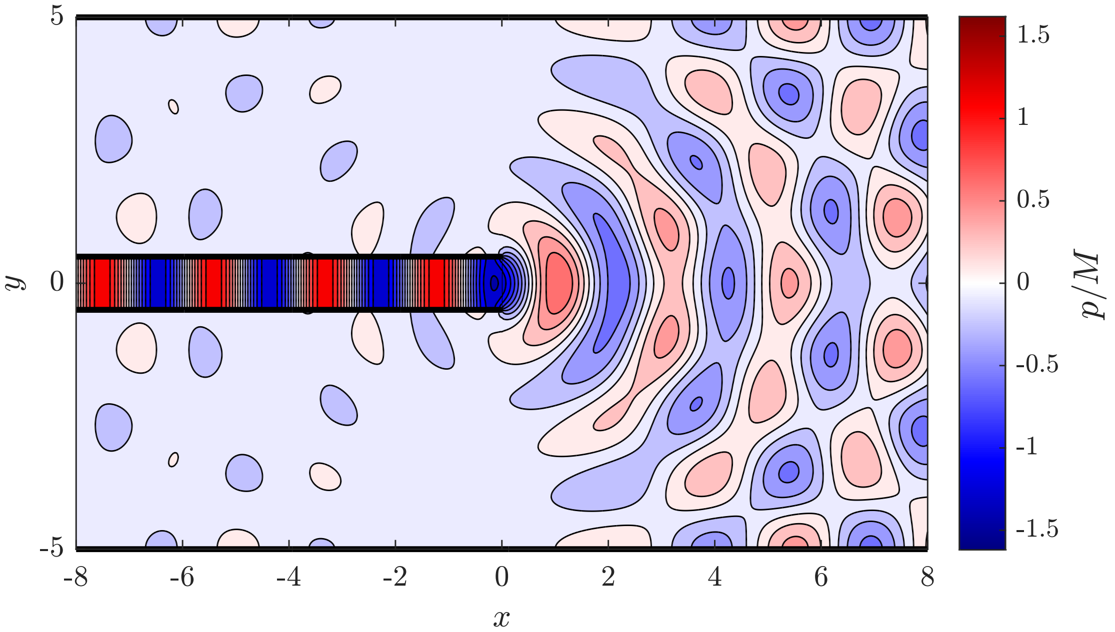

Figure 5.10: Linear acoustic field emanating from a straight duct into a duct 10 times larger, in 2D. 10 modes were used in the inner calculation and 200 modes in the outer, with $\omega X_1 = 3$ for X_1 the inner width.

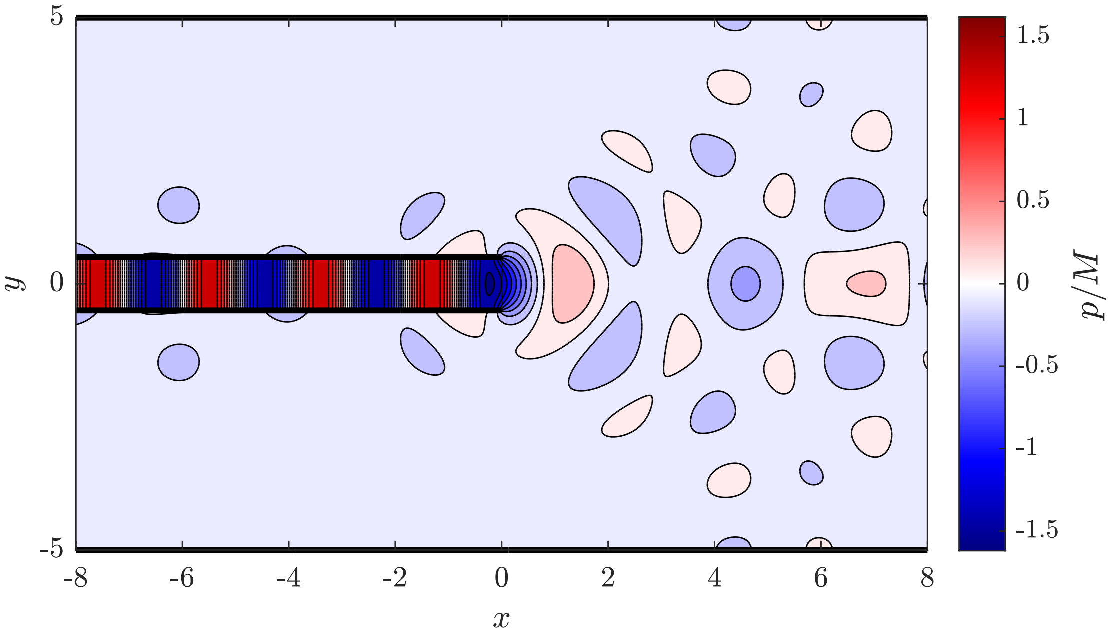

Figure 5.11: Linear acoustic field emanating from a straight duct into a duct 10 times larger, in 3D. 10 modes were used in the inner calculation and 200 modes in the outer, with $\omega R_1 = 3/2$ for R_1 the inner radius.

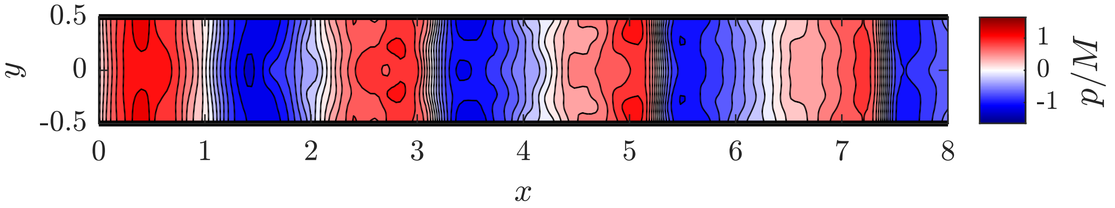

Figure 5.12: The nonlinear acoustic field within a straight duct, with a perturbation Mach number of $M = 0.10$, opening into a duct 10 times larger (outer duct not plotted), in 2D. 10 modes were used in the inner calculation and 200 modes in the outer, with $\omega X_1 = 3$ for X_1 the inner radius.

inner ducts appear to behave similarly between the two cases.

5.3.6 Nonlinear acoustics within an open straight duct in 2D

We can also calculate the acoustic field in a straight duct with an open end in the nonlinear regime, shown in the 2D case in figure 5.12 for a perturbation Mach number of $M = 0.10$. This is calculated using the same values of $(\alpha^1_{\max}, \alpha^2_{\max}, \eta) = (10, 200, 1/10)$ as above, with $a_{\max} = 10$. Extending this calculation to the outer duct is computationally costly, due to the vastly greater number of spatial modes required, but we can still apply the radiation condition and see what effect it has on the acoustics within the inner duct without incurring this extra expense. An immediately noticeable physical effect of the open end that is not achieved with the idealised characteristic boundary condition from chapter 3 is that non-plane waves are excited: since the excitation at

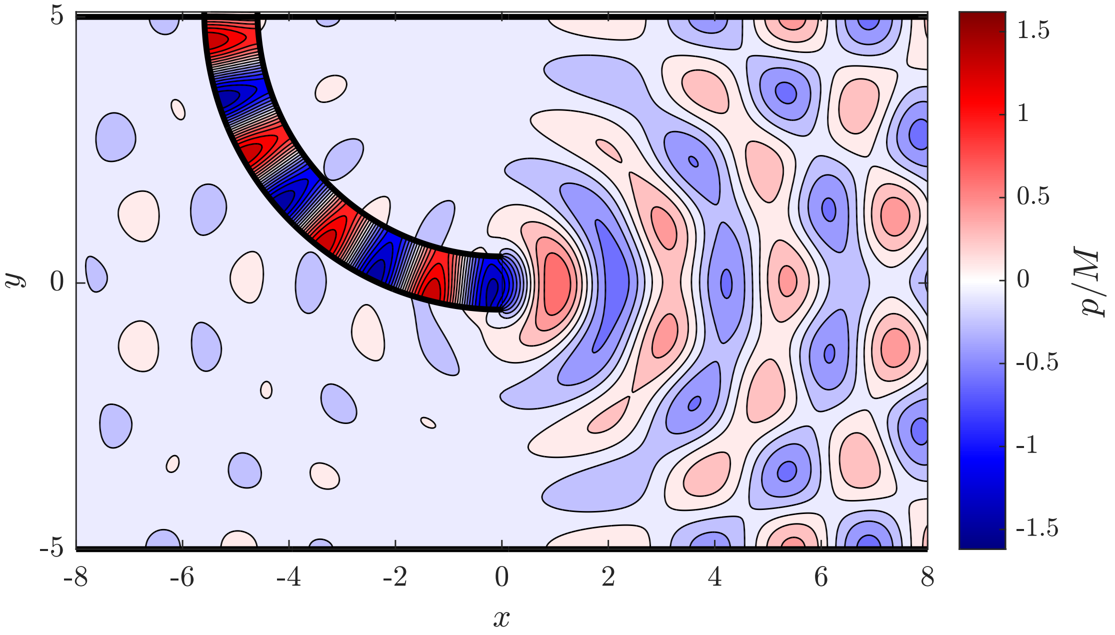

Figure 5.13: Linear acoustic field emanating from a fully-curved duct into a duct 10 times larger, in 2D. 10 modes were used in the inner calculation and 200 modes in the outer, with $\omega X_1 = 3$ for X_1 the inner radius.

the inlet is purely planar, this nonplanarity is due to the geometry of the outlet, and nonlinear reflections back from it. In the linear case, the non-plane reflections are not significant, as seen in figure 5.10, but here they are very clearly visible.

5.3.7 Linear radiation from a curved duct in 2D

Fully-curved duct

The next case we consider is that of radiation from a curved duct into a larger straight duct, in 2D, shown in figure 5.13. As before, this example was computed using the parameters $(\alpha^1_{\text{max}}, \alpha^2_{\text{max}}, \eta) = (10, 200, 1/10)$. We can see that despite the asymmetry of the source, the radiation from the end is almost symmetric across the midline. Since symmetric and antisymmetric waves are completely uncoupled in the outer duct, this suggests that the radiation from the inner duct is predominantly symmetric, with any anti-symmetric inner-duct modes being almost totally reflected from the open end. The geometry shown here demonstrates the model's versatility, since the duct exit is not restricted to being a straight section of duct; this could be useful for modelling some musical instruments (for example, the French horn) which have a notable duct curvature at the bell.

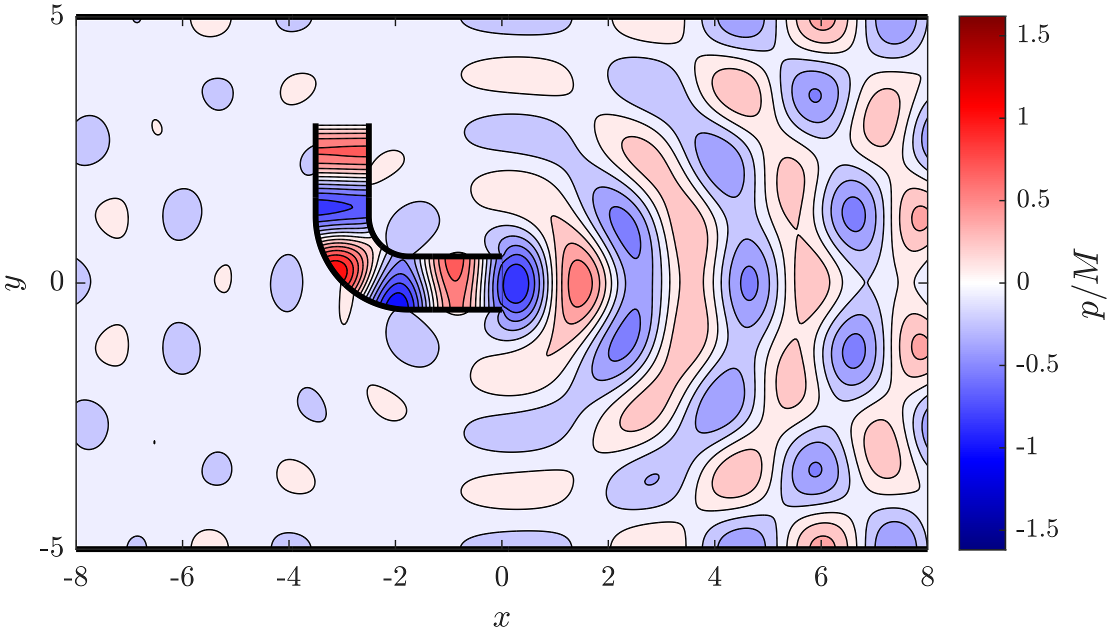

Figure 5.14: Linear acoustic field emanating from a partially-curved duct into a duct 10 times larger, in 2D. 10 modes were used in the inner calculation and 200 modes in the outer, with $\omega X_1 = 3$ for X_1 the inner radius.

Partially-curved duct

The last example was a fully-curved version of the straight ducts we have been considering in this section. We may also consider an open-ended version of the duct from section 3.9. Figure 5.14 shows the result of this calculation, performed with the usual parameters $(\alpha^1_{\max}, \alpha^2_{\max}, \eta) = (10, 200, 1/10)$. Once again, we see predominantly-symmetric radiation suggesting near-total reflection of antisymmetric modes backwards into the inner duct from its open end, and this time we also see a possible standing-wave pattern in the antisymmetric modes within the inner duct owing to inward-propagating antisymmetric modes being reflected by the bend.

5.3.8 Linear radiation from an exponential horn in 2D

The exponential horn is a useful object of study due to the existence of an approximate analytical solution [Webster, 1919]. Comparisons with this analytical solution for a duct with the characteristic admittance at the outlet were made in McTavish and Brambley [2019] and chapter 3; it was found that the approximate analytical solution's assumption of solely plane-wave propagation gave a poor quantitative agreement with the higher fidelity numerics, although the qualitative trends were correct. In figure 5.15 the same duct is used, but this time the waves are allowed to exit from the outlet into a larger domain. For this calculation, it was very clear that the choices of $\alpha^1_{\max} = 10$ and $\alpha^2_{\max} = 200$ used above were seriously under-resolving the acoustics at the outlet, likely due to the very steep duct width increase. As such, here the results were calculated

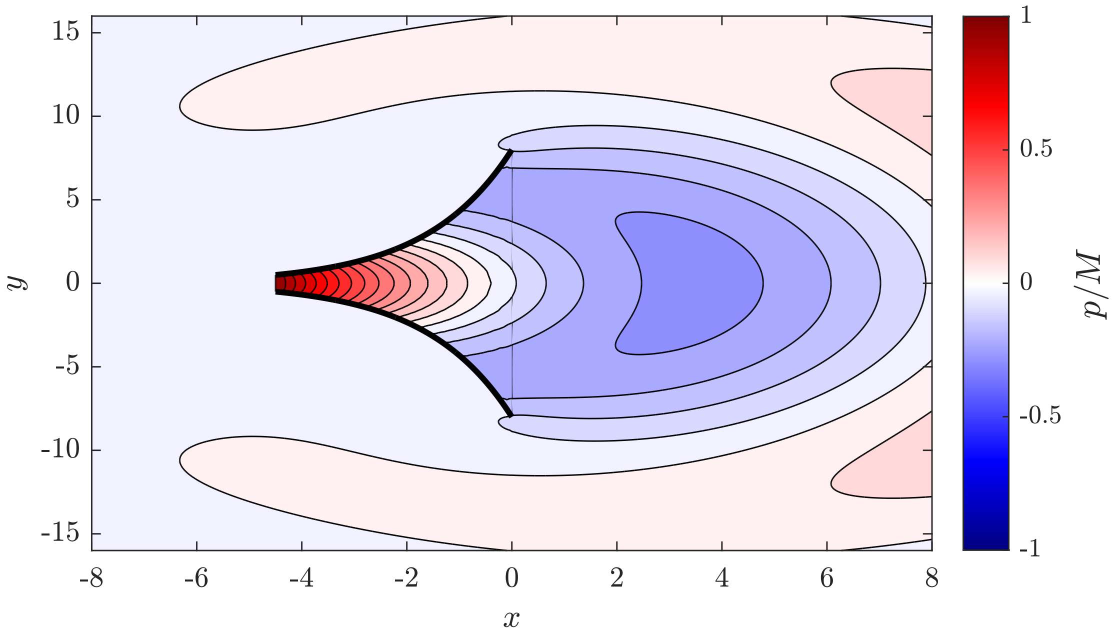

Figure 5.15: Linear acoustic field emanating from an exponential horn into a duct 10 times larger, in 2D (this plot shows a zoomed-in section of the outer duct, in order for the complete inner domain to be clearly visible). 40 modes were used in the inner calculation and 800 modes in the outer, with $\omega X_1 = 3$ for X_1 the inner radius.

using four times more modes while maintaining the width ratio of $\eta = 1/10$, resulting in $(\alpha^1_{\max}, \alpha^2_{\max}, \eta) = (40, 800, 1/10)$ and giving well-resolved results. From figure 5.15, it is observed that this outlet shape allows for more even distribution of the radiation both behind and in front of the outlet, compared with other geometries. This is both a confirmation of this geometry's favourability for musical instrument design and also a demonstration of the importance of accurate boundary conditions, given that this effect would be completely unobservable with the previously-used characteristic outlet boundary condition (see McTavish and Brambley [2019] figure 5, or alternatively figure 3.10 here).

Chapter 6

Conclusion

This thesis has formulated a model for the internal acoustics of ducts with complex geometries in 2D and 3D, taking weak nonlinearity into account. It has then extended the model to include the duct exit, allowing for modelling of resonance and external propagation in the weakly nonlinear regime. An effective model of sound in brass instruments must be able to include complex geometry, weak nonlinearity and a duct exit: this work therefore has a clear application.

Chapter 2 saw the development of a numerically tractable mathematical framework for modelling weakly-nonlinear acoustics in curved ducts of varying width. The framework unifies both 2D and 3D governing equations, and allows for torsion in 3D. The numerical advantage conferred by the framework is that it may be written in terms of large matrices and tensors that are invariant along the duct, unlike previous work in 2D where the large matrices and tensors varied with the duct geometry and therefore needed computing at each cross-section along the duct [McTavish and Brambley, 2019]. The method follows the multi-modal method of Félix and Pagneux [2001, 2002], solving first for the admittance (a generalized ratio of acoustic velocity to acoustic pressure) throughout the duct from the outlet to the inlet, and then using this admittance to calculate the acoustic pressure and velocity from the inlet to the outlet. This has the advantage that the effects of the duct geometry are encoded in the admittance and may be analyzed independently of the particular acoustic source used. The unification of 2D and 3D allows for comparison between the two cases (demonstrated in chapter 3).

While the additional physics presented in chapter 5 would need consideration for effective modelling of resonance and external acoustic radiation, the framework presented in chapter 2 is still suitable for the modelling of internal duct acoustics. This was the focus of chapter 3. First, the method was validated for a range of duct geometries where there are known analytical solutions or published numerical results. Nonlinear steepening was validated against the Fubini [1935], Blackstock [1966], and Fay [1931] solutions for a straight duct in section 3.2. Width variation in the linear case was validated against the Webster [1919] solution for an exponential horn in section 3.5;

this test case highlights the inaccuracy of approximating the full sound field by a plane wave in Webster's solution, which can be reproduced in our framework by restricting our solution to a single spatial mode or relaxed by allowing for many more spatial modes. Curvature was validated in 2D in section 3.3, in the linear regime against a result of Félix and Pagneux [2001] and in the nonlinear regime against a result for the same geometry of McTavish and Brambley [2019]. The 3D equivalent in section 3.4.1 was validated against a result of Félix and Pagneux [2002] in the linear regime, and against an unpublished result of McTavish [2018] in the nonlinear regime. This extensive validation gives confidence that the combination of width variation, curvature, and nonlinearity is correctly modelled both in the mathematical framework and its numerical implementation.

A number of duct geometries were then investigated numerically. These included a demonstration of wave leakage, where the inclusion of either slight curvature or slight nonlinearity can cause waves to propagate through a duct in which they would otherwise have been totally reflected (section 3.7). Examples with torsion in 3D (section 3.8) show plane waves becoming localized on the outside of the duct curve. The unification of 2D and 3D equations allows for the comparison of the two in section 3.9, showing that between 2D and 3D, wave steepening appears comparable but the effective acoustic length of a bend is different.

The effective length of a bend was investigated further in 2D in section 3.10. By considering the time lag in a wave propagating around a bend, a *bend correction factor* B was introduced, taking the value $+1$ for a wave propagating around the outside of the bend and -1 for a wave propagating around the inside of the bend. These results are presented in figure 3.24, and suggest that for higher curvature bends nonlinearity plays a bigger role in forcing wave propagation around the outside of the bend, whereas for lower curvature bends, the curvature takes over as the determining parameter. This tool could potentially be used in the future to investigate whether resonant frequencies are likely to change when the sound amplitude is varied.

Another topic of study was how to quantify reflections due to a bend. In section 2.2.3, we introduced splitting operators that decompose the pressure into forward- and backward-travelling components. These may be formulated strictly in terms of the straight-duct characteristic admittance, or alternatively we may also use the characteristic admittance which takes curvature into account: when applied to a geometry with continuous walls but discontinuous curvature (as is done in section 3.4.2), the differences between the resulting decompositions are stark. The former produces a continuous decomposition that appears to show constant reflection as a wave travels around a bend, and the latter produces a discontinuous decomposition that appears to show sudden reflections at each change of curvature. The competing definitions pose more of a philosophical question than a mathematical one, i.e. not how a reflected wave *can* be defined (which is answered in section 2.2.3) but rather how it *should* be defined.

Chapters 2 and 3 also covered the formulation and testing of a novel weakly-nonlinear Magnus–Möbius scheme for dealing with singularities in the admittance. An ordinary Runge-Kutta solver cannot integrate across a singularity, but when solving for the admittance, which is a ratio of velocity to pressure, a node in the pressure creates a singularity. Singularities can be 'damped' by the use of a complex wavenumber, but it is demonstrated in section 3.6 that this has a detrimental effect on the accuracy of the solution, and that the Magnus–Möbius scheme produces more accurate results. Work on the novel weakly-nonlinear extension to the scheme is at an early stage, but promising results for a straight duct with no admittance singularities were presented in section 3.2.1.

Chapter 4 took a break from nonlinear modelling to focus on the duct exit in the linear regime, a particular application of which is the end-correction problem. Originally, Rayleigh [1871] gave an empirically-calculated figure of 0.6 duct radii for the difference between the actual duct length and the acoustic resonating length; this end correction has since been modelled analytically in the plane-wave case [Levine and Schwinger, 1948] and been generalised to higher frequencies [Weinstein, 1948], using the Wiener–Hopf technique. A derivation of this (guided by Noble [1958]) is given in chapter 4, after which its solution is plotted and discussed. It is interesting to note from the Wiener–Hopf result in figure 4.1 that the classical 3D end correction of $0.6R$ is only valid at very low Helmholtz numbers, i.e. for wavelengths far longer than the duct radius; for more moderate frequencies or wavelengths, even those well below the cut-on frequency of the next-order spatial modes, the end reflection deviates significantly from $0.6R$. In the 2D case, we find, in agreement with Noble [1958], that the plane-wave end correction coefficient $\hat{s}_0/X$ tends to infinity as the Helmholtz numbers ωX tends to zero. It should not be concluded, however, that the end correction itself becomes infinite in practice. It can be shown that the end correction tends to zero on the lengthscale of the duct length as the duct width X, and hence the Helmholtz number ωX, tend to zero; the end correction just does so sublinearly in the duct width. Also notable in both 2D and 3D is that with increasing Helmholtz number, newly cut-on modes appear with nonzero end corrections, inducing sharp jumps in their respective end-correction coefficients. This stands in contrast to previous literature [Snakowska et al., 2011] and its implications are discussed in section 4.2.3.

In chapter 5, we then presented an exit condition in the admittance and its weakly nonlinear counterpart for a general 2D or 3D duct without flow. The condition is inspired by Kemp et al. [2017], Félix et al. [2018] and Mangin [2023] in its use of a larger duct, concentric with the original duct, into which sound from the original duct may be radiated. However, we do not make use of Kemp's baffle-and-dipole superposition, as this does not generalize to weak nonlinearity, nor do we add the complication of both annular and cylindrical ducts as used by Félix et al. [2018]. Instead, we model the duct outlet as an acoustic discontinuity within the larger duct, which is zero-extended to the larger duct's walls. We also set the admittances in-front-of and behind the discontinuity to be positive- and negative-characteristic, respectively, and prescribe an absorbing condition on the back face of the discontinuity (termed the 'acoustic wormhole'). The inner duct then has its internal acoustic field calculated using this outlet condition, and this acoustic field's resulting radiation into the outer duct may also be found. This is effectively an approximation of free space, which may be made more accurate by increasing the two ducts' width ratio. Within the inner duct, we follow the work of chapter 2 by using an admittance-based multi-modal method to find the pressure field; in combination with this chapter 2, a very general inner-duct geometry may be modelled in the weakly-nonlinear regime. The system can be solved in the smaller duct only (useful for modelling resonances), the outer duct only (for modelling radiation), both ducts (for the full acoustic field) or neither (for considering the exit condition in its own right).

As discussed above, a Wiener–Hopf calculation of the end correction was performed in chapter 4. The model presented in chapter 5 may also be applied to this calculation, and was validated against chapter 4's analytical work in section 5.3.1. This was done both in 2D and 3D and resulted in good agreement between the two models, providing both ideal parameters for future calculations with the outer-duct model and the confidence in its ability to accurately simulate free space. Also mentioned above was the disagreement between our calculation of the Wiener–Hopf solution and previous modelling by Snakowska et al. [2011]; here, the agreement between our numerics and the Wiener–Hopf calculation gives confidence in the correctness of our calculation.

In the nonlinear case our model remains valid, which is an advantage of this model over the Wiener–Hopf technique, and the method of Kemp et al. [2017]: in particular, in section 5.3.2, we calculated values of a novel *nonlinear end-correction coefficient*. In contrast to the linear case, wave-steepening causes this coefficient to depend upon the duct length, meaning that there is now a 3D parameter space (M, ω, L). This opens up a rich new area of study which could be approached from many directions: owing to numerical constraints, we focussed here on fixed-frequency calculations while varying duct length and Mach number. In 3D, an investigation of the effect of amplitude on the classical $0.6R$ result for low frequencies determined that for greater amplitude, the end-correction decays to zero; this effect is exaggerated in longer ducts, due to the increased opportunity for waves to steepen within the duct. This suggests that when playing a low note on a trumpet, blowing harder will cause the note to sharpen. In 2D, an intermediate frequency was investigated, and it appeared that for sufficiently long ducts, the end correction either remains stable (if the duct is an even number of half-wavelengths) or decreases (if the duct is an odd number of half-wavelengths). This suggests that when playing a high note on a trumpet, it will either sharpen or stay the same pitch, depending on how close the note is to one of the trumpet's harmonics.

On the topic of resonances, section 5.3.3 investigated values of the impedance at the duct inlet while varying the frequency, for various duct aspect ratios. This resulted in plots whose maxima or minima respectively predict the resonant frequencies of ducts closed at one end or open at both ends. Assuming the relative magnitudes of the maxima/minima predict the dominance of each resonance within the harmonic series corresponding to a particular duct geometry, shorter, fatter ducts will have a more fundamental-dominated sound, whereas longer, thinner ducts will have a greater prevalence of high harmonics. This agrees with organ pipe design: wide pipes known as *flutes* have a mellow, fundamental-dominated sound, whereas narrower pipes known as *strings* have brighter, high-harmonic-dominated spectra. We also investigated the effect of inner-duct curvature on inlet impedance, and plotted the pressure field due to a source at the third resonance, for each geometry considered.

When solving for the acoustics either inside or outside the duct, we saw in section 5.3.6 that the nonlinear reflection backward from the duct outlet results in significant deviation from the plane-wave-only predictions of the characteristic admittance (as in the Blackstock validation of chapter 3). We also experimented with more exotic inner-duct geometries: section 5.3.7 assessed the asymmetry of radiation from a curved duct, while an exponential horn representative of a brass instrument bell was modelled in section 5.3.8, so as to compare with the equivalent result from chapter 3.

6.1 Future work

In our outer-duct model, sound from within the smaller duct appears on the right of the discontinuity at the centre of the larger duct representing the smaller duct's outlet (see figure 5.1). This model was chosen as it allows the linear case to be generalized to weak nonlinearity, unlike other methods such as that of Kemp et al. [2017] and the Wiener–Hopf technique, which are limited to the linear case. However, the use of a discontinuity in the larger duct in our model necessitates the choice of a "fake" artificial condition on the back of the discontinuity, which in reality is in the space that is occupied by the smaller duct. Here, a perfectly absorbing boundary condition was chosen for that surface, which prevents unphysical reflections from this unphysical surface. Unfortunately, this boundary condition will absorb a small amount of acoustic energy, meaning that our model does not perfectly preserve acoustic energy (instead the energy vanishes into a 'wormhole'). This appears not to pose a serious problem, though: comparing the straight duct radiation in 2D and 3D in section 5.3.5, we saw that the differing energy decay rates of $1/\sqrt{x}$ and $1/r$ are captured by the model, and the validation in the linear regime against Wiener–Hopf results gives confidence that the energy leak is negligible. One alternative might have been to prescribe a perfectly reflective boundary condition on this fake surface; this would have the advantage that acoustic energy is perfectly conserved, but the disadvantage that spurious reflections would be allowed. Another possibility for future work would be to use an annular model for the outer duct behind the exit for $s < 0$, although this would require a different set of duct modes and a significant complication in both mathematical and numerical complexity, so has therefore been avoided here.

There are several other potential improvements that could be made to the duct exit model. Here, the larger duct, although modelling free space, was nonetheless modelled with rigid perfectly-reflecting walls, and an outer duct with an absorbing condition on the walls, such as the perfectly-matched layers used by Félix et al. [2018] and Mangin [2023], could instead be incorporated. While potentially difficult to implement in the weakly nonlinear case, these methods would make extreme duct width ratios unnecessary, therefore saving on numerical costs, and would eliminate the far-field interference pattern seen within the larger duct in some of the plots presented here. The numerical implementation of the existing model could also be made more efficient. A glaringly obvious example is the use of MATLAB rather than a lower-level language with better memory-handling capabilities. More efficiency would enable a more comprehensive investigation of the nonlinear end-correction coefficient, calculation of the effect of the Mach number on harmonic series, and potentially even computation of the nonlinear acoustic field in the outer duct. The first of these three currently-inaccessible problems, as mentioned above, involves a 3D parameter space (M, ω, L), in which we have only explored two subplanes here. With more efficient numerics, one could conduct nonlinear generalisations of figures 5.3 and 5.2, or replace the length variable with frequency in figures 5.5 and 5.6, as well as exploring higher Mach numbers or longer ducts than we have done here. The infinite series of coefficients was here made finite for computational purposes by truncating the number of modes, and greater efficiency could also be gained by improving this approximation: for example, by consideration of the asymptotics of matrix entries in the admittance boundary condition as the modenumber is increased and then “simulating” instead of ignoring the high-mode-number coefficients. This could result in a more accurate nonlinear exit condition for the same computational cost. It might also allow consideration of the limit in which the duct width ratio η tends to zero: while the only comparison we attempted with the Wiener–Hopf technique here was the end-correction calculation, more direct comparisons of, for example, the pressure field in the outer duct could be performed, particularly with a more accurate free-space approximation. Another area to which the Wiener–Hopf technique has been applied is that of the duct exit with mean flow [Rienstra, 1984]: a more substantial modification to the model in this paper would be the inclusion of flow, providing in turn another area of comparison with the Wiener–Hopf technique. While a mean flow would not be needed to model musical instruments, owing to their very low Mach number flows, it would allow, for example, the study of sound from ducted aircraft engines. This would provide a weakly nonlinear generalisation of the multi-modal linear work (with flow) of Mangin [2023].

The numerical solution for the admittance, and then for the pressure and velocity, is relatively standard, and future work could consider other methods of numerical solution. As described in section 2.3, the infinite series of ODEs was truncated to a finite system by specifying a maximum number of temporal and spatial modes. Since this truncation prevents the cascade of energy to higher modes and leads to artificial energy accumulating in the highest nontruncated mode, an artificial viscosity was added to help dissipate energy at higher modes. This artificial viscosity is akin to the real molecular viscosity of the gas. However, the dominant energy loss mechanism for acoustics in a duct is friction with the walls, which has been previously modelled using a fractional derivative approach [see, e.g., Rendón et al., 2010, and references therein]; a similar technique could be investigated for inclusion in the present model. The now finite set of ODEs was then integrated here using a standard Runge–Kutta method, either with a fixed (RK4) or adaptive (RK45) method. More sophisticated numerical methods that take note of the Riccati-style nature of the equations being integrated are also possible. For example, Pagneux [2010] used a Magnus–Möbius scheme in the linear case to avoid singularities of the admittance caused by the presence of pressure nodes in the duct. In chapter 2 we proposed a novel weakly nonlinear Magnus–Möbius scheme, which has produced promising results for a basic duct geometry; however, it does not cope well with the combination of curvature and wall-width variation, which may be a consequence of its being only first-order. Generalisation to higher-order would perhaps make it viable for more duct geometries, allowing it to be used for all of the results in this thesis.

Other possibilities for future research might involve the investigation of other nonlinear effects such as resonant triads [e.g. Protas et al., 2024] and musical dynamics owing to the feedback loop between a musician's lips and the reflections from the waves that they generate, or other modal representations that might yield faster numerical convergence [e.g. Maurel et al., 2014]. Appendix B contains a partially-complete model of a 3D duct with a rectangular cross-section; the resulting symmetry-breakage relative to a circular cross-section complicates matters with regard to torsion and curvature, but could produce interesting results with novel applications were the model to be completed. Even before the results stage, there would also be interesting implications when the invariant admittances (section 2.2.2) are found, since rather than just the straight, toroidal, and helical admittances found in this thesis, twist may be added to each of these scenarios, doubling the possibilities.

6.2 Applications

An obvious motivation of this work was the potential application to sound in brass instruments, where the brassy sound is caused by nonlinear wave steepening within the instrument. The use of the admittance (both the usual linear admittance and its weakly nonlinear extension) makes the present framework well suited to this, as a duct's resonances could be investigated by solving for the admittance without needing to model or specify a sound source at the inlet. Moreover, the combination of the bend correction factor of section 3.10 and the open-end condition of section 5.1 could be used to investigate whether instruments are likely to become sharper or flatter when played at louder or quieter volumes, and potentially even whether an instrument could be designed to have a stable pitch independently of the volume at which it is played, for example by replacing a tuning slide with one of a different geometry or fitting a modification to the bell to change the open-end behaviour.

A potential application of the model's extension presented in chapter 5 is harmonic-series calculations of wind or brass instruments, as well as organ pipes. The end-correction problem is of particular interest for organ pipes, and this model provides an analytical justification for the investigation of this phenomenon's relationship to nonlinearity. It can also be used to investigate the relationship between resonant frequencies and wave amplitude (or, in musical terms, between timbre and volume). Ultimately, the combination of chapter 5's exit condition work with the in-duct modelling of chapter 3 will allow for analysis of the impact of both nonlinearity and duct geometry on the sound radiated from musical instruments such as trumpets and trombones.

Citations

Bers (1983). “Space–time evolution of plasma instabilities — absolute and convective”. In Galeev and Sudan, editors, *Basic Plasma Physics*, volume 1 of *Handbook of Plasma Physics*, pages 451–517. North-Holland. ISBN 044486427X.

Blackstock (1966). “Connection between the Fay and Fubini solutions for plane sound waves of finite amplitude”. *J. Acoust. Soc. Am*, **39** 1019–1026. doi: 10.1121/1.1909986.

Briggs (1964). *Electron-Stream Interaction with Plasmas*, chapter 2, pages 8–46. MIT Press.

Carey Smith (2025). “Bessel Derivative Zeros”. www.mathworks.com/matlabcentral/fileexchange/28001-bessel-derivative-zeros. Retrieved July 29, 2025.

Casas and Iserles (2006). “Explicit Magnus expansions for nonlinear equations”. *J. Phys. A*, **39**(19) 5445–5461. doi: 10.1088/0305-4470/39/19/S07.

d’Alembert (1747). “Recherches sur la courbe que forme une corde tendue mise en vibration”. *Memoires de l’Academie royale des sciences et belles lettres. Classe de mathematique.*, **3** 214–219.

Fay (1931). “Plane sound waves of finite amplitude”. *J. Acoust. Soc. Am*, **3** 222–241. doi: 10.1121/1.1915557.

Félix and Pagneux (2001). “Sound propagation in rigid bends: A multimodal approach”. *J. Acoust. Soc. Am*, **110** 1329–1337. doi: 10.1121/1.1391249.

Félix and Pagneux (2002). “Multimodal analysis of acoustic propagation in three-dimensional bends”. *Wave Motion*, **36** 157–168. doi: 10.1016/S0165-2125(02)00009-4.

Félix, Doc, and Boucher (2018). “Modeling of the multimodal radiation from an open-ended waveguide”. *J. Acoust. Soc. Am*, **143**(6) 3520–3528. doi: 10.1121/1.5041268.

Fernando and Druon (2011). “Nonlinear waves and shocks in a rigid acoustical guide”. *J. Acoust. Soc. Am*, **129** 604–615. doi: 10.1121/1.3531799.

Fubini (1935). “Anomalie nella propagazione di ande acustiche de grande ampiezza”. *Alta Frequenza*, **4** 530–581.

Germano (1982). “On the effect of torsion on a helical pipe flow”. *J. Fluid Mech*, **125** 1–8. doi: 10.1017/S0022112082003206.

Gilbert, Menguy, and Campbell (2008). “A simulation tool for brassiness studies”. *J. Acoust. Soc. Am*, **123**(4) 1854–1857. doi: 10.1121/1.2872342.

Hill and Stokes (2018). “A note on Navier-Stokes equations with nonorthogonal coordinates”. *The ANZIAM Journal*, **59**(3) 335–348. doi: 10.1017/S144618111700058X.

Hirschberg, Gilbert, Msallam, and Wijnands (1996). “Shock waves in trombones”. *J. Acoust. Soc. Am*, **99** 1754–1758. doi: 10.1121/1.414698.

Iserles and Nørsett (1999). “On the solution of linear differential equations in Lie groups”. *The Royal Society of London. Philosophical Transactions. Series A. Mathematical, Physical and Engineering Sciences*, **357**(1754) 983–1019. doi: 10.1098/rsta.1999.0362.

Jensen and Brambley (2025). “Multimodal nonlinear acoustics in two- and three-dimensional curved ducts”. https://arxiv.org/abs/2503.11536. (submitted to J. Fluid Mech.).

Jensen, Turnbull, and Brambley (2025). “The weakly-nonlinear admittance at open ends of two- and three-dimensional acoustic waveguides”. https://arxiv.org/abs/2509.21615. (in preparation for submission to J. Fluid Mech.).

Kemp, Lopez-Carromero, and Campbell (2017). “Pressure fields in the vicinity of brass musical instrument bells measured using a two dimensional grid array and comparison with multimodal models”. *Proceedings of the 24th International Congress on Sound and Vibration*.

Levine and Schwinger (1948). “On the radiation of sound from an unflanged circular pipe”. *Physical Review*, **73**(4) 383.

Mangin (2023). *Modelling acoustic propagation in modern turbofan intakes using a multimodal method*. PhD thesis, Le Mans Université. https://theses.hal.science/tel-04355151.

Maurel, Mercier, and Pagneux (2014). “Improved multimodal admittance method in varying cross section waveguides”. *Proc. R. Soc.* A, **470** 20130448. doi: 10.1098/rspa.2013.0448.

McTavish and Brambley (2019). “Nonlinear sound propagation in two-dimensional curved ducts: A multimodal approach”. *J. Fluid Mech*, **875** 411–447. doi: 10.1017/jfm.2019.497.

McTavish (2018). *Nonlinear acoustics in a general waveguide.* PhD thesis, University of Cambridge. doi: 10.17863/CAM.35714.

Myers, Pyle, Robert W., Gilbert, Campbell, Chick, and Logie (2012). “Effects of nonlinear sound propagation on the characteristic timbres of brass instruments”. *J. Acoust. Soc. Am*, **131**(1) 678–688. doi: 10.1121/1.3651093.

Noble (1958). *Methods based on the Wiener–Hopf Technique for the Solution of Partial Differential Equations.* Pergamon. ISBN 0828403325.

Pagneux (2010). “Multimodal admittance method in waveguides and singularity behavior at high frequencies”. *J. Comput. Appl. Math.*, **234**(6) 1834–1841. doi: 10.1016/j.cam.2009.08.034.

Pagneux, Amir, and Kergomard (1996). “A study of wave propagation in varying cross-section waveguides by modal decomposition. Part I. Theory and validation”. *J. Acoust. Soc. Am*, **100** 2034–2048. doi: 10.1121/1.417913.

Pandya, Settles, and Miller (2003). “Schlieren imaging of shock waves from a trumpet”. *J. Acoust. Soc. Am*, **114**(6) 3363–3367. doi: 10.1121/1.1628682.

Protas, Kang, and Bustamante (2024). “Alignments of triad phases in extreme one-dimensional Burgers flows”. *Phys. Rev. E*, **109**(5). doi: 10.1103/PhysRevE.109.055104.

Rayleigh (1871). “V. on the theory of resonance”. *Phil. Trans. R. Soc. Lond.*, **161** 77–118. doi: 10.1098/rstl.1871.0006.

Rendón, Orduña Bustamante, Narezo, Pérez-López, and Sorrentini (2010). “Nonlinear progressive waves in a slide trombone resonator”. *J. Acoust. Soc. Am*, **127**(2) 1096–1103. doi: 10.1121/1.3277221.

Rendón, Ezeta, and Pérez-López (2013). “Nonlinear sound propagation in trumpets”. *Acta Acoust. United Acoust.*, **99** 607–614. doi: 10.3813/AAA.918640.

Rienstra (1984). “Acoustic radiation from a semi-infinite annular duct in a uniform subsonic mean flow”. *Journal of Sound and Vibration*, **94**(2) 267–288. https://doi.org/10.1016/S0022-460X(84)80036-X.

Schiff and Shnider (1999). “A natural approach to the numerical integration of Riccati differential equations”. *SIAM J. Numer. Anal.*, **36**(5) 1392–1413. doi: 10.1137/S0036142996307946.

Snakowska, Jurkiewicz, and Smolik (2011). “Open end correction for arbitrary mode propagating in a cylindrical acoustic waveguide”. *Acta Physica Polonica A*, **120**(4) 736–739. https://bibliotekanauki.pl/articles/1493260.pdf.

Webster (1919). “Acoustical impedance and the theory of horns and of the phonograph”. *Proc. Natl Acad. Sci*, **5**(7) 275–282.

Weinstein (1948). “Rigorous solution of the problem of an open-ended parallel-plate waveguide”. *Izv. Akad. Nauk, Ser. Fiz*, **12** 144–165.

Wikipedia (2025). “Buisine”. https://en.wikipedia.org/wiki/Buisine. https://en.wikipedia.org/wiki/Buisine. Accessed: 25/09/2025.

Yamaha Corp. (2017). “Yamaha Bass Flute YFL-B441S”. Wikimedia Commons. https://commons.wikimedia.org/wiki/File:Yamaha_Bass_Flute_YFL-B441S.tif. Accessed: 25/09/2025.

Yamaha Corp. (2022). “Yamaha Trumpet YTR-8335LA”. Wikimedia Commons. https://commons.wikimedia.org/wiki/File:Yamaha_Trumpet_YTR-8335LA_crop.jpg. Accessed: 25/09/2025.

Appendix A

Evaluation of integrals

Here the mode-integrals employed in the projection of the governing equations above are calculated explicitly, where possible. These are the expressions used when performing computations, in order to save time.

A.1 Integrals from the 2D formulation

$$\Xi_{\alpha\beta} = \delta_{\alpha\beta}, \tag{A.1}$$

$$\Xi_{\alpha\beta}[\xi] = \frac{\delta_{\alpha\beta}}{2} + C_\alpha C_\beta \frac{\left((-1)^{\alpha+\beta} - 1\right)(\alpha^2 + \beta^2)}{(\alpha^2 - \beta^2)^2 \pi^2}, \tag{A.2}$$

$$\Xi_{[\alpha]\beta} = \sqrt{2}\alpha^2 C_\beta \frac{(-1)^{\alpha+\beta} - 1}{\alpha^2 - \beta^2}, \tag{A.3}$$

$$\Xi_{[\alpha]\beta}[\xi] = \delta_{\alpha\beta}\frac{(1 - \delta_{\alpha 0})}{2} + (1 - \delta_{\alpha\beta})\frac{\sqrt{2}\alpha^2 C_\beta (-1)^{\alpha+\beta}}{\alpha^2 - \beta^2}. \tag{A.4}$$

$$\Xi_{\alpha\beta\gamma} = \frac{C_\alpha C_\beta}{2C_\gamma}(\delta_{\alpha+\beta,\gamma} + \delta_{|\alpha-\beta|,\gamma}), \tag{A.5}$$

$$\begin{aligned}\Xi_{\alpha\beta\gamma}[\xi] = \frac{\Xi_{\alpha\beta\gamma}}{2} + \frac{C_\alpha C_\beta C_\gamma \left((-1)^{\alpha+\beta+\gamma} - 1\right)}{4\pi^2}\Bigg(&\frac{1}{(\alpha+\beta+\gamma)^2} \\ &+ \frac{1}{(\alpha+\beta-\gamma)^2} + \frac{1}{(\alpha-\beta+\gamma)^2} + \frac{1}{(\alpha-\beta+\gamma)^2}\Bigg),\end{aligned} \tag{A.6}$$

$$\Xi_{[\alpha]\beta\gamma} = \frac{\alpha C_\beta C_\gamma \left((-1)^{\alpha+\beta+\gamma} - 1\right)}{2\sqrt{2}}\left(\frac{1}{\alpha+\beta-\gamma} + \frac{1}{\alpha-\beta+\gamma} + \frac{1}{\alpha-\beta-\gamma}\right), \tag{A.7}$$

$$\Xi_{[\alpha\beta\gamma]} = C_\alpha C_\beta C_\gamma \left((-1)^{\alpha+\beta+\gamma} - 1\right), \tag{A.8}$$

$$\Xi^{+}_{[\alpha\beta\gamma]} = C_\alpha C_\beta C_\gamma (-1)^{\alpha+\beta+\gamma}, \tag{A.9}$$

$$\Xi^{-}_{[\alpha\beta\gamma]} = C_\alpha C_\beta C_\gamma. \tag{A.10}$$

A.2 Integrals from the 3D formulation

$$\Pi_{\alpha\beta} = C_\alpha C_\beta \int_0^1 J_{p_\alpha}(\lambda_\alpha x) J_{p_\beta}(\lambda_\beta x) \mathrm{d}x, \tag{A.11}$$

$$\Pi_{\alpha\beta}[x] = C_\alpha C_\beta \int_0^1 x J_{p_\alpha}(\lambda_\alpha x) J_{p_\beta}(\lambda_\beta x) \mathrm{d}x, \tag{A.12}$$

$$\Pi_{\alpha\beta}[x^2] = C_\alpha C_\beta \int_0^1 x^2 J_{p_\alpha}(\lambda_\alpha x) J_{p_\beta}(\lambda_\beta x) \mathrm{d}x, \tag{A.13}$$

$$\Pi_{[\alpha]\beta}[x] = C_\alpha C_\beta \int_0^1 \left[p_\alpha J_{p_\alpha}(\lambda_\alpha x) - \lambda_\alpha x J_{p_\alpha+1}(\lambda_\alpha x)\right] J_{p_\beta}(\lambda_\beta x) \mathrm{d}x, \tag{A.14}$$

$$\Pi_{[\alpha]\beta}[x^2] = C_\alpha C_\beta \int_0^1 x \left[p_\alpha J_{p_\alpha}(\lambda_\alpha x) - \lambda_\alpha x J_{p_\alpha+1}(\lambda_\alpha x)\right] J_{p_\beta}(\lambda_\beta x) \mathrm{d}x, \tag{A.15}$$

$$\Phi_{\alpha\beta} = (\delta_{p_\alpha+p_\beta,0} + \delta_{p_\alpha p_\beta})\delta_{\xi_\alpha \xi_\beta}, \tag{A.16}$$

$$\Phi_{(\alpha)\beta} = -p_\alpha(-1)^{\xi_\alpha}\delta_{p_\alpha p_\beta}\delta_{\xi_\alpha+\xi_\beta,1}, \tag{A.17}$$

$$\Phi_{\alpha\beta}[\cos\phi] = \frac{1}{2}\left[(-1)^{\xi_\alpha}\delta_{p_\alpha+p_\beta,1} + \delta_{|p_\alpha-p_\beta|,1}\right]\delta_{\xi_\alpha\xi_\beta}, \tag{A.18}$$

$$\Phi_{\alpha\beta}[\sin\phi] = \frac{1}{2}\left[\delta_{p_\alpha+p_\beta,1} + (-1)^{\xi_\beta}(p_\alpha - p_\beta)\delta_{|p_\alpha-p_\beta|,1}\right]\delta_{\xi_\alpha+\xi_\beta,1}, \tag{A.19}$$

$$\Phi_{(\alpha)\beta}[\sin\phi] = -\frac{p_\alpha}{2}\left[\delta_{p_\alpha 1}\delta_{p_\beta 0}\delta_{\xi_\alpha 0} + (p_\alpha - p_\beta)\delta_{|p_\alpha-p_\beta|,1}\right]\delta_{\xi_\alpha\xi_\beta}. \tag{A.20}$$

The linear coefficient matrices in 3D always consist of a combination of a Π with a Φ, which rarely simplifies further, although the notable cases are the identity,

$$\mathsf{I}_{\alpha\beta} = \Pi_{\alpha\beta}[x]\Phi_{\alpha\beta} = \delta_{\alpha\beta}, \tag{A.21}$$

and the helicity matrix,

$$\mathsf{H}_{\alpha\beta} = \Pi_{\alpha\beta}[x]\Phi_{(\alpha)\beta} = -p_\alpha(-1)^{\xi_\alpha}\delta_{\xi_\alpha+\xi_\beta,1}\delta_{p_\alpha p_\beta}\delta_{q_\alpha q_\beta}. \tag{A.22}$$

Likewise,

$$\Pi_{\alpha\beta\gamma} = C_\alpha C_\beta C_\gamma \int_0^1 J_{p_\alpha}(\lambda_\alpha x) J_{p_\beta}(\lambda_\beta x) J_{p_\gamma}(\lambda_\gamma x) \mathrm{d}x, \tag{A.23}$$

$$\Pi_{\alpha\beta\gamma}[x] = C_\alpha C_\beta C_\gamma \int_0^1 x J_{p_\alpha}(\lambda_\alpha x) J_{p_\beta}(\lambda_\beta x) J_{p_\gamma}(\lambda_\gamma x) \mathrm{d}x, \tag{A.24}$$

$$\Pi_{\alpha\beta\gamma}[x^2] = C_\alpha C_\beta C_\gamma \int_0^1 x^2 J_{p_\alpha}(\lambda_\alpha x) J_{p_\beta}(\lambda_\beta x) J_{p_\gamma}(\lambda_\gamma x) \mathrm{d}x, \tag{A.25}$$

$$\Pi_{[\alpha]\beta\gamma}[x] = C_\alpha C_\beta C_\gamma \int_0^1 \Big(p_\alpha J_{p_\alpha}(\lambda_\alpha x) - \lambda_\alpha x J_{p_\alpha+1}(\lambda_\alpha x)\Big) J_{p_\beta}(\lambda_\beta x) J_{p_\gamma}(\lambda_\gamma x) \mathrm{d}x, \tag{A.26}$$

$$\Pi_{[\alpha\beta\gamma]}[x] = C_\alpha C_\beta C_\gamma J_{p_\alpha}(\lambda_\alpha) J_{p_\beta}(\lambda_\beta) J_{p_\gamma}(\lambda_\gamma), \tag{A.27}$$

$$\Phi_{\alpha\beta\gamma} = \frac{1}{2}\Bigg(\delta_{p_\alpha+p_\beta+p_\gamma,0} + (-1)^{\xi_\alpha}\delta_{p_\beta+p_\gamma,p_\alpha} + (-1)^{\xi_\beta}\delta_{p_\alpha+p_\gamma,p_\beta} + (-1)^{\xi_\gamma}\delta_{p_\alpha+p_\beta,p_\gamma}\Bigg)\Bigg(\delta_{\xi_\alpha+\xi_\beta+\xi_\gamma,0} - \delta_{\xi_\alpha+\xi_\beta+\xi_\gamma,2}\Bigg), \tag{A.28}$$

$$\Phi_{\alpha\beta\gamma}[\cos\phi] = \frac{1}{4}\Bigg(\delta_{p_\alpha+p_\beta+p_\gamma,1} + (-1)^{\xi_\alpha}\delta_{|p_\beta+p_\gamma-p_\alpha|,1} + (-1)^{\xi_\beta}\delta_{|p_\alpha+p_\gamma-p_\beta|,1} + (-1)^{\xi_\gamma}\delta_{|p_\alpha+p_\beta-p_\gamma|,1}\Bigg)\Bigg(\delta_{\xi_\alpha+\xi_\beta+\xi_\gamma,0} - \delta_{\xi_\alpha+\xi_\beta+\xi_\gamma,2}\Bigg), \tag{A.29}$$

$$\Phi_{(\alpha)\beta\gamma}[\sin\phi] = -\frac{p_\alpha}{4}\Bigg(\delta_{p_\alpha+p_\beta+p_\gamma,1} + \delta_{|p_\beta+p_\gamma-p_\alpha|,1}(-1)^{p_\beta+p_\gamma-p_\alpha+\xi_\alpha} + \delta_{|p_\alpha+p_\gamma-p_\beta|,1}(-1)^{p_\alpha+p_\gamma-p_\beta+\xi_\beta} + \delta_{|p_\alpha+p_\beta-p_\gamma|,1}(-1)^{p_\alpha+p_\beta-p_\gamma+\xi_\gamma}\Bigg]\Bigg) \times \Bigg(\delta_{\xi_\alpha+\xi_\beta+\xi_\gamma,0} - \delta_{\xi_\alpha+\xi_\beta+\xi_\gamma,2}\Bigg). \tag{A.30}$$

Appendix B

3D rectangular ducts with curvature and torsion

In this appendix, the ducts described in section 2.1.7 have the weakly-nonlinear gas dynamics PDEs projected onto their geometry and expanded in terms of their straight-duct spatial modes. As discussed in that section, this is an alternative to the circular cross-section used for 3D ducts throughout this thesis, which instead preserves the asymmetric width variation present in the 2D duct geometry and simply introduces another coordinate y (so the frame is then (s,x,y)). This loss of circular symmetry means that the choice of $\theta_0(s)$, previously an invisible coordinate used to rotate the frame in line with torsion and in so doing preserve the orthogonality of the coordinate system, is no longer arbitrary. The resulting geometry then has an extra degree of complication as torsion and twisting become different effects: in fact, this becomes a serious barrier to numerical efficiency, as we shall see. Nonetheless, numerical implementation of the model within this geometry should be pursued at some point, as it may result in interesting physics. The derivation here uses guidance from Hill and Stokes [2018] on writing down fluid mechanics equations in a non-orthogonal coordinate system.

B.1 Duct coordinate System

The ducts we consider here are defined by a curve $\mathbf{q}(s)$ and scalar functions $X_\pm(s)$ and $Y_\pm(s)$, which respectively represent the centreline and widths in each direction of the duct at arc length $s \in [0,1]$. The tangent, normal and binormal vectors, may be found via the Frenet-Serret formulae

$$\frac{\mathrm{d}\mathbf{q}}{\mathrm{d}s} = \mathbf{t}, \quad \frac{\mathrm{d}\mathbf{t}}{\mathrm{d}s} = \kappa\mathbf{n}, \quad \frac{\mathrm{d}\mathbf{n}}{\mathrm{d}s} = -\kappa\mathbf{t} + \tau\mathbf{b}, \quad \frac{\mathrm{d}\mathbf{b}}{\mathrm{d}s} = -\tau\mathbf{n}, \tag{B.1}$$

where $\kappa(s)$ and $\tau(s)$ are the local curvature and torsion respectively. Note that $\mathbf{b} = \mathbf{t}\times\mathbf{n}$.

Any point in the duct is then represented by coordinates (s,x,y), where $x \in$

$[X_-(s), X_+(s)]$ and $y \in [Y_-(s), Y_+(s)]$, as follows

$$\mathbf{x} = \mathbf{q}(s) + x(\cos\theta_0 \mathbf{n} - \sin\theta_0 \mathbf{b}) + y(\sin\theta_0 \mathbf{n} + \cos\theta_0 \mathbf{b}). \tag{B.2}$$

Here the phase shift $\theta_0(s)$ is the angle by which the rectangular cross-section has rotated relative to the $\mathbf{n}$, $\mathbf{b}$ frame. The basis vectors and Lamè coefficients are then

$$\begin{aligned}
\mathbf{e}_s &= (1 - \kappa x \cos\theta_0 - \kappa y \sin\theta_0)\mathbf{t} \\
&\qquad + (\tau - \theta_0') \left((-x \sin\theta_0 + y\cos\theta_0)\mathbf{n} + (x\cos\theta_0 + y \sin\theta_0)\mathbf{b} \right), && \text{(B.3)} \\
\mathbf{e}_x &= \cos\theta_0 \mathbf{n} - \sin\theta_0 \mathbf{b}, \qquad\qquad \mathbf{e}_y = \sin\theta_0 \mathbf{n} + \cos\theta_0 \mathbf{b}, && \text{(B.4)} \\
h_s &= \sqrt{{h_s^\perp}^2 + (\tau - \theta_0')^2 (x^2 + y^2)}, \qquad h_x = 1, \qquad h_y = 1, && \text{(B.5)}
\end{aligned}$$

where $h_s^\perp = 1 - \kappa x \cos\theta_0 - \kappa y \sin\theta_0$ is the longitudinal Lamè coefficient in the case of an orthogonal coordinate system. The nonzero entries g_{ij} in the metric are then

$$g_{ss} = h_s^2, \quad g_{xx} = 1, \quad g_{yy} = 1, \quad g_{sx} = g_{xs} = -y(\tau - \theta_0'), \quad g_{ys} = g_{sy} = x(\tau - \theta_0'), \tag{B.6}$$

while the inverse metric has entries

$$\begin{aligned}
g^{ss} &= \frac{1}{{h_s^\perp}^2}, & g^{xx} &= 1 + \frac{y^2(\tau - \theta_0')^2}{{h_s^\perp}^2}, & g^{yy} &= 1 + \frac{x^2(\tau - \theta_0')^2}{{h_s^\perp}^2}, \\
g^{sx} = g^{xs} &= \frac{y(\tau - \theta_0')}{{h_s^\perp}^2}, & g^{sy} = g^{ys} &= -\frac{x(\tau - \theta_0')}{{h_s^\perp}^2}, & g^{xy} = g^{yx} &= -\frac{xy(\tau - \theta_0')^2}{{h_s^\perp}^2}.
\end{aligned} \tag{B.7}$$

Taking spatial derivatives of vectors requires Christoffel symbols; we need not calculate all 18 independent entries, however, as the pressure modification ensures we have no $\mathbf{U}^a \cdot \nabla \mathbf{U}^a$ term in our equations. What we do have is a divergence term $\nabla \cdot \mathbf{U}^a$, which requires only terms Γ^i_{jk} in which $i = j$ or k, of which there are 9 independent entries. Those entries are calculated from

$$\Gamma^i_{jk} = \frac{1}{2} g^{il} \left(\partial_k g_{jl} + \partial_j g_{lk} - \partial_l g_{kj} \right), \tag{B.8}$$

and the nonzero ones turn out to be

$$\begin{aligned}
\Gamma^s_{ss} &= \frac{1}{h_s^\perp} \frac{\partial h_s^\perp}{\partial s}, \quad \Gamma^s_{sx} = \Gamma^s_{xs} = \frac{1}{h_s^\perp} \frac{\partial h_s^\perp}{\partial x}, \quad \Gamma^s_{sy} = \Gamma^s_{ys} = \frac{1}{h_s^\perp} \frac{\partial h_s^\perp}{\partial y}, \\
\Gamma^x_{xs} &= \Gamma^x_{sx} = -\frac{(\tau - \theta_0')\kappa y \cos\theta_0}{h_s^\perp}, \quad \Gamma^y_{ys} = \Gamma^y_{sy} = \frac{(\tau - \theta_0')\kappa x \sin\theta_0}{h_s^\perp}.
\end{aligned} \tag{B.9}$$

The divergence of $\mathbf{U}^a$ is then

$$\nabla \cdot \mathbf{U}^a = \left(\frac{\partial v^i}{\partial x^i} + \Gamma^i_{ij} v^j \right), \tag{B.10}$$

where we have to use the tensorial velocity components v^i, which are defined (for brevity, without assigning an a-index), as

$$v^s = \frac{U^a}{h_s}, \quad v^x = V^a, \quad v^y = W^a, \tag{B.11}$$

to ensure that our non-unit basis vectors don't interfere with the value of scalar quantities such as $\mathbf{U}^a \cdot \mathbf{U}^a$. With this in mind, we get

$$\begin{aligned}\nabla \cdot \mathbf{U}^a = \left(\frac{\partial}{\partial s} + \Gamma^s_{ss} + \Gamma^x_{xs} + \Gamma^y_{ys}\right)\left(\frac{U^a}{h_s}\right) + \left(\frac{\partial}{\partial x} + \Gamma^s_{xs}\right) V^a + \left(\frac{\partial}{\partial y} + \Gamma^s_{ys}\right) W^a \\ = \frac{1}{h_s^\perp}\frac{\partial}{\partial s}\left(\frac{h_s^\perp U^a}{h_s}\right) + \kappa(\tau - \theta_0')(x\sin\theta_0 - y\cos\theta_0)\frac{U^a}{h_s^\perp h_s} \\ + \frac{1}{h_s^\perp}\frac{\partial}{\partial x}\left(h_s^\perp V^a\right) + \frac{1}{h_s^\perp}\frac{\partial}{\partial y}\left(h_s^\perp W^a\right).\end{aligned} \tag{B.12}$$

When taking gradients of scalars, we do not need Christoffel symbols, but since we are interested in the components of the gradient, we must raise the index by multiplying with g^{-1}. As such, ∇P^a has tensorial components

$$\begin{aligned}{}[\nabla P^a]^s &= g^{ss}\frac{\partial P^a}{\partial s} + g^{sx}\frac{\partial P^a}{\partial x} + g^{sy}\frac{\partial P^a}{\partial y} = \frac{1}{{h_s^\perp}^2}\frac{\partial P^a}{\partial s} + \frac{\tau - \theta_0'}{{h_s^\perp}^2}\left(y\frac{\partial P^a}{\partial x} - x\frac{\partial P^a}{\partial y}\right), \\ [\nabla P^a]^x &= g^{xs}\frac{\partial P^a}{\partial s} + g^{xx}\frac{\partial P^a}{\partial x} + g^{xy}\frac{\partial P^a}{\partial y} = \frac{\partial P^a}{\partial x} + (\tau - \theta_0')y\,[\nabla P^a]^s, \\ [\nabla P^a]^y &= g^{ys}\frac{\partial P^a}{\partial s} + g^{yx}\frac{\partial P^a}{\partial x} + g^{yy}\frac{\partial P^a}{\partial y} = \frac{\partial P^a}{\partial y} - (\tau - \theta_0')x\,[\nabla P^a]^s,\end{aligned} \tag{B.13}$$

and the duct wall normals (left un-normalised) $\boldsymbol{\nu}_{X\pm}$ and $\boldsymbol{\nu}_{Y\pm}$ have tensorial components

$$\begin{aligned}\nu^s_{X\pm} &= \frac{-X_\pm' + y(\tau - \theta_0')}{{h_s^\perp}^2|_{x=X_\pm}}, \quad \nu^x_{X\pm} = 1 + y(\tau - \theta_0')\nu^s_{X\pm}, \quad \nu^y_{X\pm} = -x(\tau - \theta_0')\nu^s_{X\pm}, \\ \nu^s_{Y\pm} &= \frac{-Y_\pm' - x(\tau - \theta_0')}{{h_s^\perp}^2|_{y=Y_\pm}}, \quad \nu^x_{Y\pm} = y(\tau - \theta_0')\nu^s_{Y\pm}, \quad \nu^y_{Y\pm} = 1 - x(\tau - \theta_0')\nu^s_{Y\pm}.\end{aligned} \tag{B.14}$$

B.2 Governing Equations

We may now assemble the governing equations:

$$\begin{aligned}-\mathrm{i}a\omega h_s^\perp P^a + \frac{\partial}{\partial s}\left(\frac{h_s^\perp U^a}{h_s}\right) + \frac{\partial}{\partial x}\left(h_s^\perp V^a\right) + \frac{\partial}{\partial y}\left(h_s^\perp W^a\right) \\ + \kappa(\tau - \theta_0')(x\sin\theta_0 - y\cos\theta_0)\frac{U^a}{h_s} = -\mathrm{i}a\omega h_s^\perp\left(\sum_b \beta_0 P^{a-b}P^b - Q^a\right),\end{aligned}$$

$$\begin{gathered}
-\mathrm{i}a\omega h_s^{\perp}\frac{h_s^{\perp}U^a}{h_s} + {h_s^{\perp}}^2\left[\nabla P^a\right]^s = {h_s^{\perp}}^2\left[\nabla \hat{Q}^a\right]^s,\\
-\mathrm{i}a\omega V^a + \left[\nabla P^a\right]^x = \left[\nabla \hat{Q}^a\right]^x, \qquad -\mathrm{i}a\omega W^a + \left[\nabla P^a\right]^y = \left[\nabla \hat{Q}^a\right]^y.
\end{gathered}$$

V^a and W^a may next be eliminated, resulting in

$$\begin{aligned}
&\frac{\partial}{\partial s}\left(\frac{h_s^{\perp}U^a}{h_s}\right) + \frac{\tau-\theta_0'}{h_s^{\perp}}(y\partial_x - x\partial_y)\left(h_s^{\perp}\frac{h_s^{\perp}U^a}{h_s}\right)\\
&\qquad\qquad - \mathrm{i}a\omega\left[h_s^{\perp}\left(1+\frac{\nabla_{\mathrm{t}}^2}{a^2\omega^2}\right) - \frac{\kappa}{a^2\omega^2}\frac{\partial}{\partial \mathbf{n}^{\perp}}\right]P^a\\
&\quad = \mathrm{i}a\omega\left\{-\beta_0 h_s^{\perp}\sum_b P^{a-b}P^b + \left[h_s^{\perp}\left(1-\frac{\nabla_{\mathrm{t}}^2}{a^2\omega^2}\right) + \frac{\kappa}{a^2\omega^2}\frac{\partial}{\partial \mathbf{n}^{\perp}}\right]Q^a\right\},
\end{aligned} \tag{B.16a}$$

$$\begin{aligned}
&\frac{\partial P^a}{\partial s} + (\tau-\theta_0')\left(y\partial_x - x\partial_y\right)P^a - \mathrm{i}a\omega h_s^{\perp}\frac{h_s^{\perp}U^a}{h_s}\\
&\quad = \mathrm{i}\omega h_s^{\perp}\sum_b\left\{\frac{h_s^{\perp}U^{a-b}}{h_s}\left[(a-b) - b\left(1+\frac{\nabla_{\mathrm{t}}^2}{b^2\omega^2}\right)\right]P^b + \frac{\nabla_{\mathrm{t}}(h_s^{\perp}U^{a-b}/h_s)\cdot\nabla_{\mathrm{t}}P^b}{b\omega^2}\right\}\\
&\qquad\qquad + \frac{\tau-\theta_0'}{h_s^{\perp}}(y\partial_x - x\partial_y)h_s^{\perp}\sum_b\frac{{h_s^{\perp}}^2U^{a-b}U^b}{h_s^2}.
\end{aligned} \tag{B.16b}$$

Here we have

$$Q^a = \frac{1}{2}\sum_b\left(P^{a-b}P^b - \frac{{h_s^{\perp}}^2U^{a-b}U^b}{h_s^2} + \frac{\nabla_{\mathrm{t}}P^{a-b}\cdot\nabla_{\mathrm{t}}P^b}{(a-b)b\omega^2}\right), \tag{B.17}$$

and

$$\frac{\partial f}{\partial \mathbf{n}^{\perp}} = \mathbf{n}^{\perp}\cdot\nabla_t f = \cos\theta_0\frac{\partial f}{\partial x} + \sin\theta_0\frac{\partial f}{\partial y}. \tag{B.18}$$

B.2.1 Boundary conditions

The boundary conditions $\mathbf{U}^a\cdot\boldsymbol{\nu}_{X\pm}|_{x=X\pm} = 0$ and $\mathbf{U}^a\cdot\boldsymbol{\nu}_{Y\pm}|_{y=Y\pm} = 0$ are then

$$\begin{aligned}
X_{\pm}'\frac{h_s^{\perp}U^a}{h_s}\bigg|_{x=X\pm} &= \frac{h_s^{\perp}}{ia\omega}\left(\frac{\partial(P^a-Q^a)}{\partial x}\right)\bigg|_{x=X\pm} + (\tau-\theta_0')y\frac{h_s^{\perp}U^a}{h_s}\bigg|_{x=X\pm},\\
Y_{\pm}'\frac{h_s^{\perp}U^a}{h_s}\bigg|_{y=Y\pm} &= \frac{h_s^{\perp}}{ia\omega}\left(\frac{\partial(P^a-Q^a)}{\partial y}\right)\bigg|_{y=Y\pm} - (\tau-\theta_0')x\frac{h_s^{\perp}U^a}{h_s}\bigg|_{y=Y\pm}.
\end{aligned} \tag{B.19}$$

Modal projection is greatly simplified through the use of a modified velocity $\widetilde{U}^a = h_s^{\perp}U^a/h_s$.

B.3 Spatial Modes

P^a and $\widetilde{U}^a$ are now expanded about a basis of straight duct modes

$$P^a = \sum_{\alpha=0}^{\infty} P^a_\alpha(s)\psi_\alpha(s,x,y), \quad \widetilde{U}^a = \sum_{\alpha=0}^{\infty} \widetilde{U}^a_\alpha(s)\psi_\alpha(s,x,y), \tag{B.20}$$

with every ψ_α satisfying

- Helmholtz's equation with eigenvalue λ_α in 3D Cartesians (scaling out the eigenvalues' length-dependence for convenience)

$$\frac{\partial^2\psi_\alpha}{\partial x^2} + \frac{\partial^2\psi_\alpha}{\partial y^2} + \left(\frac{\lambda^{x\,2}_\alpha}{X^2} + \frac{\lambda^{y\,2}_\alpha}{Y^2}\right)\psi_\alpha = 0, \tag{B.21}$$

- a normalisation condition

$$\langle\psi_\alpha, \psi_\beta\rangle = \delta_{\alpha\beta}, \text{ where } \langle\psi_\alpha, \psi_\beta\rangle := \int_{y=Y_-}^{Y_+}\int_{x=X_-}^{X_+} \psi_\alpha\psi_\beta \, \mathrm{d}x\mathrm{d}y, \tag{B.22}$$

- and Neumann conditions on the duct walls (which ensures that the requisite Sturm–Liouville properties hold, while maintaining consistency with the no-penetration condition)

$$\left.\frac{\partial\psi_\alpha}{\partial x}\right|_{x=X_\pm} = 0, \quad \left.\frac{\partial\psi_\alpha}{\partial y}\right|_{y=Y_\pm} = 0. \tag{B.23}$$

Solutions to the Helmholtz equation are quantised by the boundary conditions, giving solutions

$$\psi_\alpha = \frac{C_\alpha}{\sqrt{XY}} \cos\left[\frac{\lambda^x_\alpha(x - X_-)}{X}\right] \cos\left[\frac{\lambda^y_\alpha(y - Y_-)}{Y}\right], \quad \lambda^x_\alpha = p_\alpha\pi, \quad \lambda^y_\alpha = q_\alpha\pi, \tag{B.24}$$

for $\alpha \in \mathbb{N}_0$ (with the $1/\sqrt{X}$ scaling being deduced from the form of the inner product). Integrating two solutions together will determine C_α to be $\sqrt{(2 - \delta_{p_\alpha 0})(2 - \delta_{q_\alpha} 0)}$. Modes are ordered in groups corresponding to the combined modenumber $p_\alpha + q_\alpha$, with intra-group ordering by increasing q_α (so for example, the first few modes have (p_α, q_α) values (0,0), (1,0), (0,1), (2,0), (1,1), (0,2) etc.).

B.4 Spatial Projection

We can then project these equations onto the basis modes, applying the boundary conditions as we do so. We make use of the following formulae along the way

$$\nabla_t(h^\perp_s \nabla_t f) = h^\perp_s \nabla^2_t f - \kappa \frac{\partial f}{\partial \mathbf{n}^\perp}, \tag{B.25a}$$

$$\iint_S f\nabla_t^2 g \mathrm{d}S = \left[\int_{Y_-}^{Y_+} f\frac{\partial g}{\partial x} - \frac{\partial f}{\partial x} g \mathrm{d}y\right]_{X_-}^{X_+} + \left[\int_{X_-}^{X_+} f\frac{\partial g}{\partial y} - \frac{\partial f}{\partial y} g \mathrm{d}x\right]_{Y_-}^{Y_+} + \iint_S g\nabla_t^2 f \mathrm{d}S, \tag{B.25b}$$

$$\iint_S f\frac{\partial g}{\partial \mathbf{n}^\perp}\mathrm{d}S = \left[\int_{Y_-}^{Y_+} \cos\theta_0 f g \mathrm{d}y\right]_{X_-}^{X_+} + \left[\int_{X_-}^{X_+} \sin\theta_0 f g \mathrm{d}x\right]_{Y_-}^{Y_+} - \iint_S g\frac{\partial f}{\partial \mathbf{n}^\perp}\mathrm{d}S. \tag{B.25c}$$

We will also use Ψ notation, with curly brackets denoting s-derivatives and $|\cdot|$ denoting a Frenet-Serret normal derivative as before. Similarly to the 2D derivation, square brackets are x-derivatives; additionally, round brackets are now y-derivatives.

The algebra will not be covered in detail here, but the derivation is similar to the 3D circular-cross-sectional case. The resulting equations are

$$\begin{aligned}
&\left[\delta_{\alpha\beta}\frac{\mathrm{d}}{\mathrm{d}s} - \Psi_{\{\alpha\}\beta} - (\tau - \theta_0')\left(\Psi_{[\alpha]\beta}[y] - \Psi_{(\alpha)\beta}[x] - \Psi_{\alpha\beta}\left[\frac{(y\partial_x - x\partial_y)h_s^\perp}{h_s^\perp}\right]\right)\right]\widetilde{U}_\beta^a \\
&\qquad - \mathrm{i}a\omega\left[\left(1 - \frac{\lambda_\alpha^{x\,2}/X^2 + \lambda_\alpha^{y\,2}/Y^2}{a^2\omega^2}\right)\Psi_{\alpha\beta}[h_s^\perp] - \frac{\kappa}{a^2\omega^2}\Psi_{|\alpha|\beta}\right]P_\beta^a \\
&\qquad\qquad = \mathrm{i}a\omega\sum_b\Bigg\{ - \beta_0\Psi_{\alpha\beta\gamma}[h_s^\perp]P_\beta^{a-b}P_\gamma^b \\
&\quad + \left[\left(1 + \frac{\lambda_\alpha^{x\,2}/X^2 + \lambda_\alpha^{y\,2}/Y^2}{a^2\omega^2}\right)\Psi_{\alpha\beta\gamma}[h_s^\perp] + \frac{\kappa}{a^2\omega^2}\Psi_{|\alpha|\beta\gamma}\right]\frac{P_\beta^{a-b}P_\gamma^b - \widetilde{U}_\beta^{a-b}\widetilde{U}_\gamma^b}{2} \\
&\qquad + \left[\left(1 + \frac{\lambda_\alpha^{x\,2}/X^2 + \lambda_\alpha^{y\,2}/Y^2}{a^2\omega^2}\right)\left(\Psi_{\alpha[\beta][\gamma]}[h_s^\perp] + \Psi_{\alpha(\beta)(\gamma)}[h_s^\perp]\right)\right. \\
&\qquad\qquad\qquad \left. + \frac{\kappa}{a^2\omega^2}\left(\Psi_{|\alpha|[\beta][\gamma]} + \Psi_{|\alpha|(\beta)(\gamma)}\right)\right]\frac{P_\beta^{a-b}P_\gamma^b}{2(a-b)b\omega^2}\Bigg\},
\end{aligned} \tag{B.26a}$$

$$\begin{aligned}
&\left[\delta_{\alpha\beta}\frac{\mathrm{d}}{\mathrm{d}s} + \Psi_{\alpha\{\beta\}} + (\tau - \theta_0')\left(\Psi_{\alpha[\beta]}[y] - \Psi_{\alpha(\beta)}[x]\right)\right]P_\beta^a - \mathrm{i}a\omega\Psi_{\alpha\beta}[h_s^\perp]\widetilde{U}_\beta^a \\
&\qquad = \Bigg\{X_+'\Psi^+_{[\alpha\beta\gamma]} - X_-'\Psi^-_{[\alpha\beta\gamma]} + Y_+'\Psi^+_{(\alpha\beta\gamma)} - Y_-'\Psi^-_{(\alpha\beta\gamma)} \\
&\quad - (\tau - \theta_0')\left(\Psi_{[\alpha\beta\gamma]}[y] - \Psi_{(\alpha\beta\gamma)}[x] - \Psi_{\alpha\beta\gamma}\left[\frac{(y\partial_x - x\partial_y)h_s^\perp}{h_s^\perp}\right]\right)\Bigg\}\sum_b\widetilde{U}_\beta^{a-b}\widetilde{U}_\gamma^b \\
&\qquad + \mathrm{i}\omega\sum_b\Bigg\{\Psi_{\alpha\beta\gamma}[h_s^\perp]\left[(a-b) - b\left(1 - \frac{\lambda_\gamma^{x\,2}/X^2 + \lambda_\gamma^{y\,2}/Y^2}{b^2\omega^2}\right)\right] \\
&\qquad\qquad + \frac{1}{b\omega^2}\left(\Psi_{\alpha[\beta][\gamma]}[h_s^\perp] + \Psi_{\alpha(\beta)(\gamma)}[h_s^\perp]\right)\Bigg\}\widetilde{U}_\beta^{a-b}P_\gamma^b.
\end{aligned} \tag{B.26b}$$

We also have the following formulae resulting from the Leibniz rule:

$$\begin{aligned}
\Psi_{\alpha[\beta][\gamma]}[h_s^{\perp}] + \Psi_{\alpha(\beta)(\gamma)}[h_s^{\perp}] =& \frac{1}{2}\Psi_{\alpha\beta\gamma}[h_s^{\perp}]\left(\frac{\lambda_{\beta}^{x\,2} + \lambda_{\gamma}^{x\,2} - \lambda_{\alpha}^{x\,2}}{X^2} + \frac{\lambda_{\beta}^{y\,2} + \lambda_{\gamma}^{y\,2} - \lambda_{\alpha}^{y\,2}}{Y^2}\right) \\
&+ \frac{\kappa\cos\theta_0}{2}\Psi_{[\alpha\beta\gamma]} + \frac{\kappa\sin\theta_0}{2}\Psi_{(\alpha\beta\gamma)} - \kappa\Psi_{|\alpha|\beta\gamma}, \qquad \text{(B.27a)} \\
\Psi_{|\alpha|[\beta][\gamma]} + \Psi_{|\alpha|(\beta)(\gamma)} =& \frac{1}{2}\Psi_{|\alpha|\beta\gamma}\left(\frac{\lambda_{\beta}^{x\,2} + \lambda_{\gamma}^{x\,2} - \lambda_{\alpha}^{x\,2}}{X^2} + \frac{\lambda_{\beta}^{y\,2} + \lambda_{\gamma}^{y\,2} - \lambda_{\alpha}^{y\,2}}{Y^2}\right) \\
&+ \frac{\lambda_{\alpha}^{x\,2}\cos\theta_0}{2X^2}\Psi_{[\alpha\beta\gamma]} + \frac{\lambda_{\alpha}^{y\,2}\sin\theta_0}{2Y^2}\Psi_{(\alpha\beta\gamma)}. \qquad \text{(B.27b)}
\end{aligned}$$

Progress has been made on this problem through the use of the modified velocity, but there are two terms where an $h_s^{\perp}$ remains in the denominator of an integral kernel. The resulting integrals will need calculation at multiple points in the duct, possibly making computations much slower. Moving ahead in spite of these, we arrive at the form of the equations used for the other geometries

$$\begin{aligned}
&\Bigg[\frac{\mathrm{d}}{\mathrm{d}s} + \frac{X'}{2X}\mathsf{W}^x + \frac{X'_-}{X}\widetilde{\mathsf{A}}^x + \frac{Y'}{2Y}\mathsf{W}^y + \frac{Y'_-}{Y}\widetilde{\mathsf{A}}^y \qquad \text{(B.28a)} \\
&\qquad - (\tau - \theta_0')\left(\mathsf{R} + \frac{Y_-}{Y}\widetilde{\mathsf{A}}^x - \frac{X_-}{X}\widetilde{\mathsf{A}}^y - \mathsf{F}(\theta_0, \kappa X, \kappa Y, \kappa X_-, \kappa Y_-)\right)\Bigg]\widetilde{\boldsymbol{u}}^a \\
&-\mathrm{i}a\omega\Bigg[\left(\mathsf{I} - \frac{\mathsf{\Lambda}^{x2}/X^2 + \mathsf{\Lambda}^{y2}/Y^2}{a^2\omega^2}\right)\Bigg((1 - \kappa\left[X_-\cos\theta_0 + Y_-\sin\theta_0\right])\mathsf{I} \\
&\qquad - \kappa\left[X\cos\theta_0\mathsf{A}^x + Y\sin\theta_0\mathsf{A}^y\right]\Bigg) - \frac{\kappa}{a^2\omega^2}\left(\frac{\cos\theta_0}{X}\widetilde{\mathsf{A}}^x + \frac{\sin\theta_0}{Y}\widetilde{\mathsf{A}}^y\right)\Bigg]\boldsymbol{p}^a \\
&= \frac{\mathrm{i}a\omega}{\sqrt{XY}}\sum_b\Bigg\{ - \beta_0\Bigg((1 - \kappa\left[X_-\cos\theta_0 + Y_-\sin\theta_0\right])\mathcal{I} \\
&\qquad\qquad - \kappa\left[X\cos\theta_0\mathcal{A}^x + Y\sin\theta_0\mathcal{A}^y\right]\Bigg)\langle\boldsymbol{p}^{a-b}, \boldsymbol{p}^b\rangle \\
&\quad + \Bigg[\left(\mathsf{I} + \frac{\mathsf{\Lambda}^{x2}/X^2 + \mathsf{\Lambda}^{y2}/Y^2}{a^2\omega^2}\right)\Bigg((1 - \kappa\left[X_-\cos\theta_0 + Y_-\sin\theta_0\right])\mathcal{I} \\
&\qquad -\kappa\left[X\cos\theta_0\mathcal{A}^x + Y\sin\theta_0\mathcal{A}^y\right]\Bigg) + \frac{\kappa}{a^2\omega^2}\left(\frac{\cos\theta_0}{X}\widetilde{\mathcal{A}}^x + \frac{\sin\theta_0}{Y}\widetilde{\mathcal{A}}^y\right)\Bigg] \\
&\qquad\qquad \times \frac{\langle\boldsymbol{p}^{a-b}, \boldsymbol{p}^b\rangle - \langle\widetilde{\boldsymbol{u}}^{a-b}, \widetilde{\boldsymbol{u}}^b\rangle}{2}
\end{aligned}$$

$$
\begin{aligned}
&+\Bigg[\left(\mathsf{I}+\frac{\mathsf{\Lambda}^{x2}/X^2+\mathsf{\Lambda}^{y2}/Y^2}{a^2\omega^2}\right)\Bigg(\left(1-\kappa\left[X_-\cos\theta_0+Y_-\sin\theta_0\right]\right)\left(\frac{\mathcal{I}^{\lambda^x}}{X^2}+\frac{\mathcal{I}^{\lambda^y}}{Y^2}\right)\\
&\quad-\kappa\left[X\cos\theta_0\left(\frac{\mathcal{A}^{x,\lambda^x}}{X^2}+\frac{\mathcal{A}^{x,\lambda^y}}{Y^2}\right)+Y\sin\theta_0\left(\frac{\mathcal{A}^{y,\lambda^x}}{X^2}+\frac{\mathcal{A}^{y,\lambda^y}}{Y^2}\right)\right]\Bigg)\\
&\qquad+\frac{\kappa}{a^2\omega^2}\left(\frac{\cos\theta_0}{X}\left[\frac{\widetilde{\mathcal{A}}^{x,\lambda^x}}{X^2}+\frac{\widetilde{\mathcal{A}}^{x,\lambda^y}}{Y^2}\right]+\frac{\sin\theta_0}{Y}\left[\frac{\widetilde{\mathcal{A}}^{y,\lambda^x}}{X^2}+\frac{\widetilde{\mathcal{A}}^{y,\lambda^y}}{Y^2}\right]\right)\Bigg]\frac{\langle\boldsymbol{p}^{a-b},\boldsymbol{p}^b\rangle}{2(a-b)b\omega^2}\Bigg\},
\end{aligned}
$$

$$
\begin{aligned}
&\left[\frac{\mathrm{d}}{\mathrm{d}s}-\frac{X'}{2X}(\mathsf{W}^x)^{\mathrm{T}}-\frac{X'_-}{X}(\widetilde{\mathsf{A}}^x)^{\mathrm{T}}-\frac{Y'}{2Y}(\mathsf{W}^y)^{\mathrm{T}}-\frac{Y'_-}{Y}(\widetilde{\mathsf{A}}^y)^{\mathrm{T}}\right. \qquad\qquad \text{(B.28b)}\\
&\qquad\qquad\left.+(\tau-\theta_0')\left(\mathsf{R}^{\mathrm{T}}+\frac{Y_-}{Y}(\widetilde{\mathsf{A}}^x)^{\mathrm{T}}-\frac{X_-}{X}(\widetilde{\mathsf{A}}^y)^{\mathrm{T}}\right)\right]\boldsymbol{p}^a\\
&\quad-\mathrm{i}a\omega\Big[\left(1-\kappa\left[X_-\cos\theta_0+Y_-\sin\theta_0\right]\right)\mathsf{I}-\kappa\left[X\cos\theta_0\mathsf{A}^x+Y\sin\theta_0\mathsf{A}^y\right]\Big]\widetilde{\boldsymbol{u}}^a\\
&=\frac{1}{\sqrt{XY}}\sum_b\Bigg\{\Bigg[\frac{X'_+}{X}\overline{\mathcal{W}}^{x+}-\frac{X'_-}{X}\overline{\mathcal{W}}^{x-}+\frac{Y'_+}{Y}\overline{\mathcal{W}}^{y+}-\frac{Y'_-}{Y}\overline{\mathcal{W}}^{y-}\\
&\quad-(\tau-\theta_0')\left(\frac{Y\overline{\mathcal{R}}^x+Y_-\overline{\mathcal{A}}^x}{X}-\frac{X\overline{\mathcal{R}}^y+X_-\overline{\mathcal{A}}^y}{Y}-\mathcal{F}(\theta_0,\kappa X,\kappa Y,\kappa X_-,\kappa Y_-)\right)\Bigg]\langle\widetilde{\boldsymbol{u}}^{a-b},\widetilde{\boldsymbol{u}}^b\rangle\\
&\quad+\mathrm{i}\omega\Bigg[\Big(\left(1-\kappa\left[X_-\cos\theta_0+Y_-\sin\theta_0\right]\right)\mathcal{I}-\kappa\left(X\cos\theta_0\mathcal{A}^x+Y\sin\theta_0\mathcal{A}^y\right)\Big)\\
&\qquad\qquad\times\left\langle\mathsf{I},(a-b)\mathsf{I}-b\left(\mathsf{I}-\frac{\mathsf{\Lambda}^{x2}/X^2+\mathsf{\Lambda}^{y2}/Y^2}{b^2\omega^2}\right)\right\rangle\\
&\qquad+\frac{1}{b\omega^2}\Bigg(\left(1-\kappa\left[X_-\cos\theta_0+Y_-\sin\theta_0\right]\right)\left(\frac{\mathcal{I}^{\lambda^x}}{X^2}+\frac{\mathcal{I}^{\lambda^y}}{Y^2}\right)\\
&\qquad-\kappa\left(X\cos\theta_0\left[\frac{\mathcal{A}^{x,\lambda^x}}{X^2}+\frac{\mathcal{A}^{x,\lambda^y}}{Y^2}\right]+Y\sin\theta_0\left[\frac{\mathcal{A}^{y,\lambda^x}}{X^2}+\frac{\mathcal{A}^{y,\lambda^y}}{Y^2}\right]\right)\Bigg)\Bigg]\langle\widetilde{\boldsymbol{u}}^{a-b},\boldsymbol{p}^b\rangle\Bigg\},
\end{aligned}
$$

where

$$
\begin{aligned}
\mathsf{I}&=\delta_{\alpha\beta}, & \widetilde{\mathsf{R}}_{\alpha\beta}&=\Xi_{[\alpha]\beta}H_{\alpha\beta}[\eta]-\Xi_{\alpha\beta}[\eta]H_{(\alpha)\beta}, && \text{(B.29a)}\\
\mathsf{W}^x_{\alpha\beta}&=\delta_{\alpha\beta}+2\Xi_{[\alpha]\beta}[\xi]H_{\alpha\beta}, & \mathsf{W}^y_{\alpha\beta}&=\delta_{\alpha\beta}+2\Xi_{\alpha\beta}H_{(\alpha)\beta}[\eta], && \text{(B.29b)}\\
\mathsf{A}^x_{\alpha\beta}&=\Xi_{\alpha\beta}[\xi]H_{\alpha\beta}, & \mathsf{A}^y_{\alpha\beta}&=\Xi_{\alpha\beta}H_{\alpha\beta}[\eta], && \text{(B.29c)}\\
\widetilde{\mathsf{A}}^x_{\alpha\beta}&=\Xi_{[\alpha]\beta}H_{\alpha\beta}, & \widetilde{\mathsf{A}}^y_{\alpha\beta}&=\Xi_{\alpha\beta}H_{(\alpha)\beta}, && \text{(B.29d)}\\
\mathcal{I}_{\alpha\beta\gamma}&=\Xi_{\alpha\beta\gamma}H_{\alpha\beta\gamma}, & & && \text{(B.29e)}\\
\mathcal{A}^x_{\alpha\beta\gamma}&=\Xi_{\alpha\beta\gamma}[\xi]H_{\alpha\beta\gamma}, & \mathcal{A}^y_{\alpha\beta\gamma}&=\Xi_{\alpha\beta\gamma}H_{\alpha\beta\gamma}[\eta],] && \text{(B.29f)}\\
\widetilde{\mathcal{A}}^x_{\alpha\beta\gamma}&=\Xi_{[\alpha]\beta\gamma}H_{\alpha\beta\gamma}, & \widetilde{\mathcal{A}}^y_{\alpha\beta\gamma}&=\Xi_{\alpha\beta\gamma}H_{(\alpha)\beta\gamma}, && \text{(B.29g)}\\
\overline{\mathcal{A}}^x_{\alpha\beta\gamma}&=\Xi_{[\alpha\beta\gamma]}H_{\alpha\beta\gamma}, & \overline{\mathcal{A}}^y_{\alpha\beta\gamma}&=\Xi_{\alpha\beta\gamma}H_{(\alpha\beta\gamma)}, && \text{(B.29h)}
\end{aligned}
$$

$$\overline{\mathcal{W}}^{x+}_{\alpha\beta\gamma} = \Xi^{+}_{[\alpha\beta\gamma]}, \qquad \overline{\mathcal{W}}^{y+}_{\alpha\beta\gamma} = \Xi^{+}_{\alpha\beta\gamma} H^{+}_{(\alpha\beta\gamma)}, \tag{B.29i}$$

$$\overline{\mathcal{W}}^{x-}_{\alpha\beta\gamma} = \Xi^{-}_{[\alpha\beta\gamma]} H_{\alpha\beta\gamma}, \qquad \overline{\mathcal{W}}^{y-}_{\alpha\beta\gamma} = \Xi^{-}_{\alpha\beta\gamma} H^{-}_{(\alpha\beta\gamma)}, \tag{B.29j}$$

$$\overline{\mathcal{R}}^{x}_{\alpha\beta\gamma} = \Xi_{[\alpha\beta\gamma]} H_{\alpha\beta\gamma}[\eta], \qquad \overline{\mathcal{R}}^{y}_{\alpha\beta\gamma} = \Xi_{\alpha\beta\gamma}[\xi] H_{(\alpha\beta\gamma)}, \tag{B.29k}$$

and

$$\mathcal{I}^{\lambda^x} = \mathcal{I}\frac{\langle(\mathsf{\Lambda}^x)^2, \mathsf{I}\rangle + \langle\mathsf{I}, (\mathsf{\Lambda}^x)^2\rangle - (\mathsf{\Lambda}^x)^2}{2}, \tag{B.29l}$$

$$\mathcal{I}^{\lambda^y} = \mathcal{I}\frac{\langle(\mathsf{\Lambda}^y)^2, \mathsf{I}\rangle + \langle\mathsf{I}, (\mathsf{\Lambda}^y)^2\rangle - (\mathsf{\Lambda}^y)^2}{2}, \tag{B.29m}$$

$$\mathcal{A}^{x,\lambda^x} = \mathcal{A}^x\frac{\langle(\mathsf{\Lambda}^x)^2, \mathsf{I}\rangle + \langle\mathsf{I}, (\mathsf{\Lambda}^x)^2\rangle - (\mathsf{\Lambda}^x)^2}{2} + \widetilde{\mathcal{A}}^x - \frac{\overline{\mathcal{A}}^x}{2}, \tag{B.29n}$$

$$\mathcal{A}^{x,\lambda^y} = \mathcal{A}^x\frac{\langle(\mathsf{\Lambda}^y)^2, \mathsf{I}\rangle + \langle\mathsf{I}, (\mathsf{\Lambda}^y)^2\rangle - (\mathsf{\Lambda}^y)^2}{2} \tag{B.29o}$$

$$\mathcal{A}^{y,\lambda^x} = \mathcal{A}^y\frac{\langle(\mathsf{\Lambda}^x)^2, \mathsf{I}\rangle + \langle\mathsf{I}, (\mathsf{\Lambda}^x)^2\rangle - (\mathsf{\Lambda}^x)^2}{2} \tag{B.29p}$$

$$\mathcal{A}^{y,\lambda^y} = \mathcal{A}^y\frac{\langle(\mathsf{\Lambda}^y)^2, \mathsf{I}\rangle + \langle\mathsf{I}, (\mathsf{\Lambda}^y)^2\rangle - (\mathsf{\Lambda}^y)^2}{2} + \widetilde{\mathcal{A}}^y - \frac{\overline{\mathcal{A}}^y}{2}, \tag{B.29q}$$

$$\widetilde{\mathcal{A}}^{x,\lambda^x} = \widetilde{\mathcal{A}}^x\frac{\langle(\mathsf{\Lambda}^x)^2, \mathsf{I}\rangle + \langle\mathsf{I}, (\mathsf{\Lambda}^x)^2\rangle - (\mathsf{\Lambda}^x)^2}{2} + \frac{(\mathsf{\Lambda}^x)^2}{2}\overline{\mathcal{A}}^x, \tag{B.29r}$$

$$\widetilde{\mathcal{A}}^{x,\lambda^y} = \widetilde{\mathcal{A}}^x\frac{\langle(\mathsf{\Lambda}^y)^2, \mathsf{I}\rangle + \langle\mathsf{I}, (\mathsf{\Lambda}^y)^2\rangle - (\mathsf{\Lambda}^y)^2}{2}, \tag{B.29s}$$

$$\widetilde{\mathcal{A}}^{y,\lambda^x} = \widetilde{\mathcal{A}}^y\frac{\langle(\mathsf{\Lambda}^x)^2, \mathsf{I}\rangle + \langle\mathsf{I}, (\mathsf{\Lambda}^x)^2\rangle - (\mathsf{\Lambda}^x)^2}{2}, \tag{B.29t}$$

$$\widetilde{\mathcal{A}}^{y,\lambda^y} = \widetilde{\mathcal{A}}^y\frac{\langle(\mathsf{\Lambda}^y)^2, \mathsf{I}\rangle + \langle\mathsf{I}, (\mathsf{\Lambda}^y)^2\rangle - (\mathsf{\Lambda}^y)^2}{2} + \frac{(\mathsf{\Lambda}^y)^2}{2}\overline{\mathcal{A}}^y. \tag{B.29u}$$

The two unsplittable integrals are (not to be confused with the restriction operator in chapter 5)

$$\mathsf{F}_{\alpha\beta}(\theta_0, \kappa X, \kappa Y, \kappa X_-, \kappa Y_-) = \Psi_{\alpha\beta}\left[\frac{(y\partial_x - x\partial_y)h^{\perp}_s}{h^{\perp}_s}\right], \tag{B.30a}$$

$$\mathcal{F}_{\alpha\beta\gamma}(\theta_0, \kappa X, \kappa Y, \kappa X_-, \kappa Y_-) = \sqrt{XY}\,\Psi_{\alpha\beta\gamma}\left[\frac{(y\partial_x - x\partial_y)h^{\perp}_s}{h^{\perp}_s}\right]. \tag{B.30b}$$

This calculation has reached a point equivalent to the end of section 2.1, i.e. before the admittance is introduced. At this point, one could easily introduce L^a and $\mathcal{N}^{ab}$ tensors and derive a Riccati-style system for the admittance in terms of those tensors' sub-blocks; however, solution of the system for a general geometry would be greatly slowed down due to the need to calculate F and $\mathcal{F}$ at every step. Programming in a more memory-efficient language or somehow reformulating the equations to disentangle the s-dependent scalar quantities θ_0, κ, X and Y from the tensors F and $\mathcal{F}$ would be the next step towards a viable numerical implementation of this appendix's work.